CARBON NANOTUBES: CHEMICAL VAPOR DEPOSITION SYNTHESIS AND APPLICATION IN ELECTROCHEMICAL DOUBLE LAYER SUPERCAPACITORS

A Thesis
Presented to
The Academic Faculty

by

Stephan Parker Turano

In Partial Fulfillment
of the Requirements for the Degree
Master of Science in Materials Science and Engineering

Georgia Institute of Technology
May 2005

CARBON NANOTUBES: CHEMICAL VAPOR DEPOSITION SYNTHESIS AND APPLICATION IN ELECTROCHEMICAL DOUBLE LAYER SUPERCAPACITORS

Approved by:

Dr. Jud Ready, Chairman
School of Materials Science and Engineering
Georgia Institute of Technology

Dr. W. Brent Carter
School of Materials Science and Engineering
Georgia Institute of Technology

Dr. Robert Snyder
School of Materials Science and Engineering
Georgia Institute of Technology

Dr. Zhong .L. Wang
School of Materials Science and Engineering
Georgia Institute of Technology

Date Approved: February 10, 2005

ACKNOWLEDGEMENTS

The author would like to express his genuine appreciation to his thesis advisor, Dr. W. Jud Ready for his wisdom, support, and patience without which the present work would have gone unfulfilled.

The author would also like to express his gratitude to his committee members, Drs. W. Brent Carter, Bob Snyder, Z.L. Wang for their interest in the work. The time commitment and knowledge given by the committee members during both his undergraduate and graduate studies helped immensely in the completion of this work.

Additional thanks goes to Mr. Mike Harris and Mr. Stan Halpern of the Georgia Tech Research Institute (GTRI) for providing materials and supplies, as well as state of the art laboratory facilities and assistance.

The author wishes to recognize Dr. Samuel Graham for providing some of the catalyst materials used in the present work, as well as insight provided through collaboration and brainstorming.

More over, the author acknowledges Dr. Linda Zhong and Maxwell Technologies for generously providing sample Electrochemical Double Layer (ECDL) ultracapacitors and testing carbon nanotube based ECDL supercapacitors.

The author wishes to thank Mr. Charlie Higgins for his contributions to the present work. He would also like to recognize Victor Kumsomboone, Erik Sunden, and Jake Thompkins for further assistance with the present work.

The author wishes to sincerely thank both Mr. Thomas and Mrs. Nancy Turano, and additionally Ms. Abby Gibson for their encouragement, support, and patience throughout the work, which was greatly appreciated.

TABLE OF CONTENTS

LIST OF TABLES

LIST OF FIGURES

LIST OF ABBREVIATIONS

μm:	Micrometer
A:	Area
Å:	Angstrom
AC:	Activated Carbon
AcHYCNT:	Acetylene Gas, High Yield Carbon Nanotubes
AcUHYCNT:	Acetylene Gas, Ultra High Yield Carbon Nanotubes
AFM:	Atomic Force Microscope
BET:	Brunauer Emmett Teller
C_{60}:	Symbol for a Carbon-60 Buckminsterfullerene Molecule
CNTs:	Carbon Nanotubes
Co:	Atomic Symbol for Cobalt
CS_2:	Symbol for a Carbon Sulfide Molecule
CVD:	Chemical Vapor Deposition
DC:	Direct Current
d_D:	Helmholtz Distance
DOS:	Density of States
e^-:	Symbol for an Electron
ECDL:	Electrochemical Double Layer
Fe:	Atomic Symbol for Iron
GTRI:	Georgia Tech Research Institute
H_2O:	Symbol for a Water Molecule
H_2O_2:	Symbol for a Hydrogen Peroxide Molecule
HiPCO:	High Pressure Carbon Monoxide
HPCNT:	High Purity Carbon Nanotube
HYCNT:	High Yield Carbon Nanotube
Hz:	Hertz
IPA:	Isopropyl Alcohol
IUPAC:	International Union of Pure and Applied Chemistry
KOH:	Symbol for a Potassium Hydroxide Molecule

LLNL:	Lawrence Livermore National Laboratory
MEMS:	Micro Electrical Mechanical Systems
MnO_2:	Symbol for a Manganese Dioxide Molecule
MWNT:	Multi Walled Nanotube
NH_4OH:	Symbol for a Ammonium Hydroxide
Ni:	Atomic Symbol for Nickel
nm:	Nanometer
OH^-:	Symbol for a Hydroxide Molecule
PECVD:	Plasma Enhanced Chemical Vapor Deposition
sccm:	Standard Cubic Centimeters
SEM:	Scanning Electron Microscope
Si:	Atomic Symbol for Silicon
SiO_2:	Symbol for a Silicon Dioxide Molecule
STM:	Scanning Tunneling Microscope
SWNT:	Single Walled Nanotube
TCE:	Tetracholoroethanol
TEM:	Transmission Electron Microscope
UHYCNT:	Ultra High Yield Carbon Nanotubes
Zn:	Atomic Symbol for Zinc
ϵ_0:	Permittivity Constant of Free Space
ϵ_r:	Relative Permittivity of a Dielectric

SUMMARY

Carbon nanotubes (CNTs) have become a popular area of materials science research due to their outstanding material properties coupled with their small size. CNTs are expected to be included in a wide variety of applications and devices in the near future. Among these devices which are nearing mass production are electrochemical double layer (ECDL) supercapacitors. The current methods to produce CNTs are numerous, with each synthesis variable resulting in changes in the physical properties of the CNT.

A wide array of studies have focused on the effects of specific synthesis conditions. This research expands on earlier work done using bulk nickel catalyst, alumina supported iron catalyst, and standard chemical vapor deposition (CVD) synthesis methods. This work also investigates the effect of an applied voltage to the CVD chamber during synthesis on the physical nature of the CNTs produced. In addition, the work analyzes a novel nickel catalyst system, and the CNTs produced using this catalyst. The results of the effects of synthesis conditions on resultant CNTs are included. Additionally, CNT based ECDL supercapacitors were manufactured and tested.

Scanning electron microscope (SEM) analysis reveals that catalyst choice, catalyst thickness, synthesis temperature, and applied voltage have different results on CNT dimensions. Nanotube diameter distribution and average diameter data demonstrate the effect of each synthesis condition. Additionally, the concept of an alignment parameter is introduced in order to quantify the effect of an electric field on CNT alignment. CNT based ECDL supercapacitors testing reveals that CNTs work well as an

active material when a higher purity is achieved. The molarity of the electrolyte also has an effect on the performance of CNT based ECDL supercapacitors.

On the basis of this research, we conclude that CNT physical dimensions can be moderately controlled based on the choice of synthesis conditions. Also, the novel nickel catalyst system investigated in this research has potential to produce bulk quantities of CNT under specific conditions. Finally, purified CNTs are recommended as a suitable active material for ECDL supercapacitors.

CHAPTER 1

INTRODUCTION

Carbon Nanotubes (CNTs) are one of the most renowned materials of the 21st century to date, due to their incredible material properties and to their nanoscale size. Some applications incorporating CNTs already exist, such as composite tennis racquets and field emission displays. These devices do not utilize the nanosize of CNTs, but rather the bulk properties. In order to integrate CNTs into applications which take advantage of both nanotube size and properties, a logical approach which utilizes both top down techniques to create intelligent device substrates and bottom up synthesis of CNTs within the device architecture must be taken. Before CNTs can achieve integration into complex electronic, mechanical, biological or other devices, controlled synthesis of CNTs must be perfected.

Chemical Vapor Deposition (CVD) synthesis of carbon nanotubes requires several inherent synthesis conditions such as temperature, time, precursor gasses, and catalyst type. Furthermore, externally applied conditions could potentially have a drastic effect on the nanotubes synthesized. The driving force for the present work was to further understand the effect of synthesis conditions on the CNTs and to tailor these conditions in order to realize controlled and predictable production of CNTs.

Electrochemical double layer (ECDL) supercapacitors are an example of a device that would benefit from controlled synthesis utilizing both nanoscale and bulk CNT properties. Electrochemical double layer supercapacitor technology is a relatively novel development in the area of rechargeable electronic power sources. The need for alternatives to traditional power sources, has seen rapid growth in the past decades due to

concerns of pollution and exhaustion of fuel sources. Supercapacitors offer benefits over traditional capacitors and batteries, including: increased energy density, extended life cycle, higher power, and absence of an acid. CNTs offer ideal properties for use as the active material in supercapacitors. By exploiting their material properties, CNT based supercapacitors could help achieve the maximum theoretical performance of ECDL supercapacitors. The production and processing techniques used to create and refine CNTs are currently factors limiting the resulting CNT-based ECDL capacitor properties. The objectives of this portion of the work herein were (1) to analyze the effect of inherent necessary synthesis conditions on carbon nanotubes, (2) to analyze the effect of additional external synthesis controls on carbon nanotubes and (3) create and test ECDL supercapacitors based on CNTs and suggest CNT synthesis pathways which may enhance ECDL properties.

The background chapter discusses the intrinsic properties of CNTs, as well as the production techniques used to synthesize CNTs. Specific attention is paid to chemical vapor deposition as the preferred production mechanism used in the present work. The chapter also identifies aspects of production which result in material property changes.

This section also discusses the concept of charge storage, as well as current charge storage device technologies. Furthermore, supercapacitor concepts and the application of CNTs as an active material for ECDL supercapacitors are presented. Electrical testing methods for supercapacitors are also presented.

The next chapter offers a comprehensive description of the experimental procedures, and chapter four contains the results of these procedures. In brief, the influence of catalyst type and catalyst layer thickness on CNT diameter is analyzed, as

well as the effect on CNT alignment of an externally applied voltage during synthesis. Furthermore, the effects of precursor synthesis gasses, deposition temperature, and deposition time on resulting CNTs are studied.

The fifth chapter is a discussion of these results. The information collected during the present work provides direction for the appropriate selection of synthesis conditions in order to achieve an element of control on the resulting CNTs.

Chapter six states the conclusions of this project, specifically concentrating on the following points: (1) The state of the catalyst materials, and the synthesis precursor gasses play an important role in CNT physical properties, (2) external synthesis controls such as applied voltages do not significantly impact the resultant CNTs, and (3) nanosize Ni powder in solution with isopropyl alcohol represents a novel and efficient way to produce bulk CNTs.

The final chapter makes recommendations for future work, most notably including both top down techniques for CNT device synthesis such as electron beam lithography. Electron beam lithography procedures should be initiated in order to create intelligent device structures which can incorporate CNTs as functioning device components such as interconnects that advance integrated circuit technology beyond silicon.

CHAPTER 2

BACKGROUND

This chapter provides an overview of carbon nanotubes. It describes in detail the manufacturing process necessary to make CNTs, as well as the properties of CNTs. Chemical vapor deposition will be analyzed in depth, as CVD is the synthesis method used for CNTs in the experimental setup for this thesis. The final sections of this chapter discuss the importance of CNTs in devices such as an electrochemical double layer supercapacitor and field emitters.

Carbon nanotubes are one of the most promising materials in the history of mankind. The applications envisioned for CNT are almost endless. However, there are currently few examples of CNT in applications today due to the relatively new sciences surrounding their manufacture. Many challenges exist in finding practical ways to produce usable nanomaterials in a large capacity. For ECDL applications, CNTs are the key materials necessary to turn theory into reality. CNTs also have fantastic field emission properties that can be used in a variety of applications.

In order to advance technologies using CNTs, an understanding of synthesis conditions must be achieved. In addition, it is necessary to produce uniform properties in CNTs for a given set of synthesis conditions. Furthermore, in order to apply CNTs to devices, synthesis methods must be easily scaled from laboratory to industry scale.

ECDL supercapacitors are an emerging technology with little market share. However, there are a number of applications, including hybrid power devices, which envision the use of these supercapacitors in order to produce an efficient power source.

This section serves to investigate previous advances in this area, and introduce concepts which may make these advances occur.

2.1 Advanced Carbon Structures

2.1.1 Carbon Fullerenes

Carbon fullerenes are large, closed caged carbon structures in a spherical shape. Fullerenes, discovered in 1985, are stable in gas form and exhibit many unique properties that have not been found in other compounds.[1] Figure 1 is a representation of a C_{60} fullerene molecule. A fullerene is a spherical structure composed of both pentagonal and hexagonal carbon rings. Fullerenes are considered zero dimensional quantum structures which exhibit interesting quantum properties.

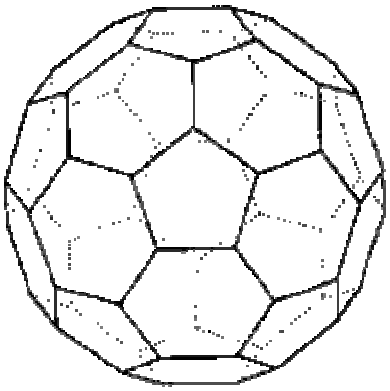

Figure 1: Representation of a Fullerene Molecule

2.1.2 Carbon Nanotubes

The first journal publication which alludes to carbon nanotubes appears to be from 1976 and discusses filamentous growth of carbon fibers through the decomposition

of benzene gas.[2] The next significant mention of nanotubes occurs in a 1987 patent, in which 'carbon fibrils' are produced in a catalytic procedure.[3] While the patent notes other instances of carbon fibril production, the patent notes that no description of the carbon fibrils is produced. It was not until 1991, when Iijima coined the term 'nanotubule' and provided high quality microscopic images, that significant interest in carbon nanomaterials began.[4]

Nanotubes are the one dimensional wire form of a fullerene; the diameter is typically one to several tens of nanometers (nm), while the length can be in the range of several micrometers (μm) to a few millimeters. Single walled nanotubes (SWNT) can be considered as a flat graphene sheet (Figure 2) cylindrically rolled into a tube. The tubes consist of two regions: the sidewall of the tube, and the end region of the tube, known as the tube tip or cap.

A significant physical property of the CNT is the tube tip. Tube tips may be open ended or close capped. Closed tips are "capped" with a structure that is similar to one half of a C_{60} fullerene molecule. The sidewalls of CNTs consist of only hexagonal carbon rings, whereas the end caps are made of pentagons and hexagons in order for curvature to exist. Due to the carbon-carbon bond symmetry of the cylindrical tube, CNT have a discreet number of directions that can form a closed cylinder (Figure 2).[5]

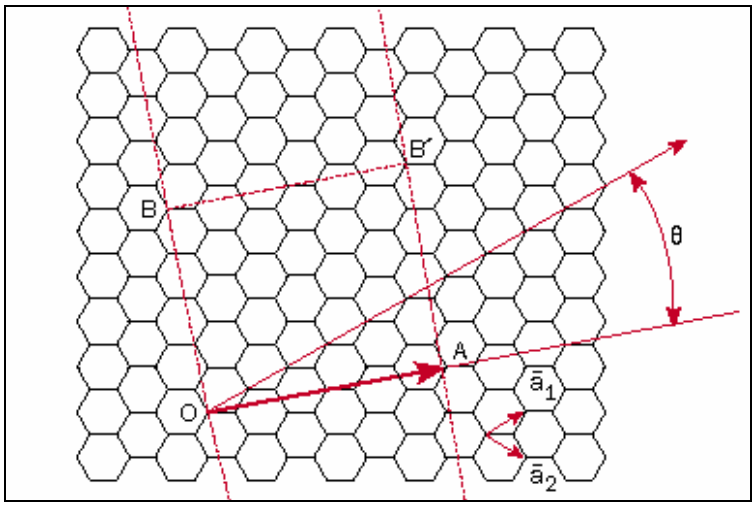

Figure 2: Graphene Sheet Illustrating Chiral Arrangements

In Figure 2, two atoms (O and A, or B and B') in the two dimensional graphene sheet are selected as the tube origin, and when the sheet is rolled, the two atoms coincide with one another. The vector OA is known as the "rollup" vector, whose length is equal to that of the circumference of the nanotube. The tube is created so that point O touches point A, and B touches B′. The tube axis is perpendicular to the rollup vector. The chiral vector of the nanotube, OA, can be defined by $C_h = n\hat{a}_1 + m\hat{a}_2$, where $\hat{a}_1$ and $\hat{a}_2$ are unit vectors in the two-dimensional hexagonal lattice, and *n* and *m* are integers. In Figure 2, n = 1 and m = 6.

Another important parameter is the chiral angle, θ, which is the angle between C_h and $\hat{a}_1$. All nanotubes can be described as having:

$$0° \leq \theta < 30° \qquad \text{(Eqn. 1)}$$

An individual CNT is known as a single walled nanotube (SWNT). Carbon atoms in single wall nanotubes (SWNTs) can be assigned to a coordinate system (n,m), with $m \leq n$ at all times. As chiral vectors change, nanotube properties change from metallic to semi-

conducting. Figure 3 shows which chiral vectors will result in semiconducting CNTs (squares in Figure 3) and which chiral vectors will result in metallic CNTs (circles in Figure 3). Approximately 70% of the chiral configurations result in semiconductor nanotubes. Although Figure 3 shows all co-ordinations of (n, m), not all of these chiralities have been observed in CNTs and the resulting conductive properties are based on theoretical calculations for these instances. The (n, 0) direction is known as a zigzag structure, while the n=m is denoted as an armchair structure (Figure 4).

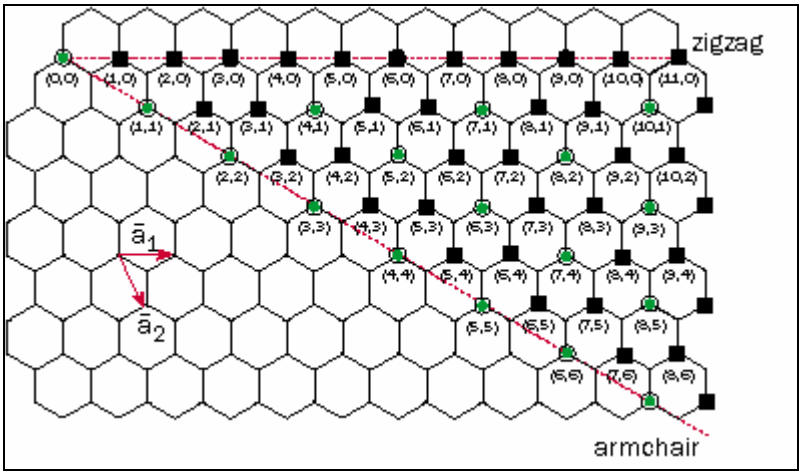

Figure 3: Possible Structures Based on Chiral Vectors for CNT. Squares Indicate Semiconducting CNT Chirality, Circles Indicate Metallic CNT Chirality

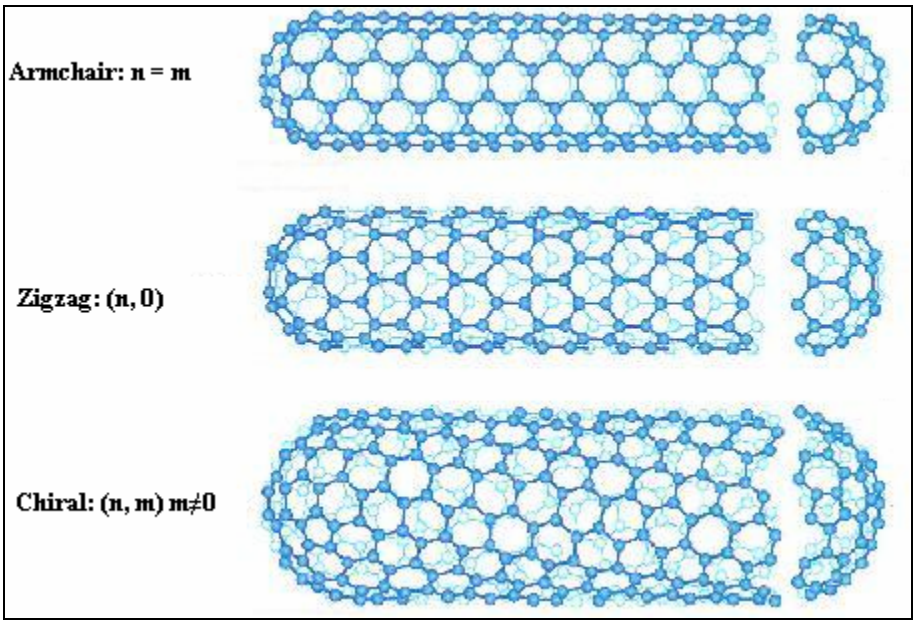

Figure 4: Armchair, Zigzag and Chiral Nanotubes

It should be noted that all armchair chiralities of CNT display metallic properties. In addition, chiral vectors with:

$$n - m = 3i \qquad \text{(Eqn. 2)}$$

where i is an integer value, yield metallic properties. All other arrangements of (n, m) in CNTs display semiconductor properties.

Chirality affects the electrical properties of nanotubes, as well as optical activity, mechanical strength, and various other properties. Deformations and defects in CNT can also have a profound impact on intrinsic properties. Junctions or bends in nanotubes can be introduced by the replacement of a hexagonal carbon ring with a pentagonal or heptagonal ring. Bends, which may be inward or outward, can severely affect the electrical conductivity of nanotubes. This is a concern in using CNTs in interconnect

applications, where CNTs may have to turn corners in order to accommodate the circuitry.

A common arrangement of CNTs is known as bundled SWNT. These are regular SWNT in very close proximity to one another, but the tubes do not share a wall. Multi-walled nanotubes (MWNT) are another regular type of fullerene structure. MWNT are concentric rings of SWNTs with different diameters centered about a common axis. Figure 5 shows Transmission Electron Microscope (TEM) images of isolated SWNT, bundled SWNT, and MWNT. Since the nested tubes in a MWNT structure are independent of one another, each tube has its own chiral vector, and therefore chiralities of individual tubes in a MWNT structure may be different.[6] Furthermore, since CNTs are simply rolled graphene sheets, the spacing between individual tubes in MWNT can be considered equal to the spacing of adjacent graphene layers in graphite, or approximately 0.34nm.[7]

In addition to these morphologies, several researchers have reported the synthesis of helical (or coiled) CNTs.[8] The first synthesis of coiled was accidental, and coiled CNTs usually appeared in low yields until recently.[9] Coiled CNTs are attractive materials for use in such application as micro electrical mechanical systems (MEMS). Furthermore, coiled CNTs possess better field emission properties than regular CNTs, and are being studied for field emission applications.[10]

2.1.3 Bonding in Carbon Nanotubes

Bonding in CNT is exactly as bonding of graphene sheets in graphite. Each carbon atom within the graphene sheet holds a covalent bond with three neighbor carbon

atoms. The bonds are due to the interaction of the each carbon atom's three sp^2 orbitals interacting with the sp^2 orbitals of neighboring carbon atoms. As a result, σ bonds are formed, and one 2p orbital is left un-hybridized. Individual tubes in MWNT experience only van der Waals forces between adjacent tube layers.

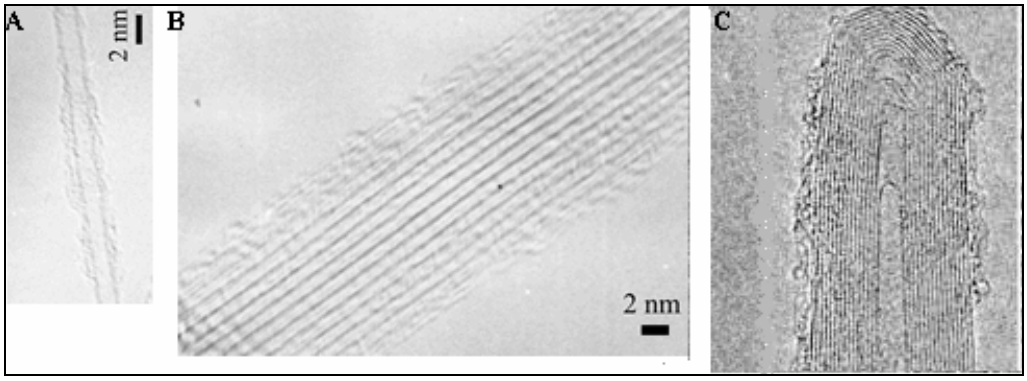

Figure 5: TEM Images of (A) SWNT, (B) Bundled SWNT, and (C) MWNT

2.1.4 Synthesis of Nanotubes

Carbon nanotubes are produced by three primary techniques: arc discharge, laser ablation, and chemical vapor deposition (CVD). Another process known as the High Pressure Carbon Monoxide (HiPCO) decomposition process is currently in use to produce bulk quantities of CNTs. This research, as with a significant amount of other CNT research being performed, will focus on CVD synthesis because this method can be easily extended into bulk production methods.[11] CVD is a widely used materials processing technology.[12] The main application of CVD involves applying thin film coatings to the surface of a bulk material. The CVD process, at the most basic level, is conducted by flowing precursor gasses into a chamber where a heated substrate is to be

coated. The energy supplied by heat is given to the gasses, causing chemical reactions to occur on or near the substrate surface. These chemical reactions result in the deposition of the constituents of the gas as a solid thin film onto the surface.

Carbon nanotube synthesis requires putting a gaseous carbon source into an atomically reactive phase. Typical precursor gasses used are acetylene, methane, carbon monoxide and various others carbon containing gasses. A heated coil, or other energy source, such as plasma, decomposes the source gas into reactive carbon atoms. The temperature of the substrate and CVD chamber is typically between 600 and 900° C. CVD synthesis can produce either multi walled nanotubes or single wall nanotubes based on the precursor gasses used, the gas flow rate, and the CVD furnace temperature. CVD synthesis creates some low quality, or impure, nanotubes which may contain chemical impurities such as catalyst particles, graphitic carbon particles, and amorphous carbon.[13] Another flaw of CVD produced CNT is the poorly defined graphene structure.[14]

Nanotube synthesis occurs on catalyst particles existing on the substrate. The only known pure metal catalysts producing practical CNTs are the transition metals Iron, Nickel, and Cobalt (many alloys containing these metals also work). Synthesis of SWNT can also take place on some complex polymer catalysts. Each catalyst has a different effect on the tubes that are synthesized. The catalyst can be applied to the substrate in a number of ways.[15] Catalysts may be sputtered or evaporated onto the substrate in the form of a thin film, and then catalyst particle nucleation is induced either by thermal annealing or chemical etching. The catalysts form small nanoclusters on the substrate. Cluster size can be controlled and can have a profound affect on nanotube properties.

Catalyst patterning may be achieved through several standard methods including photolithography, soft lithography, offset printing or catalyst self assembly.

Synthesis may also occur on gaseous catalyst particles. These gaseous catalysts are referred to as floating catalysts since they are not affixed to a deposition substrate. The most well known floating catalyst CVD synthesis method of CNTs is the HiPCO process. HiPCO synthesis utilizes ferrocene gas, which contains iron, as well as carbon monoxide gas. Other carrier gasses, such as xylene may be used as well. The process is performed under high pressure, and at temperatures typical to CVD processes. CNTs synthesized via the floating catalyst CVD method are usually deposited as a film on pristine substrates such as quartz glass.

2.1.5 Purification of Carbon Nanotubes

The poorly defined graphene structure of CNT produced by CVD is due to the relatively low synthesis temperature. A simple graphitization process can rectify this structural problem, and has also been shown to remove iron catalyst particles. The graphitization process is done by heating nanotubes in an inert atmosphere to 2600°C.

SWNT can be highly purified by hydrogen peroxide reflux with chemical washings followed by several filtration steps. Hydrogen Peroxide (H_2O_2) reflux reacts preferentially with amorphous carbon and removes most of this impurity. CNTs are next rinsed with carbon sulfide (CS_2), which removes excess fullerenes, and then rinsed in methanol. To remove nickel and cobalt catalyst particles, the nanotubes are filtered through 0.8- 2 μm porous membranes several times. Other common purification techniques include acid treatment, annealing, ultrasonication, micro filtration and

magnetic purification techniques. These methods involve separation of unwanted agglomerates and impurities, or complete removal of unwanted phases.

2.1.6 Nanotube Growth Mechanism

Although the exact mechanism for nanotube growth is unknown, CNT growth follows the well known growth process of macro sized graphitic carbon filaments on metal micro-particles.[16] As mentioned before, iron, nickel, and cobalt are the only known pure metal catalysts which assist in CNT growth. This is due to each metal's ability to (1) decompose volatile, atomically reactive carbon, and (2) to form meta-stable carbides.

Due to CNT catalyst metals ability to form carbides, ordered carbon can be produced through diffusion and precipitation over the metal particle. This means that graphitic structures, such as the graphene sheets composing CNT, only form near the metal particle. Reactions of the carbon precursor gases that occur further away from the metal catalyst lead to undesirable amorphous carbon impurities.

Carbon filament growth occurs on metal catalyst particles when the particle diameter size is on the order of a micron or smaller.[17] The resulting diameter of the carbon filament has a similar size. Filament growth occurs in two manners: (1) the metal catalyst particle remains in contact with the substrate, while a graphitic carbon filament grows upward (root growth), or (2) the catalyst particle is supported by the growing carbon tube (tip growth). Figure 6 shows these growth methods.

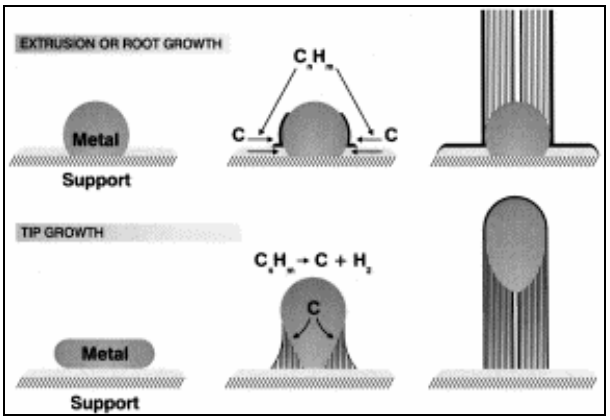

Figure 6: Growth Mechanisms of Carbon Filaments

Most models for CNT growth are based on the carbon filament model proposed by Baker, et al. According to that model, the hydrocarbon decompose at the surface of the catalyst. Carbon atom dissolve into the catalyst material, creating a solid solution. When the solution becomes supersaturated, carbon precipitates form at the surface of the catalyst. For carbon filaments, crystalline graphitic layers form. When CNT growth is occurring, the carbon precipitates form hexagonal carbon rings which arrange into tubular structures.[18]

Sinnot, et al. have presented results to backup the theory that CNT growth is related to carbon filament growth. The range of size of the metal catalyst particle in CNT synthesis is from a few nanometers to a few hundred nanometers. TEM observations show that iron catalyst particles remain in the enclosed end of the nanotube. The open ended side of the tube is in direct contact with the substrate, and contains no catalyst particle

Vinciguerra, et al.[19] suggest that tip growth or root growth of CNTs depends solely on the strength of the interaction of the catalyst particle with the substrate. Metal particles in poor mechanical contact with the substrate break off, and the resulting CNT

that form from the particle with grow directly from the substrate while supporting the particle (tip growth). Catalyst particles which are anchored to the substrate will remain in contact with the substrate, and resultant nanotubes will grow upwards from the particle (root growth).

The growth of coiled carbon microfibers is similar to carbon fiber growth as well. The difference between the extrusion (growth) rate is the cause for microfiber coiling. Fiber coils occur when the growth rate of regular fibers has been accelerated.[20] The mechanism for CNT coiling has not yet been completely clarified.[21]

2.1.7 Effect of Catalyst Type on Carbon Nanotube Growth

The metal catalyst used in CNT synthesis plays an important role in the resulting nanotube diameter, growth rate, wall thickness, morphology, and microstructure.[22] CNTs grown on nickel particles in a plasma enhanced CVD exhibit aligned growth perpendicular and vertical from the substrate. Nanotubes grown under the same conditions on iron or cobalt particles are generally kinked, twisted, or warped. The warped tubes exhibit openings in the sidewalls of the nanotubes. The defects in the CNTs grown from iron and cobalt particles are a result of non-uniform catalytic activity.

Catalyst type, as well as initial catalyst film thickness, directly affect CNT diameter. The initial catalyst film sputtered onto the substrate plays a key role in the resulting catalyst particle size.[23] Smaller initial film thickness results in smaller catalyst particle size. In turn, smaller particle size results in a smaller CNT tube diameter. As film thickness increases, nanotube diameter increases. For a uniform initial catalyst film thickness, CNTs grown on nickel result in larger tube diameters than for CNTs grown on

iron or cobalt. Tubes grown from iron exhibit a slightly larger diameter than those grown on cobalt.

It follows that the rate of CNT growth increases with catalyst size. Nickel catalysts yield the fastest growth rate, while iron exhibits a slightly higher growth rate than cobalt in a PECVD system.

2.1.8 Aligned Growth of Nanotubes

Substrate design and type play a crucial role in CNT growth. Recent research by Dai, et al.[24] has shown that with logical substrate design, CNTs can be grown in patterns, or directed to grow in a specific direction with the direct connection of an electric field. Suspended SWNT can be synthesized as suspended ropes over a specifically patterned substrate. Lithographically created silicon posts are stamped with polymer catalyst via contact printing. During CVD, SWNT grow from post to post, resembling power lines strung between poles. The nanotubes are self-oriented because of van der Waals interactions between the tubes and the posts.

Suspended SWNT can be aligned via an electric field, however the resulting nanotubes are parallel to the substrate, suspended over a trench like region. Dai, et al. [25] demonstrated this case in which Molybdenum electrode layers are deposited onto a silicon substrate with a thin thermal oxide layer. Catalyst is applied on the Mo electrode, and a field is applied during synthesis. The influence of the electric field causes the tubes to align, and grow straight across the gap between the catalyst posts (Figure 7). The growth is attributed to high polarizability and large induced dipole moments. Directed

growth for SWNT has high implications for quantum wire architecture and quantum wire devices.

MWNT can be grown in ordered arrays which result in three dimensional blocks of highly aligned MWNT. In this case, the substrate was patterned with square regions of Fe catalyst particles.[26] The resulting MWNT grew only on the patterned catalyst areas.

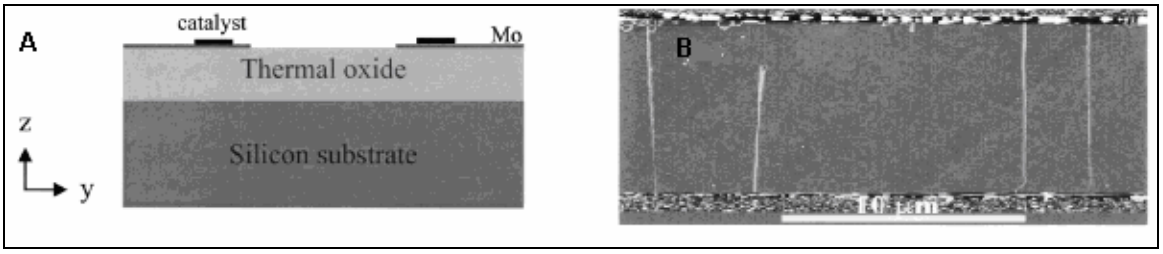

Figure 7: (A)Cross-Sectional View Substrate Prepared for Aligned, Suspended SWNT Growth, (B)Top Down View of CNTs Grown Under Influence of Electric Field[25]

Large arrays of aligned SWNTs without the influence of an electric field have been produced in a variety of ways. In general, CVD synthesis of aligned CNT arrays involves patterning catalyst on a porous silicon, porous silica or SiO_2 substrate. The resulting CNTs are repeatable blocks with a large degree of alignment perpendicular to the substrate (Figure 8).[26] It is important to note that while the arrays are well aligned, individual nanotubes still display a degree of anisotropy. Also note that all experiments producing self aligned SWNT in traditional CVD process result in arrays. Individually aligned tubes must be produced by a direct electrical contact as shown before, or with a more advance CVD process, such as plasma enhanced CVD (PECVD).

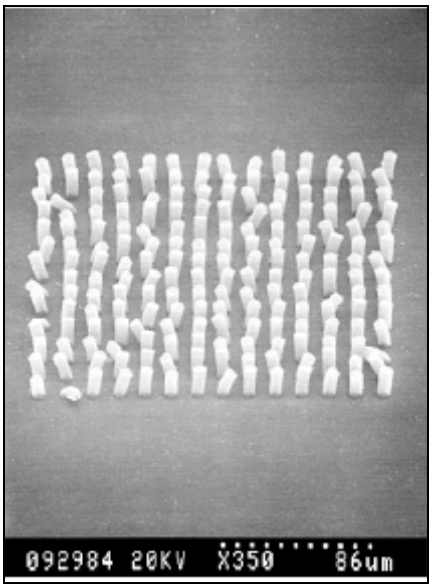

Figure 8: Arrays of Aligned SWNT Produced by CVD

Alignment of individual SWNT (Figure 9) has been shown by Ren, et al. by using PECVD in conjunction with an electrically biased hot filament.[14] The study showed that nickel catalyst particles resulted in better alignment than iron or cobalt catalyst particles.

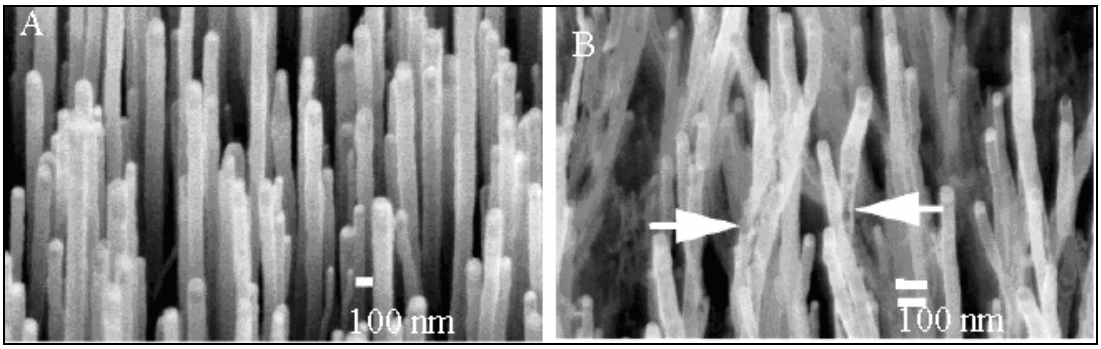

Figure 9: Aligned Individual SWNT (a) Nickel Catalyst (b) Iron Catalyst

2.2 Properties of Carbon Nanotubes

2.2.1 Chemical Reactivity

Compared to a graphene sheet, the reactivity of CNTs is high.[27] The enhancement in reactivity is due to the curvature of the tube. Increased curvature of a graphene sheet results in π bonding orbital mismatch (Figure 10).

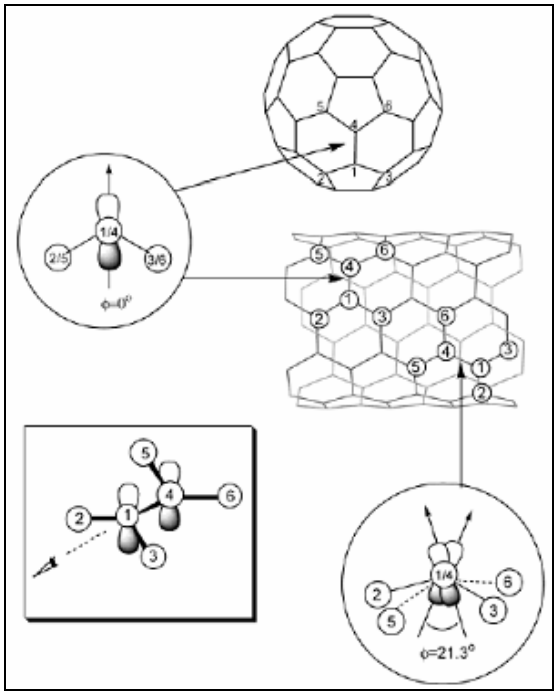

Figure 10: Mismatch Between π Bonding Orbitals in a Nanotube

It is important to note that highly curved tube end caps have a higher chemical reactivity than do the slightly curved tube walls. Open end tubes are also highly reactive. A carbon atom in the sidewall, or in a closed end cap, has three bonds to its nearest neighbor carbon atoms. Carbons at the termination of an open ended tube only have two bonds. Therefore, it is easy to introduce foreign molecules to the structure. CNTs can be

functionalized by the preferential addition of one or more species. Functionalization is a way to enhance properties for specific applications. ECDL supercapacitors can utilize functionalized CNTs in order to enhance capacitance.

2.2.2 Mechanical Properties

Mechanical property testing of CNTs has been challenging work due to difficulties in producing homogenous, usable samples, and the inability to manipulate nano size objects. CNT properties were estimated by model calculations for graphene sheets. The development of advanced microscopy techniques, such as TEM and atomic force microscopy (AFM), has allowed for accurate testing of CNT properties. In addition some researchers have used dynamic simulations to estimate strength and stiffness properties.[28]

Among the first measurements made on the Young's Modulus of a CNT was done through TEM observations of vibrations in MWNT. The average value deduced in these experiments was found to be 1.8 ± 0.9 TPa.[29] Clearly testing methods need to be refined in order to more accurately measure CNT mechanical properties. Other investigations, using AFM techniques, have found similar values for Young's modulus in MWNT. Table 1 lists these values. These results agree with earlier calculations based on graphene sheet models.

Table 1: Young's Modulus Data for MWNT

Researcher	Technique	Young's Modulus
Treacy	TEM Observations	1.8 ± 0.9 TPa
Wong[30]	AFM Observations	1.28 ± 0.59 TPa
Salvetat[31]	AFM Observations	0.81 ± 0.41 TPa
Yu[32]	AFM Observations	0.27 ± 0.950 TPa
Lu[33]	Dynamic modelling	1.0 Tpa

SWNT exhibit similar moduli to MWNT. The extremely high strength of CNTs, coupled with their relatively low weight, makes them an attractive material for many structural applications. Additionally, CNTs are ideal candidates for use in composite materials.

2.2.3 Thermal Properties

Thermal conductivity is the measure of heat flux that will flow through a material if a specific temperature gradient is present. Thermal transport is a key property in nano-based electronic devices. The transport of heat occurs via phonons; quantized energy of atomic vibrations. Thermal transport occurs rapidly in diamond because of sp^3 bonding, making it the best thermal conducting material. Graphite is another excellent thermal conductor, although only in the in-plane direction. It should follow that CNT exhibit similar high thermal conductivity because of the relationship to carbon structures.

The sp^2 bonds in nanotubes allow for rapid phonon transport along the axial direction of CNTs. Indeed, theoretical work has shown room temperature thermal

conductivity of CNTs as high as 660 W/m·K. [34] Other estimates place the thermal conductivity as high as 6000 W/m·K.[35]

The specific heat of CNTs, however, is not similar to that of two dimensional graphene sheets and three dimensional graphite, especially at low temperatures.[36] Hone, et al.[36] suggest that this deviation from typical graphene behavior is due to one dimensional quantization of the phonon band structure. Measurements show that the specific heat of SWNTs is lower than that of graphene at low temperature, but higher than graphite. At room temperature, the specific heat of SWNTs does in fact follow that of graphene, with a value of approximately 600 mJ/g·K.

2.2.4 Electrical Properties

The electrical properties of SWNTs are significantly dependant on tube chirality, as well as tube diameter.[37] CNTs are electrical conductors, and conductivity is extremely high as is the case for in-plane graphite. Resistance to conductance is due to quantum mechanical effects, and is independent of tube length. CNTs have the ability to exhibit metallic or semiconducting properties; this is a behavior that is not achieved by any other solid.[38] Energy band structure in SWNTs is one dimensional, and can be achieved by folding the two dimensional band structure of graphene sheets. Electronic density of states (DOS) of SWNTs exhibit spike like structures known as von Hove singularities. Figure 11 shows scanning tunneling microscope (STM) images of an isolated (8, 8) SWNT (A) and the corresponding DOS (B). The observed experimental DOS data is shown above the calculated DOS data. Parts C and D of Figure 11 show a STM image of a (8, 8) bundled SWNT, and the corresponding DOS data respectively. At the Fermi

energy level, the DOS of semiconducting SWNTs is zero, and very small for metallic SWNT.

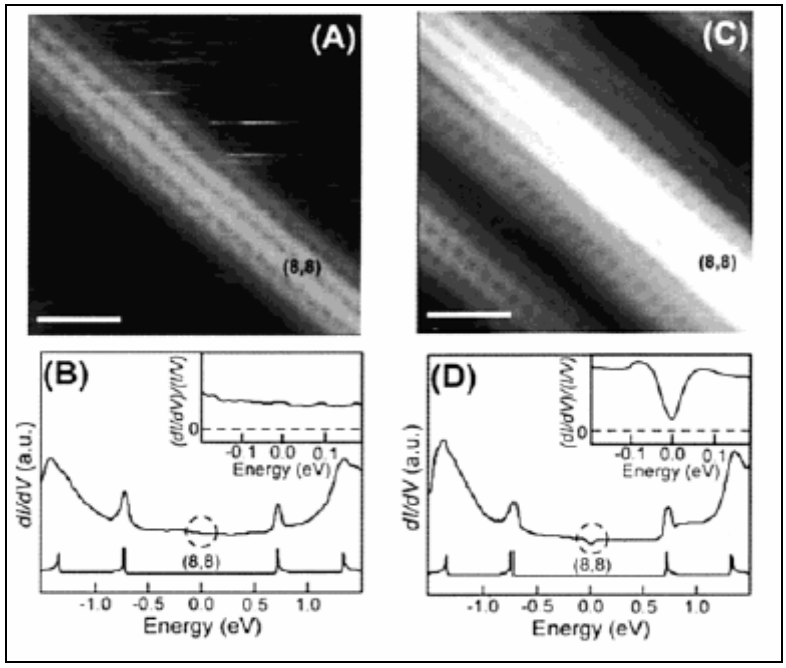

Figure 11: STM Image of SWNTs and Corresponding Electronic Density of States [38]

Ouyang, et al. have shown that isolated armchair SWNT are in fact truly metallic, with no one dimensional energy band gap structure. It was also shown that zigzag CNTs previously predicted to be metallic are actually semi-metallic. Zigzag nanotubes experience a shift in the Fermi level due to finite curvature effects because of the tubular construction. This behavior results in the formation of small band gaps that introduce semiconducting characteristics. The band gaps are very small, and are inversely proportional to the square of the tube radius. Bundled armchair SWNT exhibit "pseudo gaps," which modify electrical transport. These gaps also make SWNT susceptible to dopants which may enable them as sensor materials.

Maiti, et al. [39] have shown that defects and bending can have a significant impact on electrical conductivity in SWNT. Atomically sharp AFM tips were used to introduce

deformations in both metallic zigzag and armchair SWNT. Metallic armchair tubes remained highly conductive under deformation, as well as under bending. Zigzag tubes, however, experienced a drop in conductance of several orders of magnitude under deformation. Bending zigzag CNTs also results in a drop in conductivity, although not nearly as significant as under AFM tip loading. This again suggests that CNT can be used as an active material in sensor applications.

2.3 Charge Storage

Electrical energy is stored in two fundamentally different ways.[40] Batteries indirectly store electrical energy as potentially available chemical energy. A Faradaic mechanism in batteries is a process in which electron transfer occurs, and results in an oxidation state change in the electro-active materials. Faradaic oxidation and reduction is required for the electro-active chemical reagents within the battery to release electrical charges. These released charges produce electric energy as they travel across the voltage difference on the oppositely charged poles of a battery cell.

Capacitors store charge directly in an electrostatic manner. Capacitance is a measure of a materials capability to store charge. The amount of charge stored in a given capacitor is proportional to the applied field strength.[41] Positive and negative charges are stored in a non-Faradaic process on the plates of a capacitor. A non-Faradaic process requires no transfer of electrons. Unlike a battery, no chemical or phase change reactions are required for electrical charge storage in a capacitor. These reactions in a battery cell are irreversible, and thus batteries cannot effectively be charged, discharged and then

recharged for an extended number of cycles in a rechargeable battery. In contrast, capacitors have virtually unlimited life cycles since no chemical or phase change reactions are required in charging and discharging.

Pseudocapacitance is another mechanism of charge storage arising from occurrence of Faradaic reactions on electrode materials in ECDL capacitors. The capacitance in this case originates from quick Faradaic reactions as well as electrostatic charging. Pseudocapacitive behavior is essential to expanding the capacitive properties of ECDL capacitors, and the reactions and properties of pseudocapacitance will be discussed in depth later in this chapter.

Two important terms in charge storage are power density and energy density. Power density is the radiant power per unit area upon a surface measured in watts per square meter ($W\ m^{-2}$), or watts per kilogram ($W\ kg^{-1}$). Energy density is a measure of the obtainable energy per unit weight in Watt hours per kilogram ($Wh\ kg^{-1}$). Energy density is determined by measuring the capacity of the device, and monitoring the average potential during discharge.

2.4 Charge Storage Devices

2.4.1 Traditional Capacitors

A difference between a capacitor and a battery is that a capacitor can be completely discharged in a fraction of a second, where a battery takes a much longer time to completely discharge.

A conventional capacitor consists of two metal electrodes separated by a dielectric insulator material (Figure 12). In its most basic form, the dielectric can be air

separating the two plates. A simple way to increase the capacitance is to connect many capacitors in parallel which can be done in a space efficient way by "rolling" a simple parallel plate capacitor into a multilayer cylindrical capacitor. The entire structure is then encapsulated by a thermoset epoxy resin. When a voltage is applied to the capacitor, electrons are forcibly removed from the cathode, and collected on the anode. When the applied voltage to the capacitor is large enough, the electrons can jump from the anode to the cathode. This is known as dielectric breakdown, and is a severe, catastrophic failure in a capacitor.

Capacitance, measured in Farads (F), is governed by the equation:

$$C = \frac{\varepsilon_0 \varepsilon_r A}{d} \qquad \text{(Eqn. 3)}$$

where A is the surface area of the electrode, ε_o is the permittivity of free space, ε_r is the relative permittivity of the dielectric material, and d is the separation of the electrodes (dielectric thickness).[42] Permittivity is a measure of a materials ability to store charge. Equation 3 demonstrates the importance of a thin dielectric material, as well as large electrode area, for the value of capacitance to be high. Most capacitors used in electronic and portable devices today have capacitance values in the microfarad (μF) range.

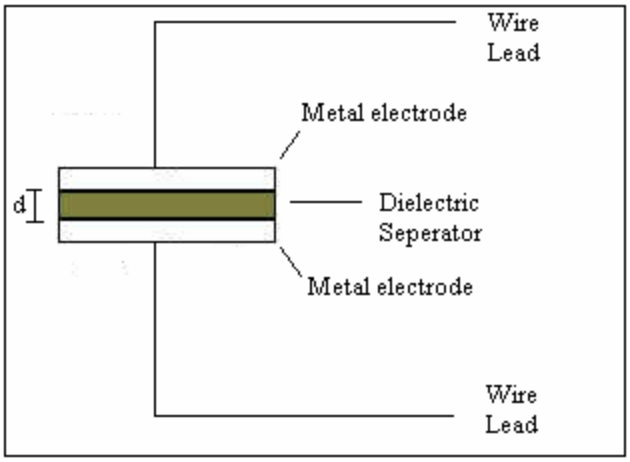

Figure 12: Conventional Capacitor Schematic

Conventional capacitors traditionally have much higher power densities than batteries, ranging from 100 to $2.7x10^{10}$ kW kg^{-1}. Conventional capacitors have extended life cycles (>10^4) and a short time application (<10^{-2}s). The small energy density (70mW kg^{-1}) of capacitors is a drawback for many applications which require a large amount of energy storage.

Dielectric materials for conventional capacitors are typically insulating ceramics, and the choice of material used is based on the required capacitance for the specific application, as well as the frequency range applied. Common dielectric materials include air, paper, mica, polystyrene, polyester, alumina, polycrystalline titania, barium titinate based ceramics and strontium titanate. The electrode plates are generally a conducting metal, with aluminum being the most commonly used material.

2.4.1.1 Electrolytic Capacitors

An electrolytic capacitor is similar to any other type of electrical capacitor in that it consists of two conducting electric surfaces separated by an insulating or dielectric medium. The capacity of an electrolytic capacitor is determined by the same factors

which apply to any other electrical capacitor. That is, capacitance in dictated by the area of the conducting electrode surfaces, as well as the thickness of the dielectric medium.

The electrolytic capacitor, however, departs from the more conventional types of electrical capacitors in that only one of its conducting surfaces is a metallic plate, the other conducting surface being a chemical compound or electrolyte. The dielectric employed is a very thin film of oxide of the metallic plate used in the structure.

This oxide typically aluminum oxide (Al_2O_3 or alumina) or Tantalum Oxide, which constitutes the dielectric, possesses remarkable characteristics as an insulator. Due to these insulator properties, electric field strengths in the dielectric can be on the order of ten million volts per centimeter of thickness. This results in capacities in the μF range with very small physical dimensions. Electrolytic capacitors are divided into two general types; the wet electrolytic capacitor and the dry electrolytic capacitor. Fundamentally, there is no difference between these two types of capacitors with the exception of the type of electrolyte used.

Electrolytic capacitors provide a higher capacitance for a given area at a lower cost per microfarad than conventional dielectric capacitors.[43] In an electrolytic capacitor (Figure 13), typically the electrodes are an Aluminum foil.

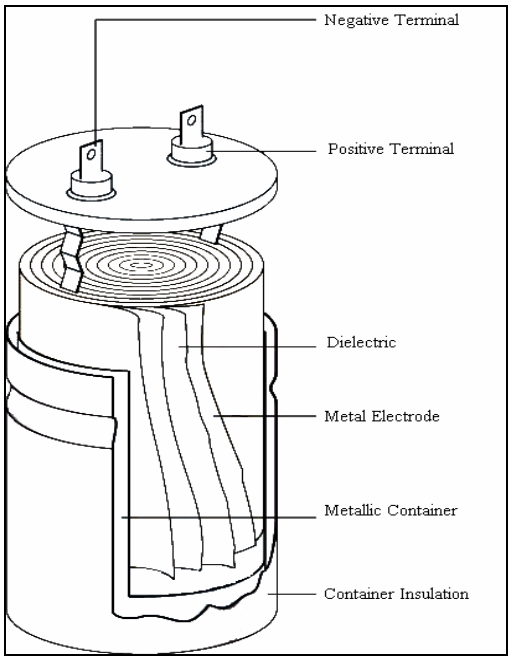

Figure 13: Schematic Diagram of an Electrolytic Capacitor

2.4.2 Electrochemical Double Layer Supercapacitors

The electrochemical double layer (ECDL) capacitor, has been highly researched in the past decade due to its efficient energy storage (it should be noted that the term "electrochemical double layer capacitor" is often denoted as EDLC). Known more commonly as supercapacitors (the tradename coined by the first commercial producer, NEC), ECDL capacitors can potentially bridge the gap between conventional capacitors and standard batteries. The term ultracapacitor is another common industry name, with its origin coming from ECDL capacitors produced for the US military by Pinnacle Research Institute. As energy storage devices, ECDLs could be applied to many emerging technologies such as electric vehicles and pulse power applications.

Typical properties for batteries, conventional capacitors and supercapacitors are listed in Table 2.[44] Supercapacitors offer high power density as well as high energy

density and long cycle life.[45] Many applications are emerging where ECDL technology can offer vast benefits compared with traditional devices. Conventional capacitors are limited in energy storage by dielectric breakdown. Dielectric materials necessary for traditional capacitors are not needed for ECDL capacitors. Many batteries are not reusable, and are therefore limited by cycle life. ECDL capacitors have the ability to be cycled many times ($>10^6$).

Table 2: Overview of Charge Storage Device Properties

	Capacitors	ECDL Capacitors	Batteries
Energy Density [Wh/kg]	10^{-1}	0.3×10^{1}	10^{2}
Power Density [W/kg]	10^{7}	3×10^{3}	10^{2}
Time of Charge [s]	10^{-3} - 10^{-6}	0.3×10^{-1} -0.3×10^{2}	10^{3}
Time of Discharge [s]	10^{-3} - 10^{-6}	0.3×10^{-1} -0.3×10^{2}	10^{3}-10^{4}
Cycle life [cycles]	10^{10}	10^{6}	10^{3}
Lifetime [years]	0.3×10^{2}	0.3×10^{2}	0.5×10^{1}

2.5 Supercapacitor Construction

Supercapacitors consist of two electrodes immersed in or impregnated with an electrolyte solution with a semi-permeable membrane serving as a separator.[46] The electrode is a metallic current collecting material in contact with an active material. When an electric potential is applied to the electrodes, a potential difference is created at the electrode-electrolyte interface. This electrostatic interface is a Helmholtz double layer of ions in the electrolyte and the electronic charges of the electrode.[47] The separation of

the electronic and ionic charges is the source of the energy storage in an ECDL capacitor. The "active material" used in an electrode is where this charge separation occurs. Active materials are in contact with a metal electrode, and also become charged. Solvated ions of opposite charge are attracted to the active material, and are accumulated at the interface between the active material and the electrolytic solution. This charge storage process is non-Faradaic. Figure 14 is a schematic diagram of a typical ECDL supercapacitor. The separator is necessary in order to prevent electrical contact between the anode and cathode, but still allows for solvated electrolyte ion migration.

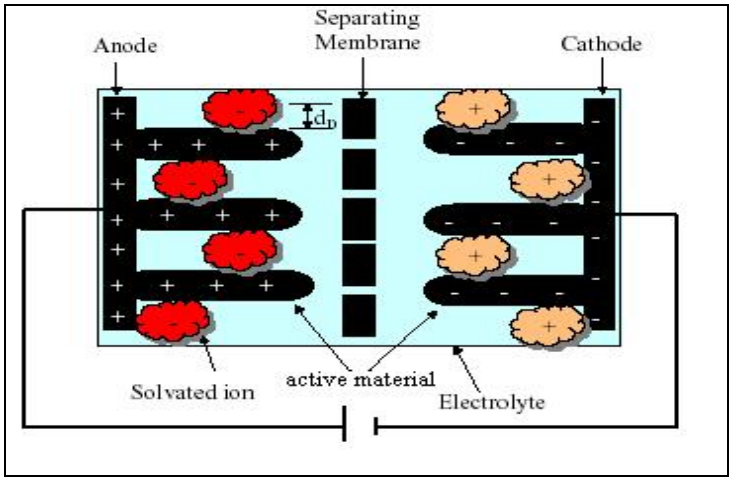

Figure 14: A schematic diagram of an ECDL supercapacitor (not to scale)

Equation 3 can be modeled to ECDL capacitors, and d is reduced to the Helmholtz double layer distance, d_D, defined as half the diameter of the adsorbed ions at the electrode-electrolyte interface (see Figure 14). This implies that no dielectric material is necessary in an ECDL supercapacitor. The dielectric material that allows for the occurrence of charge storage in conventional capacitors is also the limiting factor for capacitance, resulting is capacitance values of a few μF. [48] The Helmholtz double layer is

approximately 10Å thick, thus increasing theoretical capacitance values by more than two orders of magnitude.

2.5.1 Active Electrode Materials

In order to achieve high capacitance, a material with high surface area should be chosen as the active material for a supercapacitor.[49] Material surface conditions are extremely important for capacitance, with porosity playing a large role in charge storage. Since ionic/electronic charge separation is the means by which charge is stored, it is necessary for ions to freely transport from the electrolyte onto the active material surface. Therefore, an active material must have pores of sufficient size in which ions can reside.

Surface area is directly related to the total pore volume in a material. Active materials for supercapacitor electrodes must have a high surface area of open volume, percolated and networked pores. Brunauer-Emmett-Teller (BET) measurements are the most common way to calculate surface area. BET calculations are based on the adsorbtion of gas molecules on material surface. The most prevalent materials being investigated for supercapacitors are carbon structures – including both CNTs and activated carbon (AC), metal oxides and conducting polymers – all of which have extremely high BET surface areas, as well as a large volume of open pores.

A closed pore will not allow ion migration. However, in addition to being open, the pore must be a specific size in order to store charge effectively. Pore size of electrode materials must correspond with ion size; therefore, it is important that pore size of the electrode material must match well with the size of ion for a given electrolyte.[50]

Pore sizes are classified according to The International Union of Pure and Applied Chemistry (IUPAC). Micropores are defined as having a radius less than 20Å, Mesopores have a radius between 20 and 50Å, and Macropores are any pores larger than 50Å. As pore size increases from small micropores to large micropores, specific capacitance increases (Figure 15).[51] Micropores are not easily wetted by the electrolyte solution.[52] Jang, et al. suggest that even if micropores are wetted by electrolyte, ionic motion is not easily facilitated in micropores. In general, it is desired that the structure of electrodes for supercapacitors is designed so that the specific surface area contributions of mesopores and macropores are maximized, and the contribution of micropores to surface area is minimized.[53]

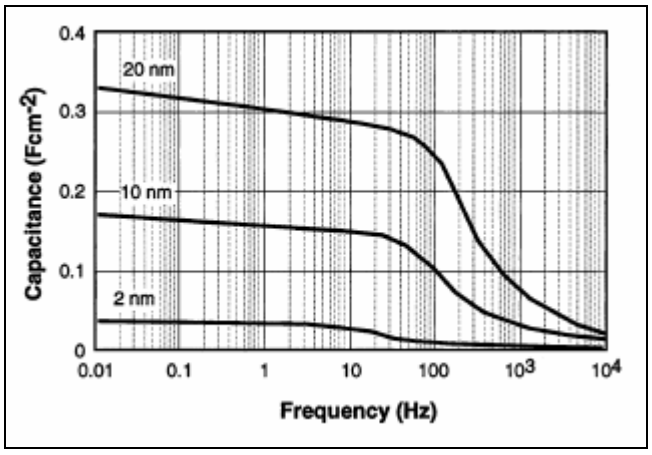

Figure 15: Specific Capacitance as a Function of Pore Diameter

2.5.1.1 Carbon Electrodes

Electrochemical capacitors have employed carbon structures as electrode materials since their origin. Carbon is widely used because of its availability, low cost, ease of processing, and properties which allow for good capacitance. Carbons are

'activated' and altered using innovative techniques including air-cycling activation and electrochemical oxidation. Activated Carbons are high surface area, high porosity carbon materials of two dimensional hexagonal rings formed into a 'graphene sheet'. A drawback of AC is that a significant amount of pores is closed. While these closed pores contribute to a high BET surface area, they do not allow for increased capacitance. Moreover, a specific proportionality between surface area and specific capacitance does not exist. Variances in processing methods and subsequent treatments of AC result in different specific double layer capacitances. Carbon aerogels (air-filled foams) developed at Lawrence Livermore National Laboratory (LLNL) and carbon xerogels are also being researched as electrode materials.

2.6 Carbon Nanotubes as an Active Electrode Material in ECDL Supercapacitors

CNTs contain a more open pore volume than AC, and thus CNTs with a smaller surface area can achieve capacitance values of AC with a larger surface area. Although the BET surface area of CNTs is not as high as in activated carbon, Niu, et al. [54] report that surface area is more accessible in CNTs, and the pore size distribution lies mostly within the mesopore range due to the density of CNT packing. The micropore volume in samples of CNTs is negligible. Mesopores are preferable in an active electrode material because their size allows for ion transport. Activated carbon contains a larger portion of micropores than CNT, which accounts for a significant portion of the materials surface area. Micropores do not allow easy ion transport, thus causing a reduction in the charge storage ability of activated carbon. Nanotubes also offer chemical and mechanical

stability which makes them attractive candidates as an active material in a supercapacitor electrode.

Further analysis of the CNT electrode structures shows a random network of entangled and cross-linked tubes. The nanotubes used in this experiment were MWNT created by the DC arc method, and then functionalized with oxygenate groups such as -COOH , -OH, and >C=O. This type of structure allows for easy ion migration because all the pores are connected within the nanotube network. This ease of migration result in capacitance values of 49 F/g at 100Hz, and up to 113 F/g at 0.001Hz. The high capacitance values at higher frequencies indicate a good frequency response, which results in better power performance.

It is important to note that the capacitance per unit weight is not as significant as the capacitance per unit area/volume. Emenegger notes that capacitance can be significantly increased by increasing the thickness of the active material, based on the theory outlined by Kötz and Carlen. In order to achieve a thicker layer of MWNT, a paste was created with CVD grown MWNT, binder solution, water and methanol. The paste was then applied as the active material to an aluminum foil substrate. The CNT paste produced higher capacitance than CNTs grown directly on the substrate, since more active layer material was contributing to energy storage. Similarly, Ma, et al. [55] used CNTs with a binder solution to form solid electrodes.

Frackowiak, et al.[56] have shown that capacitance in carbon nanotubes can be enhanced using chemical activation. MWNT activated in KOH resulted in a significant increase in surface area, with weight loss around 45%. The higher surface area and resultant high capacities can be attributed to the redox reaction between carbon and KOH.

This reaction is efficient at forming holes while not disturbing the morphology of the nanotubes.

Others have used ruthenium oxide to functionalize MWNTs in order to increase capacitance.[57] RuO_2 stores charge through non-Faradic processes. RuO_2 exhibits "pseudo-capacitive" behavior, and is able to achieve high capacitance by itself, but is quite expensive and loses its capacitive ability over time. When MWNTs were prepared with approximately 1 wt. % hydrous ruthenium oxide, the capacitance increased by over an order of magnitude. Conducting polymers also utilize non-Faradic charge storage, and are currently being investigated to functionalize CNTs for electrodes.[58]

SWNTs have also been used as an active electrode material with moderate success. When SWNTs were used with a polyvinylchloride (PVC) binder, maximum specific capacitance was found with a ratio of 70% SWNTs to 30% PVC binder.[59] It was also shown that a post processing high heat treatment temperature (1000°C) significantly increased the BET surface area, and appropriate pore sizes (70Å). Capacitance properties for various ECDL supercapacitors based on CNT electrodes are listed in Table 3.

Table 3: Capacitance Values for CNT Based ECDL Supercapacitors

Authors	Active Material	BET Surface Area(m^2g^{-1})	C_{sp} ($F\ cm^{-2}$)	C_{sp} ($F\ g^{-1}$)
Niu et al.	MWNT	430	0.08-0.17	49-102
An et al.	SWNT	357	0.3-0.8	71-178
Ma et al.	MWNT	120	-	15-25
Frackowiak et al.	MWNT activated w/KOH	220-1035	-	85-95
Emenegger et al.	MWNT with paste	57	0.09	10
Emenegger et al.	MWNT w/o paste	47-64	0.0004	12
Arabale et al.	MWNT w/RuO_2	-	-	80
Xiao et al.	MWNT w/conducting polymer	-	-	45-87

2.7 Summary

This chapter discussed novel carbon structures necessary for an understanding of CNTs. The synthesis, growth mechanisms, treatment and properties of CNTs were discussed at length. Physical properties of CNT were addressed in brief. This chapter also reviewed the principles of charge storage, as well as capacitive charge storage devices. In addition, the concept of electrochemical double layer supercapacitors was introduced, and their structure and properties were explained in detail. Finally, CNTs were examined as an active material for charge storage in ECDL supercapacitors.

CHAPTER 3

PROCEDURE

This chapter describes in detail the laboratory experiments which have been carried out. It discusses experimental aspects including substrate and catalyst preparation, CVD synthesis conditions, post synthesis analysis, and procedures for assembling and testing novel CNT-based ECDL supercapacitors.

3.1 Catalyst and Substrate Preparation

For this work, two primary catalysts were used; iron and nickel. Iron catalyst was in liquid form as alumina supported iron. The preparation of the alumina supported iron catalyst will be discussed later in this section. Alumina supported iron catalyst and nickel catalyst were both applied to silicon wafer substrates. Nickel catalyst was either used as pure metal film, or as a dispersion of nanoparticles in solution. The application procedure for each catalyst is described in the next sections. The silicon wafers were diced into small chips (~ 1cm x 1cm squares or larger) for catalyst application, CNT growth and analysis.

3.1.1 Preparation and Application of Alumina Supported Iron Catalyst

In an appropriately sized vial, 40 mg of iron (III) nitrate nonohydrate [$Fe(NO_3)_3 \cdot 9H_2O$], 30mg of aluminum oxide, and 3 mg of Bis(acetlyacetonato)-dioxomolybedenum (VI) were mixed with 30mL of methanol. The mixture was then sonicated for 30 minutes. The catalyst is ready for application at this point. However, if

the suspension has settled to the bottom of the vial, the mixture must be sonicated again for a short period of time (approximately 5 minutes).

Using a micropipette, approximately 2 mL of the alumina supported iron catalyst was applied to the silicon wafer chips. The liquid catalyst was left on the substrate for up to 5 minutes, at which point the catalyst was blown dry using nitrogen gas. The substrate chips with dry catalyst were next placed into a Precision model 29 furnace and baked at 150°C for five minutes. At this point, the substrate chips are ready for CNT synthesis.

3.1.2 Preparation and Application of Pure Nickel Metal Film Catalyst

Nickel films were applied to the silicon wafers before the wafers were diced into chips. Nickel film thickness of 100, 80, 60, 40, and 20 nm were deposited onto the wafer using Georgia Tech Research Institute's (GTRI's) VEECO dual chamber electron beam evaporator. Nickel atoms were applied at a rate of 3.0 Å/s or less until the desired film thickness was achieved. Some substrates were prepared with patterned nickel films using a photolithography procedure.

3.1.2.1 Photolithography Procedure for Patterned Nickel Catalyst

First, the silicon wafer was cleaned using successive rinses of tetrachloroethanol (TCE), methanol, and distilled water. The wafer was then blown dry with nitrogen gas. Microchem Photoresist 1818 was spin coated onto the wafer at 5000 revolutions per minute for 25 seconds. The wafer was then baked at 95°C for 25 minutes. Next, the substrate was placed under the desired pattern screen, and exposed to ultraviolet light with the Karl Suss MJB Exposure system for six seconds at a power density of

250mW/cm^2. The substrate was then soaked in chlorobenzene for ten minutes, blown dry with nitrogen gas and subsequently baked at 95°C for ten minutes.

The substrate wafer was then developed for 60 seconds in a mixture of 140 mL distilled H_2O and 40 mL Microchem Developer AZ 351. The substrate was blown dry with nitrogen gas and visually inspected for the desired pattern. If the pattern was clear, the wafer was ready for cleaning prior to catalyst evaporation. If the pattern was not fully clear, the wafer was developed for another 20 seconds. Once the pattern was visible, the wafer was cleaned for 10 seconds in a mixture of 5mL NH_4OH and 50mL H_2O, followed by a 15 second rinse with distilled H_2O. The substrate wafer was then blown dry with nitrogen gas, and placed in the dual chamber evaporator for nickel film application. Once the desired nickel film thickness was achieved, the substrate wafer was soaked in acetone for 10 minutes and subsequently rinsed with acetone and distilled H_2O until complete photoresist removal was observed.

The pattern used in these experiments consists of a nickel rectangle with dimensions of 900 μm on the top and bottom, and 600 μm on the sides (Figure 16). The rectangle has small 40 μm squares in the center where there is no catalyst material, and the substrate material is exposed. In addition, there is a smaller 20 μm square in the top right corner of the rectangle where there is no catalyst material, and the substrate is exposed.

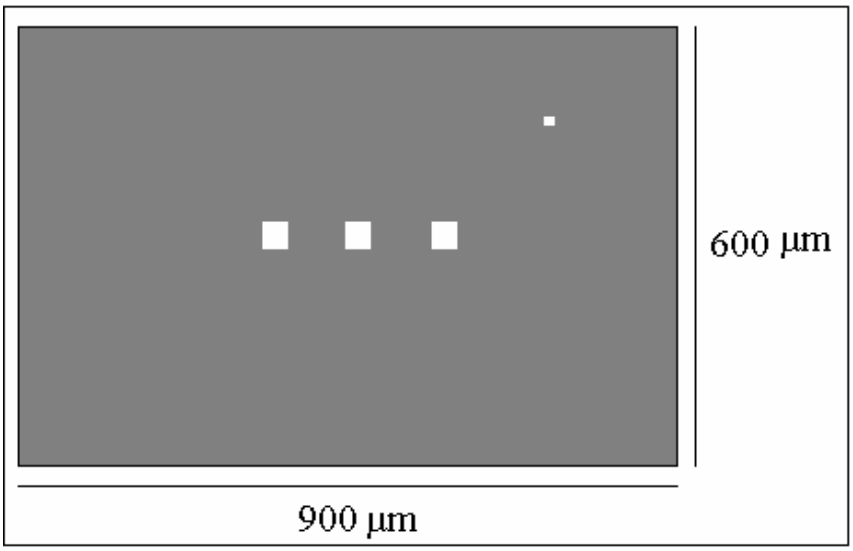

Figure 16: Nickel Pattern on Silicon Substrate Wafer

3.1.2.2 Preparation and Application of Nickel Nanoparticle Catalyst Solution

The nickel nanoparticle catalyst was prepared by dissolving an unknown mass of 62nm nickel nanoparticle powder in an unknown volume of isopropyl alcohol (IPA). The catalyst was prepared by Dr. Samuel Graham's group in the Mechanical Engineering school at Georgia Tech. The solution required agitation before being applied to the substrate via a pipette. Approximately 10-12 mL of the suspended nanoparticles were applied to each silicon catalyst chip until the surface was fully coated. After the catalyst solution was applied, the substrate chips were placed in the Precision furnace at 150°C for five minutes. Upon removal from the furnace, the substrates contained only nickel nanoparticles on the surface, and were ready for CNT synthesis.

3.2 Chemical Vapor Deposition Synthesis of Carbon Nanotubes

3.2.1 Easy Tube CVD Furnace

The CVD system used for synthesis of CNTs is the Firstnano EasyTube 1000 CVD furnace. A schematic diagram of the system is shown in Figure 17. The furnace section consists of a two inch quartz tube surrounded by heating coils. A thermocouple measures the temperature at the center of the tube.

A quartz boat controlled by a motorized loader is inserted into the quartz tube and sealed by a stainless steel end cap (Figure 18). The gas cabinet portion of the furnace contains four independent gas mass flow controllers (MFCs) which operate at flow rates from 0-1000 standard cubic centimeters per minute (sccm).

The entire system is controlled by a Windows 2000™ based 800MHz Pentium III computer, which controls the furnace temperature (based on thermocouple and programmed data) and the flow rates of the carrier and precursor gasses (based on MFC data and programmed data). The computer acquires and stores data for each synthesis.

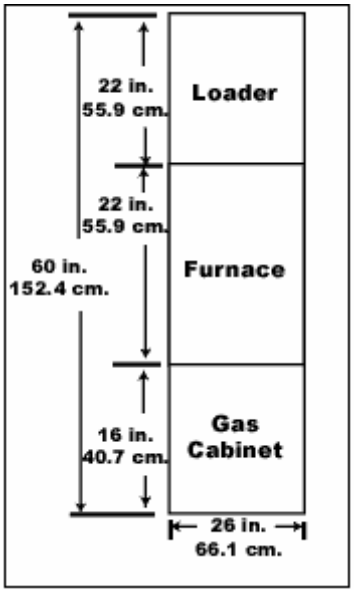

Figure 17: EasyTube CVD System (Top Down View)

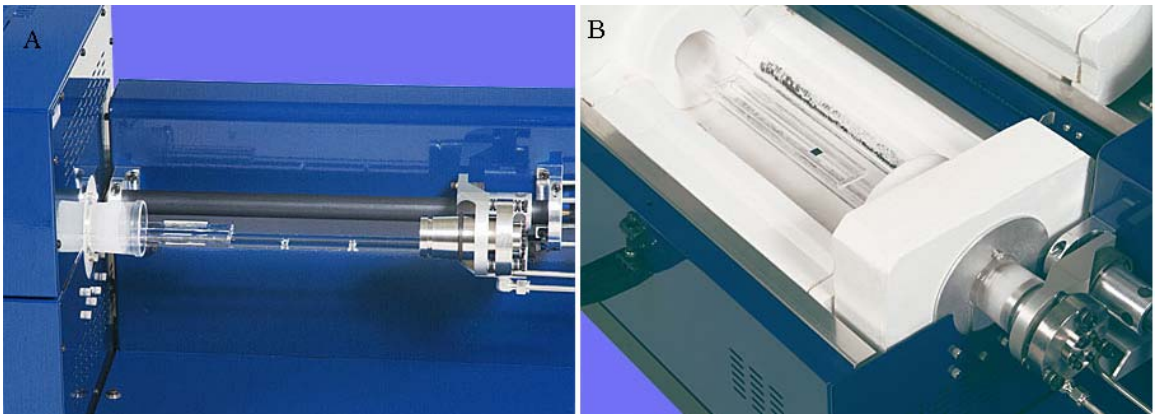

Figure 18: CVD Quartz Loader Boat (A) Open (B) Closed, Inside Quartz Tube

3.2.1.1 Electric Field Feed Through Setup

An electric field was applied to the furnace during the synthesis for several samples. The field was generated by a Keithley 2400 sourcemeter supplying a direct current (DC) voltage. The voltage applied to the furnace chamber during CNT synthesis ranged from 10V to 50V in increments of 10V. The setup of the CVD furnace both with

and without electric leads is shown in Figure 19. A special end cap fitted for electric leads was used to close the system. A schematic of this electric feed through end cap is shown in Figure 20.

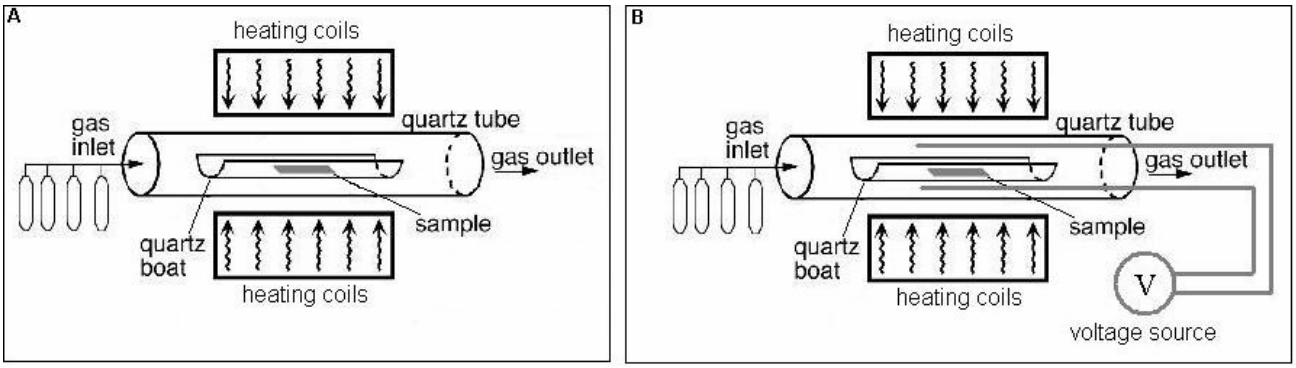

Figure 19: (A) Schematic Diagram of CVD Furnace (B) With Electric Leads

The voltage source was connected to the end cap outside leads. The leads in the furnace were each coupled with a tungsten rod with a diameter of 1 mm. The rods were approximately 16 inches in length, and extend just beyond the quartz boat sample holder. One rod was positioned above the quartz boat, and the other was positioned below the boat. The distance between the tungsten rods was approximately 14 mm.

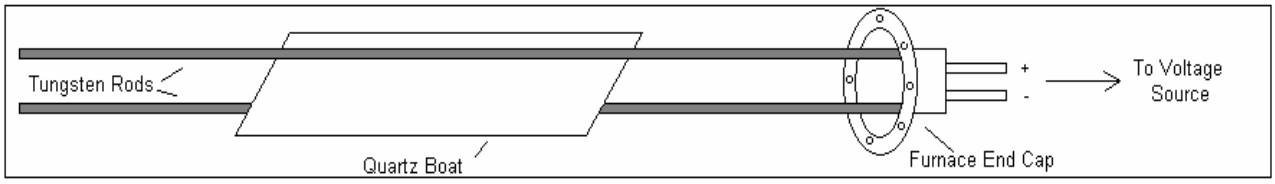

Figure 20: Diagram of Electric Feed-Through Setup

3.2.2 Chemical Vapor Deposition Synthesis Variables

The following variables were altered and applied in various systematic combinations for each catalyst type: synthesis (soak) time, soak temperature, precursor gasses, precursor gas flow rate, and applied voltage. The precursor gasses used in the present work were methane, ethylene, and acetylene. Purge and carrier gasses used in the present work were argon and hydrogen. Specific combinations of precursor, purge and carrier gasses are denoted as a particular 'recipe'. Names and abbreviations for each recipe are listed in

Table 4. Additional information for recipes, as well as a reference to sample gas flow rate figures for each recipe, is found in Table 5. The synthesis recipe used and the catalyst type used were documented for each sample. Each sample was stored in a sample box for later analysis with imaging tools.

A sample time vs. temperature plot is shown in Figure 21. The thin dotted line represents the programmed furnace temperature. The thick dashed line is the actual data recorded from the CVD process. The fluctuating temperature is due to the thermocouple control over the furnace. It is important to note that the temperature and soak time varies for each sample. However, CNT synthesis always occurs at constant temperature during the soak of a single sample.

For each synthesis, argon gas was used to purge the CVD furnace during the initial temperature ramp stage until the soak temperature was reached. At this point, carrier and precursor gasses were flowed into the chamber based on the selected recipe. At the end of the soak stage, argon was flowed through the chamber for the first 15 minutes of the cooling stage. After this point, the furnace was cooled in air until an

adequate temperature was reached, at which point the furnace was opened and the sample removed.

For certain experiments, a five minute pretreatment of the substrate was applied. The pretreatment consisted of 500 sccm of hydrogen gas flowing through the CVD deposition chamber after the soak temperature had been achieved but before the flow of carbonaceous precursor gasses occurred in the soak stage. Experiments utilizing a pretreatment will be denoted as "(RECIPE NAME) with 5 minute Hydrogen gas pretreatment" in future sections. A sample plot of the BULK CNT with five minute hydrogen gas pretreatment recipe is shown in Figure 29.

Table 4: Synthesis Recipe Details

Abbreviation	Recipe Name	Soak Time (minutes)	Methane Flow Rate (sccm)	Ethylene Flow Rate (sccm)	Acetylene Flow Rate (sccm)	Hydrogen Flow Rate (sccm)
MWNT	Multi Wall Nanotubes	20	0	700	0	0
HPCNT	High Purity Carbon Nanotubes	10	500	0	0	500
HYCNT	High Yield Carbon Nanotubes	15	1000	20	0	500
Bulk CNT	Bulk Yield Carbon Nanotubes	20	1000	20	0	500
UHYCNT	Ultra High Yield Carbon Nanotubes	20	1000	100	0	500
AcHYCNT	Acetylene gas High Yield Carbon Nanotubes	10	1000	0	20	500
AcUHYCNT	Acetylene gas Ultra High Yield Carbon Nanotubes	20	1000	0	100	500

Table 5: Additional Synthesis Recipe Information

Abbreviation	Additional Info	Sample Synthesis Plot
MWNT	Temperature fixed at 700°C	Figure 22
HPCNT		Figure 23
HYCNT	5 minute hydrogen purge after soak	Figure 24
Bulk CNT		Figure 25
UHYCNT		Figure 26
AcHYCNT		Figure 27
AcUHYCNT		Figure 28

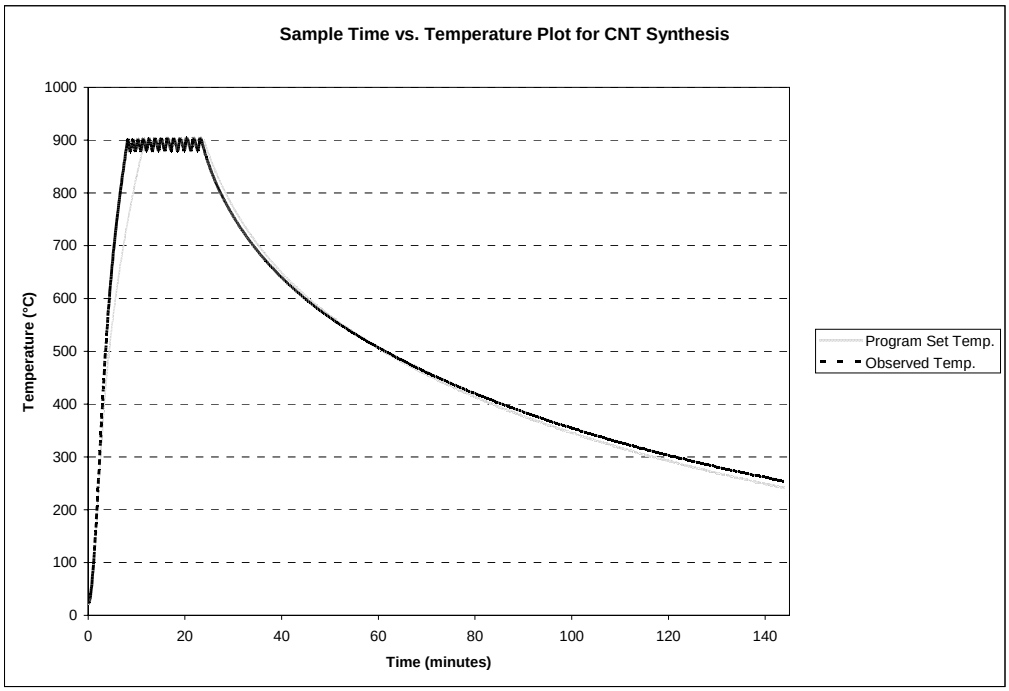

Figure 21: Sample Time vs. Temperature Plot for CNT Synthesis

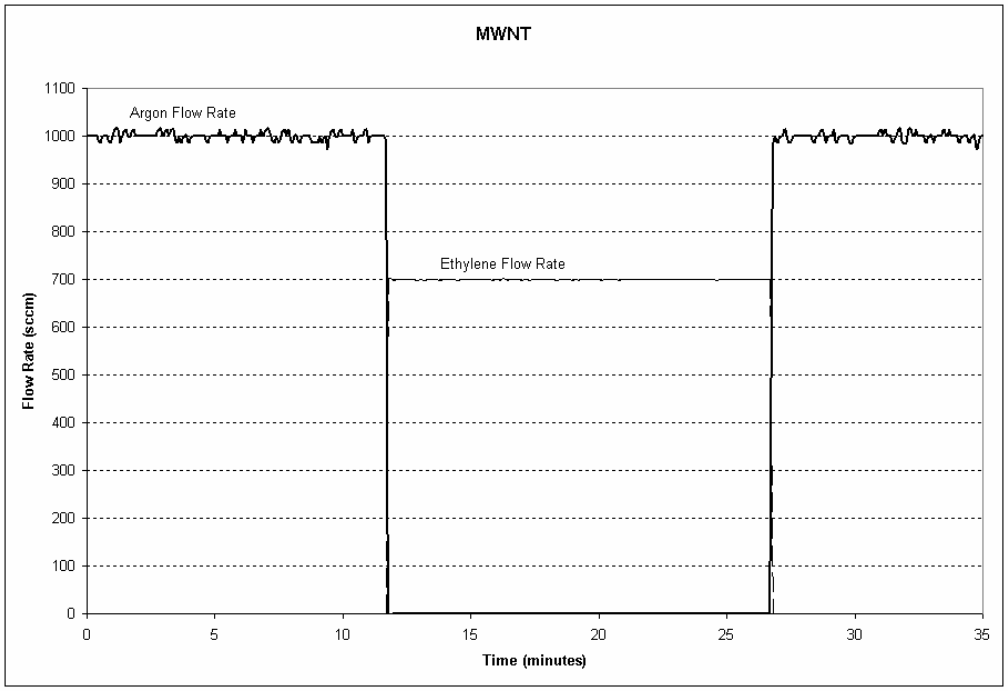

Figure 22: Sample Soak Detail for MWNT Recipe

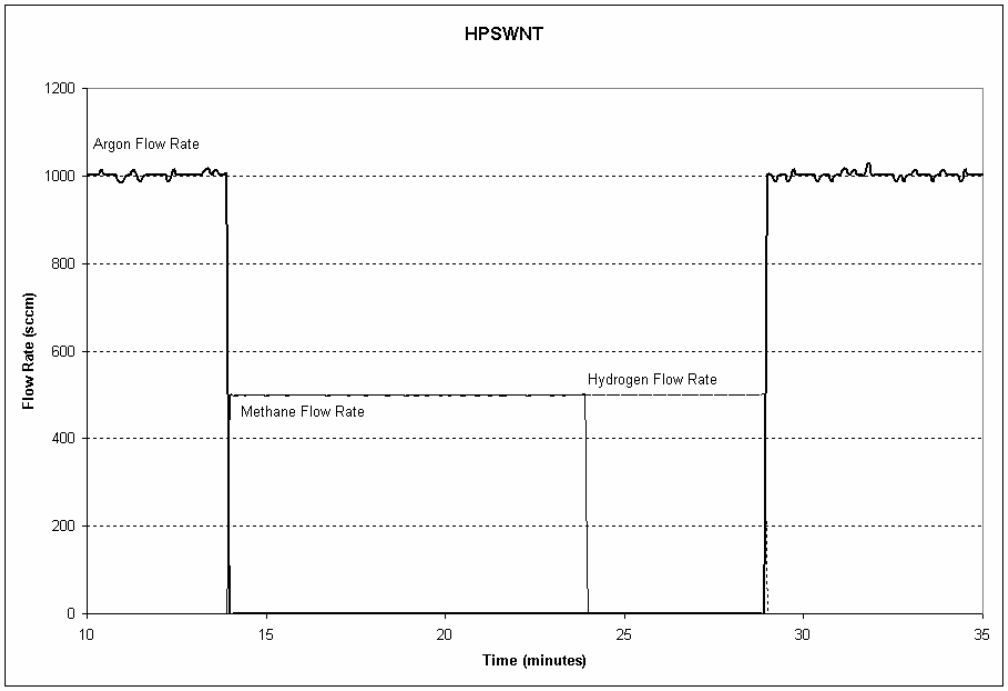

Figure 23: Sample Soak Detail for HPCNT Recipe

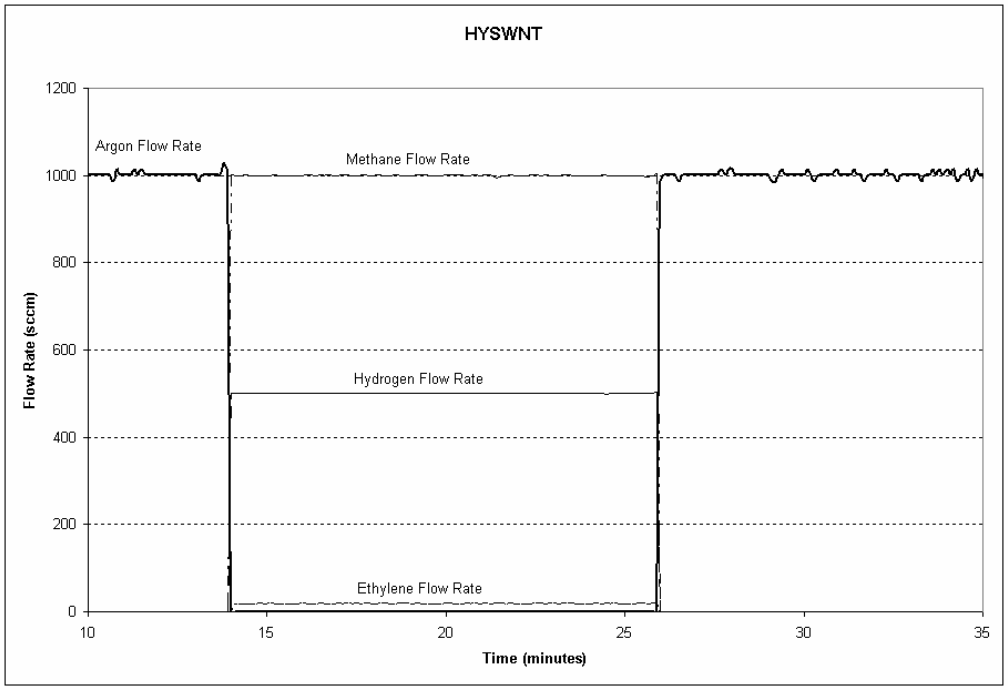

Figure 24: Sample Soak Detail for HYCNT Recipe

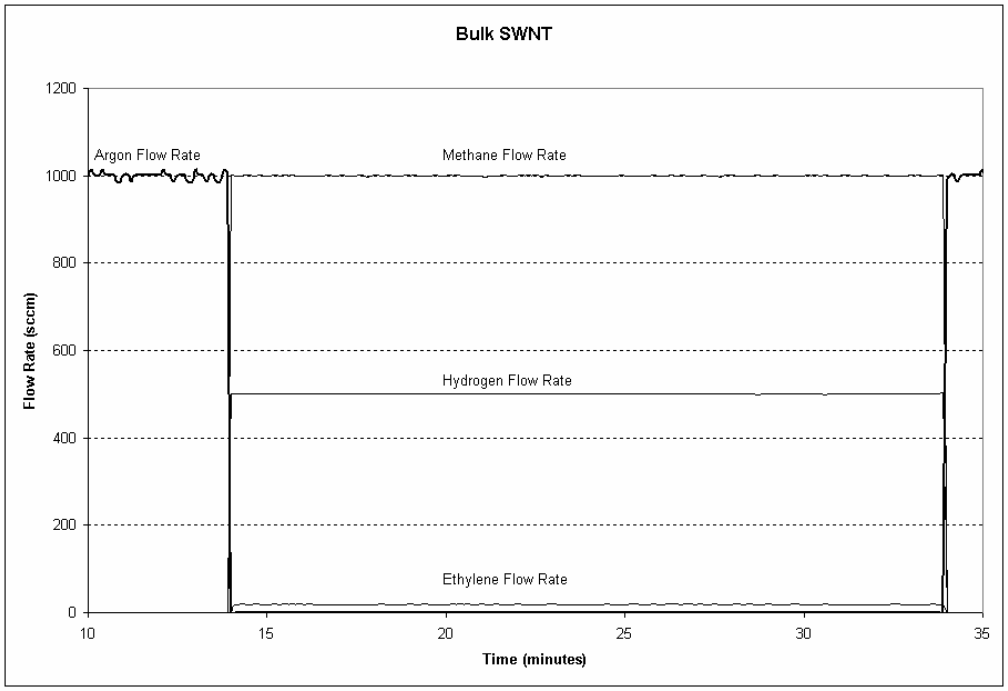

Figure 25: Sample Soak Detail for Bulk CNT Recipe

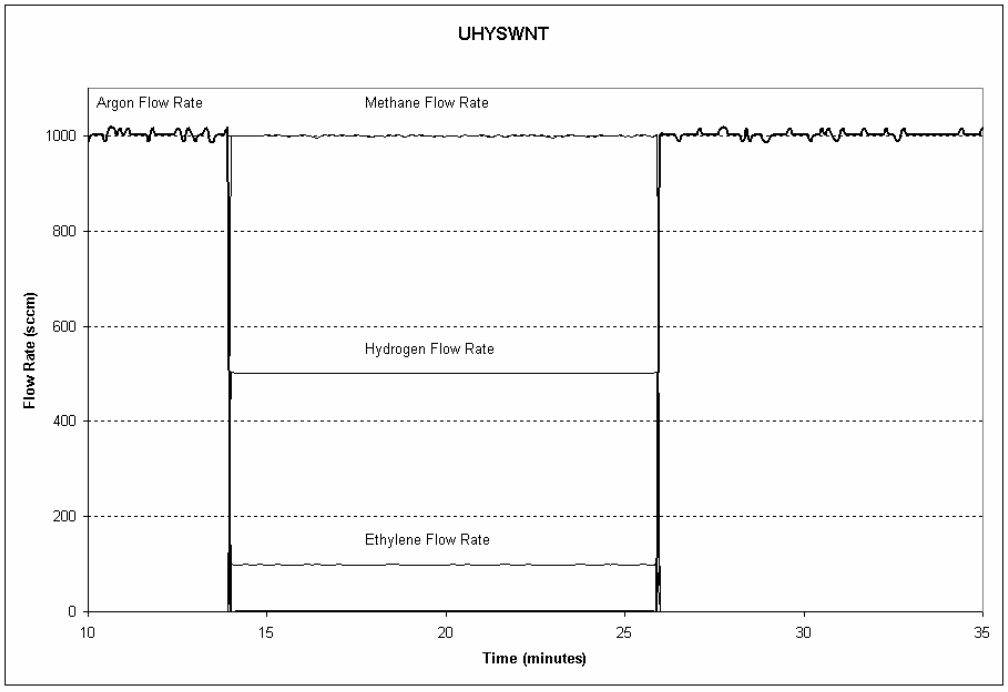

Figure 26: Sample Soak Detail for UHYCNT Recipe

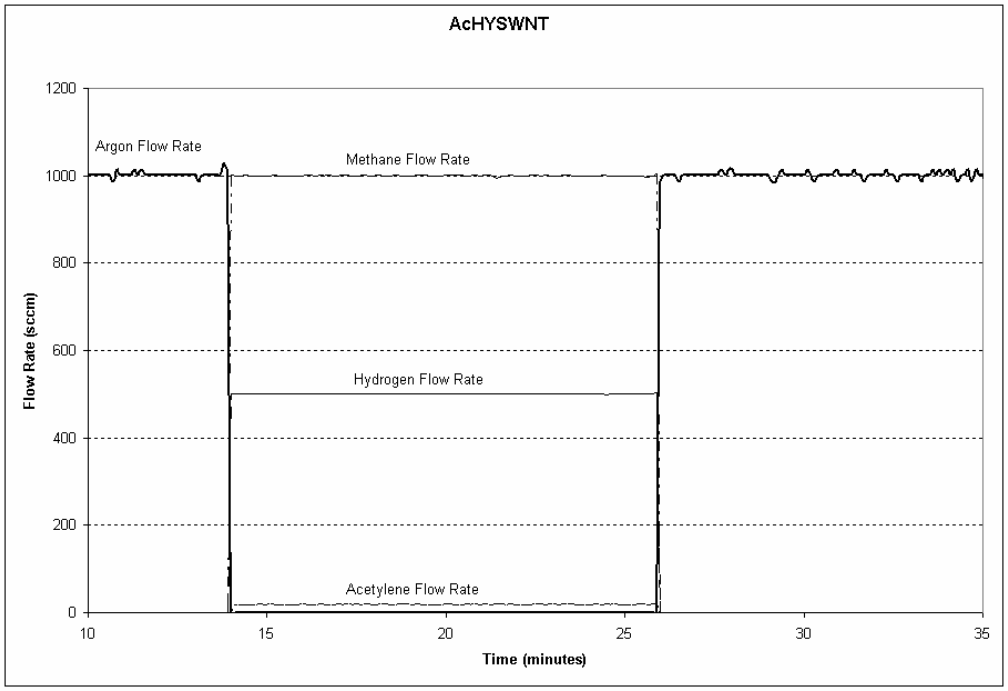

Figure 27: Sample Soak Detail for AcHYCNT Recipe

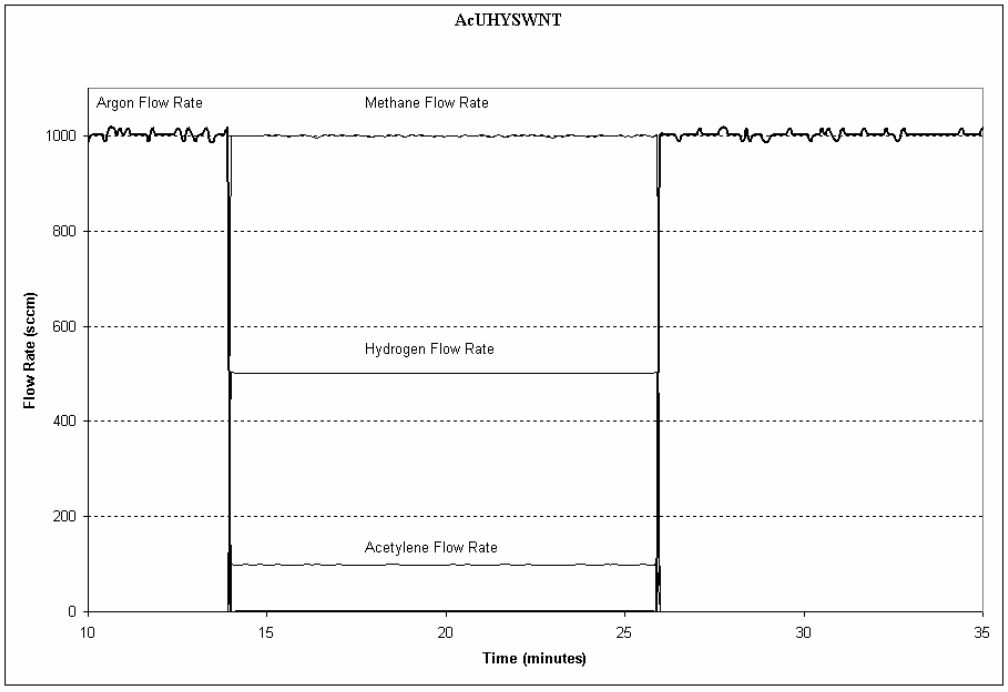

Figure 28: Sample Soak Detail for AcUHYCNT Recipe

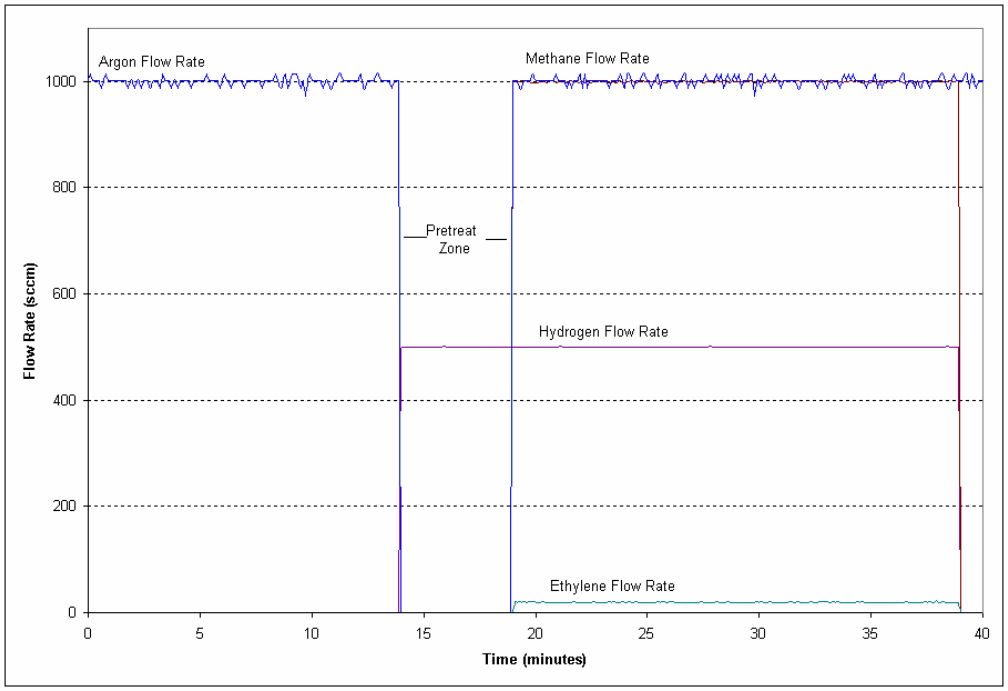

Figure 29: Sample Soak Detail for BULK CNT Recipe with 5 Minute Hydrogen Gas Pretreatment

3.3 Analysis of Synthesized Carbon Nanotubes

3.3.1 Scanning Electron Microscopy Analysis

The CNTs produced in the present work were analyzed with Scanning electron microscopes (SEM) to determine physical properties such as tube diameter, and where appropriate tube length and alignment. The microscopes used for analysis were a Hitachi S800 FEG SEM and a LEO 1530 Thermally-Assisted FEG SEM. The microscopes were operated at an accelerating voltage between 5 and 15kV. Each sample was analyzed at various magnifications, and multiple regions of each sample were analyzed. A limited number of measurements of tube diameter and length were taken using the software associated with the LEO SEM due to time constraints. Other measurements of tube properties were done manually, or with the assistance of Image Pro Plus software.

3.4 Electrochemical Double Layer Supercapacitor Construction

3.4.1 Electrode Construction

Electrodes were made from industrial supercapacitor aluminum foil provided by Maxwell Technologies. The foil was cut into square plates with a small rectangular tab extending from the upper left corner of each square. The square region of each electrode varied between 1 in^2 and 2 in^2. The rectangular tab on each electrode was used as a connection point to perform electrical testing. The active material was applied to the square region of each electrode. Once the active material was applied to each electrode, an electrolyte was applied to the active material.

The Electrolyte used in this solution was Tetraethylammonium tetrafluoroborate/Acetonitrile (TEATFB/ACN) solution of various molarities (0.1M, 1.0M and 1.5M) was prepared by dissolving a known quantity of Tetraethylammonium tetrafluoroborate powder in a known quantity of acetonitrile liquid. The electrolyte was applied to the active material on each electrode using a disposable pipette until the active material was sufficiently saturated. Approximately 3-5 mL of electrolyte was used for each electrode.

Once the electrodes were fully prepared with both active material and a specific electrolyte, a Celgard 2400 Microporous Membrane separator was placed between the two electrodes. The electrodes were then sandwiched together with the active material on each electrode facing each other, separated by Celgard Membrane (Figure 30A). The supercapacitor was then sealed using Kapton insulating tape. Figure 30B is a picture of a completely constructed supercapacitor ready for testing.

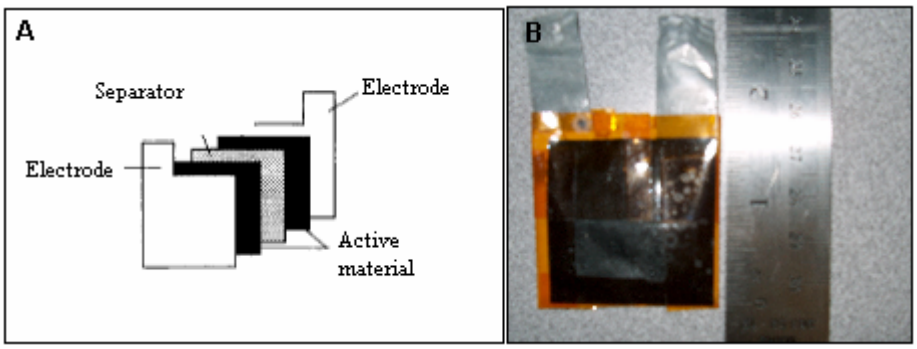

Figure 30: (A) Diagram of ECDL Supercapacitor Construction (B) Picture of Fully Constructed Supercapacitor

3.4.2 Preparation of Carbon Nanotube Active Material

The active electrode material for the ECDL supercapacitors was prepared with 19 vol.% CNT, 24 vol.% Carboxyl Methyl Cellulose (CMC) binder, 29 vol.% Methanol, and 28 vol.% Distilled Water. These constituents were measured and placed in a 50 mL beaker and manually stirred with a glass stirring rod vigorously for 5 minutes. The resulting mixture had a paste like consistency. The CNT used to create the active material were unpurified CNTs produced via the HiPCO process and purified CNTs (produced both by HiPCO and laser ablation), both provided by Dr. Leonard Yowell of NASA. The CNT active material paste was applied to the electrode manually with a stainless steel spatula, and spread manually over the surface of the electrode. The paste was allowed to dry for a period of at least thirty minutes before the electrolyte was applied to the active material.

3.4.3 Electrochemical Double Layer Supercapacitor Testing

The ECDL supercapacitors produced in the present work were tested using a Keithley 2400 Digital Sourcemeter in conjunction with LabView software programming. The supercapacitors were tested against control model PC10 2.5 V, 10 F supercapacitors

supplied by Maxwell Technologies. Each supercapacitor was tested using the standard industry method of cyclic voltammetry.

3.4.3.1 Cyclic Voltammetry

Cyclic voltammetry (CV) tests a supercapacitors response to a changing voltage, and can be used to calculate capacitance. CV testing involves applying a voltage which increases constantly with time (referred to as a voltage sweep). The supercapacitor's responsive current to the voltage sweep is recorded. The capacitance was calculated from the following relationship:

$$C = I/s \qquad \text{(Eqn. 4)}$$

Where I is the current generated by the supercapacitor and s is the sweep rate. The supercapacitors were tested at various sweep rates. The results of the CV testing were plotted as a voltammogram, which gives insight into the capacitive and pseudocapacitive behavior of the ECDL supercapacitor.

3.5 Chapter Summary

This chapter has detailed the CVD process for the synthesis of carbon nanotubes, the preparation of catalysts materials, the photolithography patterning process, and the post synthesis image analysis techniques. Also discussed in this section was the preparation of ECDL electrodes, the creation of CNT active materials for ECDL supercapacitors, the electrolytes used, and the construction of ECDL supercapacitors. Finally, the methods used to test the supercapacitors were discussed.

CHAPTER 4

RESULTS

This chapter presents the results of the experimental procedures that were observed with analytical techniques. SEM images presented in the work are shown as examples, and numerous other images besides these examples were used for analysis and are included in Appendix A. Note that some results, such as CNT length, are not easily quantified due to the non-linear nature of the CNTs.

4.1 Effect of Nickel Catalyst Film Thickness

CNT diameter was analyzed as a function of catalyst film thickness while holding all other synthesis variables constant. The synthesis recipe used for growth was the 'BULK CNT' recipe. Nickel catalyst films of 100 nm, 80 nm, 60 nm, 40 nm and 20 nm thicknesses were used. Nanotube diameter distribution plots are shown by plotting the percent of tubes which fall into a specific range. For each catalyst film thickness, the following ranges were used: (0-9 nm), (10-19 nm), (20-29 nm), (30-39 nm), (40-49 nm), (50-59 nm), (60-69 nm), (70-79 nm), and (80 nm +). Error bars in plots of nanotube diameter distribution indicate the percent error in diameter measurement of each tube analyzed unless otherwise noted.

Table 6 shows the CNT diameter data collected for each catalyst film thickness and references diameter distribution plots for each film thickness. Also included in Table 6 are references to SEM micrographs for each sample.

Table 6: Average Nanotube Diameter for Decreasing Catalyst Film Thickness for BULK CNT Recipe

Catalyst Film Thickness (nm)	100	80	60	40	20
Average Diameter (nm)	45.7	45.4	41.5	33.1	29.6
Standard Deviation (nm)	9.2	5.3	7.9	6.8	9.6
Diameter Distribution Plot	Figure 31	Figure 33	Figure 35	Figure 37	Figure 39
SEM Micrograph	Figure 32	Figure 34	Figure 36	Figure 38	Figure 40

4.1.1 Bulk CNT, 100 nm Nickel Catalyst Film

This recipe results in a wide distribution of tube diameters, with approximately 94% of tubes having an outer diameter less than 80 nm. Tubes are estimated to have lengths exceeding 5 μm. The bright spots at the end of the tubes are encapsulated Ni particles, indicating tip growth.

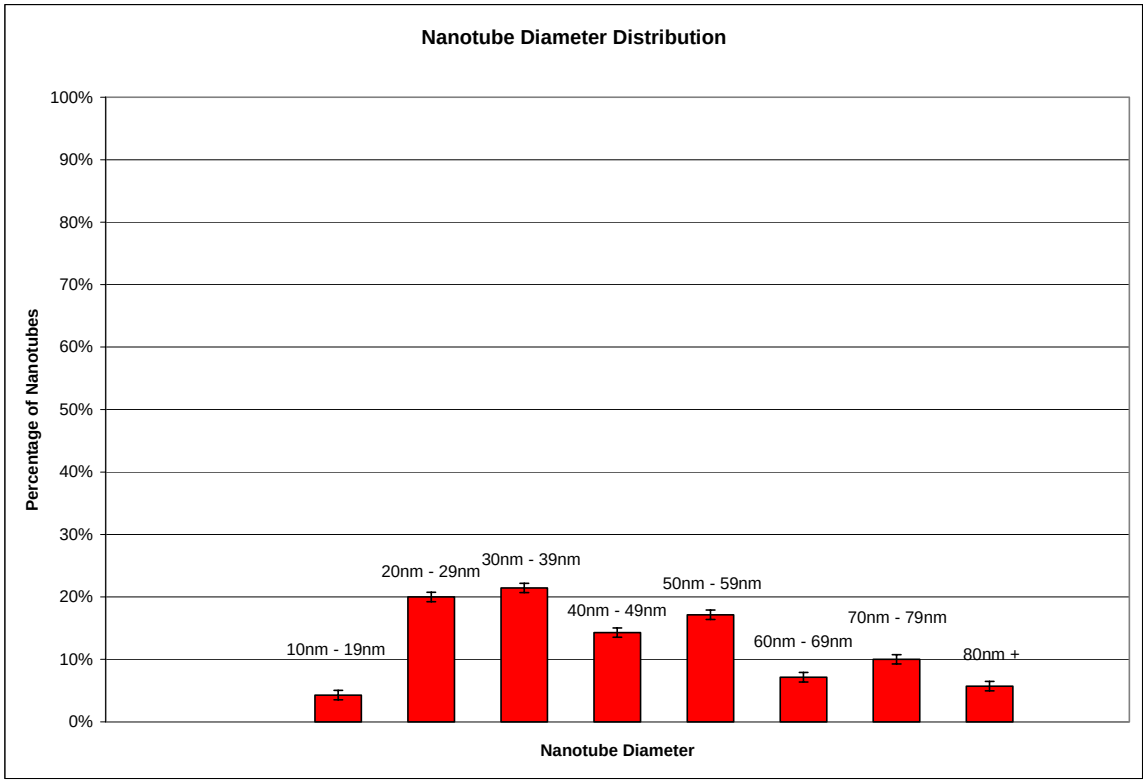

Figure 31: Distribution of Nanotube Diameter for Bulk CNT Recipe on 100 nm Nickel Film

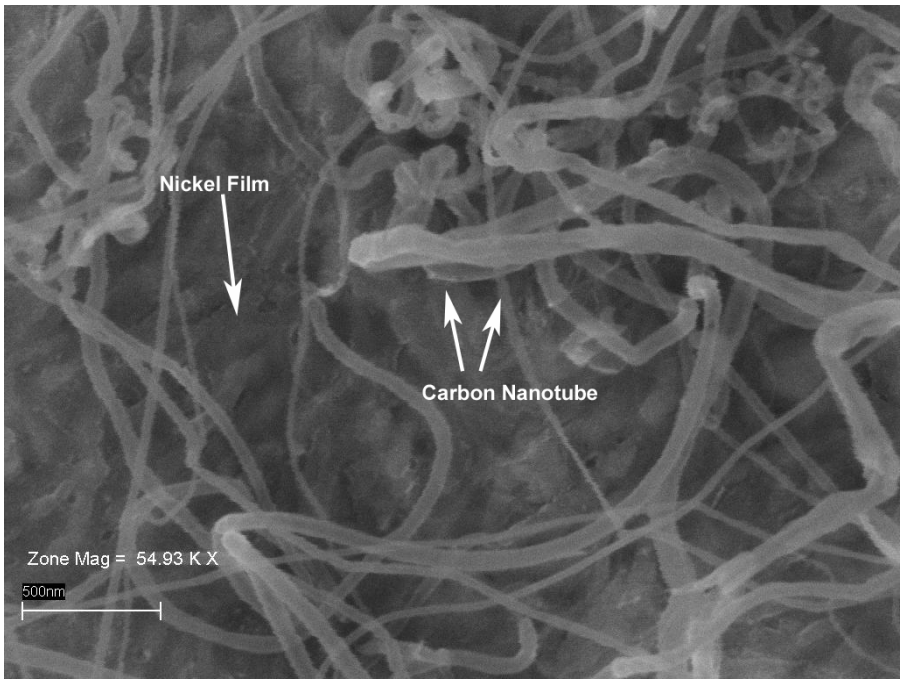

Figure 32: SEM Micrograph of CNTs Grown with Bulk CNT Recipe on 100 nm Nickel Film

4.1.2 Bulk CNT, 80 nm Nickel Catalyst Film

Approximately 92% of the CNTs have diameters less than 80 nm. The lengths of the tubes are difficult to measure precisely, but are estimated to exceed 5 μm. Large Ni clusters have formed from the decomposition of the film and are present as large white aggregates in Figure 34.

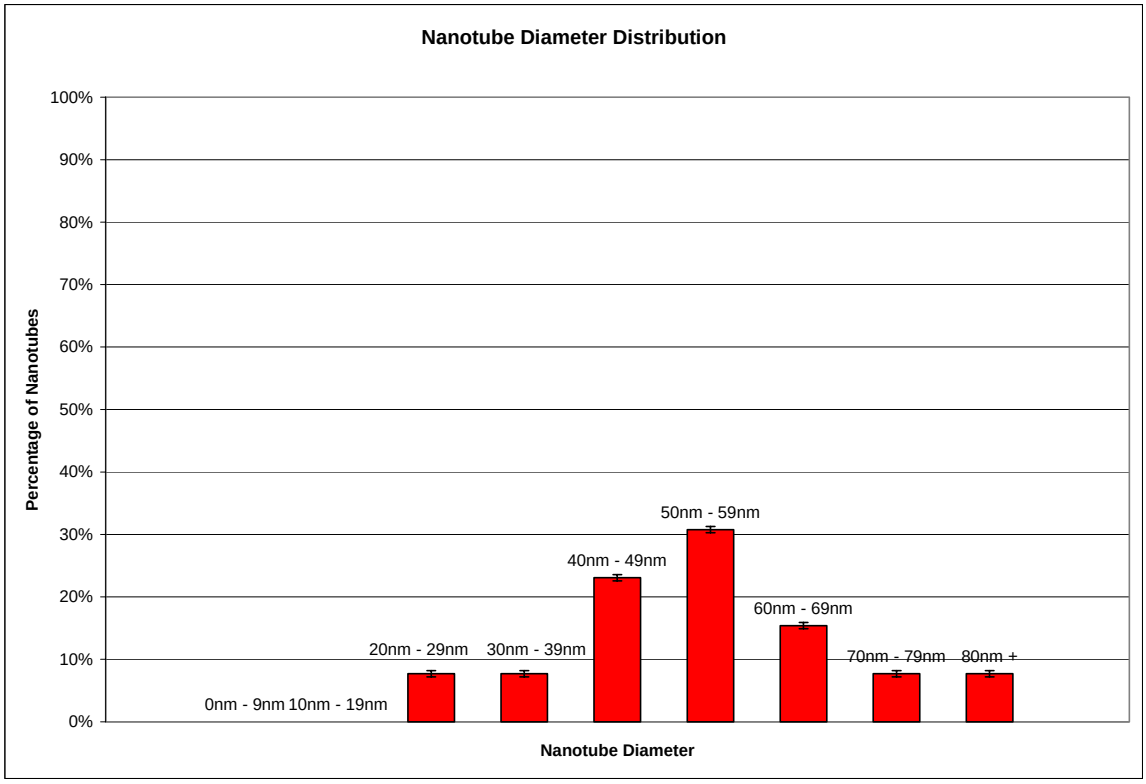

Figure 33: Distribution of Nanotube Diameter for Bulk CNT Recipe on 80 nm Nickel Film

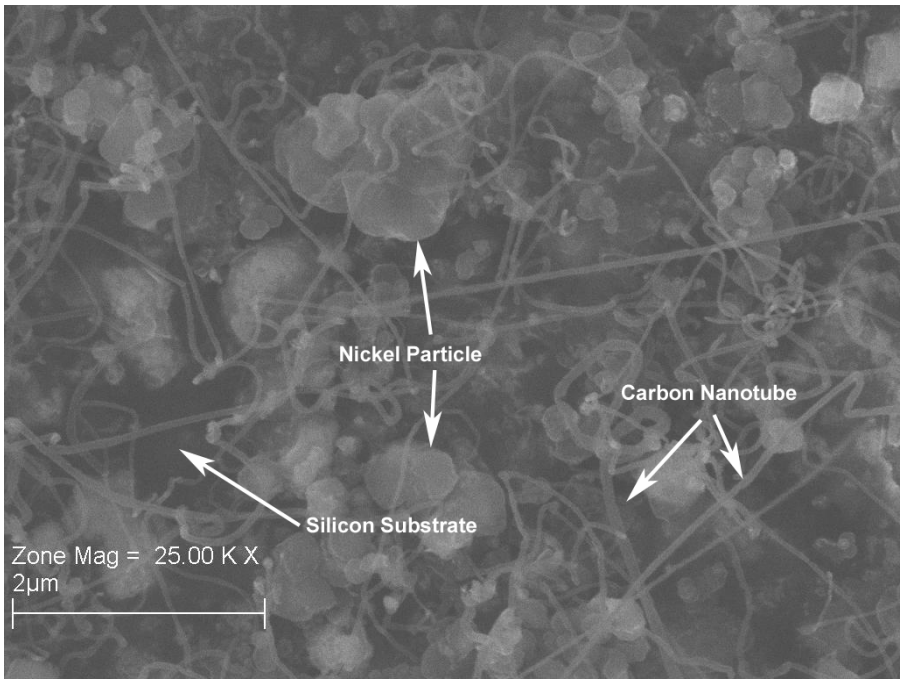

Figure 34: SEM Micrograph of CNTs Grown with Bulk CNT Recipe on 80 nm Nickel Film

4.1.3 Bulk CNT, 60 nm Nickel Catalyst Film

This recipe results in a somewhat Gaussian distribution of tube diameters, with approximately 97% of tubes having an outer diameter less than 80 nm. The largest tube from the sampled region had a diameter of approximately 84 nm, while the smallest tube in the same sample region had a diameter of approximately 14 nm. The lengths of the tube vary widely, with tube lengths exceeding 5 µm and approaching 10 µm.

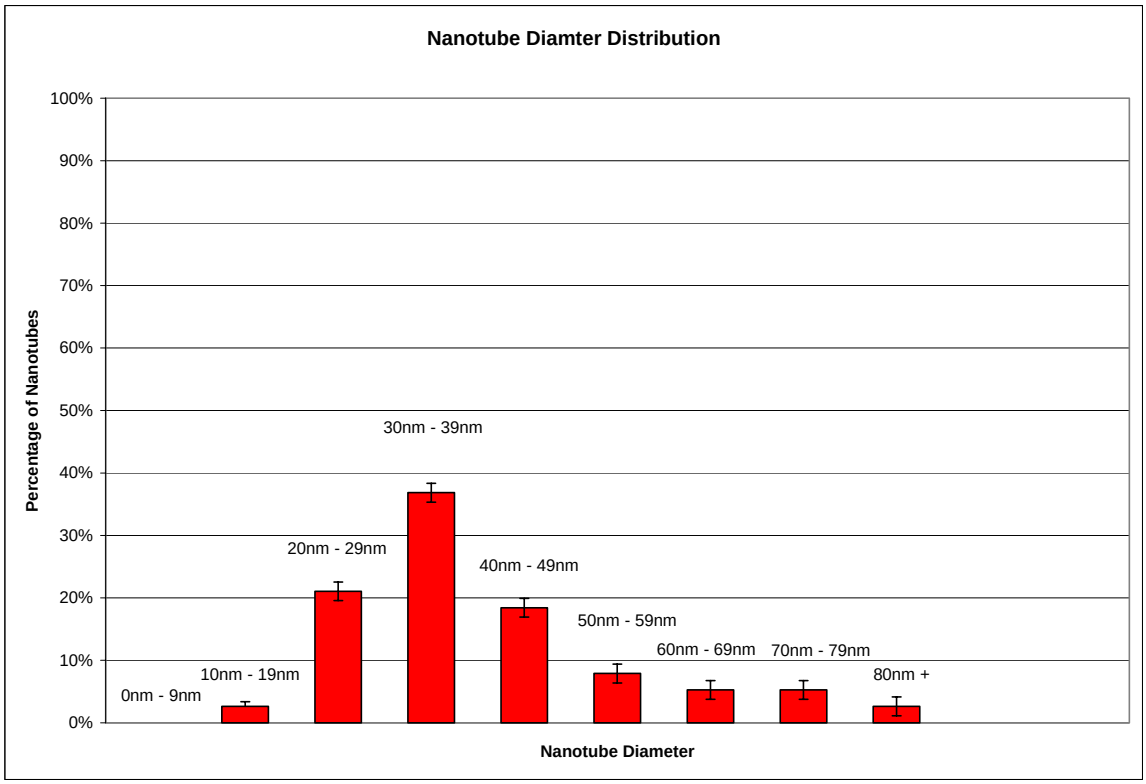

Figure 35: Distribution of Nanotube Diameter for Bulk CNT Recipe on 60 nm Nickel Film

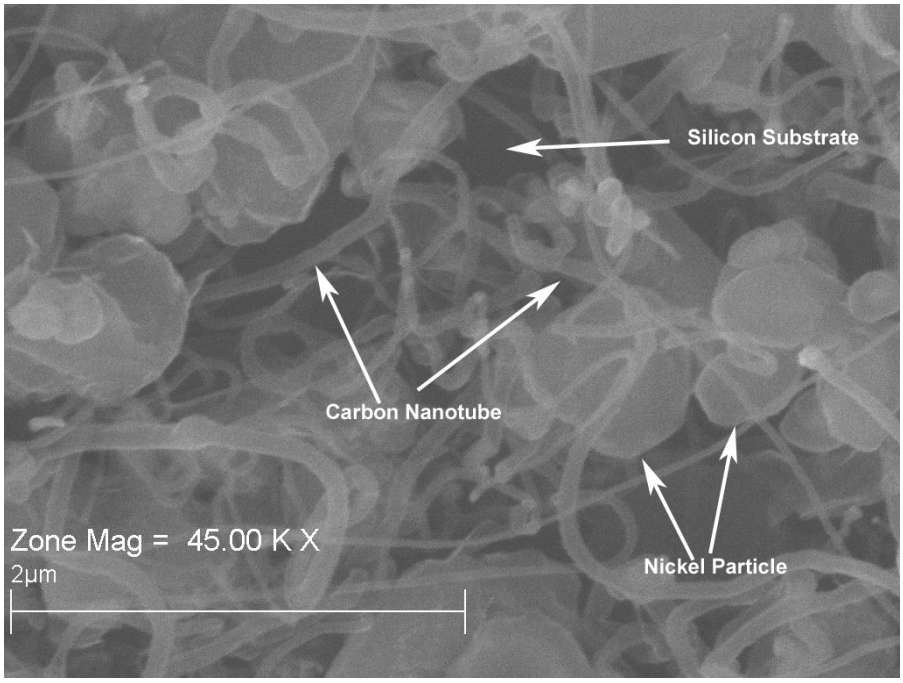

Figure 36: SEM Micrograph of CNTs Grown with Bulk CNT Recipe on 60 nm Nickel Film

4.1.4 Bulk CNT, 40 nm Nickel Catalyst Film

This recipe results in a Gaussian distribution of tube diameters, with approximately 96 % of tubes having an outer diameter less than 50 nm. The largest tube from the sampled regions had a diameter of approximately 54 nm, while the smallest tube in the same sample region had a diameter of approximately 9 nm. The tube lengths for this case are generally shorter, but some nanotubes still achieve lengths surpassing 5 µm.

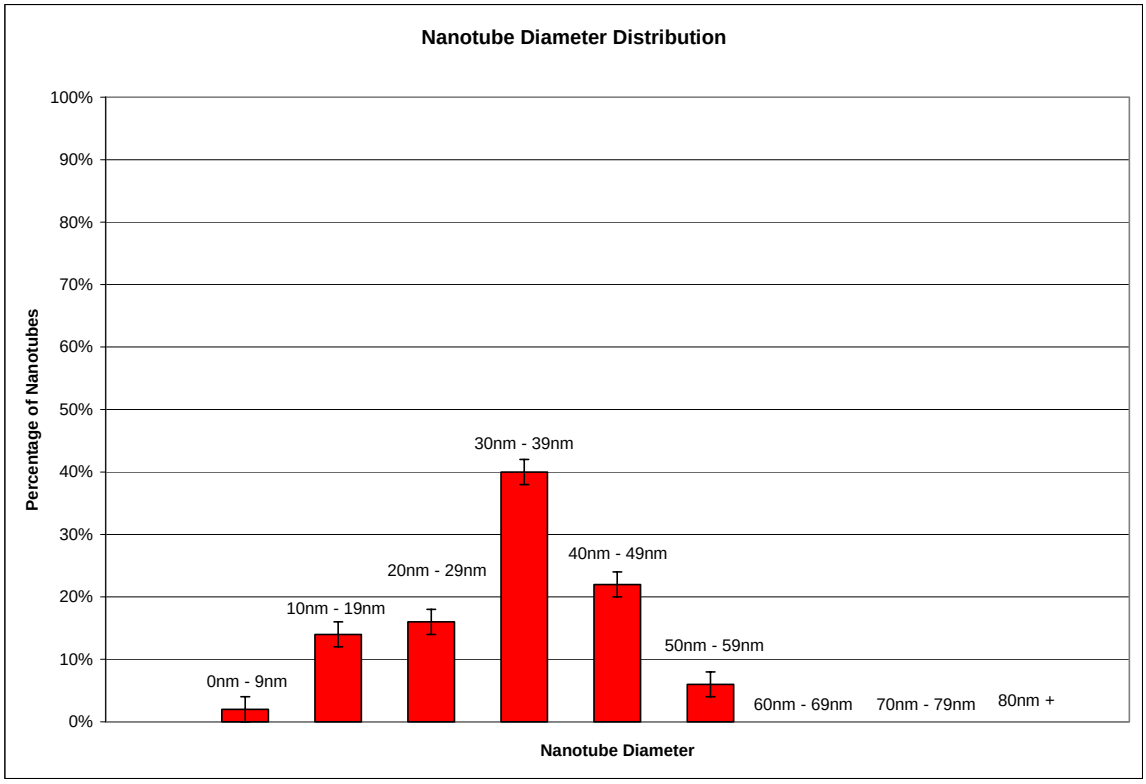

Figure 37: Distribution of Nanotube Diameter for Bulk CNT Recipe on 40 nm Nickel Film

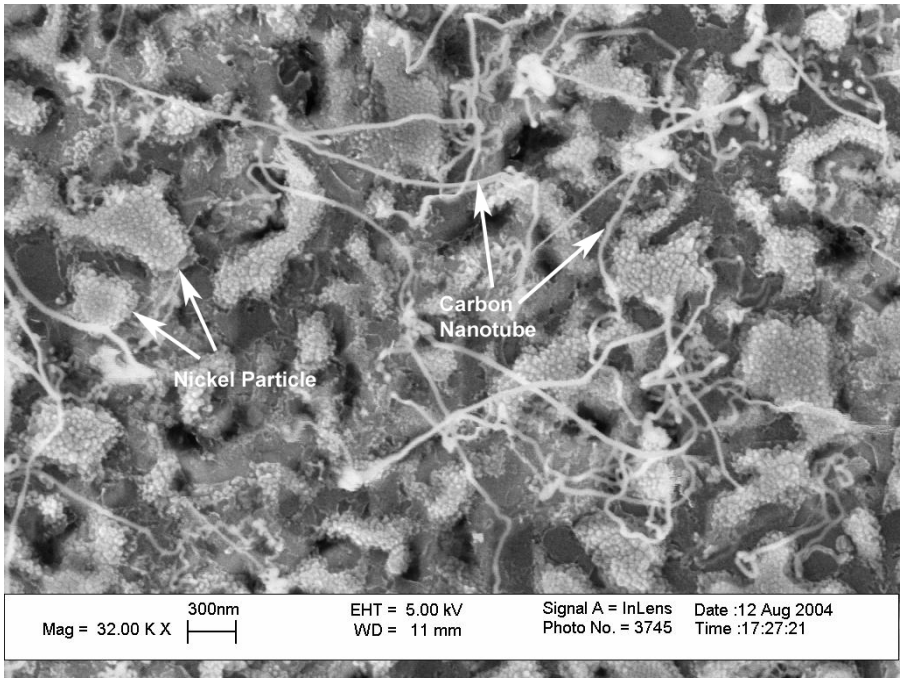

Figure 38: SEM Micrograph of CNTs Grown with Bulk CNT Recipe on 40 nm Nickel Film

4.1.5 Bulk CNT, 20 nm Nickel Catalyst Film

This recipe results in a Gaussian distribution of tube diameters, with approximately 97 % of tubes having an outer diameter less than 50 nm and approximately 83% of the CNTs having an outer diameter less than 40 nm. The largest tube from the sampled regions had a diameter of approximately 54 nm, while the smallest tube in the same sample region had a diameter of approximately 14 nm. The tube lengths for this case are generally shorter than 3 μm, but some nanotubes still achieve lengths surpassing 5 μm.

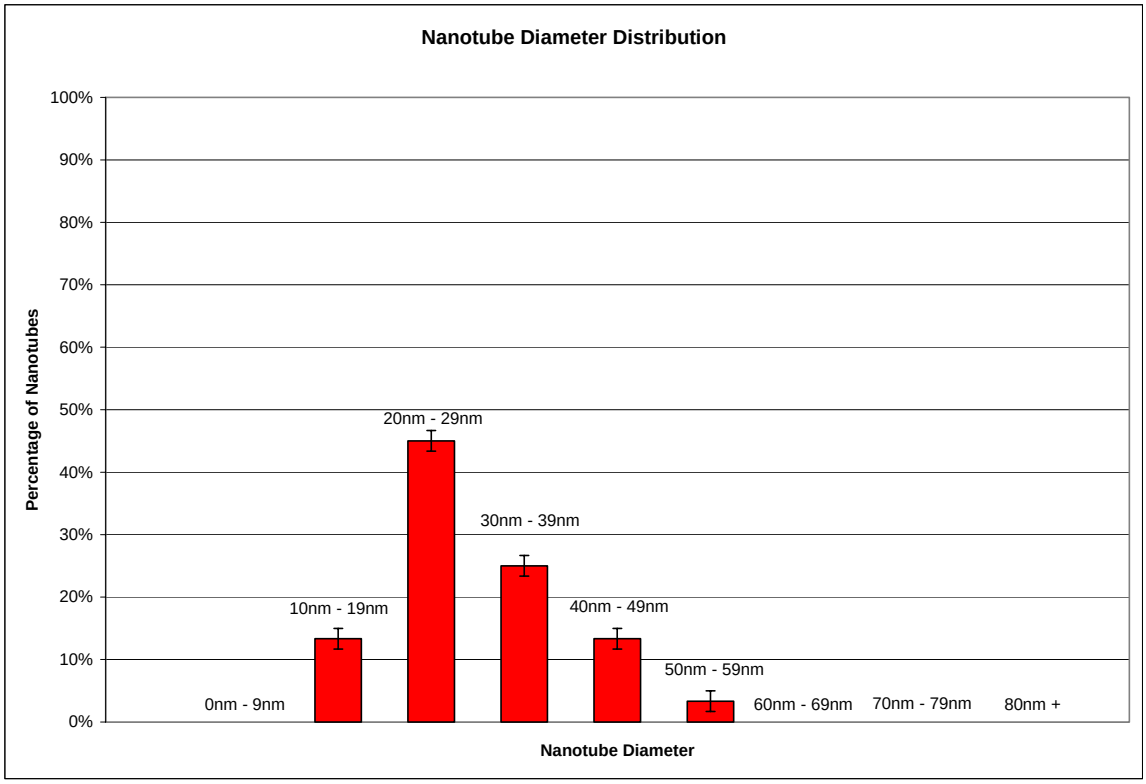

Figure 39: Distribution of Nanotube Diameter for Bulk CNT Recipe on 20 nm Nickel Film

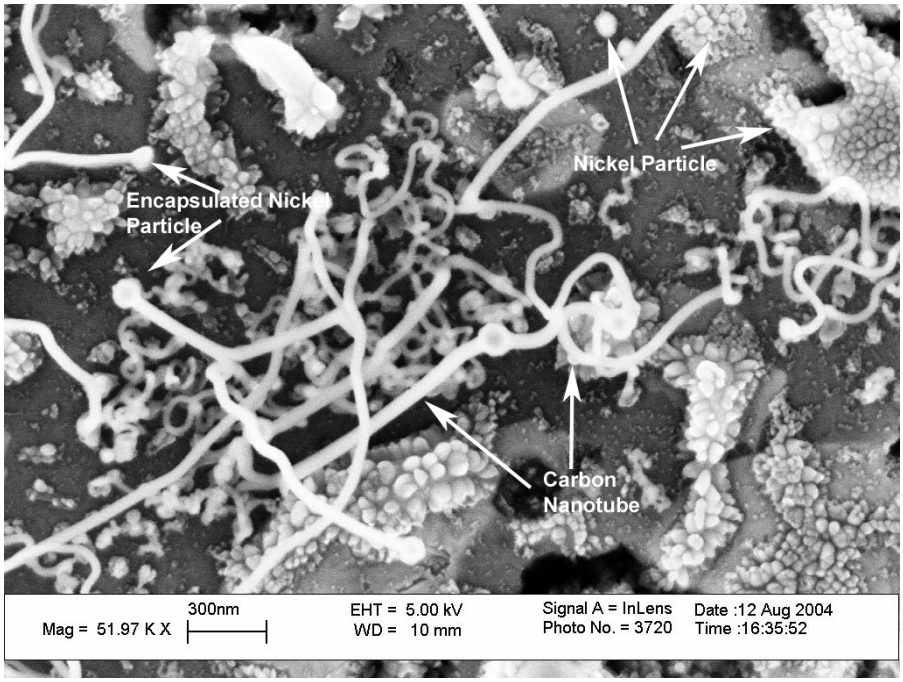

Figure 40: SEM Micrograph of CNTs Grown with Bulk CNT Recipe on 20 nm Nickel Film

4.1.6 Bulk CNT, Nickel Catalyst Film Summary

Figure 41 shows the relationship between the thickness of the Nickel catalyst film and the resultant average diameter of CNTs synthesized on that film using the Bulk CNT recipe. The error bars in the figure represent one standard deviation from the calculated average CNT diameters.

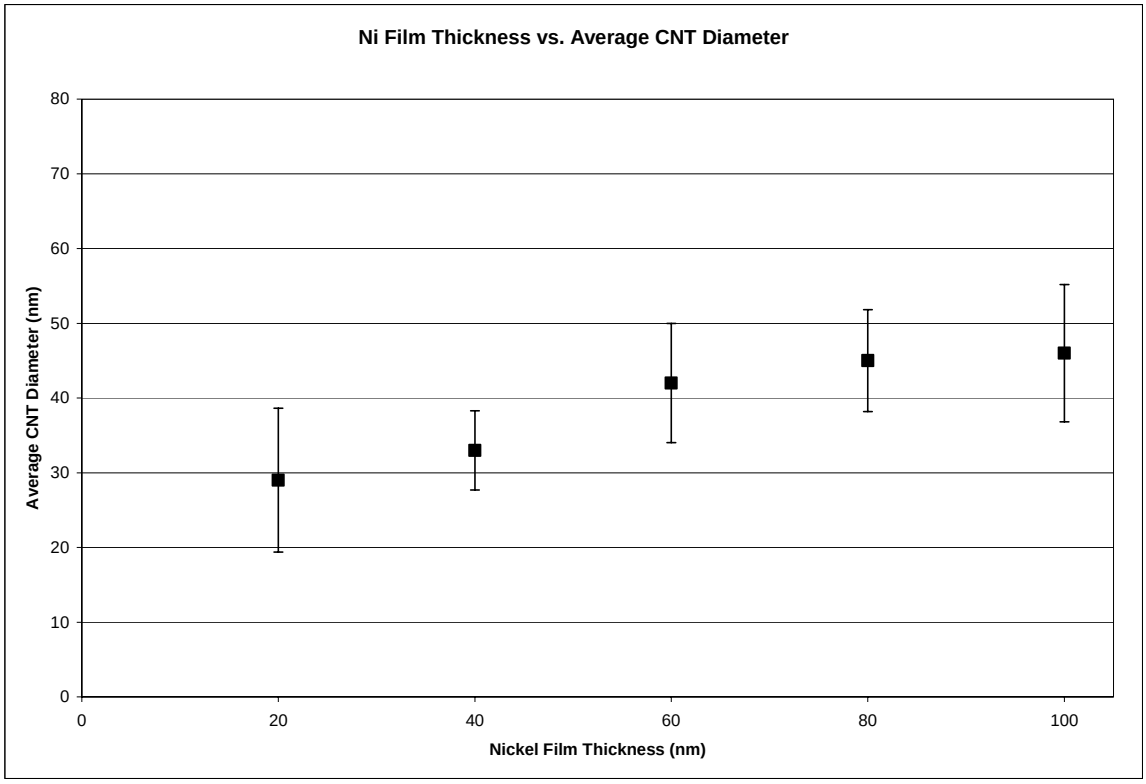

Figure 41: Nickel Film Thickness vs. Average CNT Diameter. Error Bars Represent One Standard Deviation

4.2 Effect of Five Minute Hydrogen gas Pretreatment Prior to Soak Stage

CNT diameter was analyzed as a function of catalyst film thickness while holding all other synthesis variables constant. The synthesis recipe used for growth was the BULK CNT with five minute Hydrogen Pretreatment recipe. Nickel catalyst films of 100 nm, 80 nm, 60 nm, 40 nm and 20 nm thicknesses were used. Nanotube diameter distribution plots are created by plotting the percent of tubes that fall into a specific range. For each catalyst film thickness, the following ranges were used: (0-9 nm), (10-19 nm), (20-29 nm), (30-39 nm), (40-49 nm), (50-59 nm), (60-69 nm), (70-79 nm), and (80

nm +). Error bars in plots of nanotube diameter distribution indicate the percent error in diameter measurement of each tube analyzed unless otherwise noted.

Table 7 shows the CNT diameter data collected for each catalyst film thickness and references diameter distribution plots for each film thickness. Also included in Table 7 are references to SEM micrographs for each sample.

Table 7: Average Nanotube Diameter for Decreasing Catalyst Film Thickness for BULK CNT with Five Minute Hydrogen Pretreatment Recipe

Catalyst Film Thickness (nm)	100	80	60	40	20
Average Diameter (nm)	44.5	40.8	38.2	39.6	29.8
Standard Deviation (nm)	3.1	4.3	4.8	5.6	4.2
Diameter Distribution Plot	Figure 42	Figure 44	Figure 46	Figure 48	Figure 50
SEM Micrograph	Figure 43	Figure 45	Figure 47	Figure 49	Figure 51

4.2.1 Bulk CNT with Five Minute Hydrogen Pretreatment on 100 nm Nickel Catalyst

This recipe results in a narrow distribution of tube diameters, with approximately 95% of tubes having an outer diameter less than 60 nm and 81% of nanotubes with a diameter of less than 50 nm (Figure 42). The nanotubes synthesized in this recipe have maximum lengths approaching 4 μm. The bright spots at the end of the tubes are encapsulated Ni particles, indicating tip growth (Figure 43).

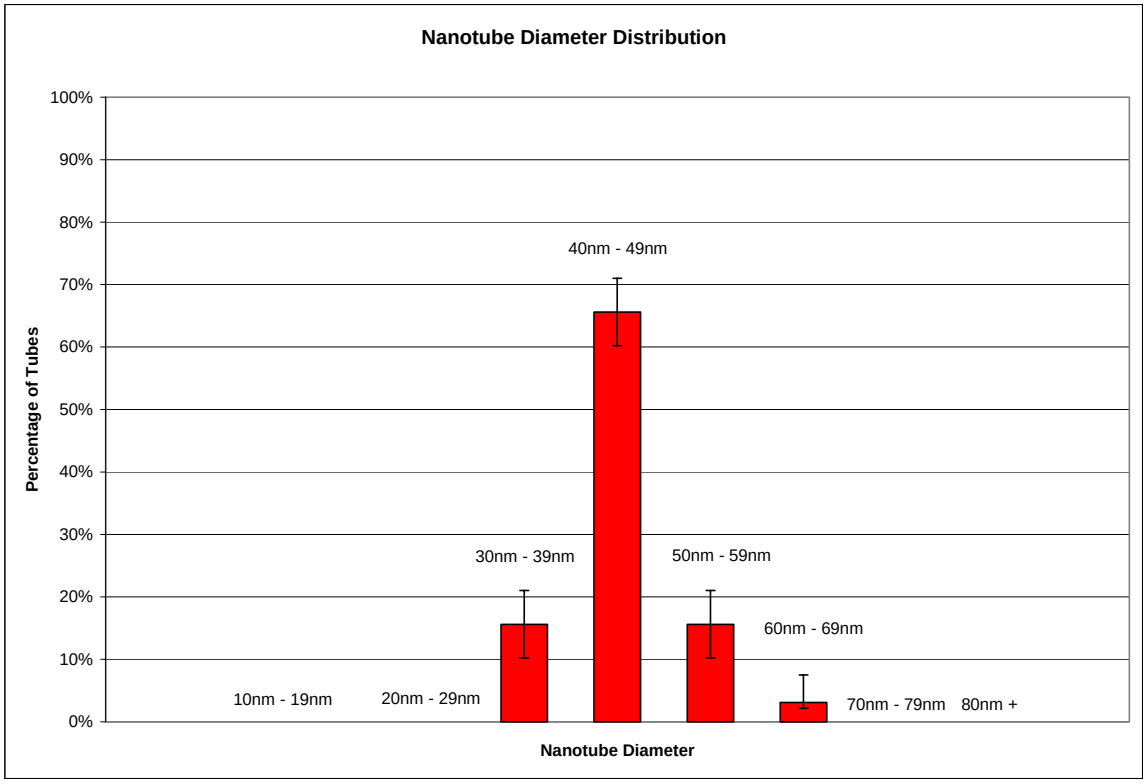

Figure 42: Distribution of Nanotube Diameter for Bulk CNT with Five Minute Hydrogen Pretreatment Recipe on 100nm Nickel Film

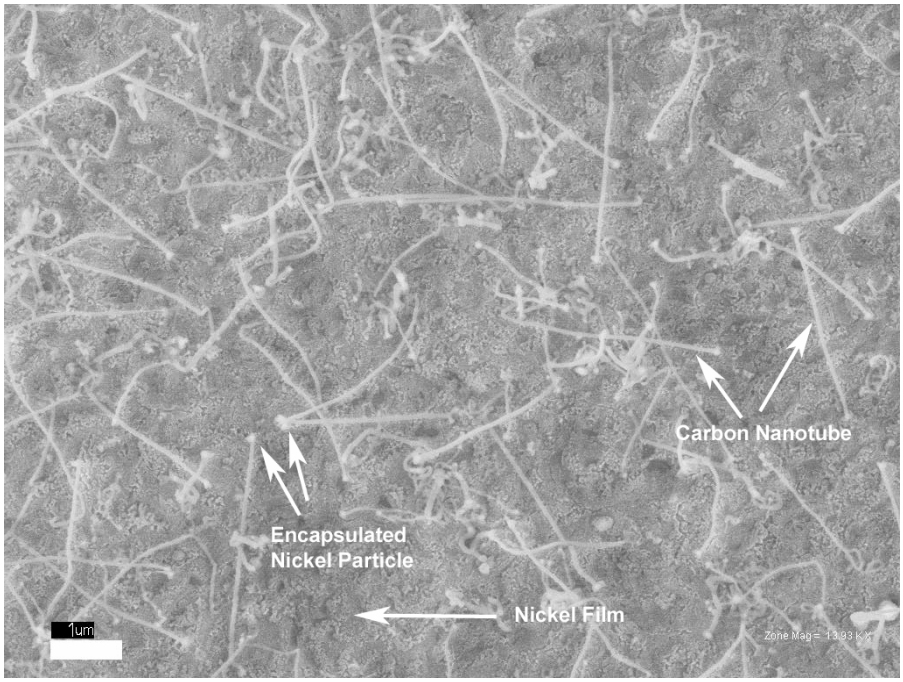

Figure 43: SEM Micrograph of CNTs Grown with Bulk CNT with Five Minute Hydrogen Pretreatment Recipe on 100 nm Nickel Film

4.2.2 Bulk CNT with Five Minute Hydrogen Pretreatment on 80 nm Nickel Catalyst

This recipe results in a narrow distribution of tube diameters, with approximately 97% of tubes having an outer diameter less than 60 nm and 90% of nanotubes with a diameter of less than 50 nm (Figure 44). The nanotubes synthesized in this recipe have maximum lengths in excess of approximately 5 µm.

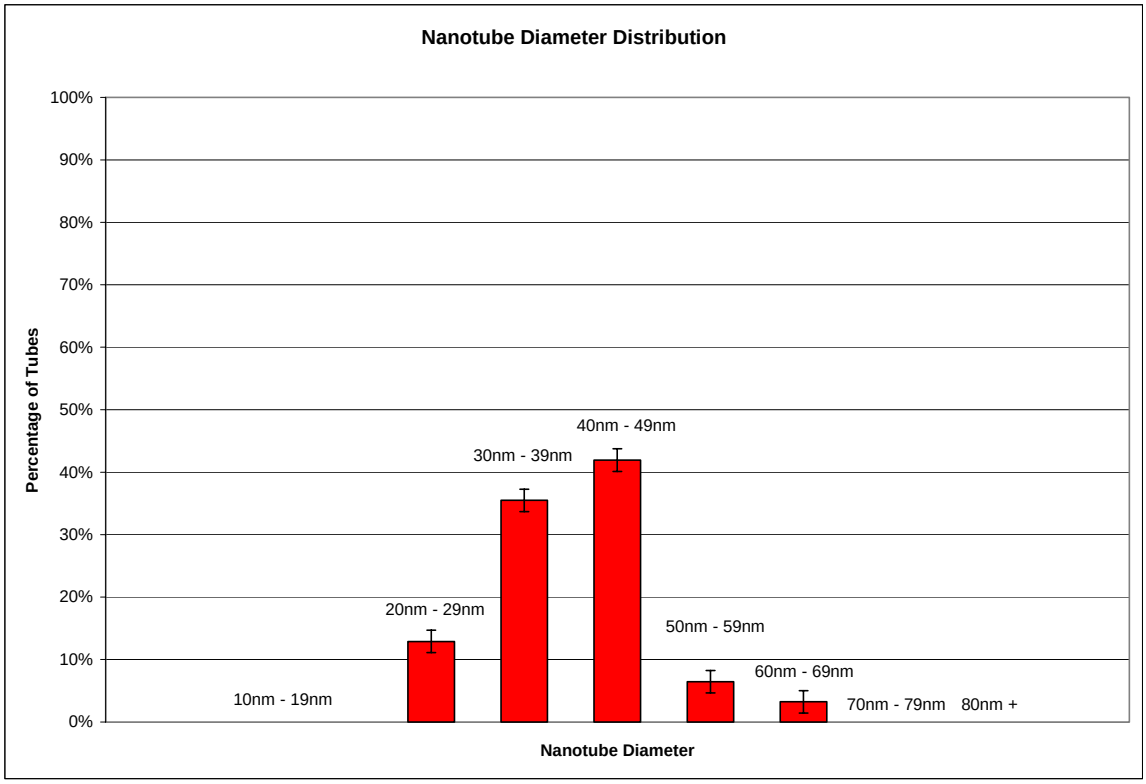

Figure 44: Distribution of Nanotube Diameter for Bulk CNT with Five Minute Hydrogen Pretreatment Recipe on 80 nm Nickel Film

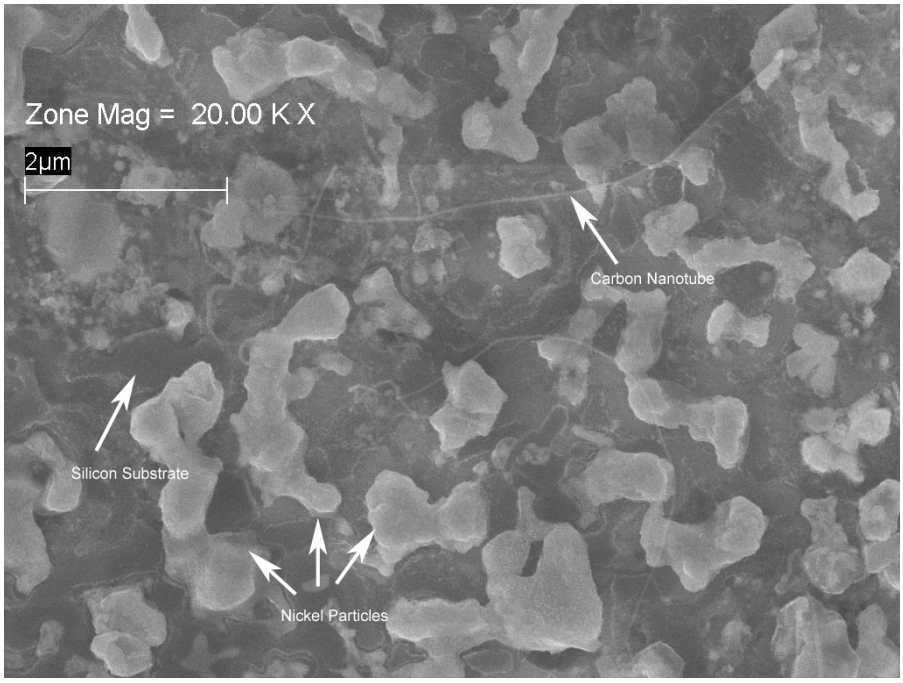

Figure 45: SEM Micrograph of CNTs Grown with Bulk CNT with Five Minute Hydrogen Pretreatment Recipe on 80 nm Nickel Film

4.2.3 Bulk CNT with Five Minute Hydrogen Pretreatment on 60 nm Nickel Catalyst

This recipe results in a narrow distribution of tube diameters, with approximately 83% of tubes having an outer diameter less than 60 nm and 87% of nanotubes with a diameter of less than 50 nm (Figure 46). Tubes have maximum lengths approaching 4 µm. The bright spots at the end of the tubes are encapsulated Ni particles, indicating tip growth (Figure 47).

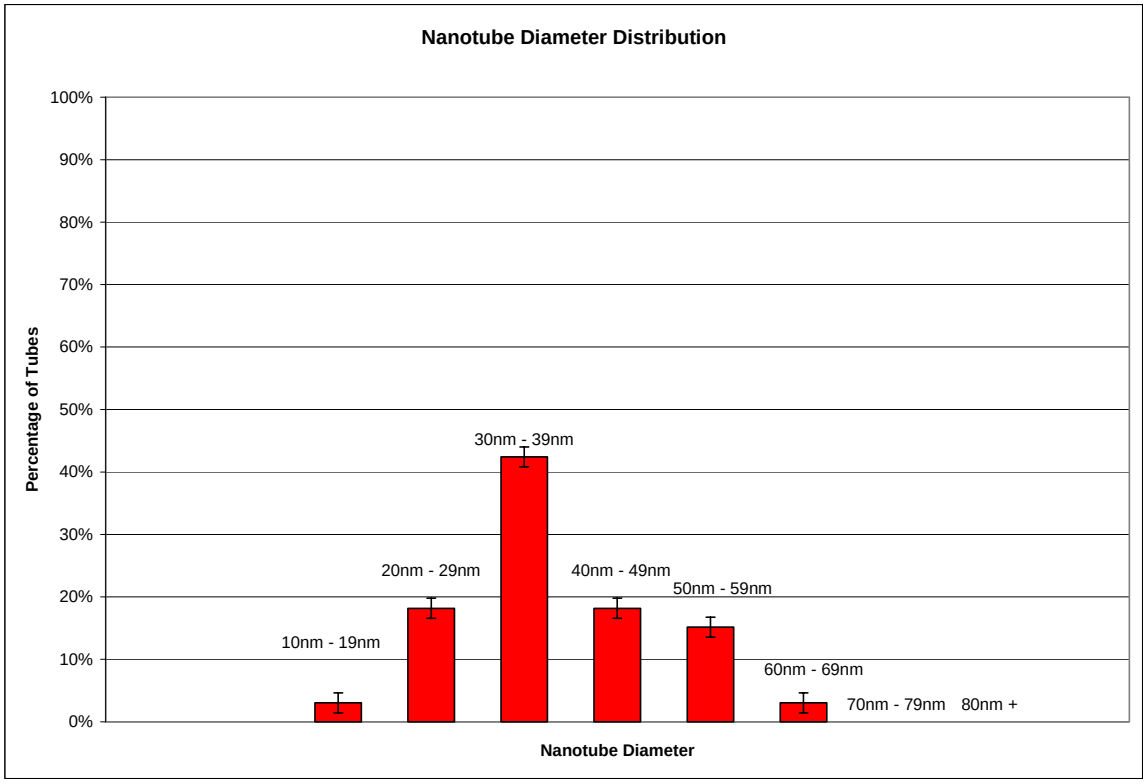

Figure 46: Distribution of Nanotube Diameter for Bulk CNT with Five Minute Hydrogen Pretreat Recipe on 60 nm Nickel Film

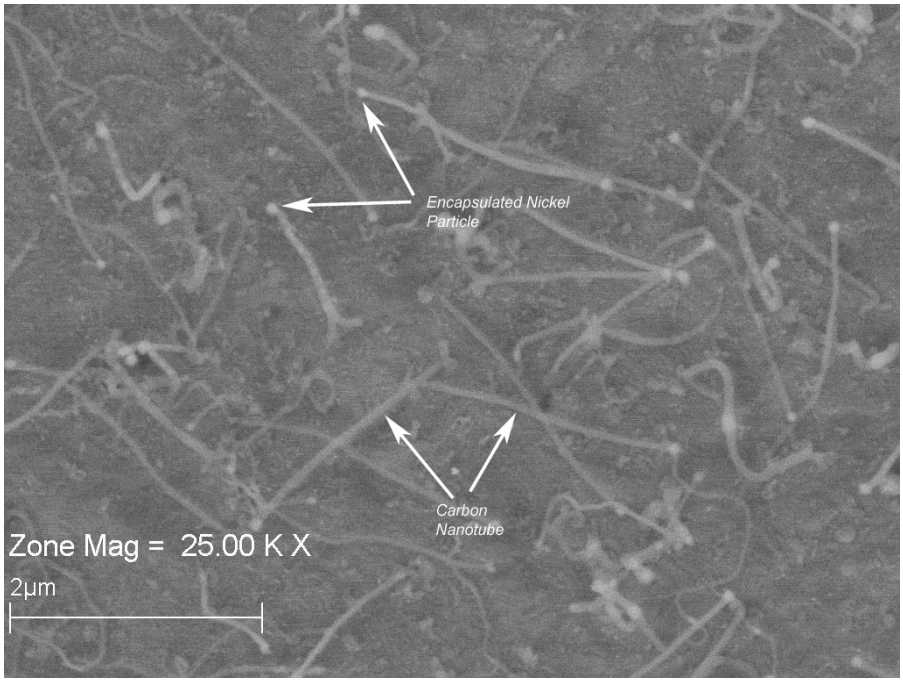

Figure 47: SEM Micrograph of CNTs Grown with Bulk CNT with Five Minute Hydrogen Pretreatment Recipe on 60 nm Nickel Film

4.2.4 Bulk CNT with Five Minute Hydrogen Pretreatment on 40 nm Nickel Catalyst

This recipe results in a wider distribution of tube diameters compared to other catalyst film thickness using the same recipe. Nevertheless, approximately 93% of tubes having an outer diameter less than 60 nm and 82% of nanotubes with a diameter of less than 50 nm (Figure 48). The majority of CNTs synthesized on the 40nm thick film have lengths less than 2 μm.

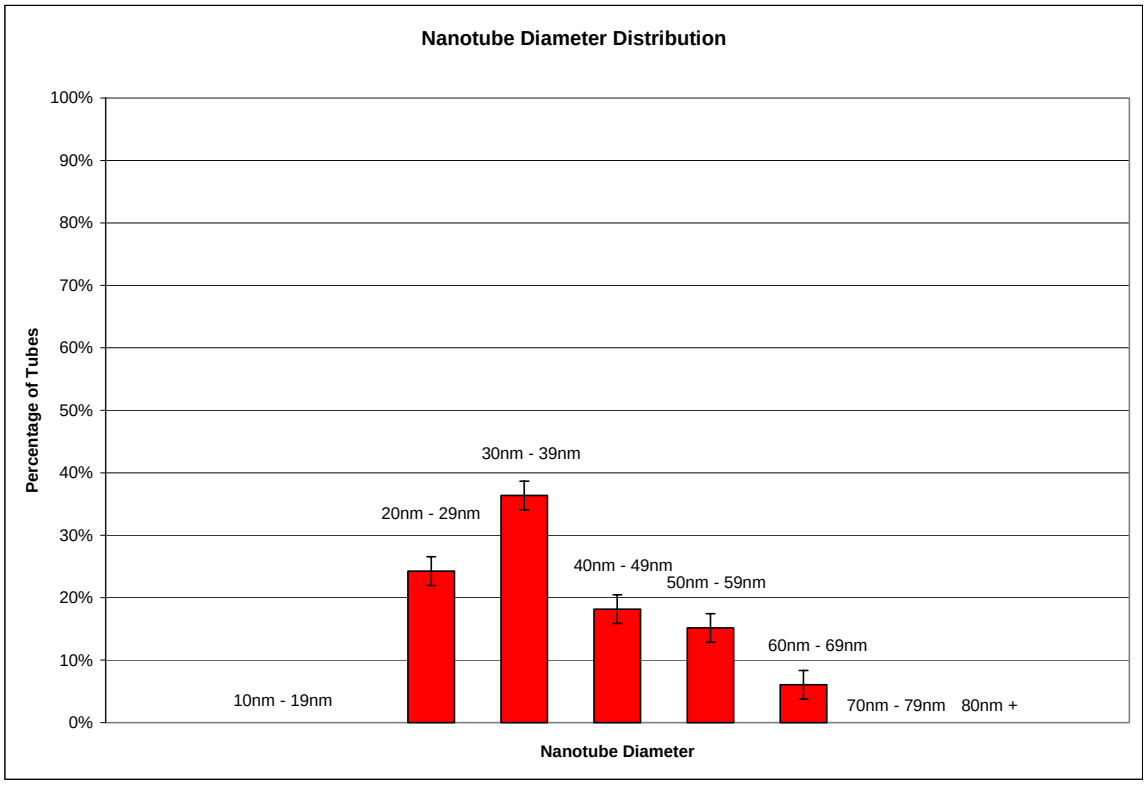

Figure 48: Distribution of Nanotube Diameter for Bulk CNT with Five Minute Hydrogen Pretreatment Recipe on 40 nm Nickel Film

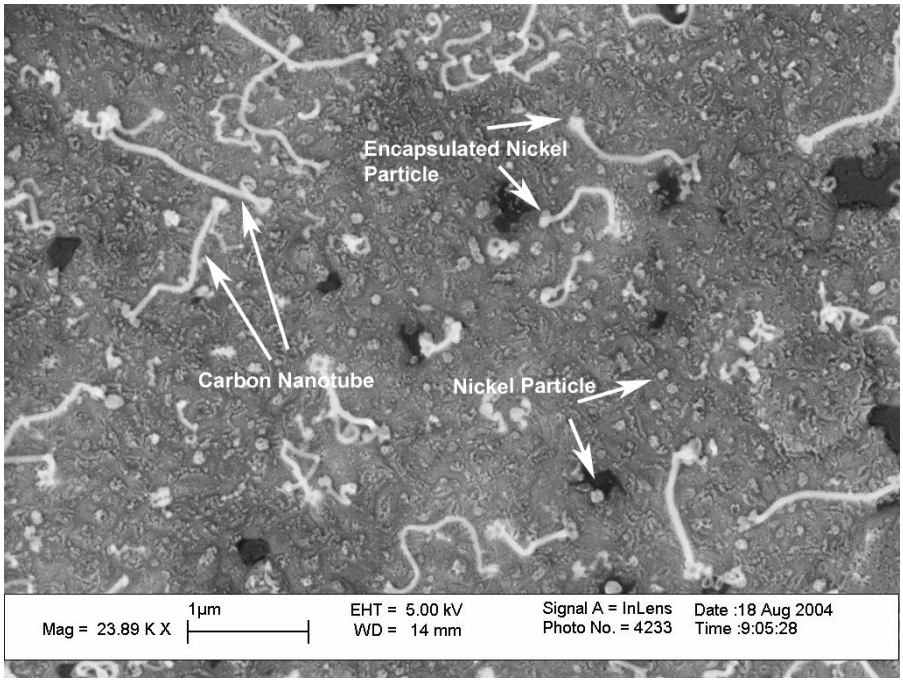

Figure 49: SEM Micrograph of CNTs Grown with Bulk CNT with Five Minute Hydrogen Pretreatment Recipe on 40 nm Nickel Film

4.2.4 Bulk CNT with Five Minute Hydrogen Pretreatment on 20 nm Nickel Catalyst

This recipe results in a narrow distribution of tube diameters, with approximately 100% of tubes having an outer diameter less than 60 nm and 82 % of nanotubes with a diameter of less than 40 nm (Figure 50). The maximum length observed for CNTs synthesized on the 20 nm Nickel film have lengths less than 2 μm.

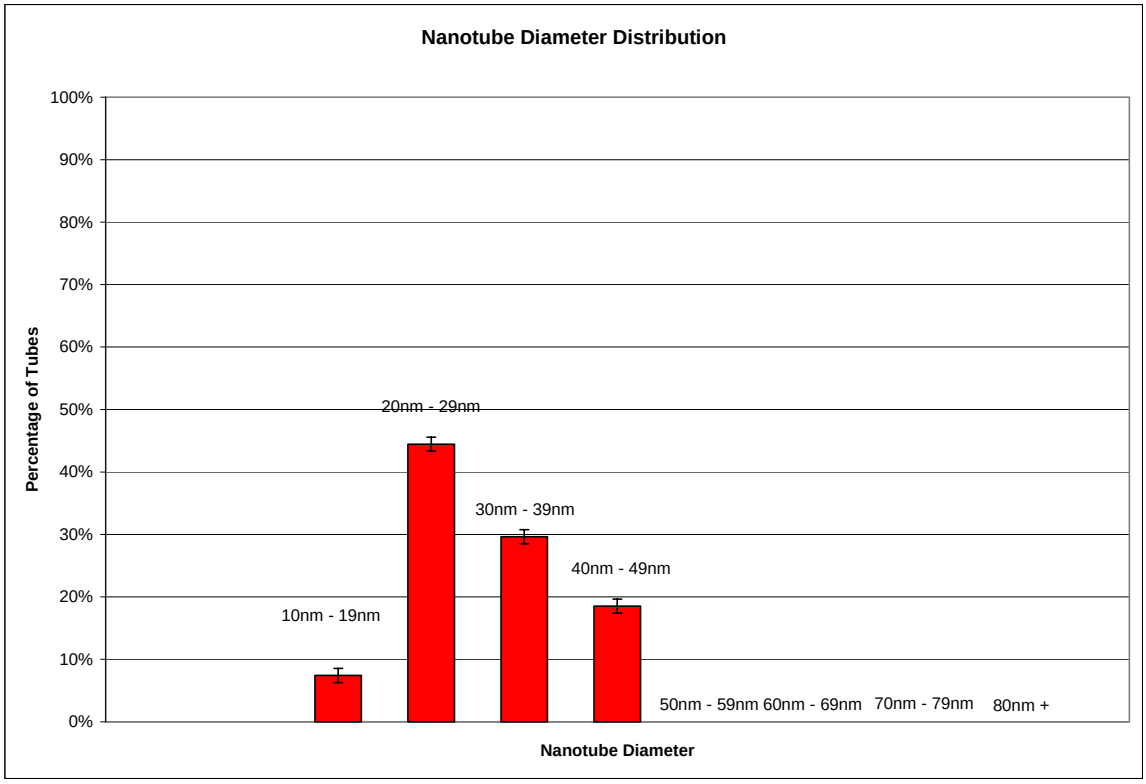

Figure 50: Distribution of Nanotube Diameter for Bulk CNT with Five Minute Hydrogen Pretreatment Recipe on 20 nm Nickel Film

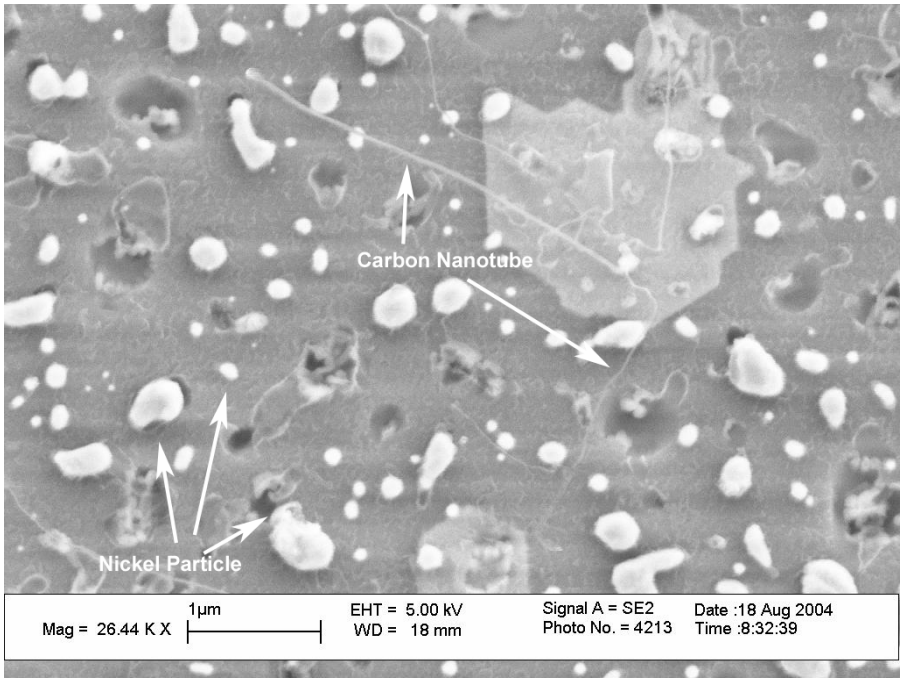

Figure 51: SEM Micrograph of CNTs Grown with Bulk CNT with Five Minute Hydrogen Pretreatment Recipe on 20 nm Nickel Film

4.2.5 Bulk CNT with Five Minute Hydrogen Pretreatment on Nickel Catalyst Summary

Figure 52 shows the relationship between the thickness of the Nickel catalyst film and the resultant average diameter of CNTs synthesized on that film using the Bulk CNT with five minute hydrogen pretreatment recipe. The error bars in the figure represent one standard deviation from the calculated average CNT diameters.

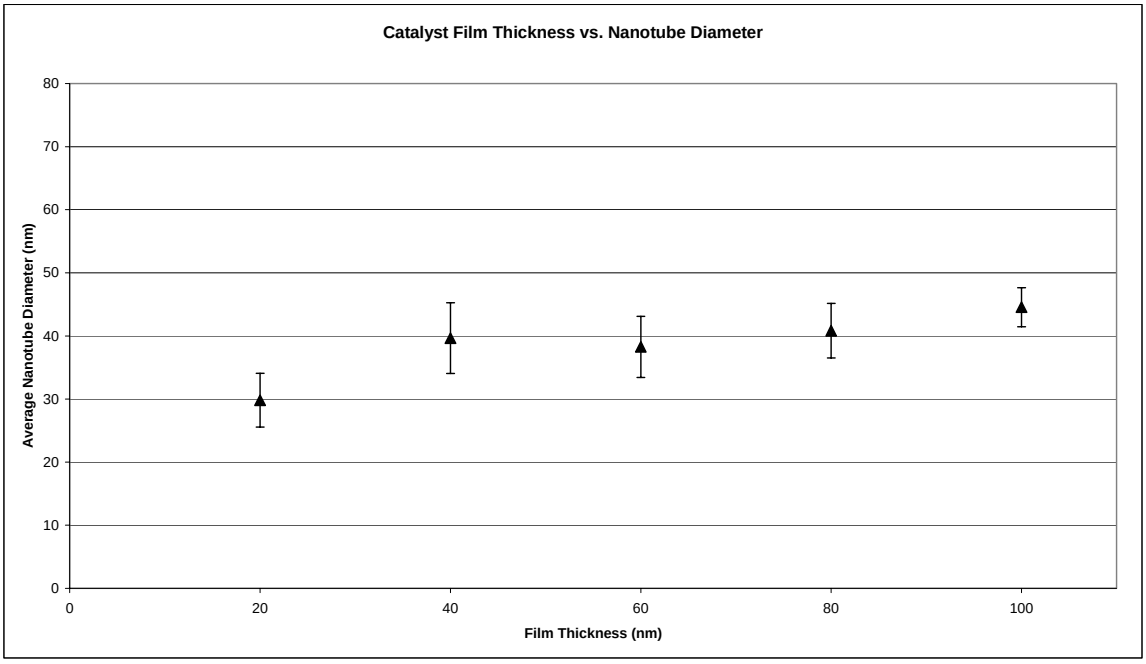

Figure 52: Nickel Film Thickness vs. Average CNT Diameter. Error Bars Represent One Standard Deviation

4.3 Effect of Soak Time

CNT diameter was analyzed as a function of synthesis soak time while holding all other synthesis variables constant. The synthesis recipe used for growth was the 'HYCNT' recipe. Alumina supported Iron catalyst was applied to 1 cm silicon squares as described in the procedure section. Soak time was raised by 3 minutes for each sample, beginning with a three minute soak for the first sample, and ending with a fifteen minute soak for the fifth sample. Plotting the percent of tubes that fall into a specific range results in nanotube diameter distribution plots. For each soak time, the following ranges were used: (0-29 nm), (30-59 nm), (60-89 nm), (90-119 nm), (120-149 nm), (150 nm +).

Table 8 shows the CNT diameter data collected for each soak time and references diameter distribution plots for each sample as well. Also included in Table 8 are references to SEM micrographs for each sample.

Table 8: Average Nanotube Diameter for Increasing Soak Time for UHYCNT Recipe on Fe Catalyst

Soak Time (minutes)	3	6	9	12	15
Average Diameter (nm)	80.8	72.88	78.2	73.0	65.5
Standard Deviation (nm)	26.5	23.3	25.2	22.3	19.8
Diameter Distribution Plot	Figure 53	Figure 55	Figure 57	Figure 59	Figure 61
SEM Micrograph	Figure 54	Figure 56	Figure 58	Figure 60	Figure 62

4.3.1 HYCNT, Three Minute Soak Time

This recipe results in an extremely wide distribution of tube diameters, with diameters ranging from 23 nm to 196 nm. The length of the tubes is difficult to analyze

due to the twisted orientations of the tubes. The longest tube length observed was approximately 7 μm.

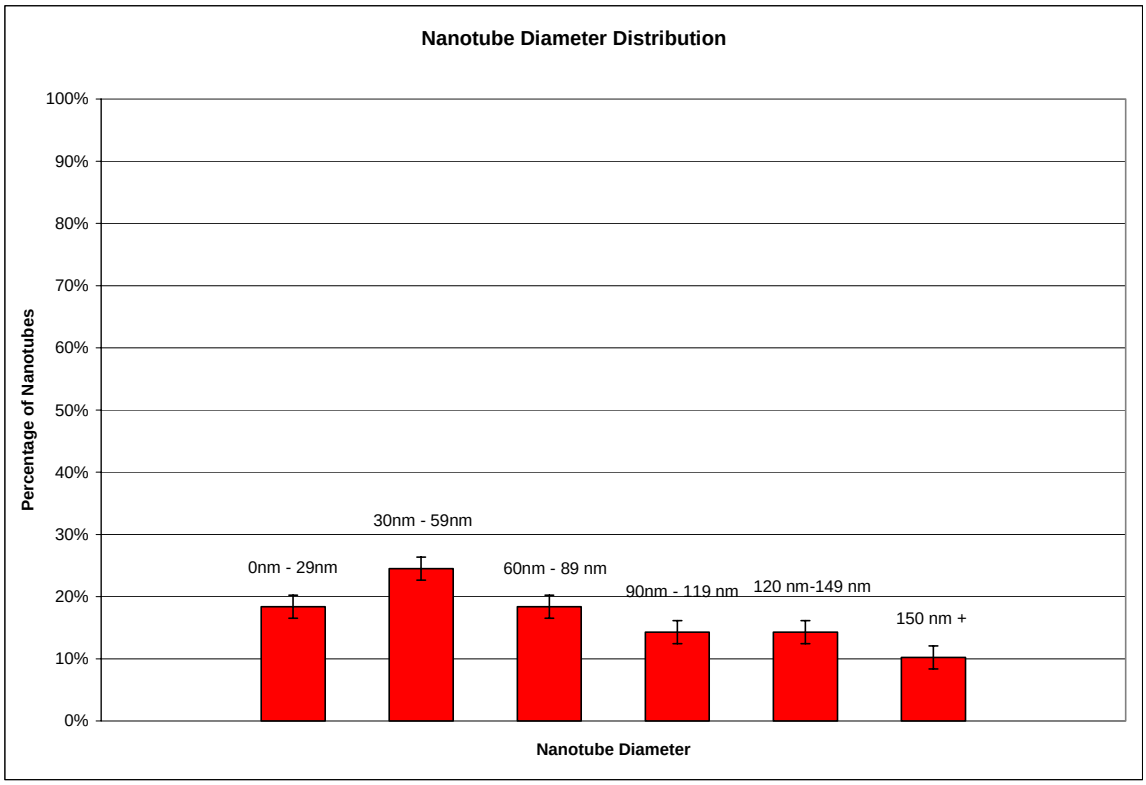

Figure 53: Distribution of Nanotube Diameter for HYCNT Three Minute Soak Recipe on Iron Catalyst

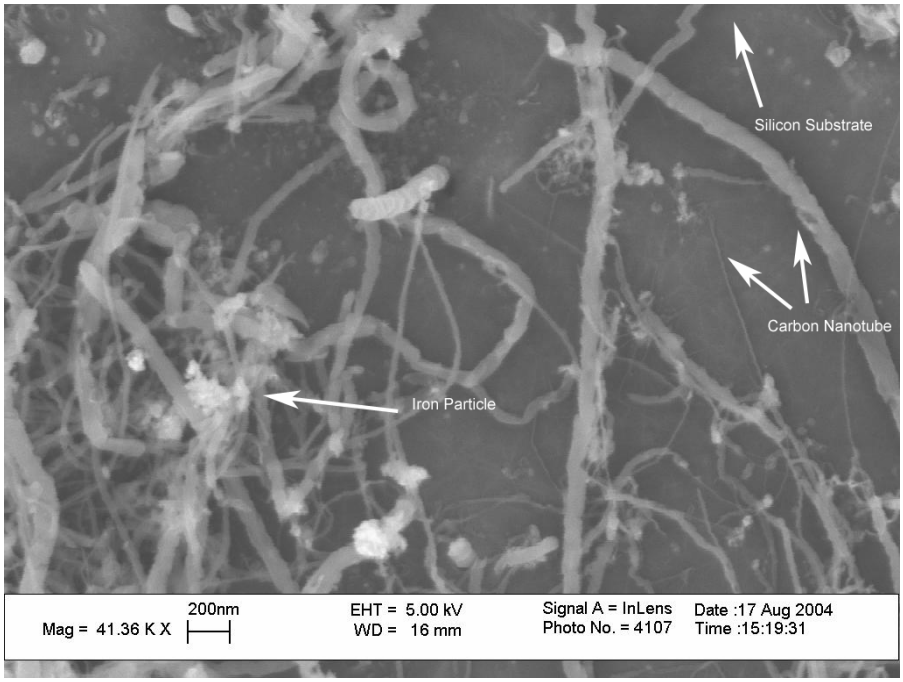

Figure 54: SEM Micrograph of CNTs Grown with HYCNT Three Minute Soak Recipe on Iron Catalyst

4.3.2 HYCNT, Six Minute Soak Time

This recipe results in an extremely wide distribution of tube diameters, with diameters ranging from 24 nm to 182 nm. Tubes are estimated to have lengths exceeding 8 μm.

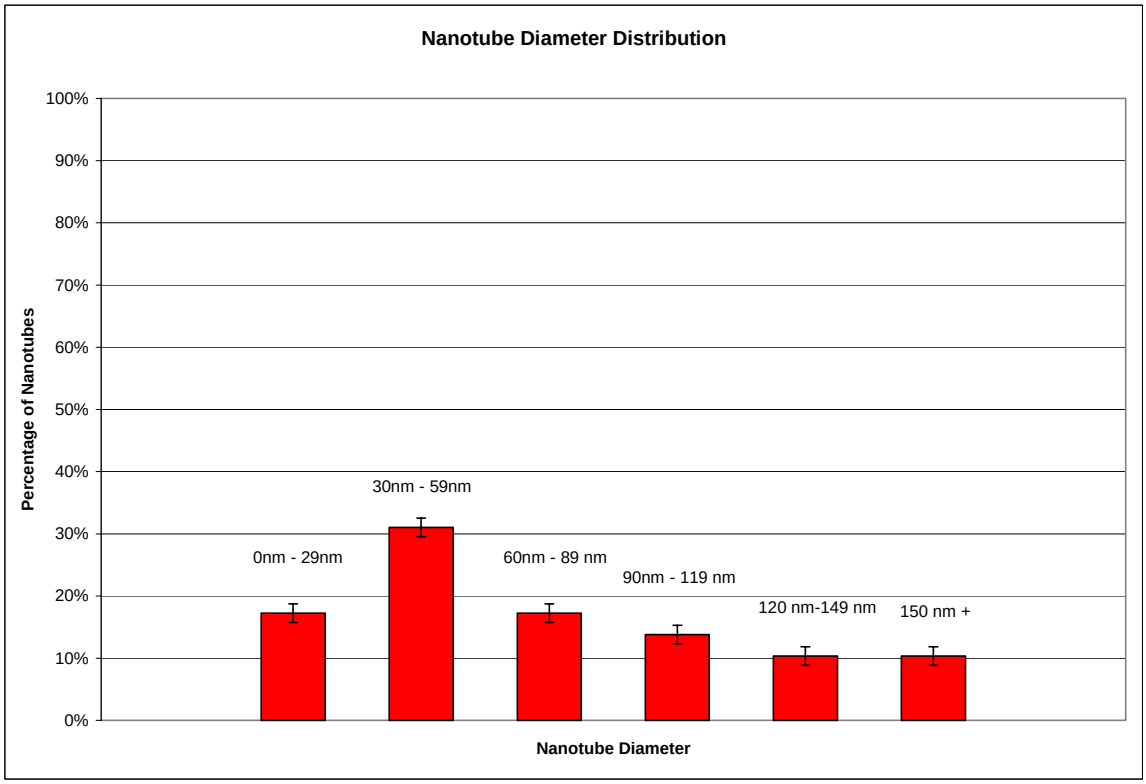

Figure 55: Distribution of Nanotube Diameter for HYCNT Six Minute Soak Recipe on Iron Catalyst

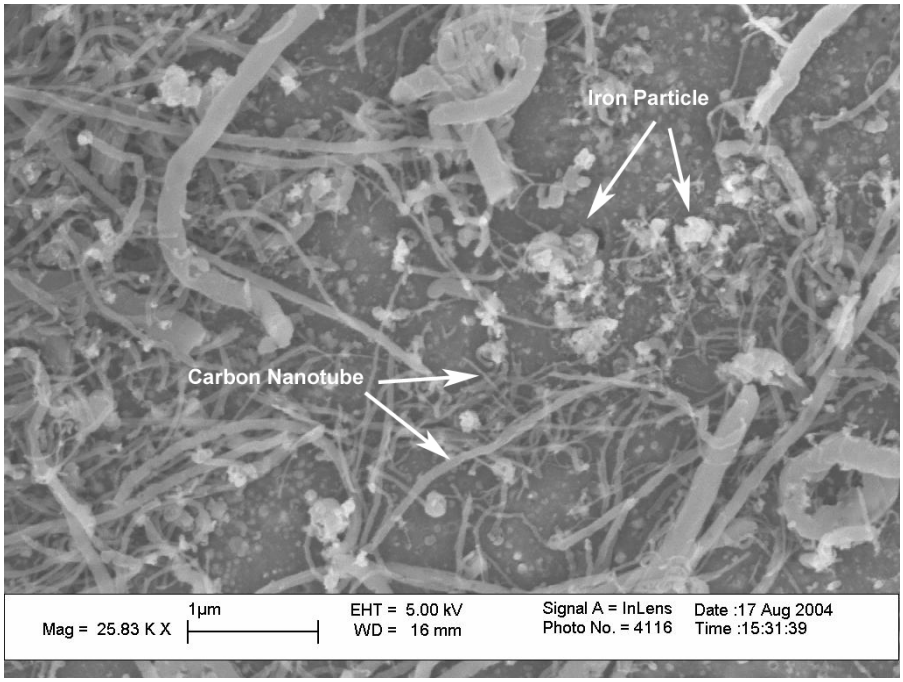

Figure 56: SEM Micrograph of CNTs Grown with HYCNT Six Minute Soak Recipe on Iron Catalyst

4.3.3 HYCNT, Nine Minute Soak Time

This recipe results in an extremely wide distribution of tube diameters, with diameters ranging from 24 nm to 212 nm. The largest observed tube length was approximately 9 µm.

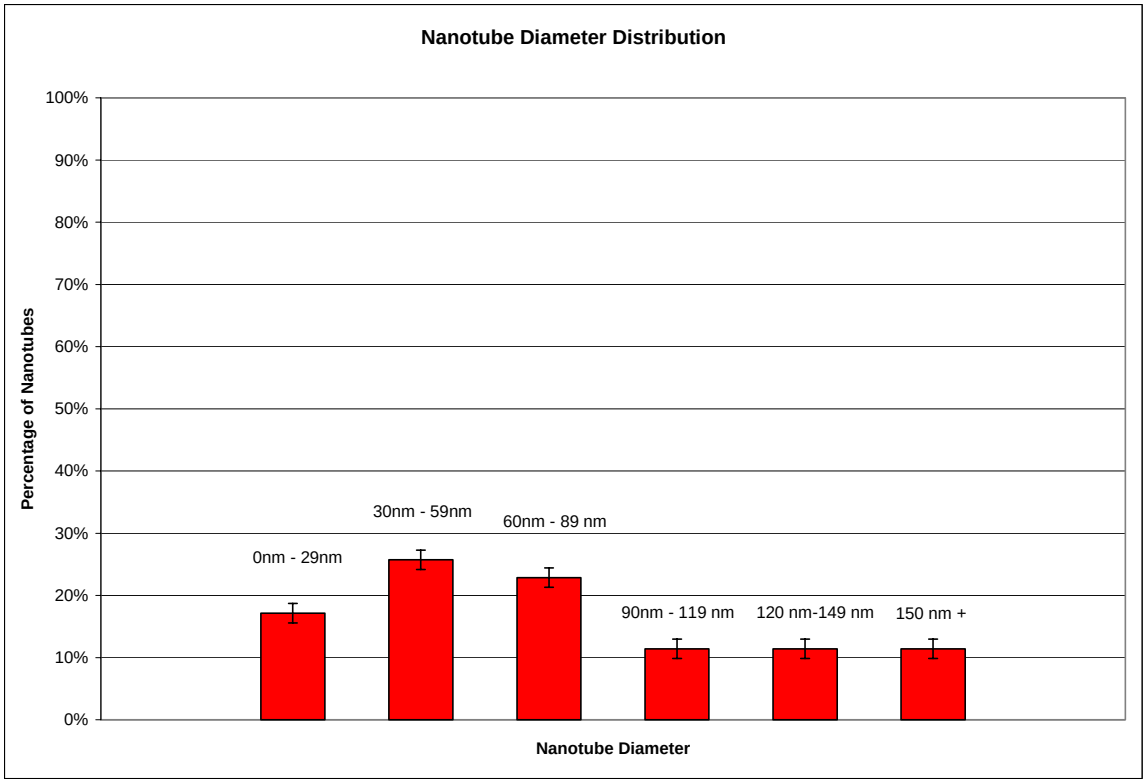

Figure 57: Distribution of Nanotube Diameter for HYCNT Nine Minute Soak Recipe on Iron Catalyst

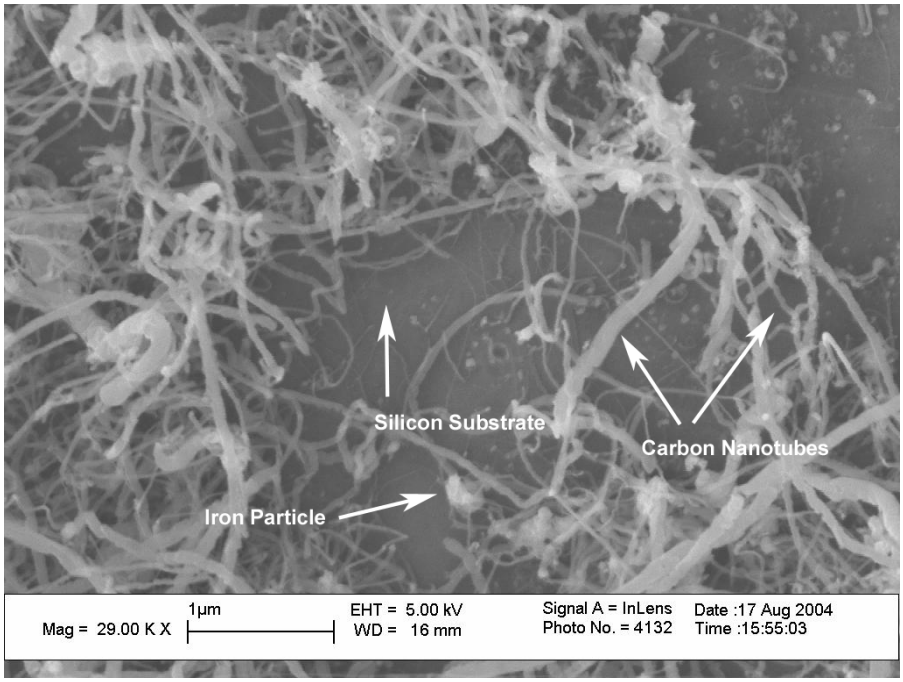

Figure 58: SEM Micrograph of CNTs Grown with HYCNT Nine Minute Soak Recipe on Iron Catalyst

4.3.4 HYCNT, Twelve Minute Soak Time

This recipe results in an extremely wide distribution of tube diameters, with diameters ranging from 2 nm to 177 nm. Tube length ranges from approximately 500 nm to 8 μm.

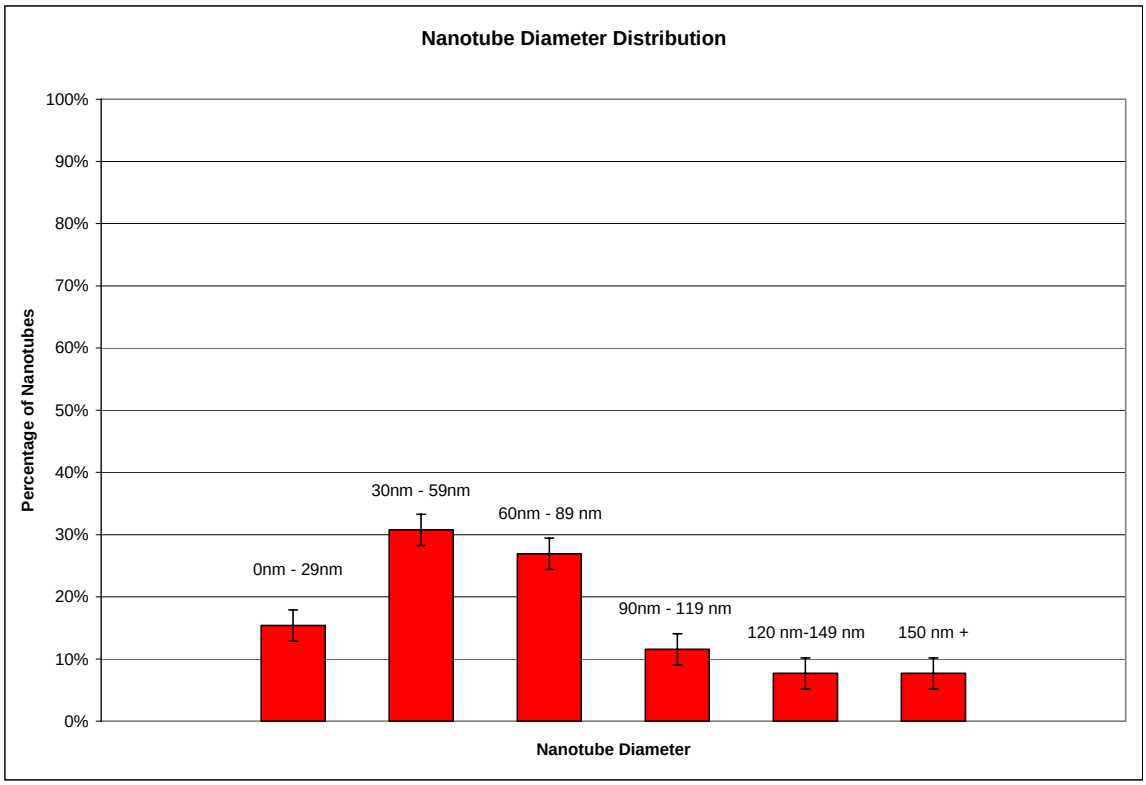

Figure 59: Distribution of Nanotube Diameter for HYCNT Twelve Minute Soak Recipe on Iron Catalyst

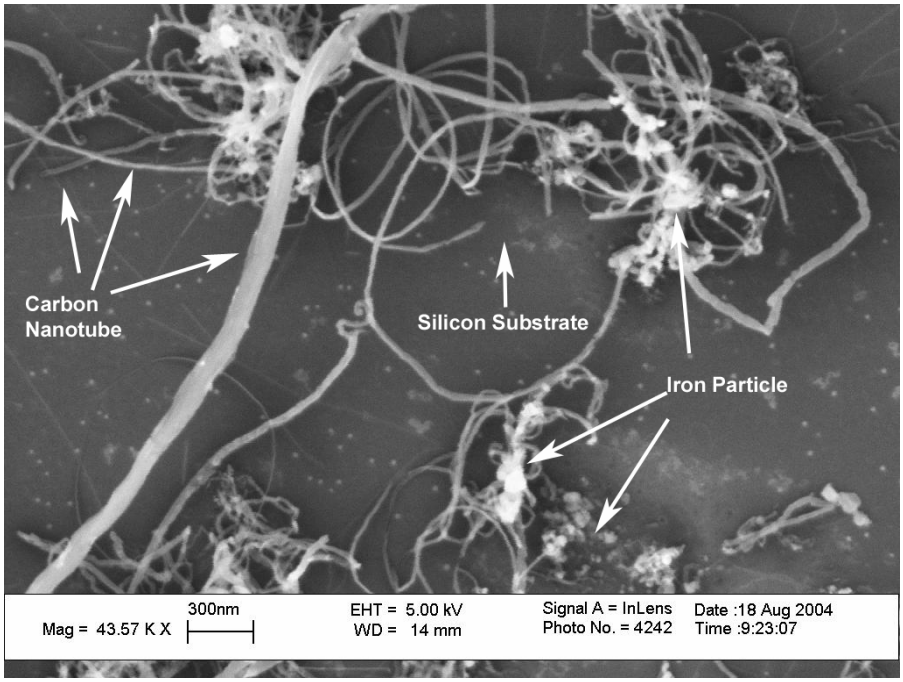

Figure 60: SEM Micrograph of CNTs Grown with HYCNT Twelve Minute Soak Recipe on Iron Catalyst

4.3.5 HYCNT, Fifteen Minute Soak Time

This recipe results in an extremely wide distribution of tube diameters, with diameters ranging from 22 nm to 155 nm. Tube lengths range between 300 nm and 10 μm.

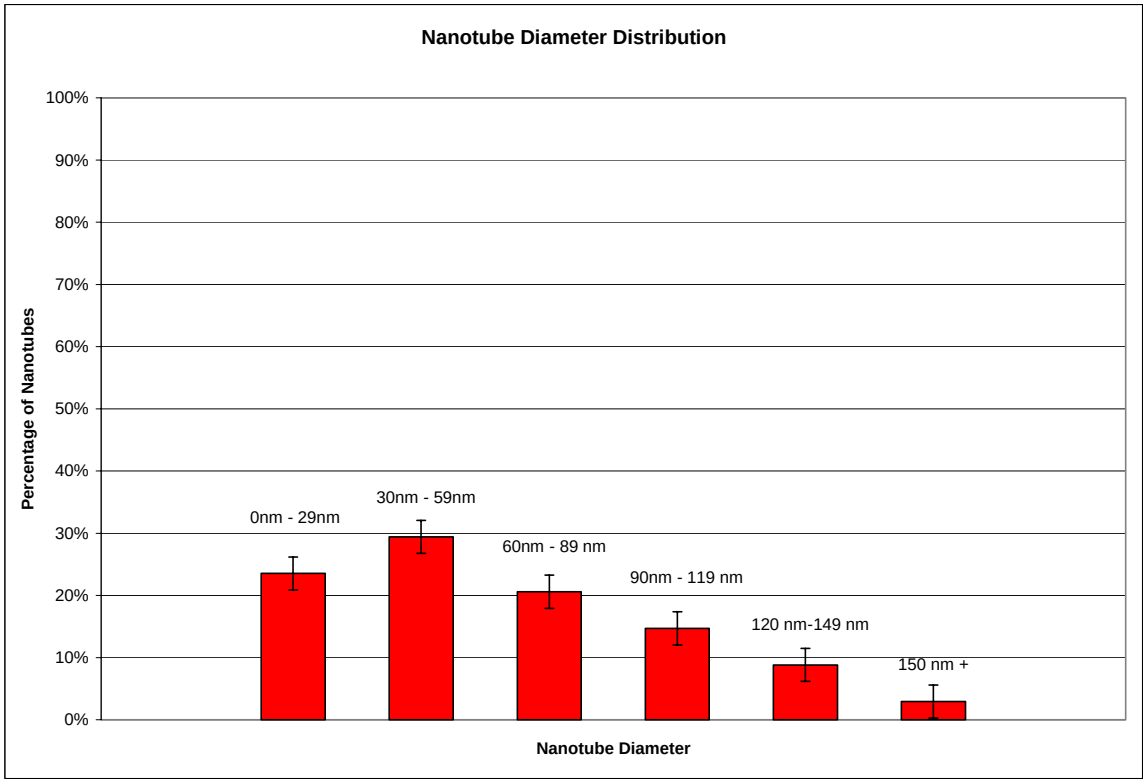

Figure 61: Distribution of Nanotube Diameter for HYCNT Fifteen Minute Soak Recipe on Iron Catalyst

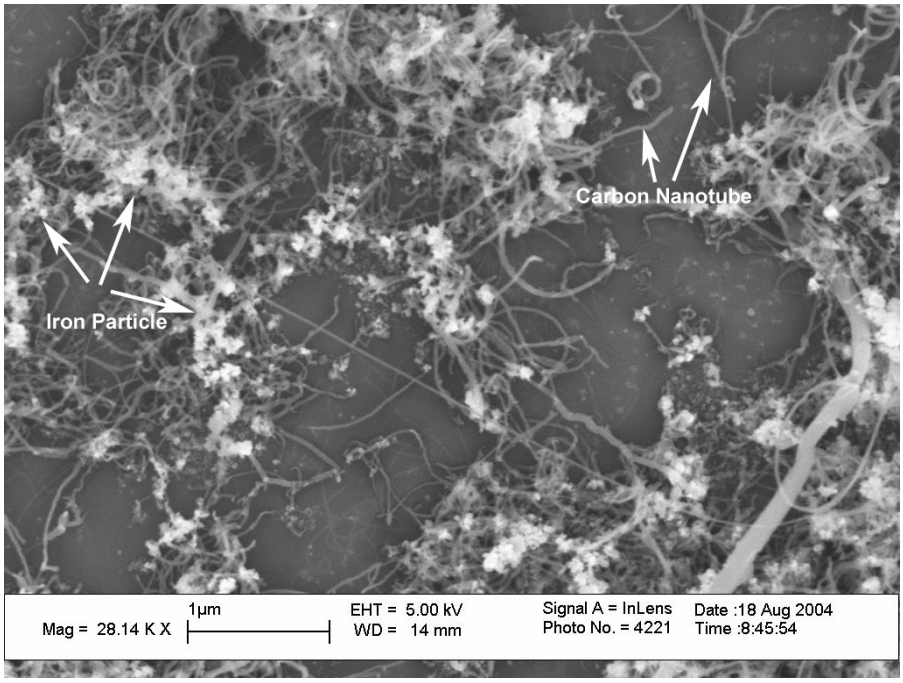

Figure 62: SEM Micrograph of CNTs Grown with HYCNT Fifteen Minute Soak Recipe on Iron Catalyst

4.3.6 HYCNT Summary

Figure 63 shows the relationship between the soak time and the resultant average diameter of CNTs synthesized on iron catalyst using the Bulk CNT recipe. The error bars in the figure represent one standard deviation from the calculated average CNT diameters.

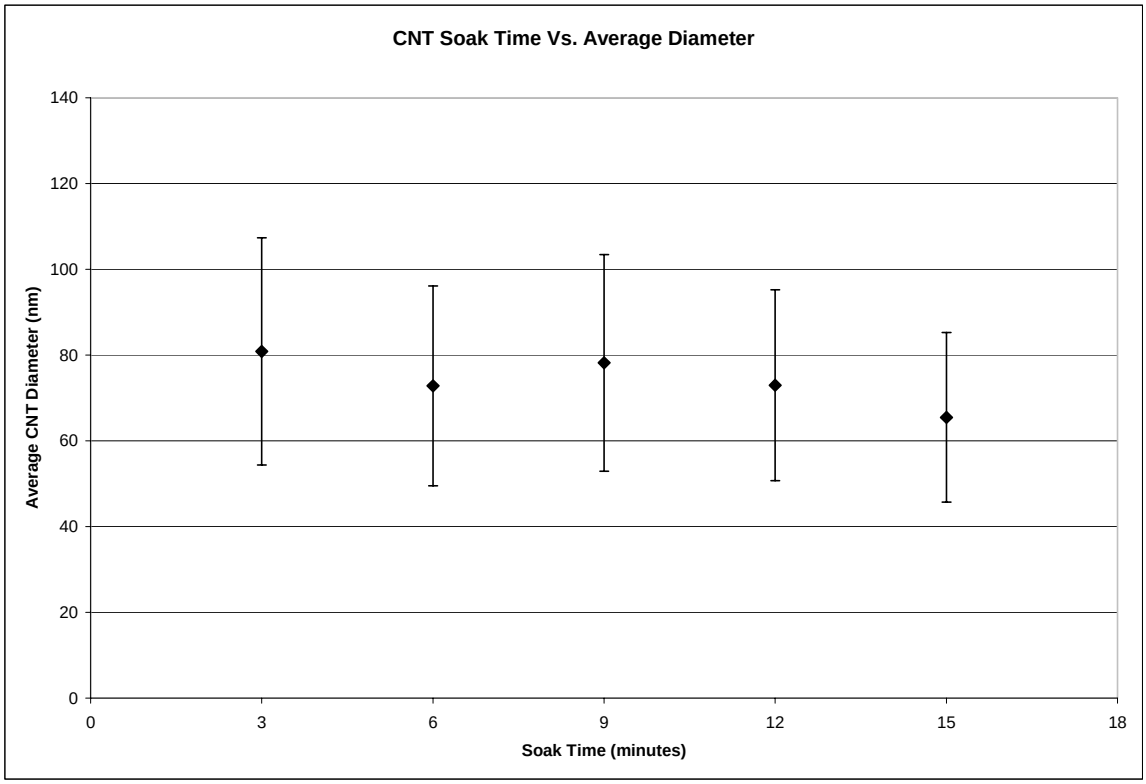

Figure 63: CNT Soak Time vs. Average CNT Diameter. Error Bars Represent One Standard Deviation

4.4. Effect of Applied Voltage During CNT Synthesis

An electric field was applied to the CVD furnace chamber as described in the procedure section. The voltage was increased in increments of 10V from a minimum of 10V to a maximum value of 50V. The negatively charged wire was below the substrate and the positively charged wire was above the substrate for each sample. The synthesis recipe used was the UHYCNT recipe and Alumina supported Iron catalyst on silicon substrates was used as catalyst. There was virtually no alignment observed for any of the samples. Some samples exhibited slight alignment in small, localized regions. Table 9 below lists references to SEM micrographs of each sample. An unexpected result was an increased rate of appearance of coiled nanotubes.

Table 9: Alignment Data for CNTs Grown with UHYCNT Recipe

Applied Voltage	10 V	20 V	30 V	40 V	50 V
SEM micrograph(s)	Figure 64	Figure 65	Figure 66	Figure 67	Figure 68

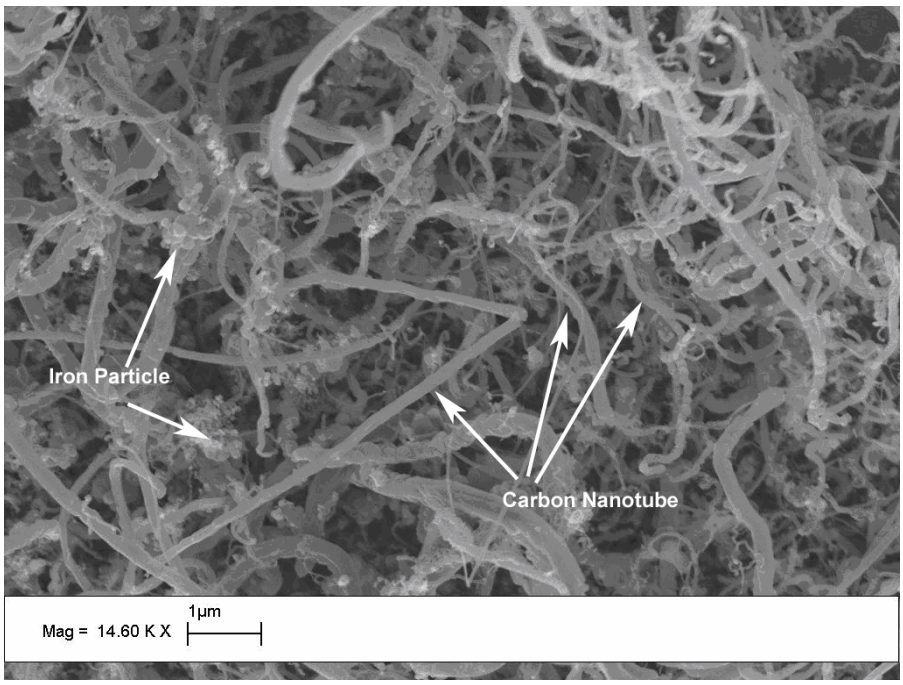

Figure 64: SEM Micrograph Showing CNTs Grown with UHYCNT Recipe and 10 Volt Field

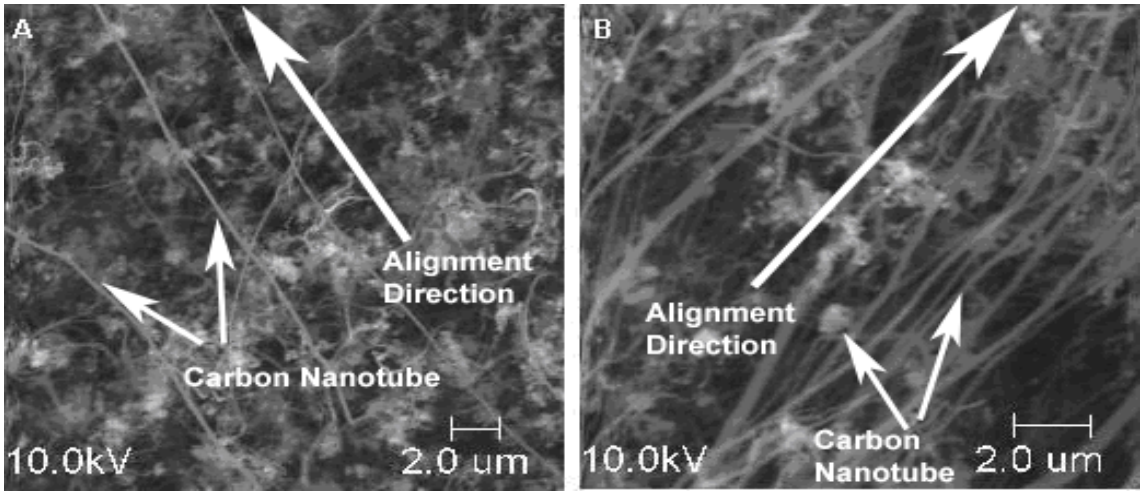

Figure 65: (A), (B) SEM Micrograph Showing Slight CNT Alignment Grown with UHYCNT Recipe and 20 Volt Field

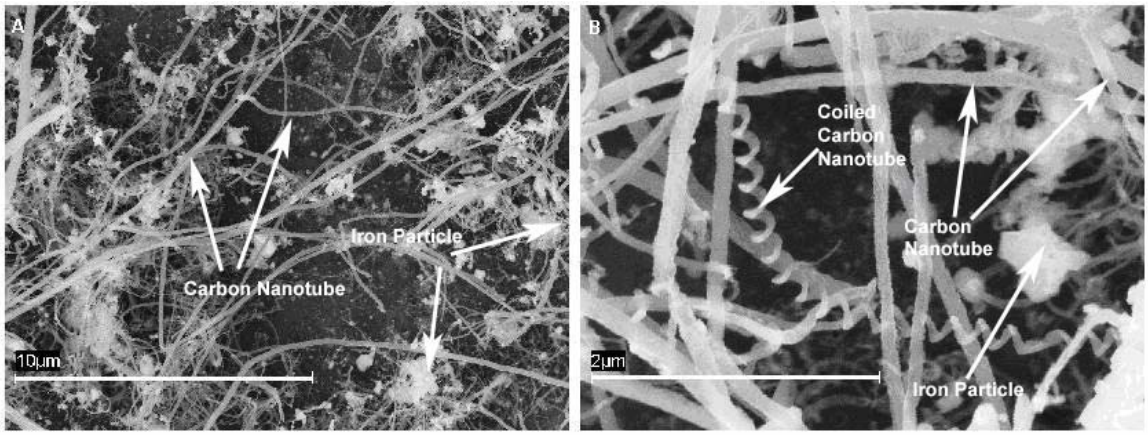

Figure 66: (A) SEM Micrograph Showing CNTs (B) SEM Micrograph Showing CNT Coiling Grown with UHYCNT Recipe and 30 Volt Field

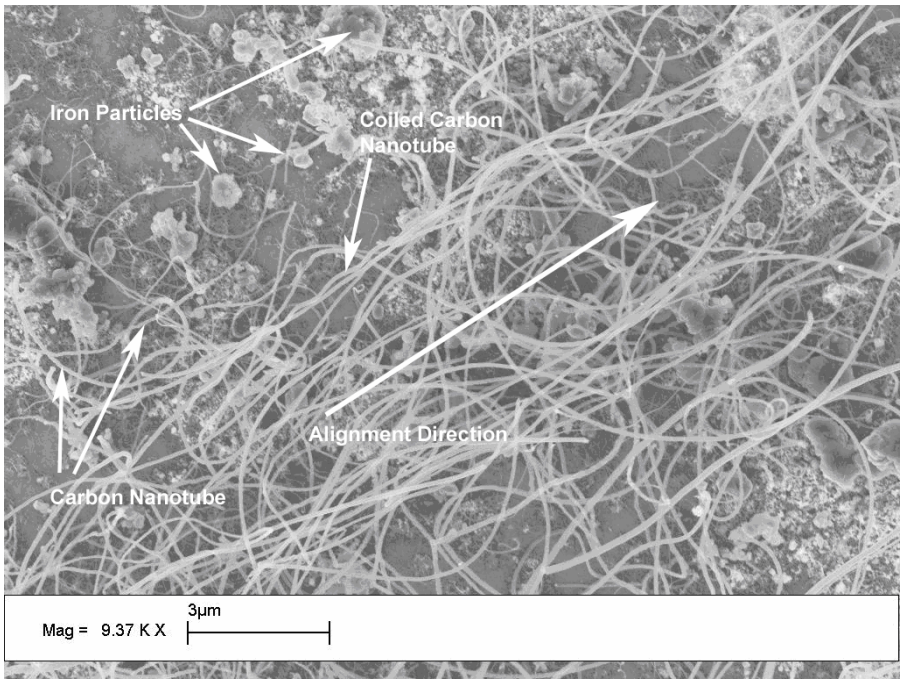

Figure 67: SEM Micrograph Showing Slight CNT Alignment and Slight Coiling Grown with UHYCNT Recipe and 40 Volt Field

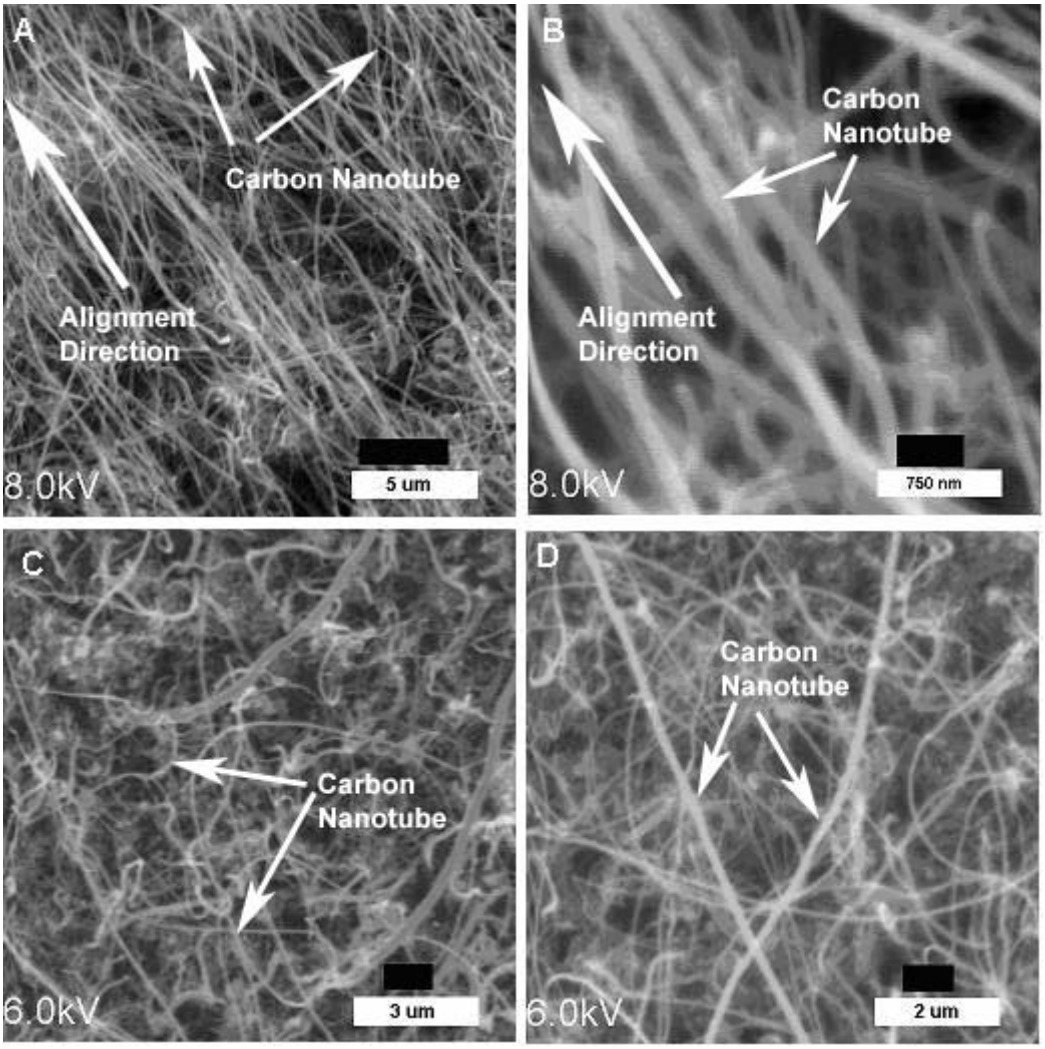

Figure 68: (A) SEM Micrograph of Highly Aligned CNTs; (B) Close Up View of (A); (C), (D) SEM Micrograph of Randomly Aligned Regions of Sample Grown with UHYCNT Recipe and 50 Volt Field

4.4.1 Effect of Polarity of Applied Voltage

CNTs were synthesized under the same conditions as those in Section 4.4, however, the polarity of the electric leads were switched to determine if alignment is affected. The applied voltage for each sample was 50V. SEM micrographs of CNTs synthesized with the cathode wire above the sample are shown in Figure 69, while CNTs synthesized with the anode above the sample are shown in Figure 70.

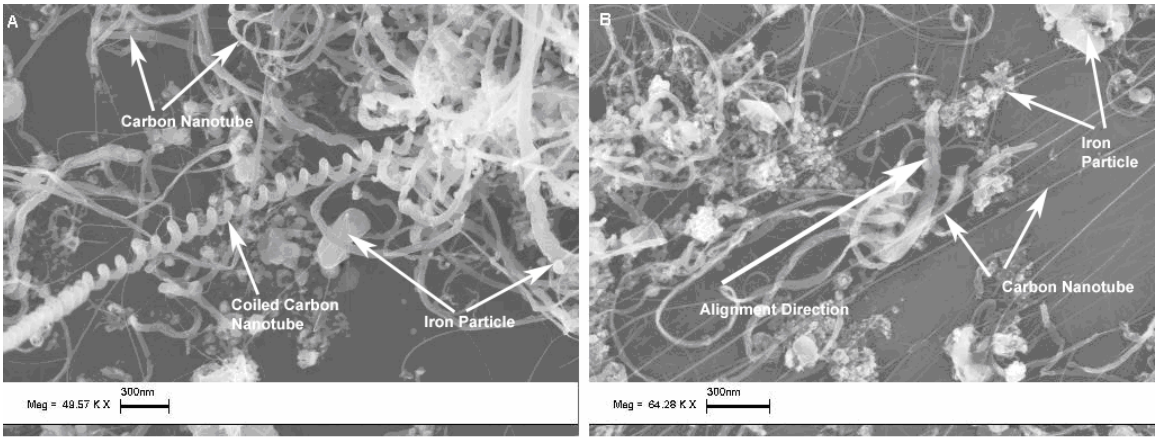

Figure 69: SEM Micrograph of CNTs Synthesized with Cathode Wire Above the Sample

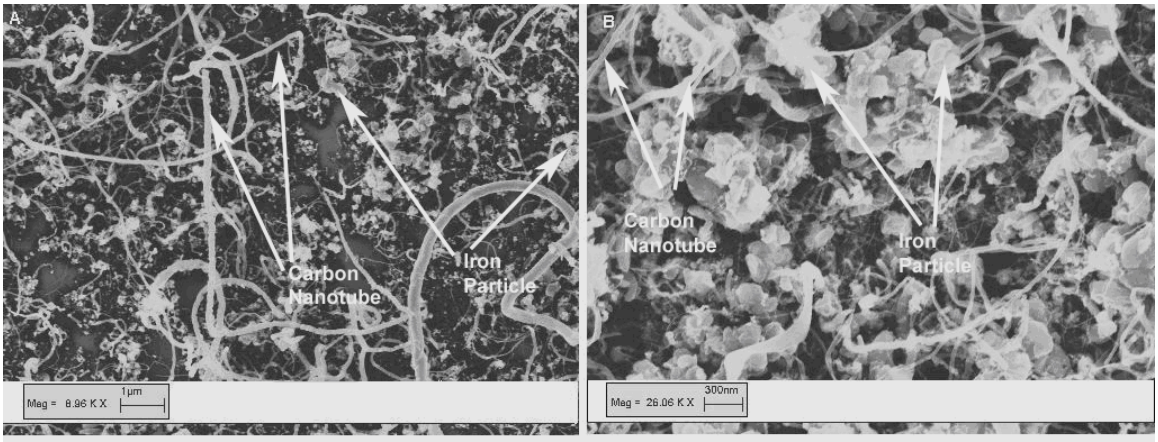

Figure 70: SEM Micrograph of CNTs Synthesized with Cathode Wire Below the Sample

4.4.2 Effect of Applied Voltage on Precursor Gas

CNTs were synthesized on Alumina supported iron catalyst with an applied voltage under the same conditions as before, however, acetylene gas replaced ethylene gas during the synthesis process (AcUHYCNT recipe). Several combinations of voltage and soak temperatures were attempted. There was no evidence of alignment occurring

during synthesis. However, coiled CNTs occurred with a much higher frequency. Approximately 10% to 20% of the CNTs produced show regular coil morphology. Evidence is presented in Figure 71 and Figure 72.

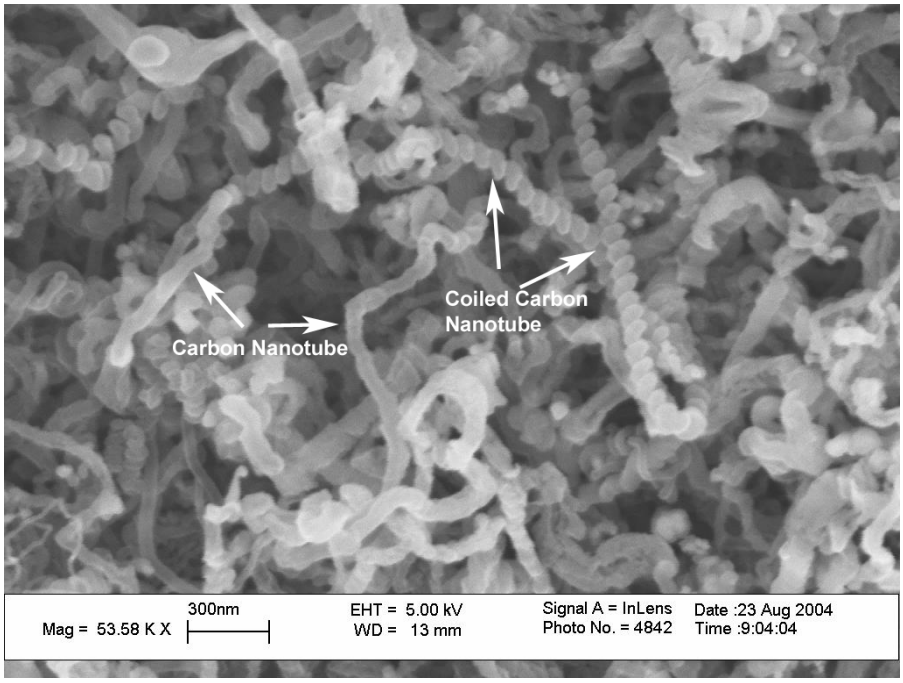

Figure 71: Coiled CNTs Grown on Iron Catalyst System with AcUHYCNT Recipe with 50V Applied During Synthesis

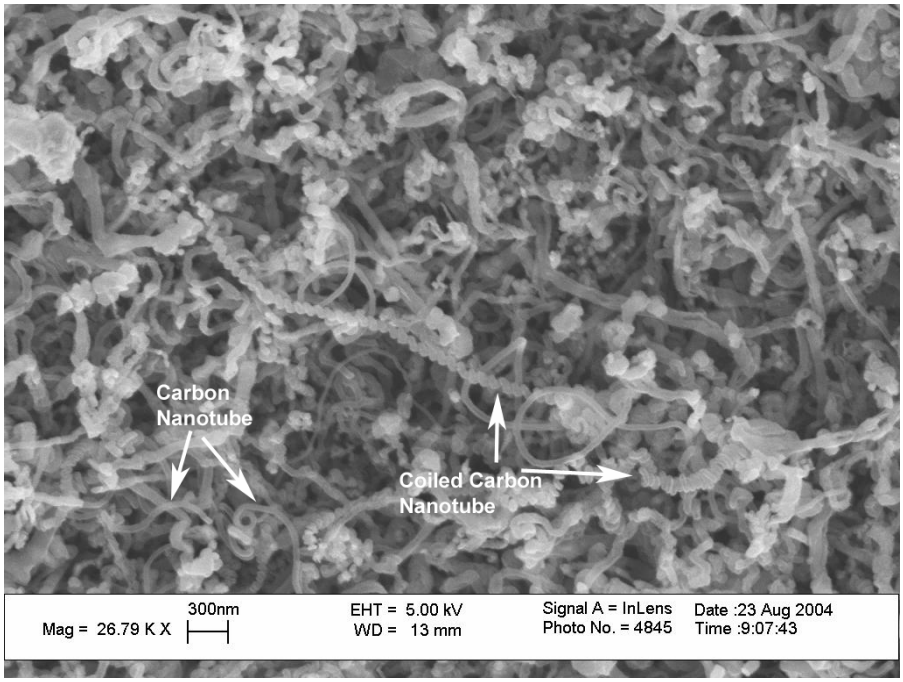

Figure 72: Coiled CNTs Grown on Iron Catalyst System with AcUHYCNT Recipe with 50V Applied During Synthesis

4.4.3 Effect of Applied Voltage During Synthesis on Nickel Catalyst System

CNTs were synthesized on nickel catalysts layers under the influence of a voltage field as described above. CNTs were grown on several samples, varying both the applied voltage as well as catalyst thickness layer. No evidence of alignment was observed for the nickel catalyst synthesis under the influence of applied voltage.

However, coiled CNTs were produced on the nickel catalyst, an effect which was also observed for the iron catalyst. The coiled CNTs produced on the nickel catalyst appeared less frequently than on the iron catalyst. Additionally, the coil pitch and morphology of coiled CNTs on nickel was irregular compared to those synthesized on iron catalyst. SEM micrographs of CNTs grown on nickel catalyst are shown in Figure 73 and Figure 74.

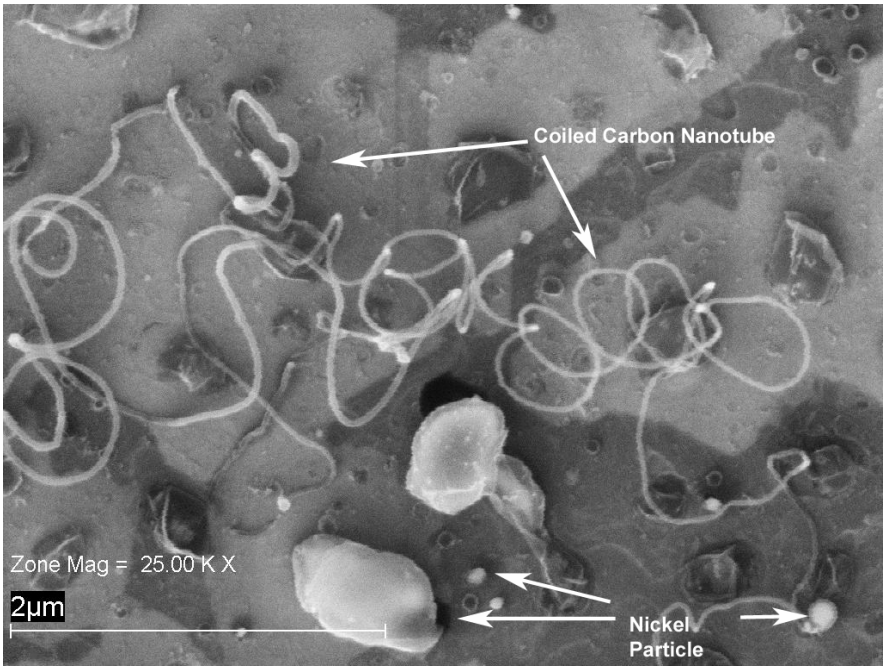

Figure 73: Carbon Nanotubes Produced on 40 nm Nickel Catalyst Layer with 50V Electric Field Applied During Synthesis

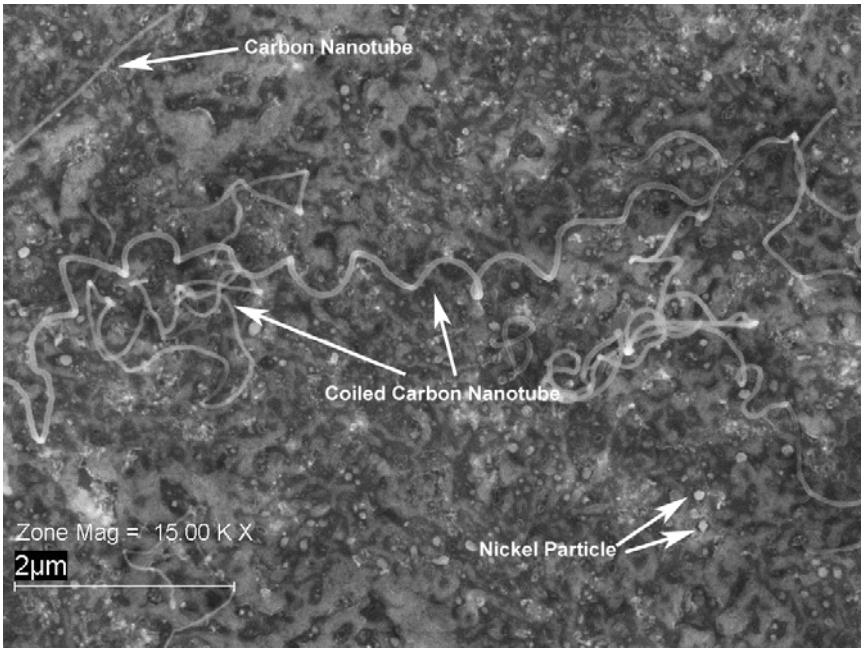

Figure 74: Carbon Nanotubes Produced on 80 nm Nickel Catalyst Layer with 50V Electric Field Applied During Synthesis

4.5 Self Aligned Carbon Nanotubes

CNTs were synthesized using Alumina supported Iron catalyst on SiO_2 wafers. The catalyst was applied as described on page 40. Additionally, the iron catalyst was patterned onto the SiO_2 wafers using photolithography techniques described on page 40. The pattern used was different than the pattern used for the bulk nickel films. In this case, the pattern consisted of 40 μm by 40 μm squares spaced 10 μm apart in each direction. Synthesis variables such as temperature, deposition gas type, and applied voltage were altered in order to produce CNTs aligned perpendicular to the SiO_2 substrate.

It was found that using acetylene gas at flow rates between 20 and 100 sccm and temperatures between 700°C and 780°C produced nanotubes aligned perpendicular to the substrate. Figure 75 shows a film of CNTs which are aligned perpendicular to the substrate. The film resembles a dense field of grass. Inspection of the film showed that CNT morphology is random and "spaghetti-like" (Figure 76). The diameters of self aligned CNTs are all between 3 and 10nm. Applying the iron catalyst to a patterned substrate resulted in controlled growth regions of aligned CNT films (Figure 77).

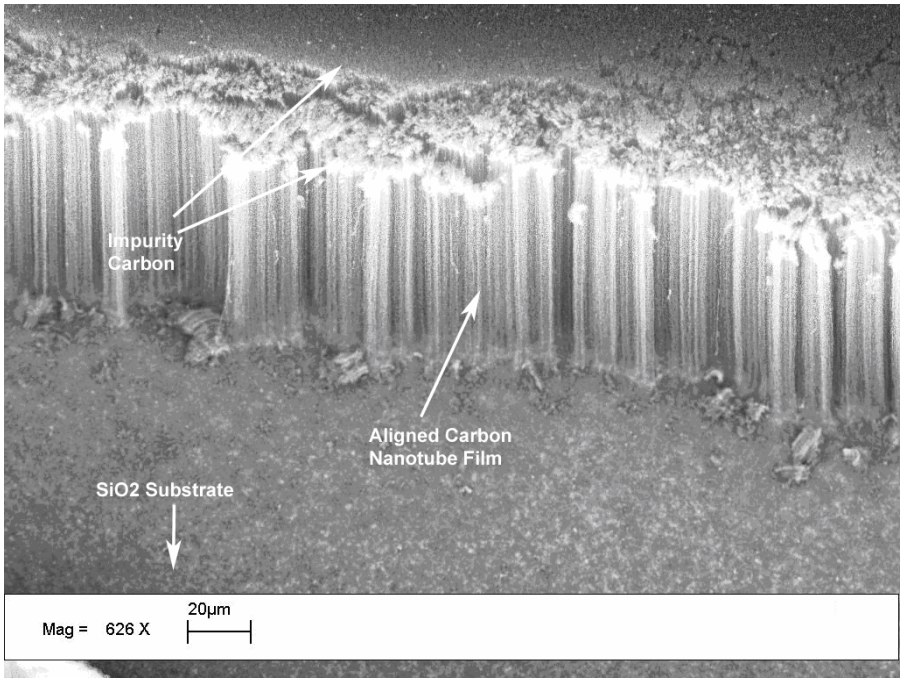

Figure 75: SEM Micrograph of Aligned CNT Film Grown with AcUHYCNT Recipe on Iron Catalyst at 740°C

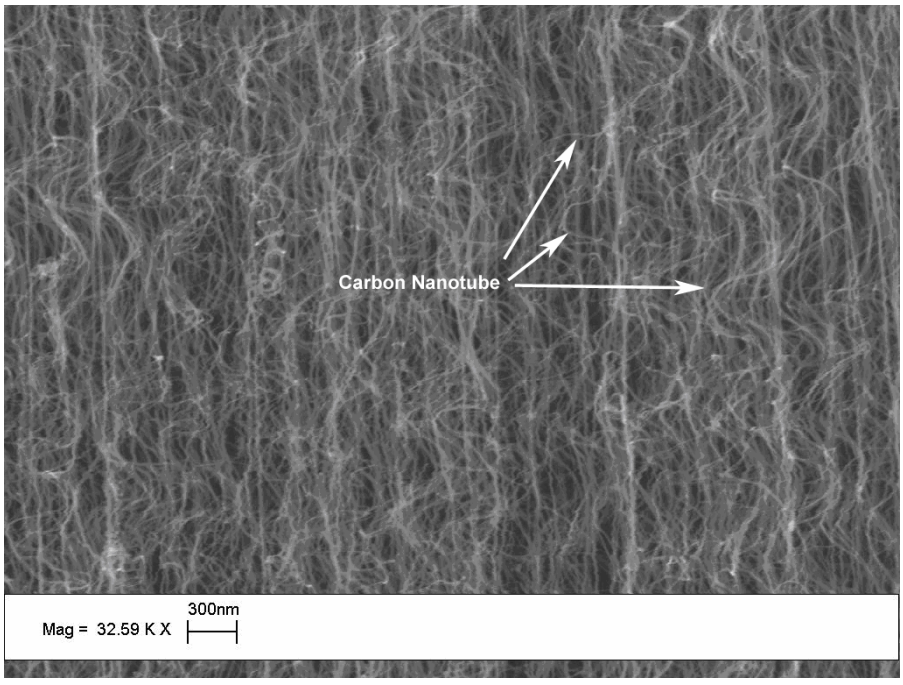

Figure 76: High Magnification SEM Micrograph of Aligned CNTs Shown in Figure 75

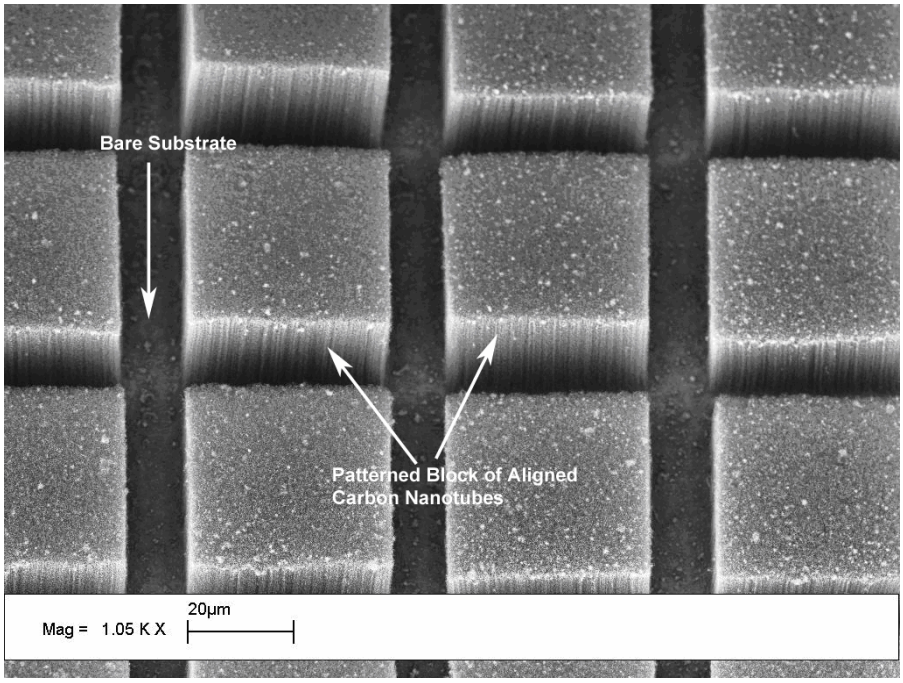

Figure 77: SEM Micrograph of Patterned Blocks of Aligned CNTs grown with AcUHYCNT Recipe

Due the nature of drying the liquid catalyst on the un-patterned substrate oddly shape catalyst regions were observed. CNTs aligned nearly perpendicular to the substrate while maintaining the odd shape of the catalyst region. The aligned CNTs formed bundled structures, some of which resemble sea sponges (Figure 78). Again, individual CNTs do not conform to a straight morphology. However, within each structure bundle, the aligned CNTs exhibit wave like behavior. Figure 79 is a close-up SEM micrograph of the CNT structure from Figure 78.

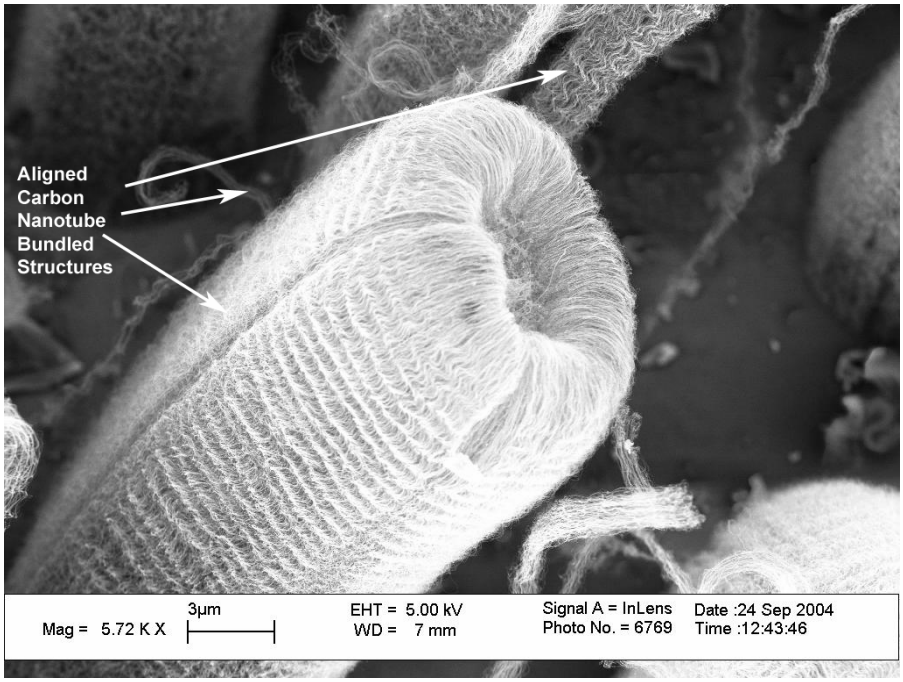

Figure 78: SEM Micrograph of Bundled, Aligned CNT Structure

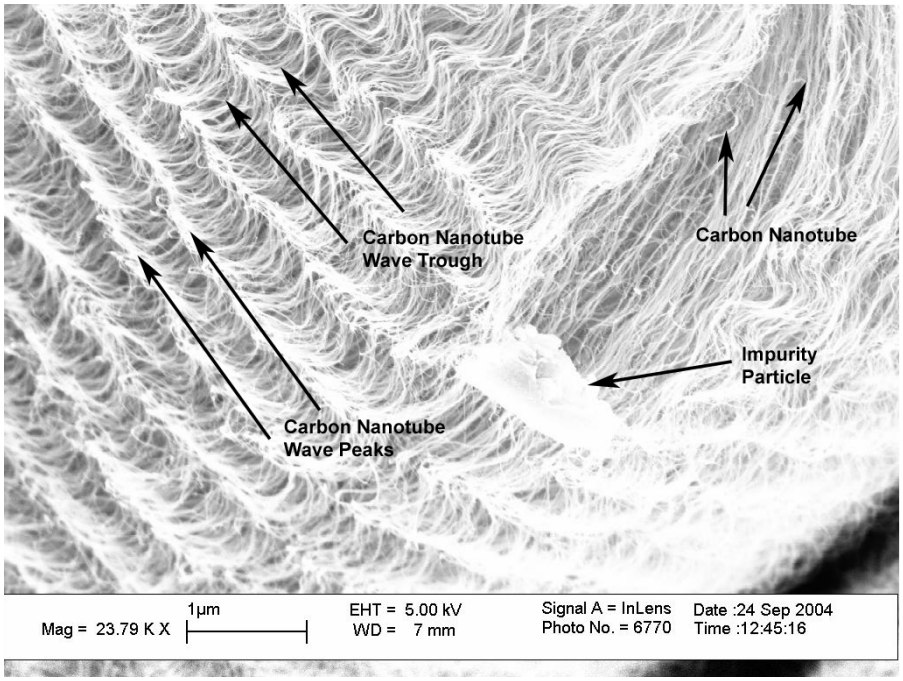

Figure 79: High Magnification of Bundled, Aligned CNT Structure in Figure 78

The wave like morphology of CNTs in the odd shaped structures existed without the influence of an applied voltage. A voltage was applied to the CVD furnace during

CNT synthesis to examine the effect of the wave like morphology. Table 10 lists the average distance between wave peaks in the CNT structures for various applied voltages. All CNTs were grown at 740°C using the AcUHYCNT recipe.

Table 10: Average CNT Wave Peak to Peak Distance for Applied Voltage at 740°C

Applied Voltage (V)	Average Peak to Peak Distance (nm)
0	810 +/- 20
10	674 +/- 20
50	679 +/- 20
100	647 +/- 20
150	664 +/- 20
200	618 +/- 20

Raising the synthesis temperature to 800°C while still using the AcUHYCNT recipe resulted in CNTs which are not aligned (Figure 80). Furthermore, the distribution of diameters of the CNTs which do not self aligned varies widely. CNT synthesis was performed with temperatures of 850°C and 900°C and did not yield self aligned CNTs.

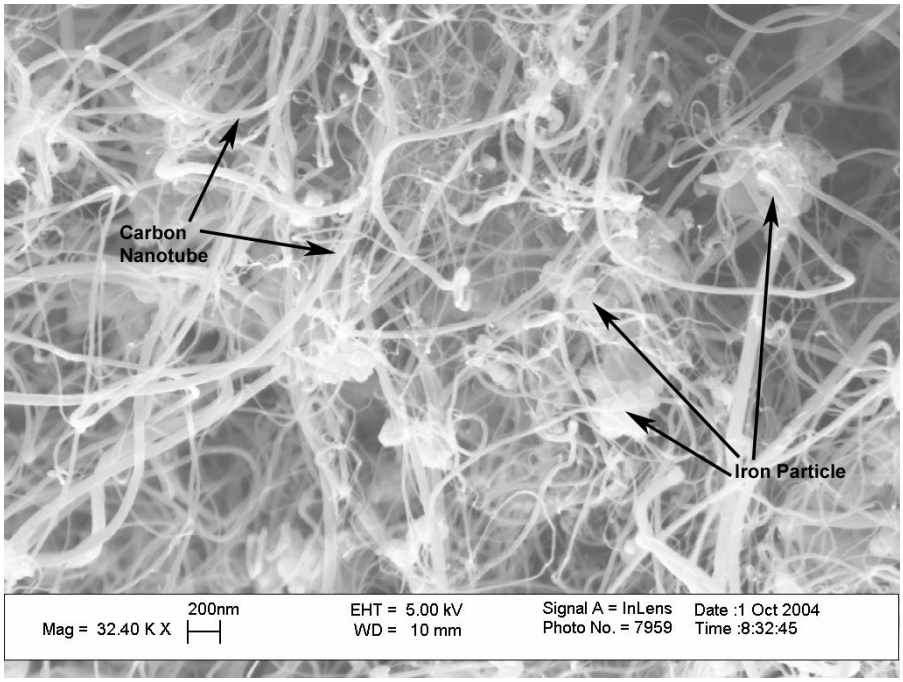

Figure 80: SEM Micrograph of CNTs Grown with AcUHYCNT Recipe on Iron Catalyst at 800°C

4.6 Effect of Precursor Gasses and Flow Rates

CNT diameter was analyzed as a function of synthesis precursor gas as well as gas flow rate, while holding all other synthesis variables constant. The synthesis recipes used for growth were HPCNT, BULK CNT, UHYCNT, AcUHYCNT. The HYCNT recipe was not used since the precursor gasses and gas flow rate are the same and only the soak time differs. All samples were grown on a 60 nm Ni catalyst layer which was patterned on silicon substrates as described in the previous chapter. Plotting the percent of tubes that fall into a specific range results in nanotube diameter distribution plots. For each catalyst film thickness, the following ranges were used: (0-9 nm), (10-19 nm), (20-29 nm), (30-39 nm), (40-49 nm), (50-59 nm), (60-69 nm), (70-79 nm) and (80 nm +).

Table 11 summarizes the average diameter of CNTs produced with each recipe. In addition, Table 11 references Diameter Distribution Plots for each of the synthesis recipes and sample SEM Micrographs of CNTs produced with each recipe.

Table 11: Nanotube Diameter Data For Various Synthesis Recipe for CNTs Grown on 60 nm Nickel Catalyst Layer

Synthesis Recipe	Average Diameter	Standard Deviation	Diameter Distribution Plot	SEM Micrograph
HPCNT	51.0	7.9	Figure 81	Figure 82
BULK CNT	41.5	7.9	Figure 35	Figure 36
UHYCNT	53.6	22.4	Figure 83	Figure 84
AcUHYCNT	80.2	24.8	Figure 85	Figure 86

4.6.1 HPCNT

This recipe uses only methane as a precursor gas and has a short 10 minute soak period. Nanotubes were only observed at the edges of the nickel catalyst pattern. The tubes exhibit tip growth, and show a somewhat narrow distribution of tube diameters. All tubes were observed as having a length of less than 1.5 μm.

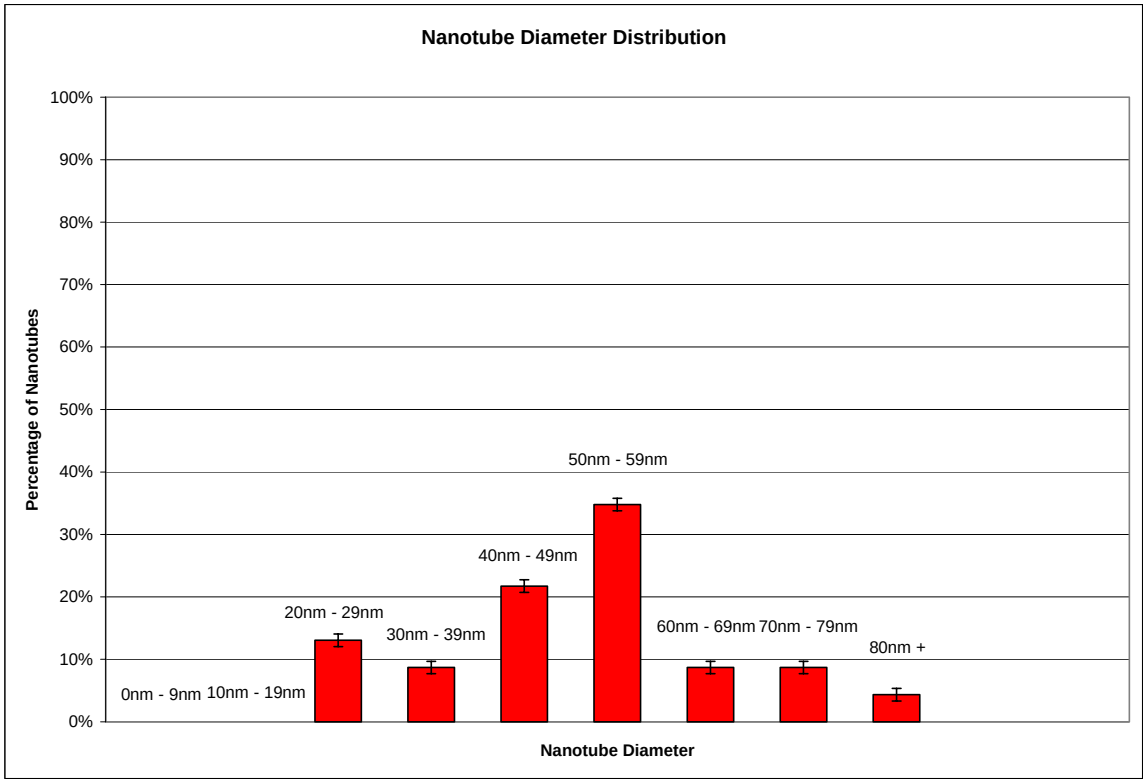

Figure 81: Distribution of Nanotube Diameter for HPCNT Recipe Grown on 60 nm Nickel Catalyst Layer

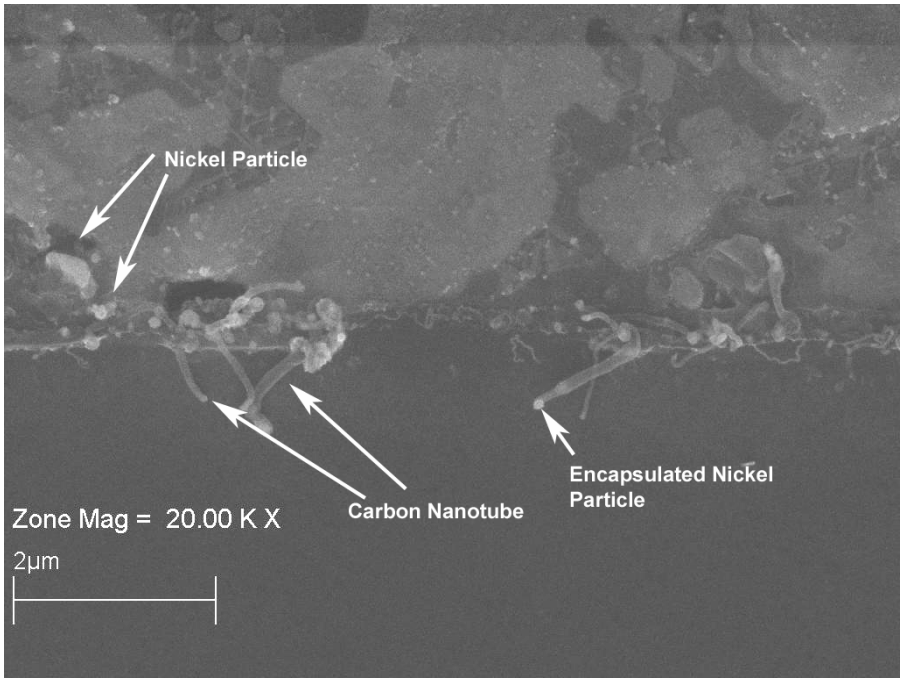

Figure 82: SEM Micrograph of CNTs Grown with HPCNT Recipe on 60 nm Nickel Catalyst Layer

4.6.2 BULK CNT

This recipe results in a somewhat Gaussian distribution of tube diameters, with approximately 97% of tubes having an outer diameter less than 80 nm. The largest tube from the sampled region had a diameter of approximately 84 nm, while the smallest tube in the same sample region had a diameter of approximately 14 nm. The lengths of the tube vary widely, with tube lengths exceeding 5 μm and approaching 10 μm.

4.6.3 UHYCNT

The diameter distribution for the recipe is extremely wide, and shows little preference for any diameter ranges (Figure 83). This program produces a significantly higher volume of CNTs than the BULK CNT or HYCNT (Figure 84). Tubes were observed to have lengths approaching 10 μm. Some tubes show a bamboo like structure, or a build up of amorphous carbon.

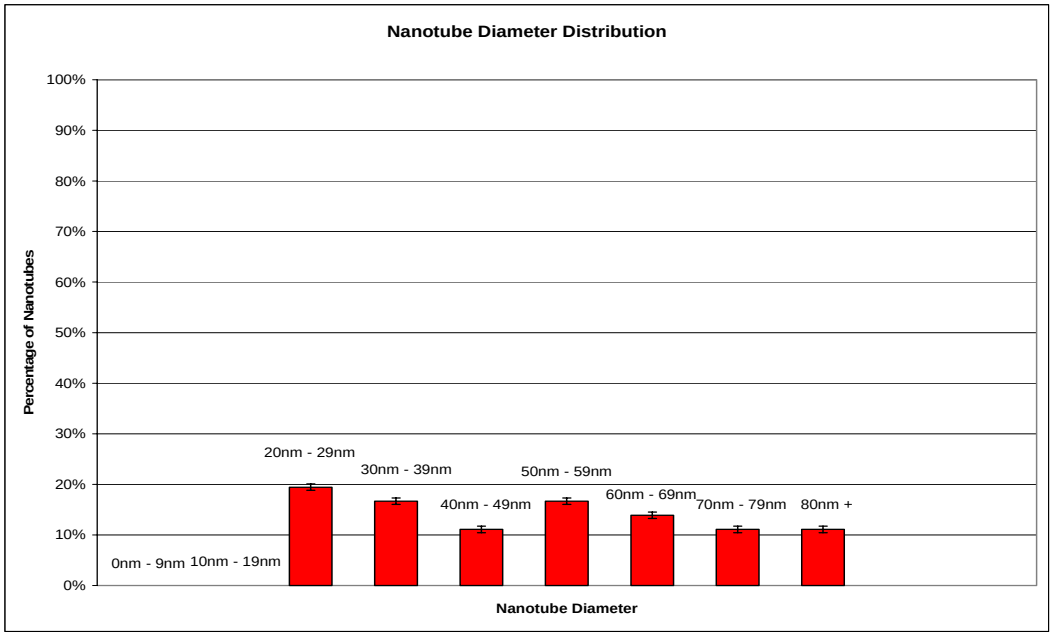

Figure 83: Distribution of Nanotube Diameter for UHYCNT Recipe Grown on 60 nm Nickel Catalyst Layer

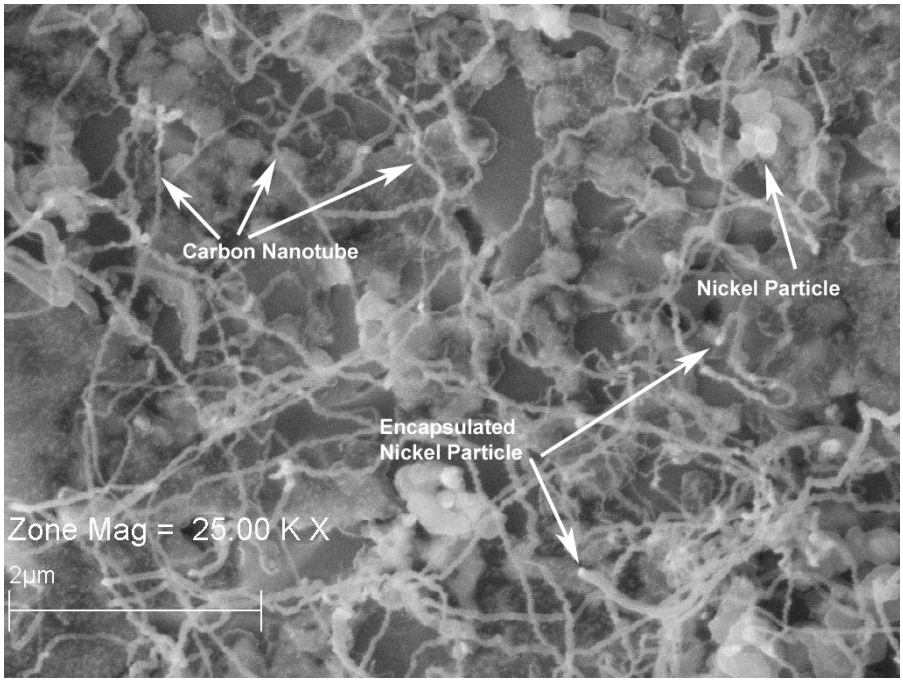

Figure 84: SEM Micrograph of CNTs Grown with UHYCNT Recipe on 60 nm Nickel Catalyst Layer

4.6.4 AcUHYCNT

The use of acetylene gas produced tubes which had a majority of diameters above 70 nm (Figure 85). Once again, the volume of nanotubes produced is significantly higher compared to other recipes (Figure 86). Some impurity carbon is present on the outer tube walls.

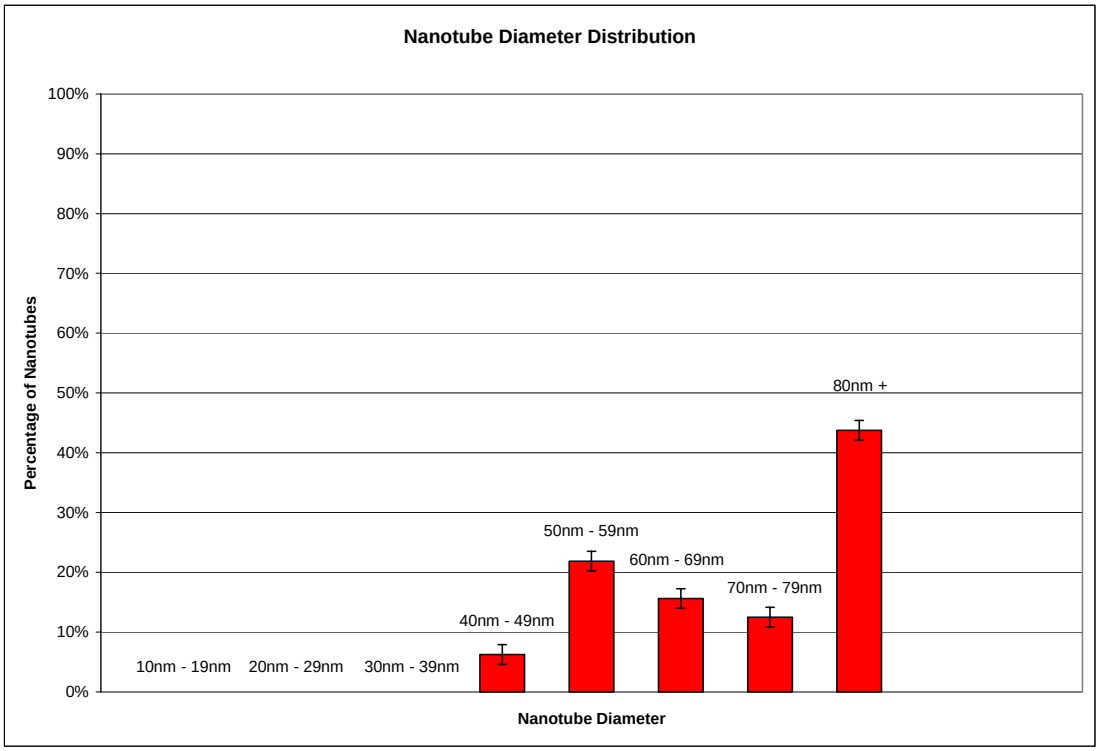

Figure 85: Distribution of Nanotube Diameter for AcUHYCNT Recipe Grown on 60 nm Nickel Catalyst Layer

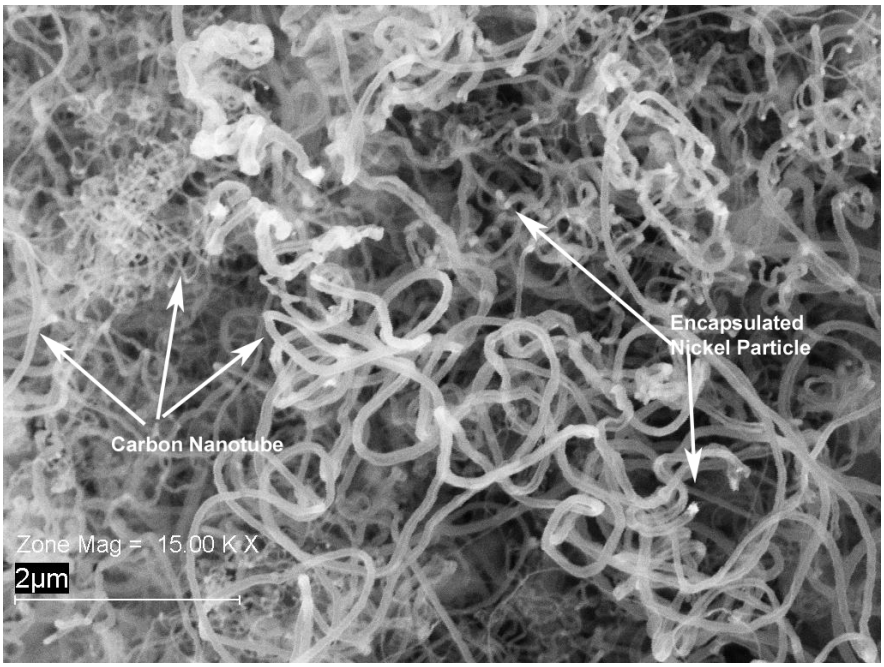

Figure 86: SEM Micrograph of CNTs Grown with AcUHYCNT Recipe on 60 nm Nickel Catalyst Layer

4.7 Effect of Synthesis Temperature

CNT diameter was analyzed as a function of synthesis temperature while holding all other synthesis variables constant. The synthesis recipe used for growth was the BULK CNT recipe. Nickel nanoparticle catalyst in IPA was applied to 1 cm silicon squares as described in the procedure section. Soak temperature was raised by 100°C for each sample, beginning with a 500°C soak for the first sample, and ending with a 900°C soak for the fifth sample. Plotting the percent of tubes that fall into a specific range results in nanotube diameter distribution plots. For each catalyst film thickness, the following ranges were used: (0-29 nm), (30-59 nm), (60-89 nm), (90-119 nm), (120-149 nm), (150 nm +).

Table 12 shows the CNT diameter data collected for each soak temperature and references diameter distribution plots for each sample as well. Also included in Table 12 are references to SEM micrographs for each sample.

Table 12: Nanotube Diameter Data for Increasing Synthesis Temperature for CNTs Grown on Nickel Nanoparticle Catalyst with Bulk CNT Recipe

Soak Temperature	Average Diameter	Standard Deviation	Diameter Distribution Plot	SEM Micrograph
500°C	73.6	23.4	Figure 87	Figure 88
600°C	54.5	15.9	Figure 89	Figure 90
700°C	25.4	3.9	Figure 91	Figure 92
800°C	N/A	N/A	N/A	Figure 93
900°C	69.0	19.3	Figure 94	Figure 95

4.7.1 Bulk CNT on Nickel Nanoparticles, 500°C

This particular catalyst system, synthesis recipe and temperature result in a wide distribution of CNT diameters and length (Figure 87). Approximately 85% of the CNTs

have diameters less than 150 nm. The volume of nanotubes produced has increased dramatically over other recipe/catalyst combinations, and is estimated to be 200-300 microliters. The CNT film produced is too thick to make reasonable estimations of length. Tip growth is evident from the SEM micrograph (Figure 88).

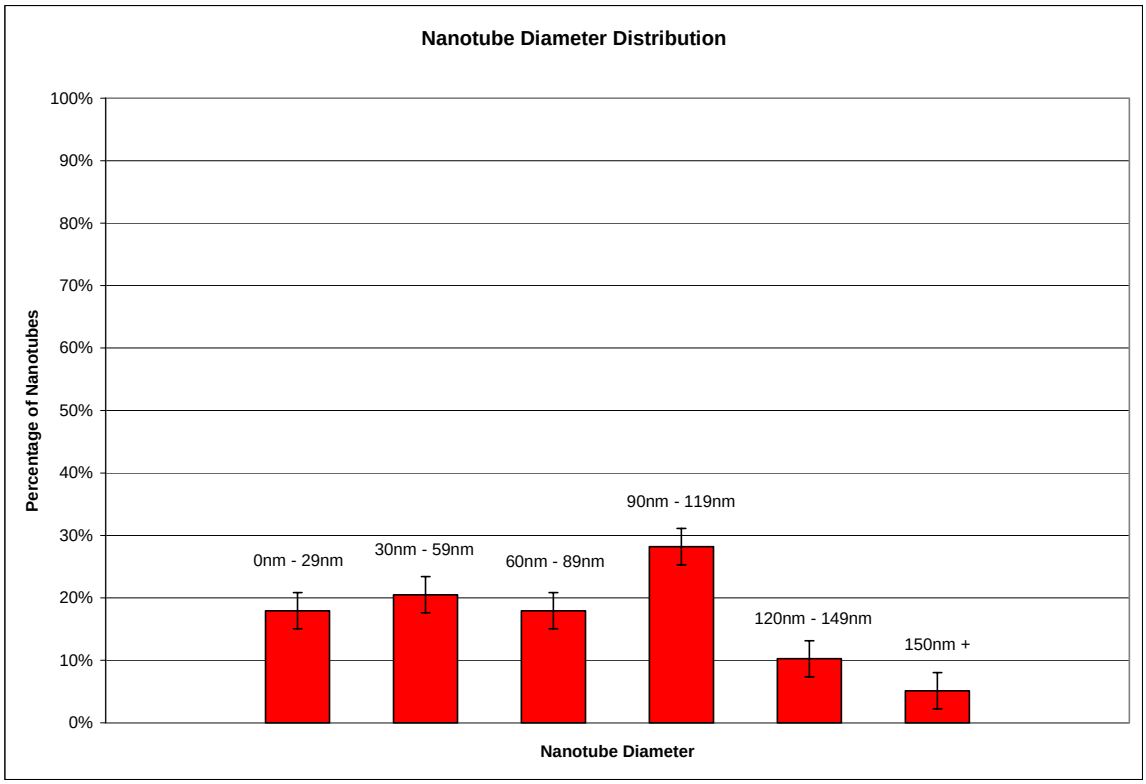

Figure 87: Distribution of Nanotube Diameter for BULK CNT Recipe on Nickel Nanoparticle Catalyst at 500°C

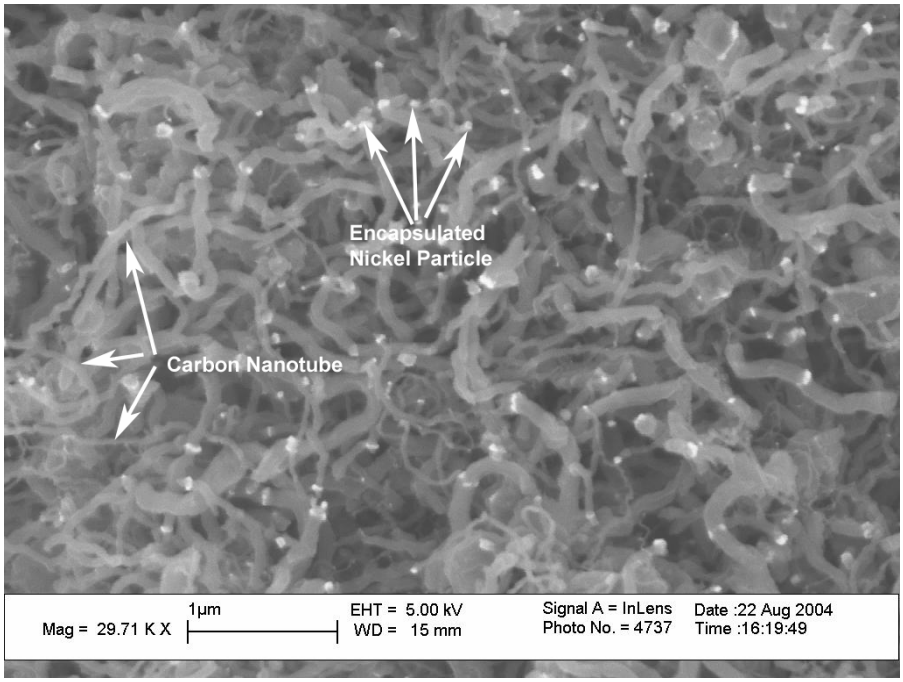

Figure 88: SEM Micrograph of CNTs Grown with BULK CNT Recipe on Nickel Nanoparticle Catalyst at 500°C

4.7.2 Bulk CNT on Nickel Nanoparticles, 600°C

Increasing the temperature by 100°C narrows the distribution of tube diameters (Figure 89). Approximately 80% of the CNTs have diameters less than 90 nm. The volume of nanotubes produced is again quite large, approximately 300 microliters.

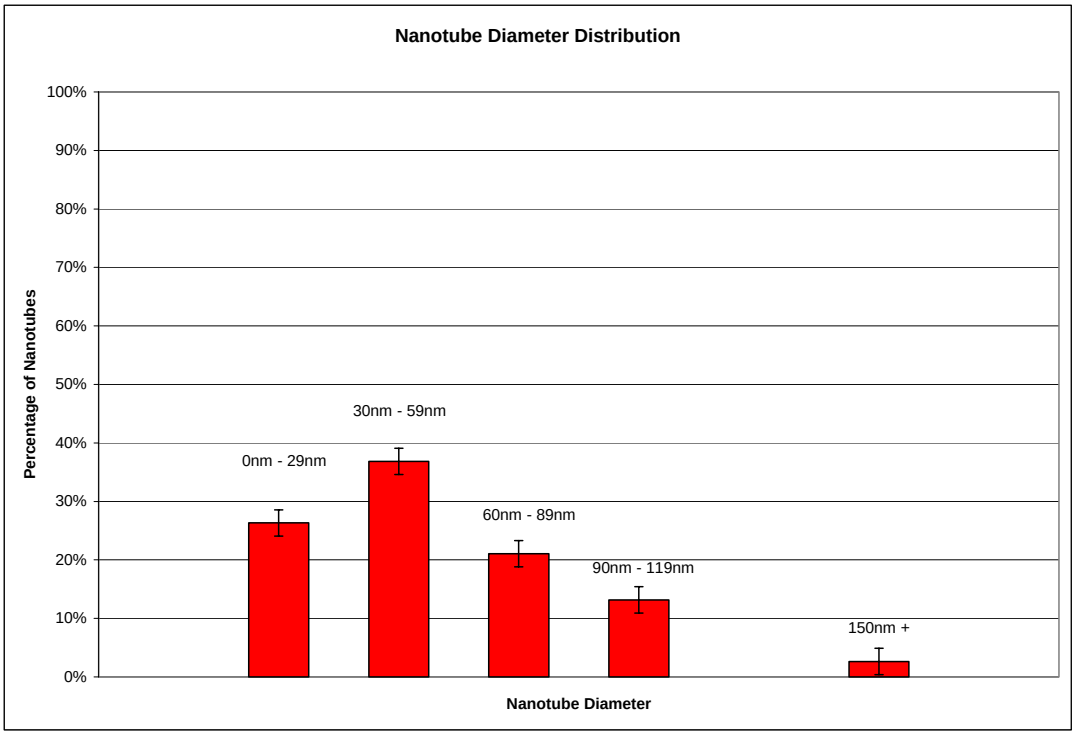

Figure 89: Distribution of Nanotube Diameter for BULK CNT Recipe Grown on Nickel Nanoparticle Catalyst at 600°C

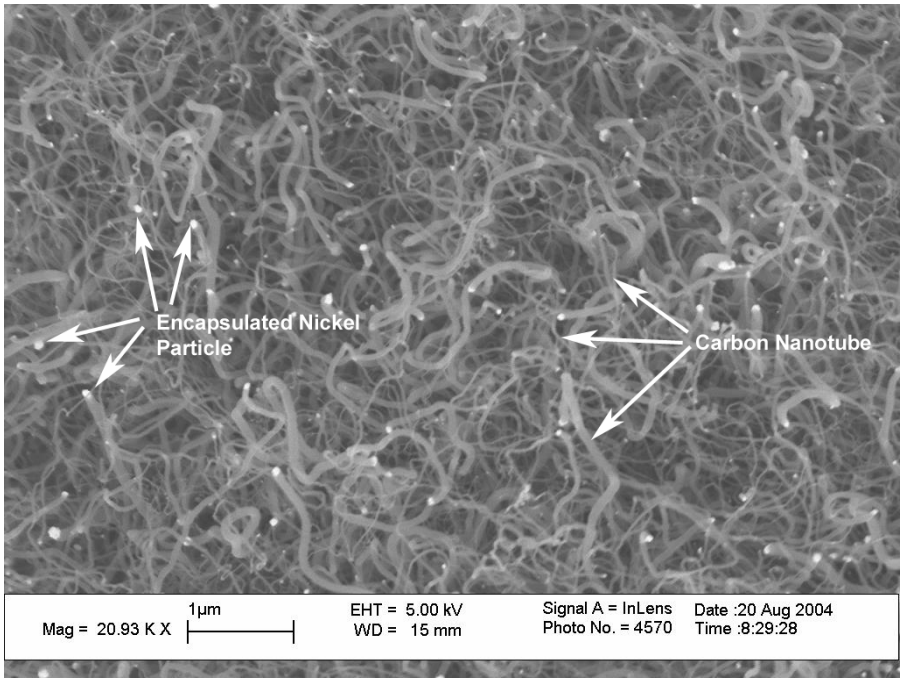

Figure 90: SEM Micrograph of CNTs Grown with BULK CNT Recipe on Nickel Nanoparticle Catalyst at 600°C

4.7.3 Bulk CNT on Nickel Nanoparticles, 700°C

Increasing the temperature to 700°C drastically reduces the diameters of the resulting CNTs (Figure 91). Approximately 80% of the CNTs have diameters less than 30 nm. The volume of nanotubes produced has reduced significantly compared to the 500°C and 600°C synthesis. Large nickel agglomerates are prominent in Figure 92. The length is difficult to estimate in this case due to the twisted nature and coalescence of the nanotubes.

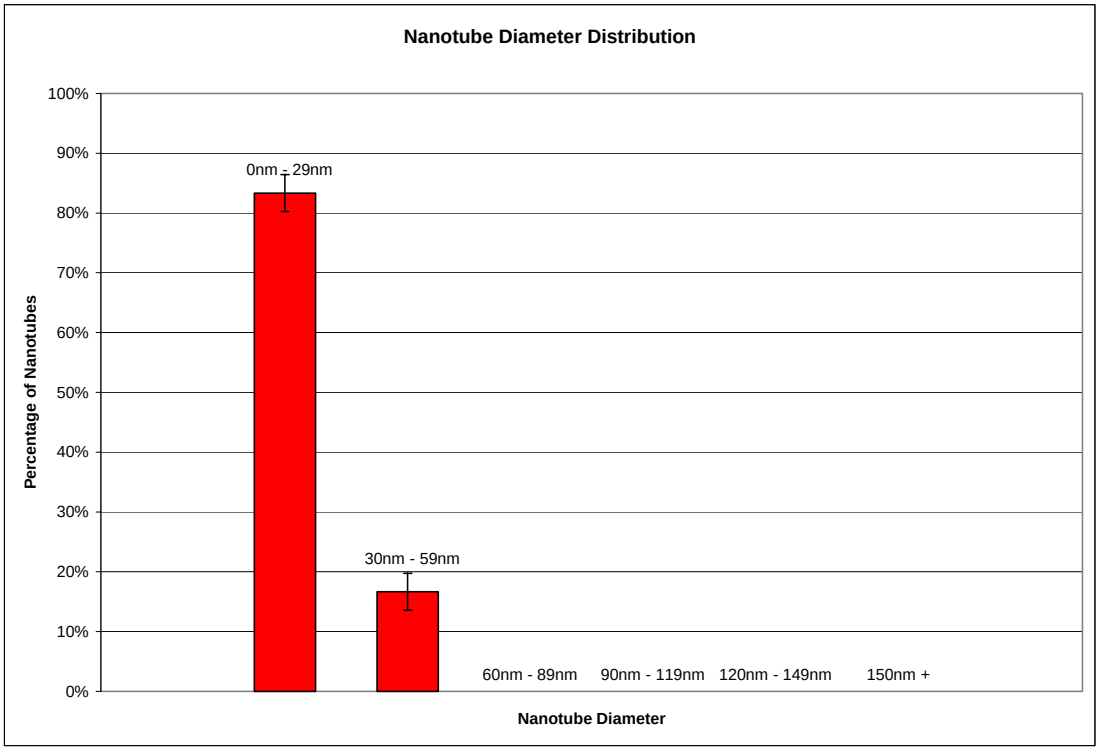

Figure 91: Distribution of Nanotube Diameter for BULK CNT Recipe on Nickel Nanoparticle Catalyst at 700°C

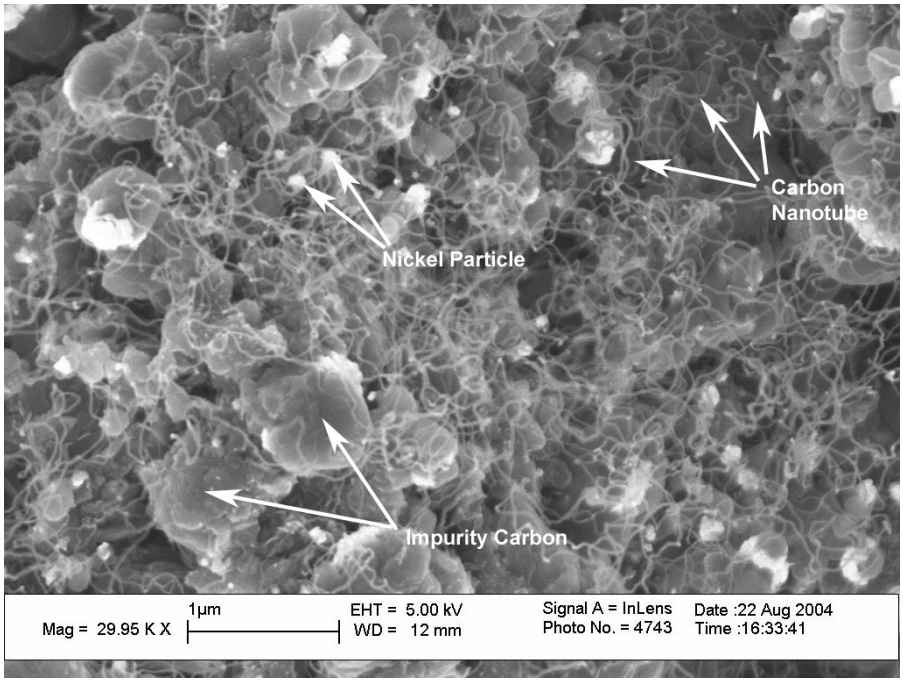

Figure 92: SEM Micrograph of CNTs Grown with BULK CNT Recipe on Nickel Nanoparticle Catalyst at 700°C

4.7.4 Bulk CNT on Nickel Nanoparticles, 800°C

No nanotubes were produced at this temperature after repeated attempts. Figure 93 shows only the state of the catalyst material after the attempted synthesis. Impurity carbon was present in each sample.

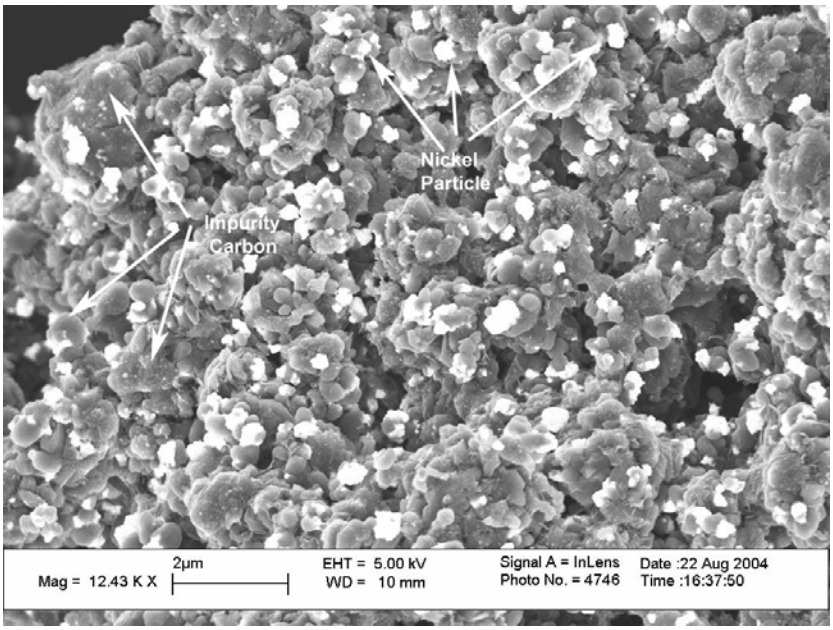

Figure 93: SEM Micrograph of Nickel Nanoparticle Catalyst After Attempted BULK CNT Synthesis at 800°C

4.7.5 Bulk CNT on Nickel Nanoparticles, 900°C

Increasing the temperature to 900°C produces a fairly narrow distribution of CNTs (Figure 94). Approximately 80% of the CNTs have diameters less than 90 nm. The volume of nanotubes produced has reduced significantly compared to the 500°C and 600°C synthesis and is more comparable to the quantity produced in the 700°C synthesis. Large nickel agglomerates are prominent in Figure 95. The CNTs from this synthesis were generally straighter than those from other temperatures, and length appears to be significantly higher as well.

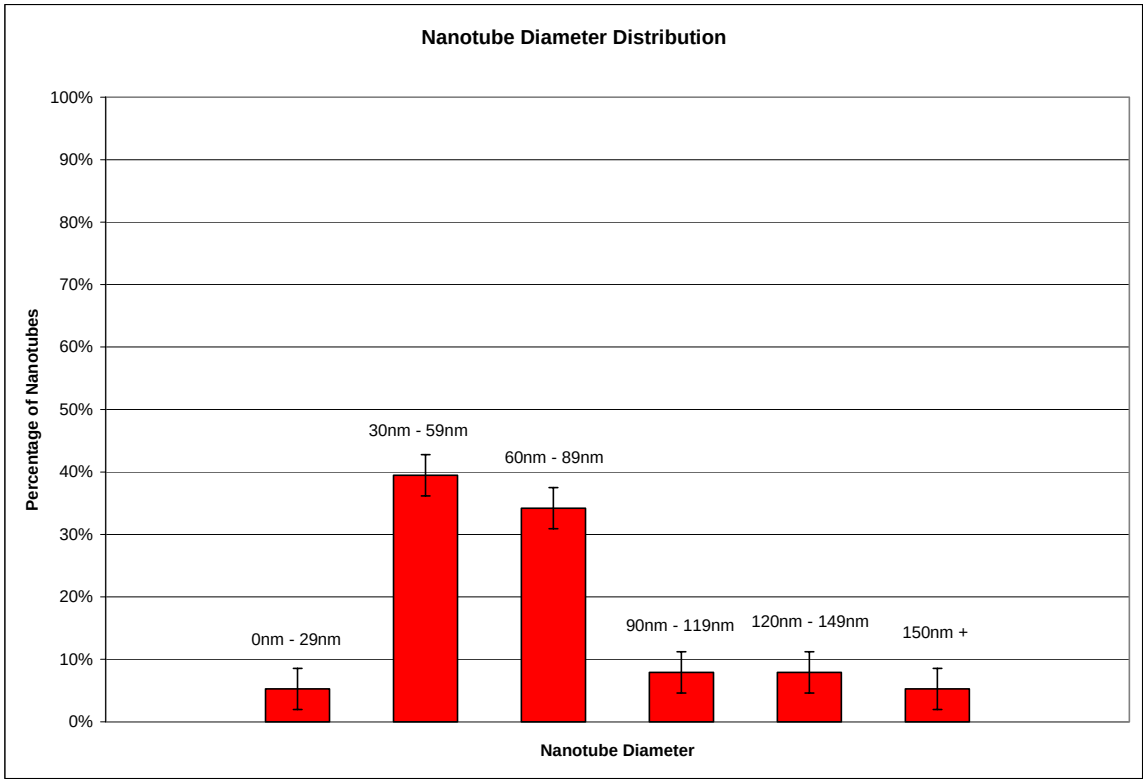

Figure 94: Distribution of Nanotube Diameter for BULK CNT Recipe on Nickel Nanoparticle Catalyst at 900°C

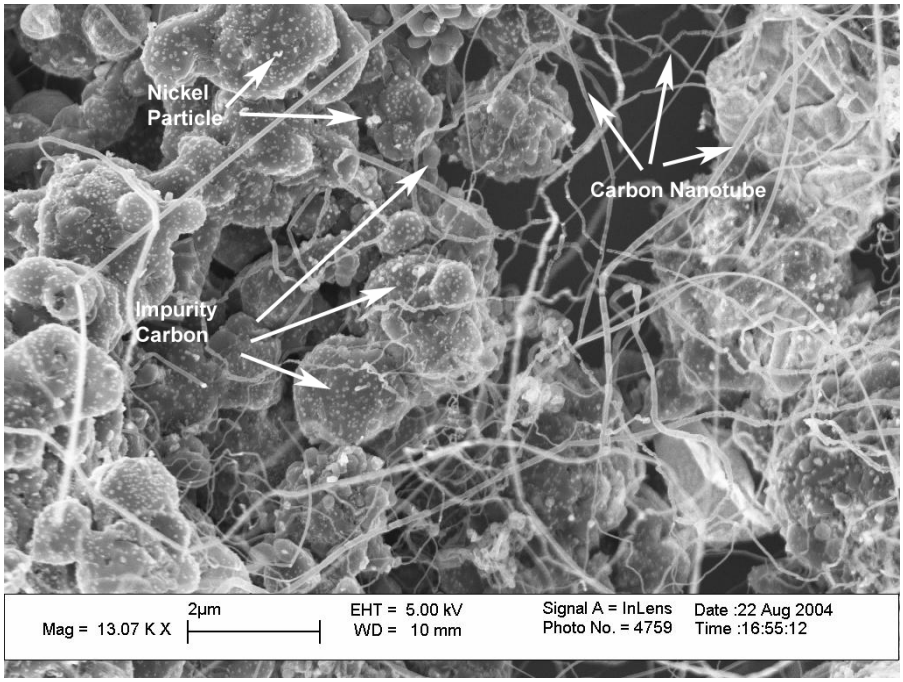

Figure 95: SEM Micrograph of CNTs Grown with BULK CNT Recipe on Nickel Nanoparticle Catalyst at 900°C

4.7.6 Bulk CNT on Nickel Nanoparticles Summary

Figure 96 shows the relationship between the soak temperature and the resultant average diameter of CNTs synthesized on nickel nanoparticles using the BULK CNT recipe. The error bars in the figure represent one standard deviation from the calculated average CNT diameters.

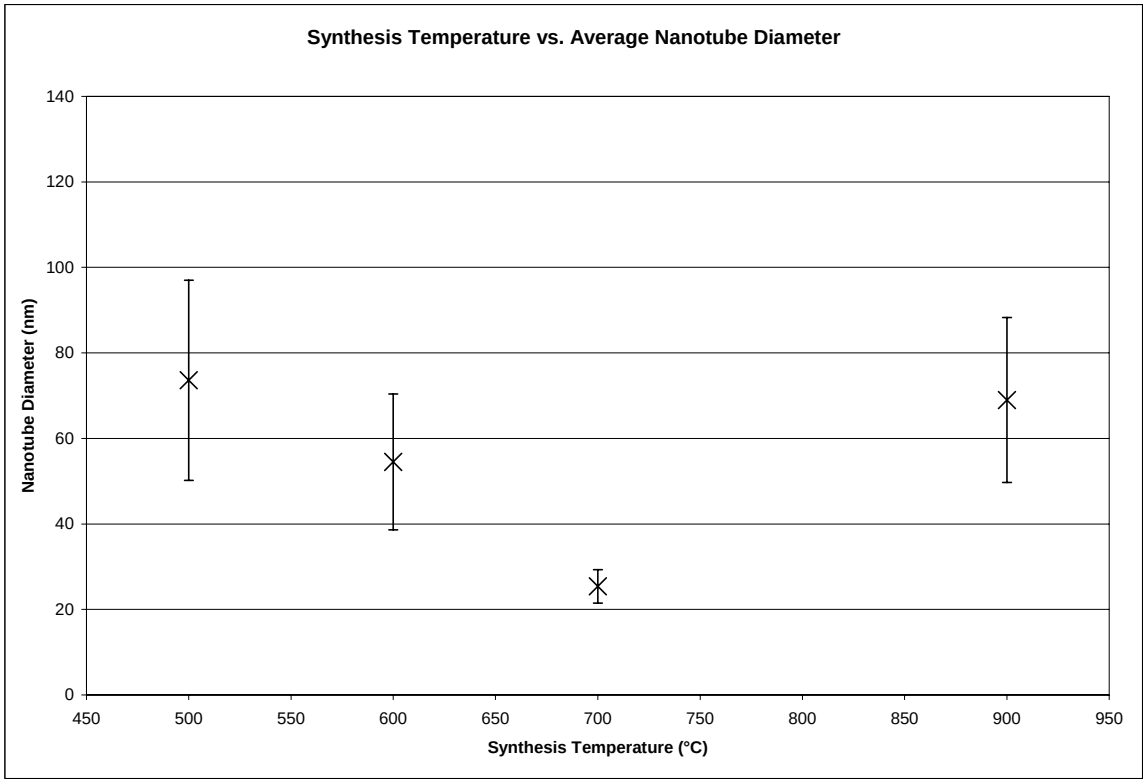

Figure 96: Average Nanotube Diameter for BULK CNT Recipe on Nickel Nanoparticle Catalyst. Error Bars Indicate One Standard Deviation.

4.8 Effect of Synthesis Temperature Using Acetylene Precursor Gas

CNT diameter was analyzed as a function of synthesis temperature while holding all other synthesis variables constant. The synthesis recipe used for growth was the AcUHYCNT recipe. Nickel nanoparticle catalyst in IPA was applied to 1 cm silicon squares as described in the procedure section. Soak temperature was raised by 100°C for each sample, beginning with a 500°C soak for the first sample, and ending with a 900°C soak for the fifth sample. Plotting the percent of tubes that fall into a specific range resulted in nanotube diameter distribution plots. For each catalyst film thickness, the following ranges were used: (0, 29 nm), (30, 59 nm), (60, 89 nm), (90, 119 nm), (120, 149 nm), (150 nm +). However, these ranges are too broad and at times do not accurately

portray data for some recipes, thus the following ranges were used: (10, 19 nm), (20, 29 nm), (30, 39 nm), (40, 49 nm), (50, 59 nm), (60, 69 nm), (70, 79 nm), and (80 nm +).

Table 12 shows the CNT diameter data collected for each soak temperature and references diameter distribution plots for each sample as well. Also included in Table 12 are references to SEM micrographs for each sample.

Table 13: Nanotube Diameter Data for Increasing Synthesis Temperature for CNTs Grown on Nickel Nanoparticle Catalyst Grown with AcUHYCNT Recipe

Soak Temperature	Average Diameter	Standard Deviation	Diameter Distribution Plot	SEM Micrograph
500°C	95.5	27.6	Figure 97	Figure 98
600°C	61.8	16.7	Figure 99	Figure 100
700°C	27.7	5.9	Figure 101	Figure 102
800°C	67.9	11.6	Figure 103	Figure 104
900°C	N/A	N/A	N/A	Figure 105

4.8.1 AcUHYCNT on Nickel Nanoparticles, 500°C

This particular catalyst system, synthesis recipe and temperature result in a wide distribution of CNT diameters and length. Approximately 82% of the CNTs have diameters less than 150 nm (Figure 97). The volume of nanotubes produced has increased even more than with use of ethylene gas. A weight gain of 3.3mg +/- 0.1mg was recorded for a sample using this recipe. Additionally, approximately 20% of the CNTs from this recipe are coiled, as shown in Figure 98. The CNTs are too twisted to make reasonable estimations of length.

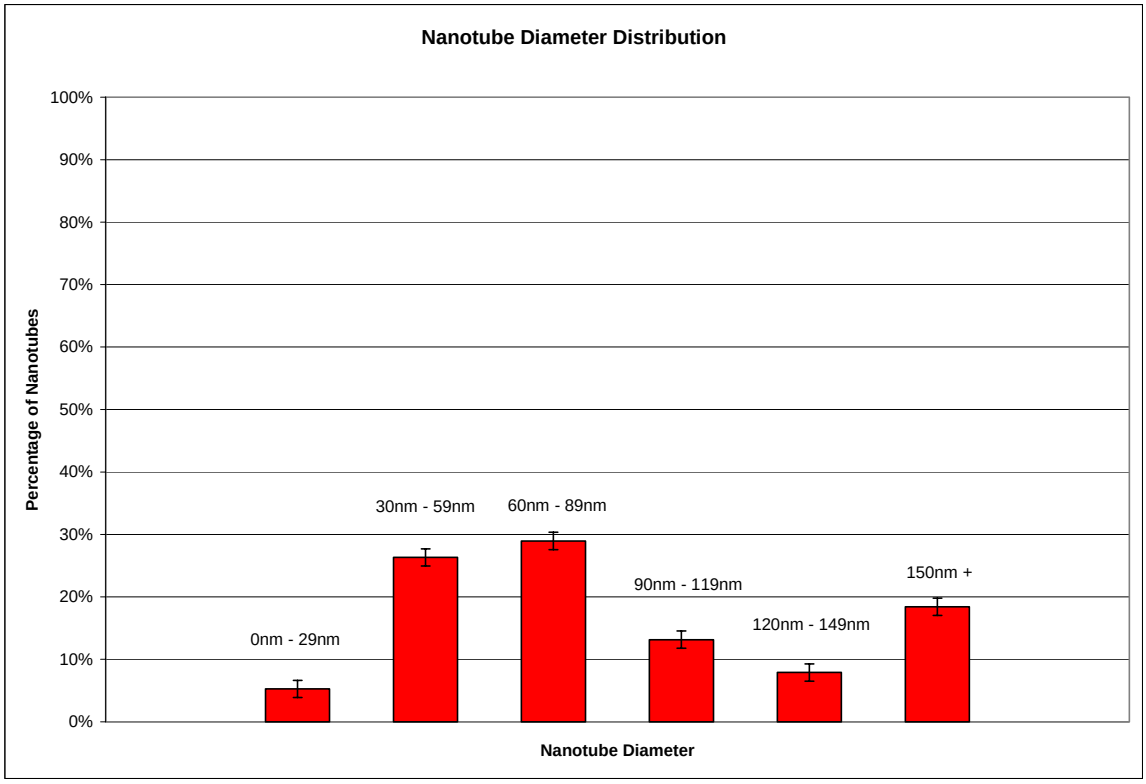

Figure 97: Distribution of Nanotube Diameter for AcUHYCNT Recipe Grown on Nickel Nanoparticle Catalyst at 500°C

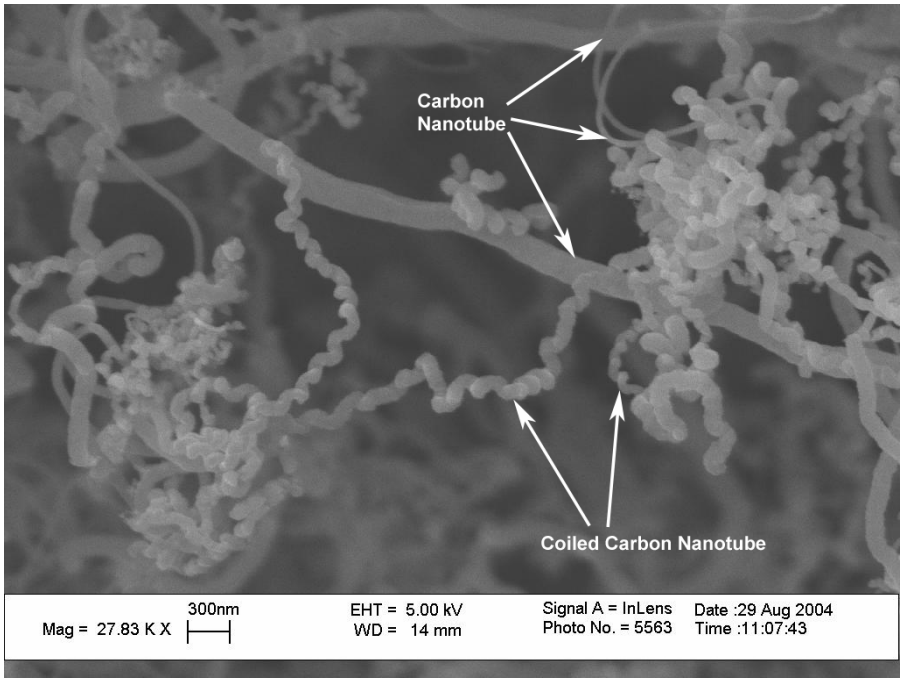

Figure 98: SEM Micrograph of CNTs Grown with AcUHYCNT Recipe on Nickel Nanoparticle Catalyst at 500°C

4.8.2 AcUHYCNT on Nickel Nanoparticles, 600°C

Raising the temperature to 600°C resulted in a narrow distribution of diameters for the CNTs, and it was necessary to use smaller ranges for to plot the distribution (Figure 99). Approximately 92% of the CNTs have diameters less than 80 nm. A weight gain of 1.3mg +/- 0.1mg was recorded for a sample using this recipe. Coiled CNTs were not observed in samples produced using this recipe (Figure 100), but an alarming amount (30-40 vol%) of amorphous carbon materials was observed. The density of the CNTs in regions free of amorphous carbon made it difficult to analyze tube length.

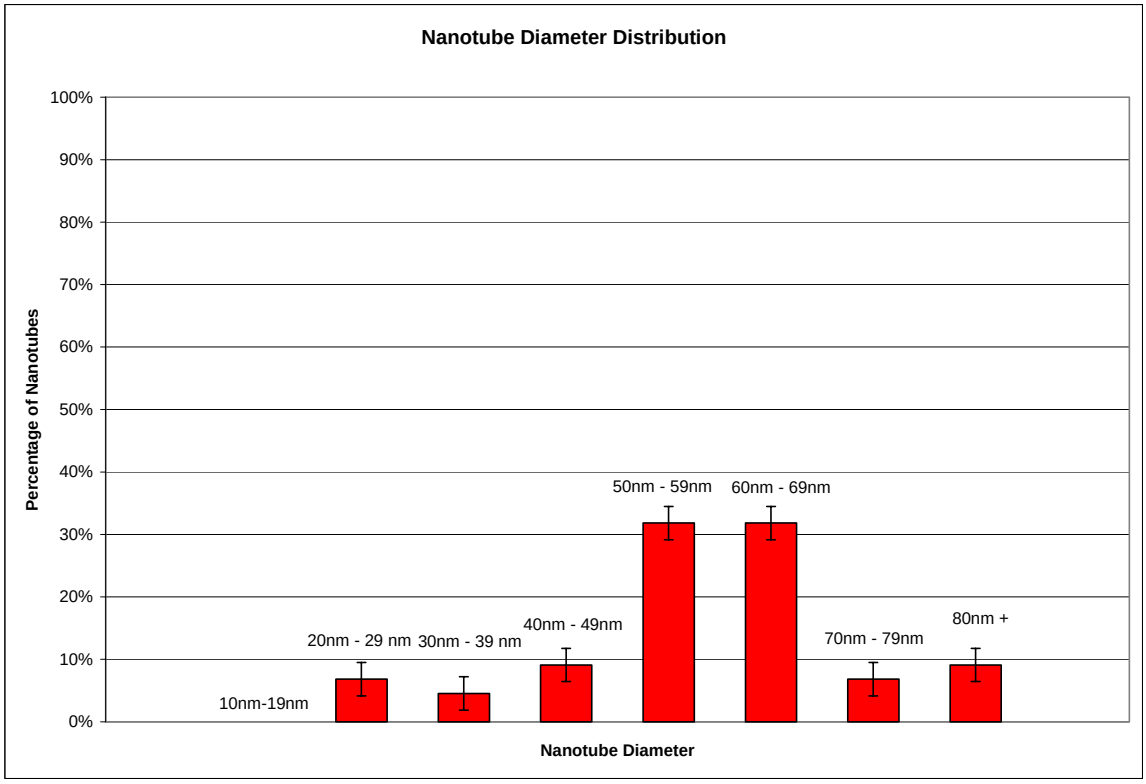

Figure 99: Distribution of Nanotube Diameter for AcUHYCNT Recipe Grown on Nickel Nanoparticle Catalyst at 600°C

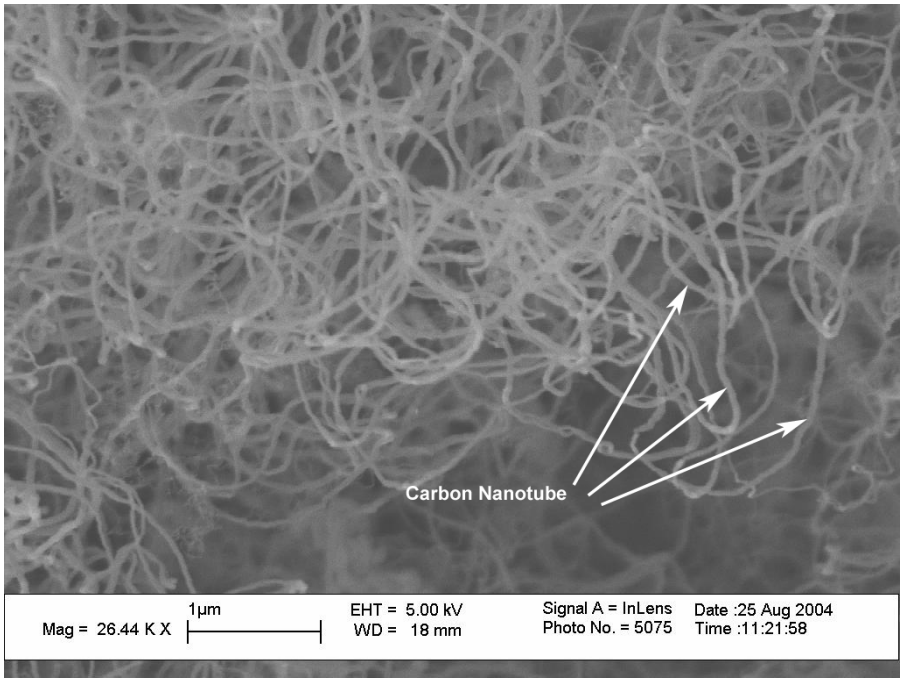

Figure 100: SEM Micrograph of CNTs Grown with AcUHYCNT Recipe on Nickel Nanoparticle Catalyst at 600°C

4.8.3 AcUHYCNT on Nickel Nanoparticles, 700°C

Raising the temperature to 700°C narrows the distribution of diameters for the CNTs even further. Again, it was necessary to use smaller ranges to plot the distribution (Figure 101). Approximately 98% of the CNTs have diameters less than 60 nm. The quantity of CNTs produced was smaller than the limit of the scale for samples produced with this recipe. Structures similar to large MWNT were observed under these synthesis conditions, but such structures were regarded as impurity materials (Figure 102). Coiled CNTs were observed in samples produced using this recipe, but the frequency of their occurrence is minimal (<<1 vol.%). Copious amounts of amorphous carbon were also observed using this synthesis recipe.

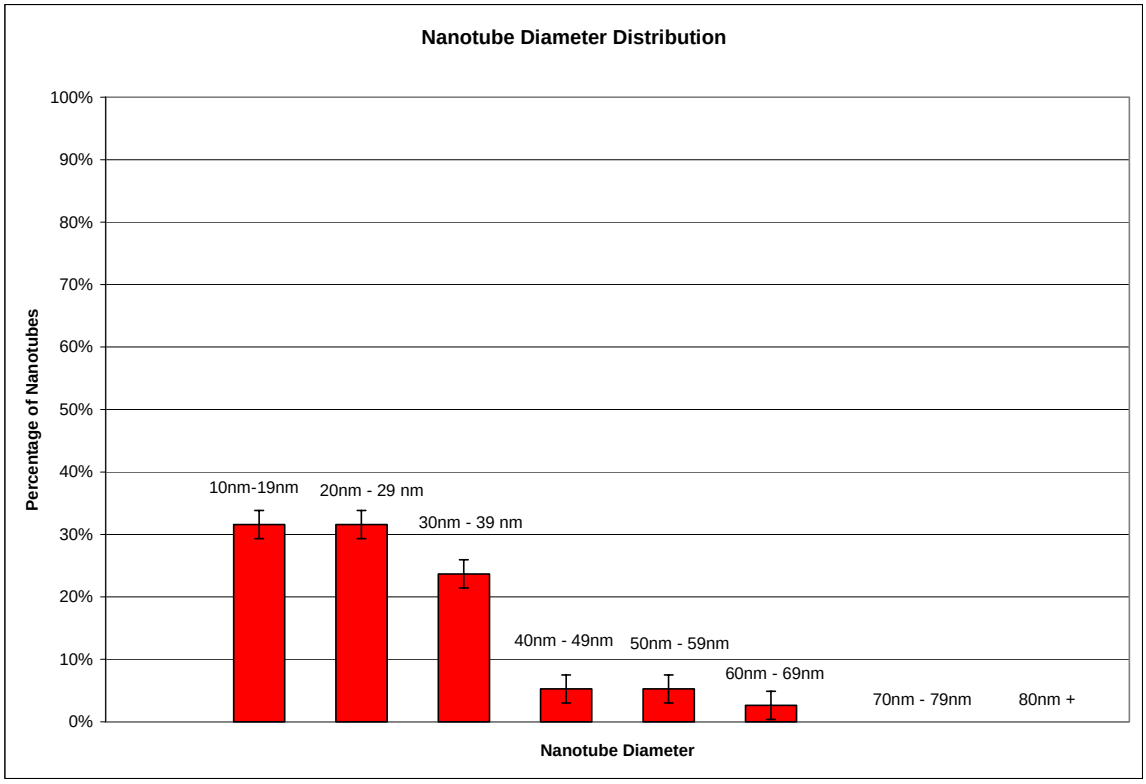

Figure 101: Distribution of Nanotube Diameter for AcUHYCNT Recipe Grown on Nickel Nanoparticle Catalyst at 700°C

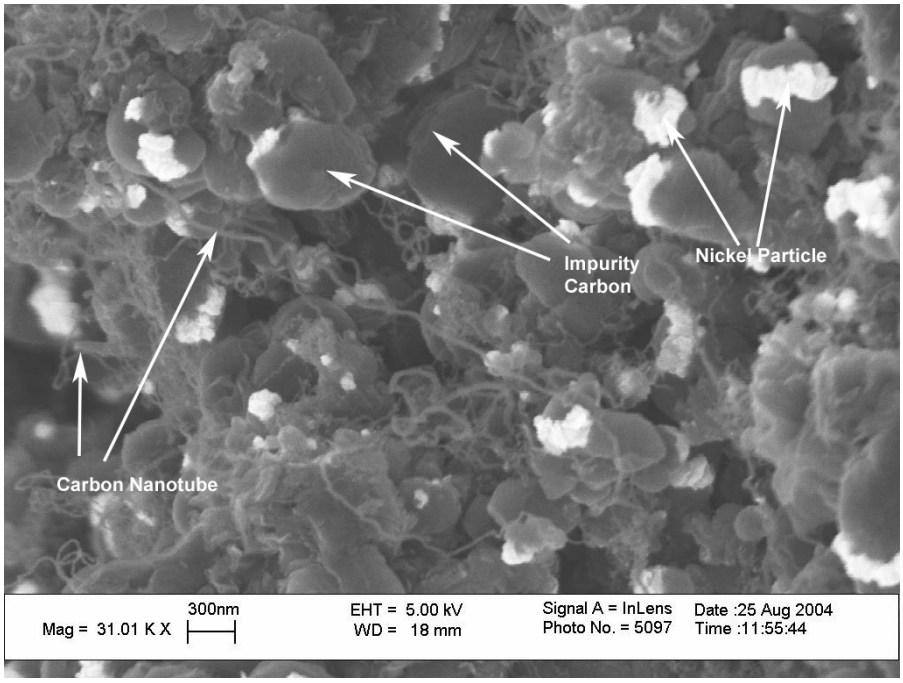

Figure 102: SEM Micrograph of CNTs Grown with AcUHYCNT Recipe on Nickel Nanoparticle Catalyst at 700°C

4.8.4 AcUHYCNT on Nickel Nanoparticles, 800°C

Raising the temperature to 800°C widened the distribution of diameters for the CNTs. Larger ranges were used to plot the distribution (Figure 103). Approximately 87% of the CNTs have diameters less than 120 nm. The quantity of CNTs produced was immeasurable for samples produced with this recipe. A small amount of amorphous carbon (5-10 vol%) was observed for samples produced with this recipe. Coiled CNTs were observed in samples produced using this recipe, with minimal frequency (2-5 vol%). An SEM micrograph of CNTs produced with this recipe is shown in Figure 104.

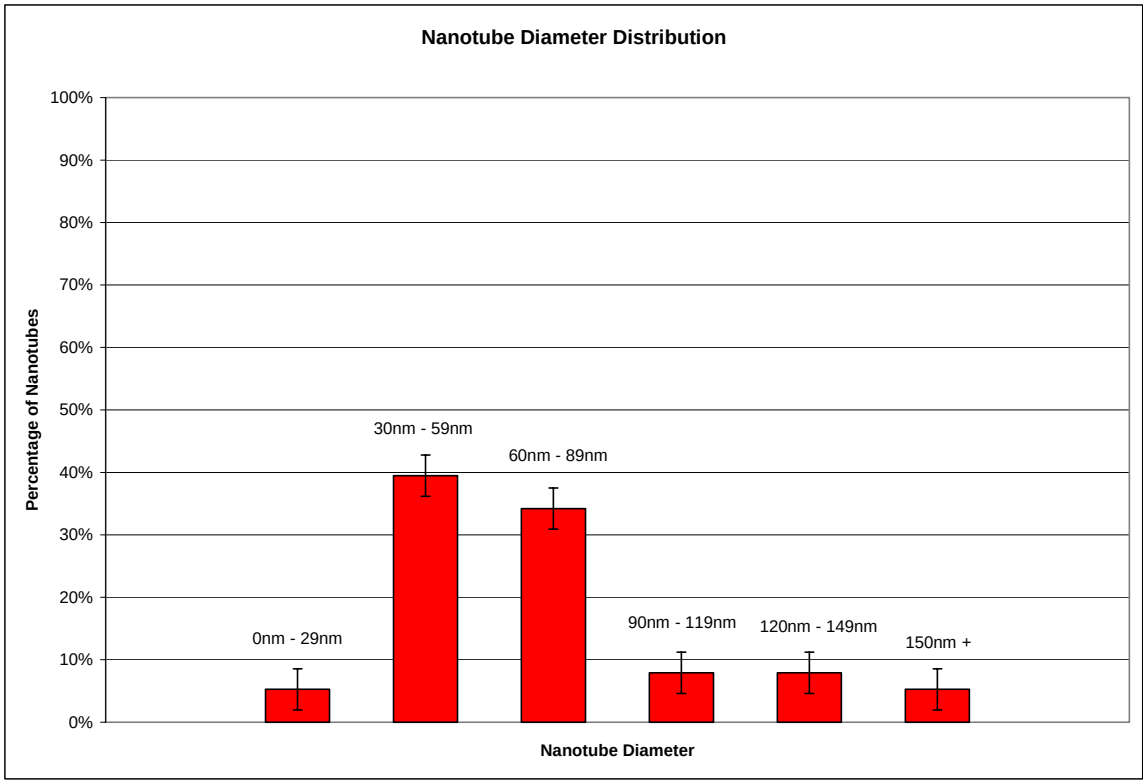

Figure 103: Distribution of Nanotube Diameter for AcUHYCNT Recipe Grown on Nickel Nanoparticle Catalyst at 800°C

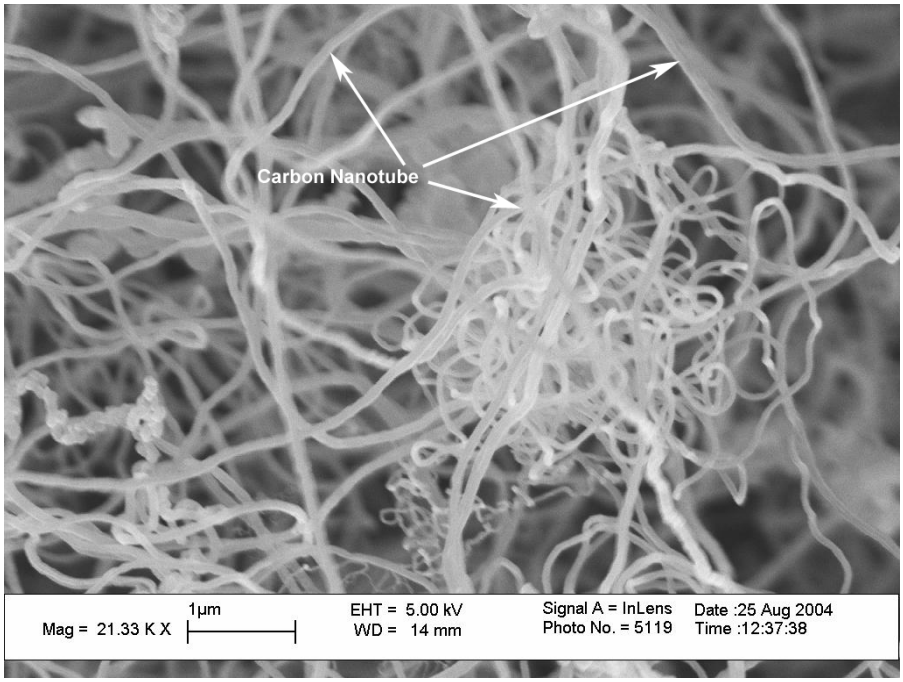

Figure 104: SEM Micrograph of CNTs Grown with AcUHYCNT Recipe on Nickel Nanoparticle Catalyst at 800°C

4.8.5 AcUHYCNT on Nickel Nanoparticles, 900°C

Raising the temperature to 900°C resulted in no CNT growth over several attempts. Nearly 100% of the products of recipes under these synthesis conditions were carbon impurities. An SEM micrograph of the resulting material is shown in Figure 105.

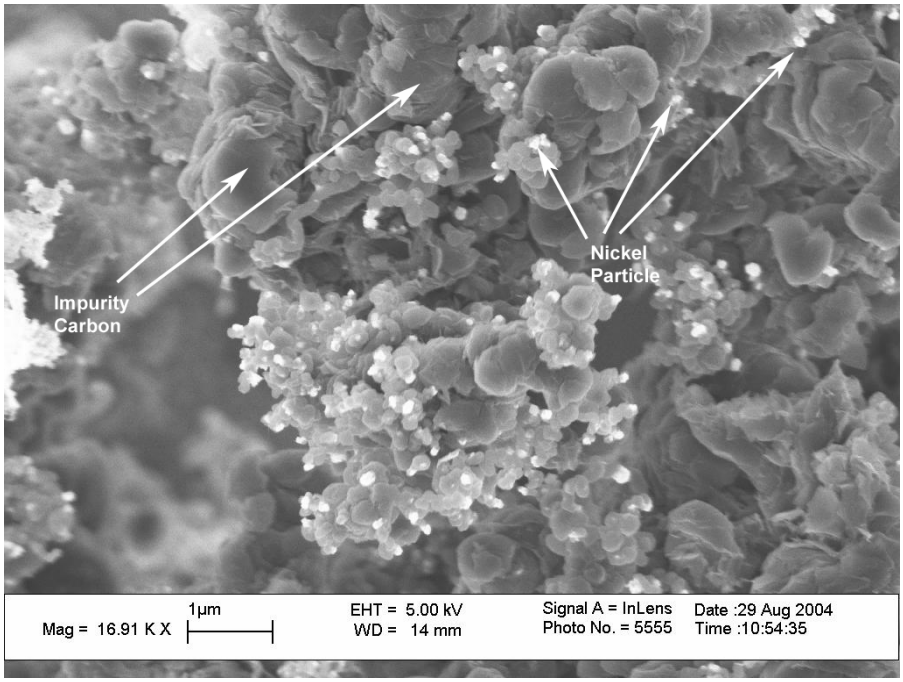

Figure 105: SEM Micrograph of AcUHYCNT Recipe on Nickel Nanoparticle Catalyst at 900°C

4.8.6 AcUHYCNT on Nickel Nanoparticles Summary

Figure 106 shows the relationship between the soak temperature and the resultant average diameter of CNTs synthesized on nickel nanoparticles using the BULK CNT recipe. The error bars in the figure represent one standard deviation from the calculated average CNT diameters.

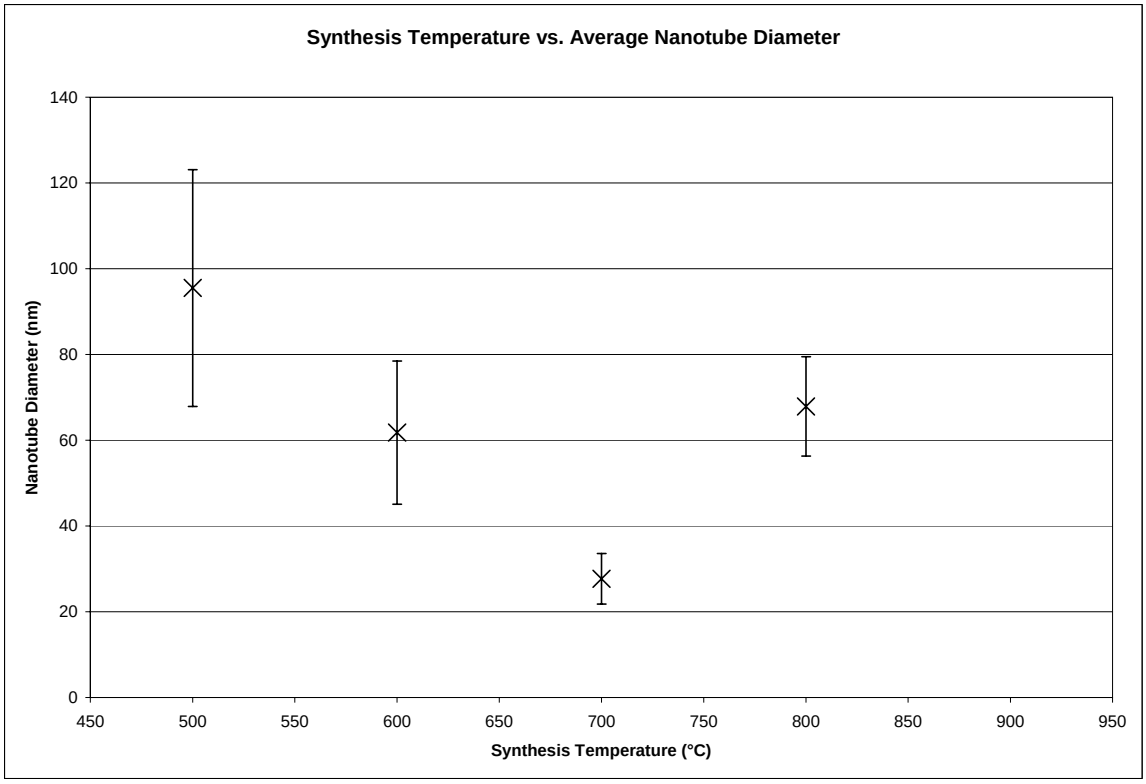

Figure 106: Average Nanotube Diameter for AcUHYCNT Recipe on Nickel Nanoparticle Catalyst. Error Bars Indicate One Standard Deviation.

4.8.7 Effect of Applied Voltage, AcUHYCNT on Nickel Nanoparticles

A 50V electric field was applied to the furnace during synthesis with all other synthesis conditions remaining the same. The average CNT diameter for each temperature was consistent with synthesis without an applied field. A weight gain of 0.0041g +/- 0.0001g was recorded for a sample using this recipe. The only difference was in the amount of coiled CNTs produced at 500°C. Coiled CNTs accounted for roughly 70% of the total CNTs produced under these synthesis conditions. Figure 107 is an SEM micrograph showing coiled CNTs produced under these conditions.

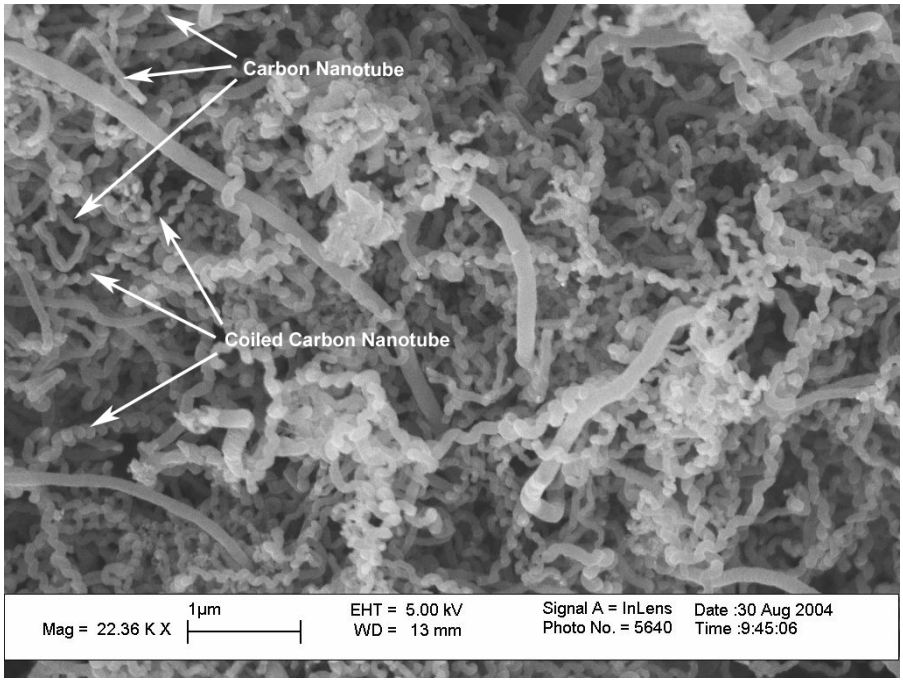

Figure 107: Coiled CNTs Grown with AcUHYCNT Recipe on Nickel Nanoparticle Catalyst at 500°C with 50V Applied Electric Field

4.9 Macro Scale Results

Many observations of CNTs and the effects of synthesis have already been presented in the previous sections. Synthesis variables used in the present work also led to some results which are not easily quantifiable, such as sample weight gain, because the mass of CNT produced was on the order of micrograms or smaller. CNT length was difficult to measure due to the non-linear nature of CNTs themselves. The following section will present these results, and provide SEM micrographs as examples.

4.9.1 Quantity of CNTs Produced

Some recipes produced a larger quantity of nanotubes than others, however specific masses were not able to be recorded due to the insignificant quantities of CNTs. Despite the inability to specifically measure a mass, low magnification SEM images

confirm the presence of a larger quantity of tubes. Figure 108 is a micrograph of nanotubes produced with the MWNT recipe. The dark, misshapen rectangle shapes are actually 'films' of MWNTs. The films are thick connected networks of MWNT. The lighter patterns are areas where the nanotube film has been displaced due to handling. Additionally, some films were simply reduced to ash if manipulated with tweezers or other handling devices.

By comparison, Figure 109 is a low magnification micrograph of CNTs produced with the BULK CNT recipe. The darker regions of each catalyst pattern are areas where nanotube synthesis occurred. The lighter areas of the catalyst pattern yielded few, if any, nanotubes. It is important to note the difference in the growth regions when comparing to the MWNT films. The dense clusters of CNTs in Figure 109 have a more open network with no impurity carbon material in open areas (see Figure 32).

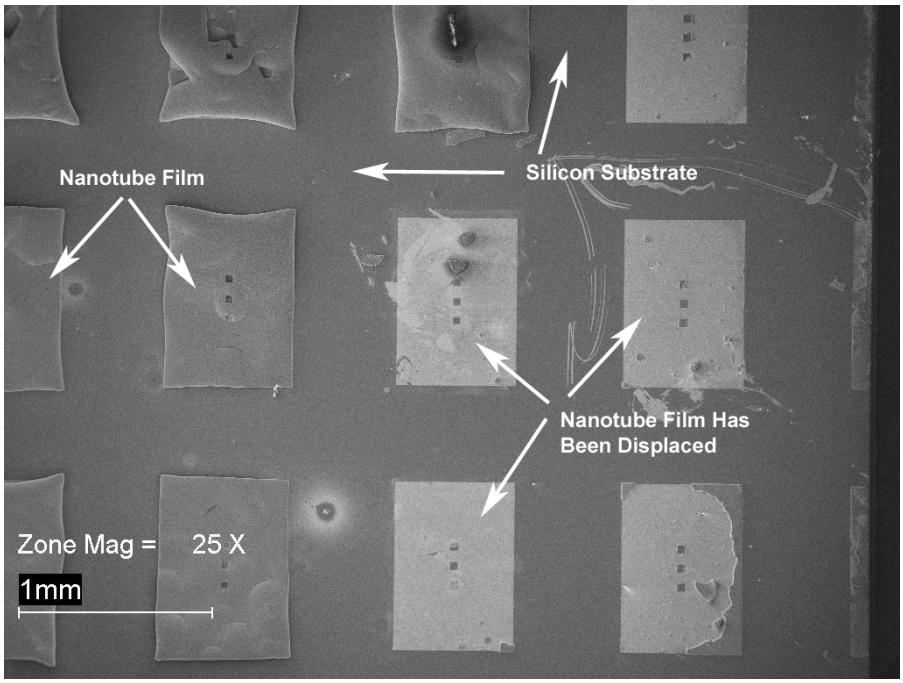

Figure 108: Low Magnification SEM of CNT Films Produced with MWNT Recipe on 100 nm Ni Catalsyt Layer

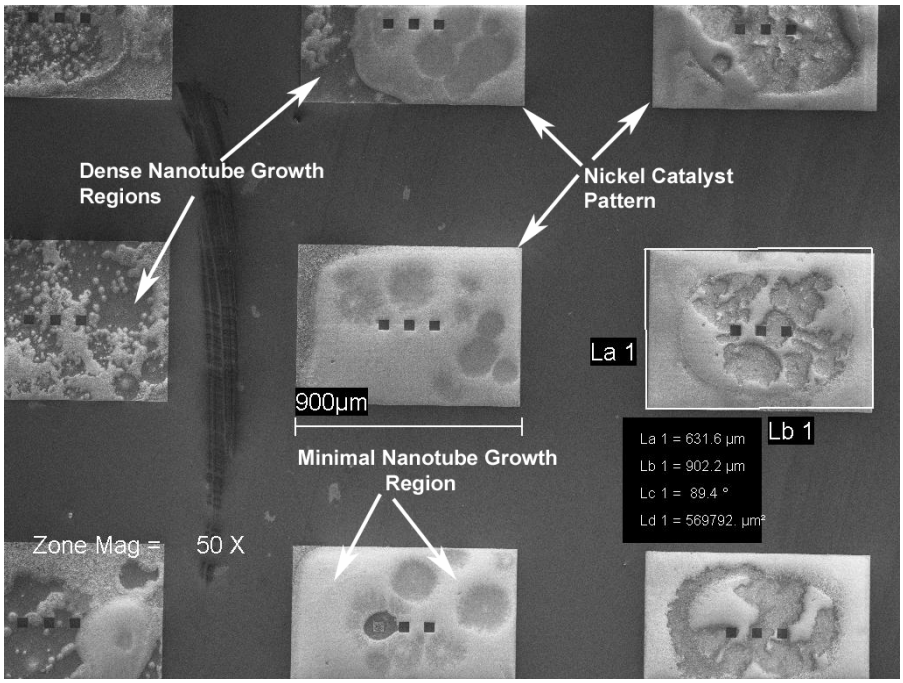

Figure 109: Low Magnification of CNTs Produced with BULK CNT Recipe on 100 nm Ni Catalyst Layer

Furthermore, Figure 110 is a low magnification micrograph of CNTs produced with the AcUHYCNT recipe. Again, darker regions are indicative of dense nanotube growth regions. The nanotubes synthesized with acetylene gas reached such significant lengths that they extend beyond the patterned nickel regions and are visible at low magnifications. No other recipes resulted in nanotubes exhibiting this behavior. Additionally, the white arrow in indicates a nickel impurity particle. A dense cluster of CNTs were synthesized in this region as well.

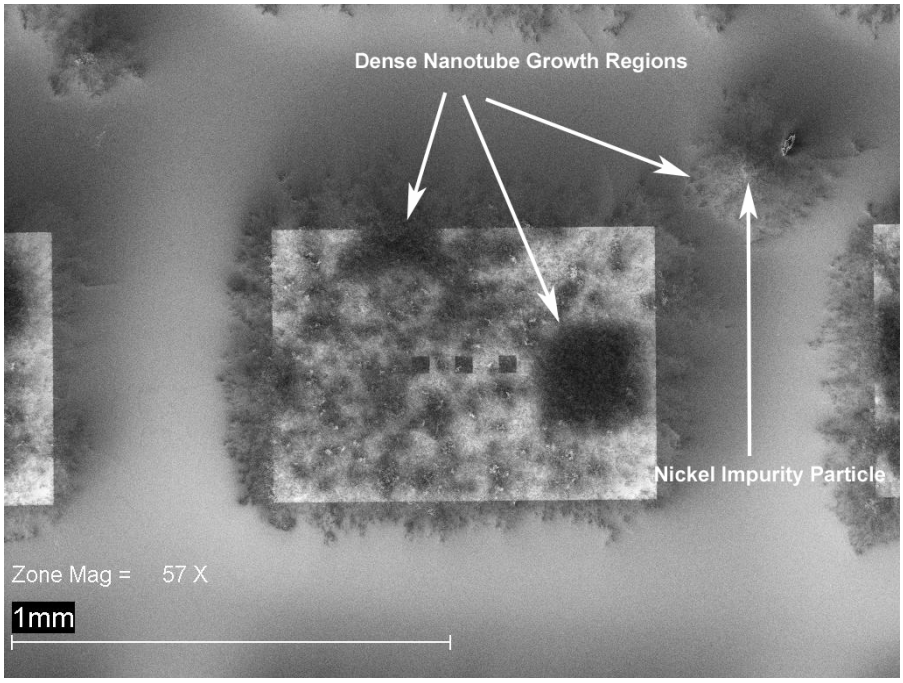

Figure 110: Low Magnification of CNTs Produced with AcUHYCNT Recipe on 100 nm Ni Catalyst Layer

The Ni/IPA catalyst system also resulted in a large quantity of nanotubes. The resulting CNTs from the BULK CNT recipe on this catalyst resulted in 'macro-films' similar to those of the CNTs synthesized with the MWNT recipe on nickel patterned substrates (although the CNTs are more similar to SWNT than MWNT). The films of CNTs from this recipe were equally susceptible to floating away, or being crushed into ash upon handling. Figure 111 is an SEM micrograph depicting this.

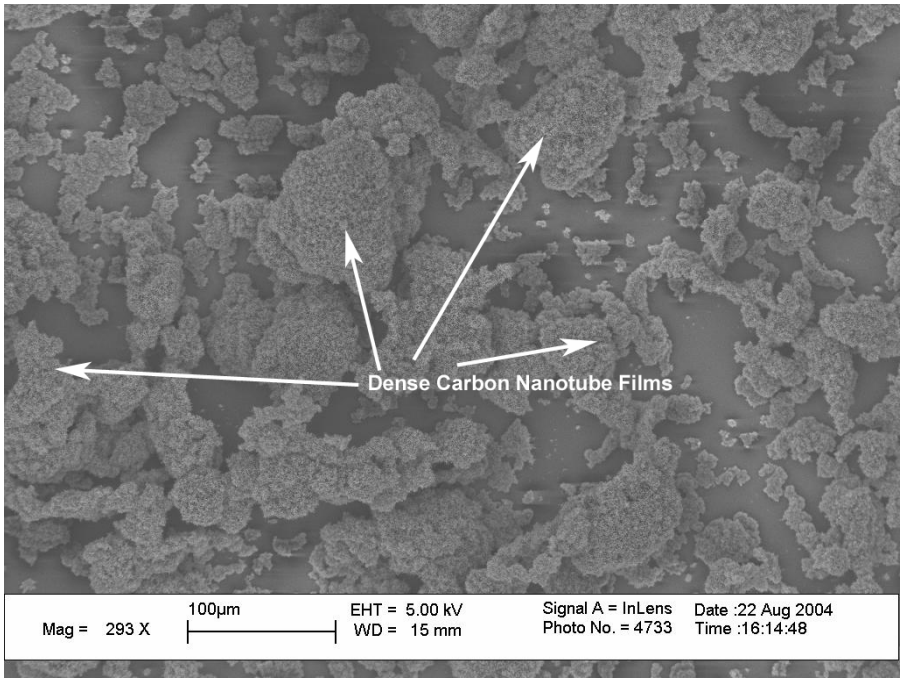

Figure 111: Low Magnification of CNT Film Produced with BULK CNT Recipe on Ni/IPA Catalyst

A final observation is on preferential growth areas. In Figure 112, CNTs grow in preferred areas on the nickel catalyst pattern. Almost all of the patterns show a preference of CNT growth in the featureless regions (that is regions which are free of edges or empty squares). Patterns which have less dense CNT growth show only growth in the featureless regions (far left of Figure 112). As CNT density increases, CNT growth spreads out to other regions of the catalyst patterns (far right of Figure 112).

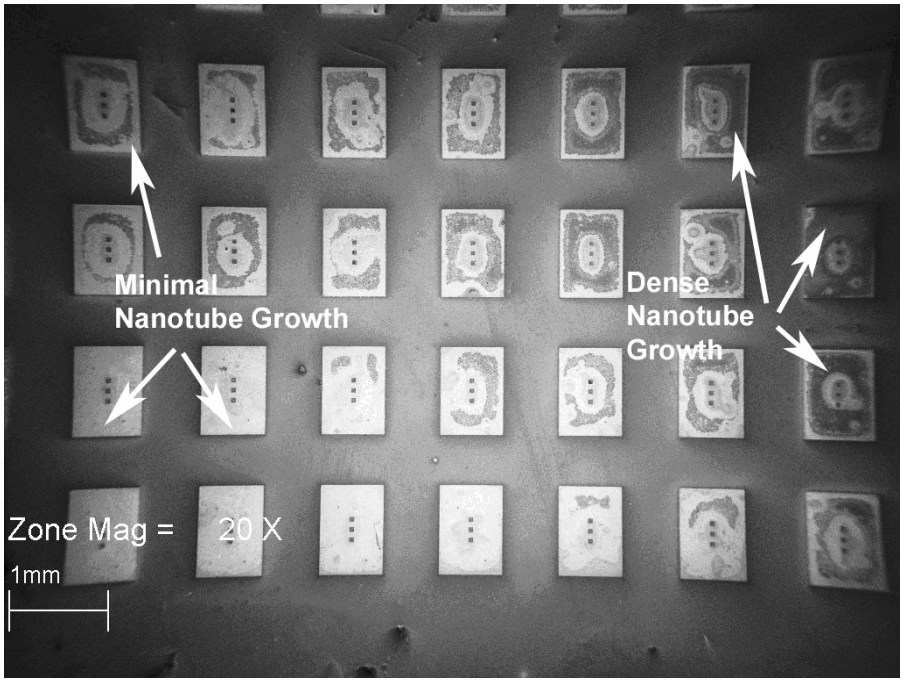

Figure 112: Low Magnification SEM Micrograph Showing Preferred CNT Growth Areas

4.10 ECDL Supercapacitor Results

Figure 113 is a plot of current vs. voltage for a Maxwell ECDL supercapacitor, an ECDL supercapacitor based on purified CNTs, and an ECDL supercapacitor based on unpurified CNTs. While the maximum current of ECDL supercapacitors produced in this research is not as high as the commercially available standard (indicating a lower capacitance), it is important to note the shape of the two CV lines. The similarity in shape indicates that the response of each supercapacitor is roughly equivalent. From this CV plot, a plot of capacitance vs. voltage can be made (Figure 114). Maximum capacitance and specific capacitance (F/g) for a commercially available supercapacitor and for a purified CNT capacitor are listed in Table 14. Specific capacitance is based on total product weight, not simply active material weight

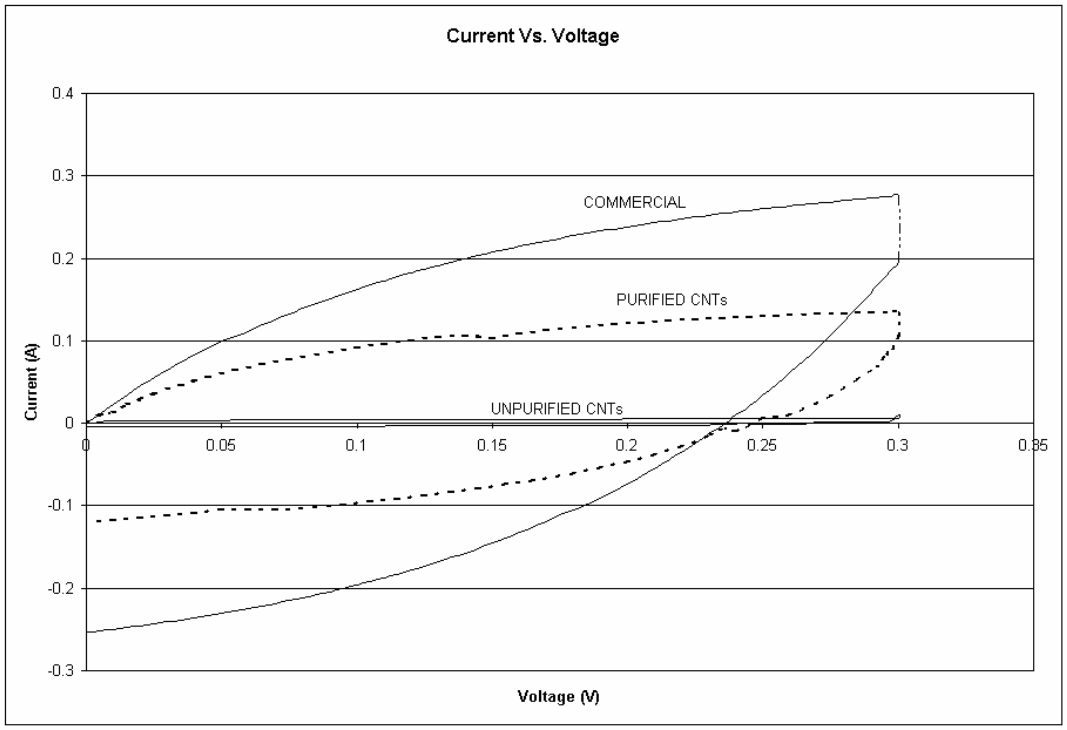

Figure 113: Current vs. Voltage Plot for Commercial Supercapacitor and CNT Supercapacitors

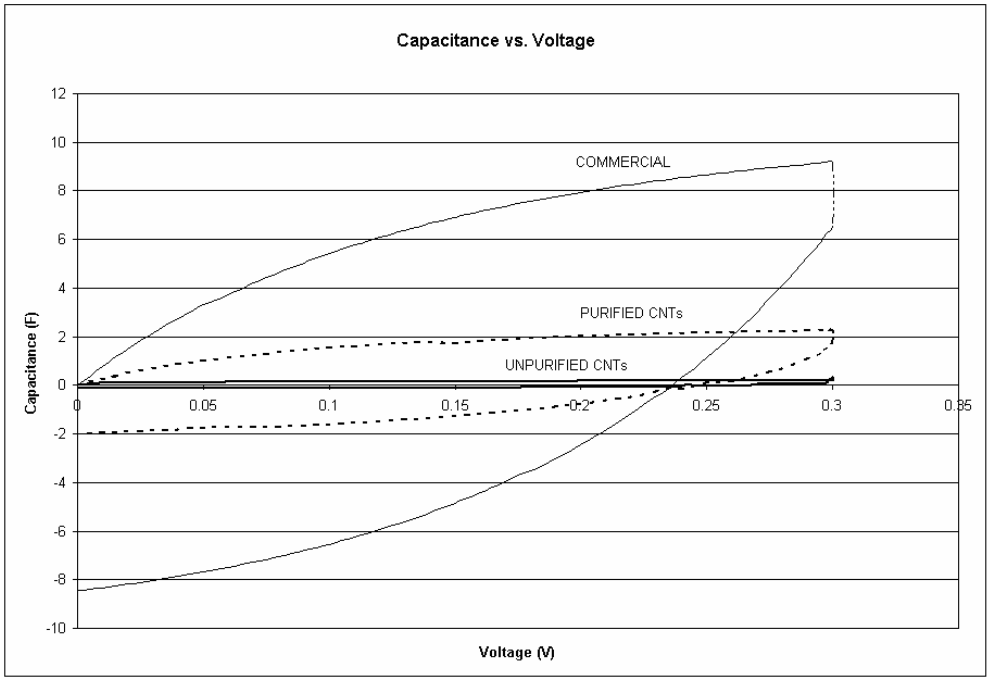

Figure 114: Capacitance vs. Voltage Plot for Commercial Supercapacitor and CNT Supercapacitors

Table 14: Comparison of Maxwell and Purified CNT Supercapcitors

	MAXWELL	PURIFIED CNT
Maximum Capacitance	9.18 F	2.24 F
Specific Capacitance	1.6 F/g	2.1 F/g

Cyclic Voltammetry was performed on capacitors made with purified CNTs while changing the molarity of the electrolyte between 0.1 mol/L, 1.0 mol/L, and 1.5 mol/L. The voltage swep rate for each molarity was held constant at 0.030V/s. The maximum applied voltage limit was set to 0.3V. Figure 115 shows the results for each electrolyte concentration on the same plot. CV was performed on the supercapacitors for slower sweep rates as well. In Figure 116, the sweep rate has been slowed to 0.015V/s, and the maximum voltage limit was set to 0.15V.

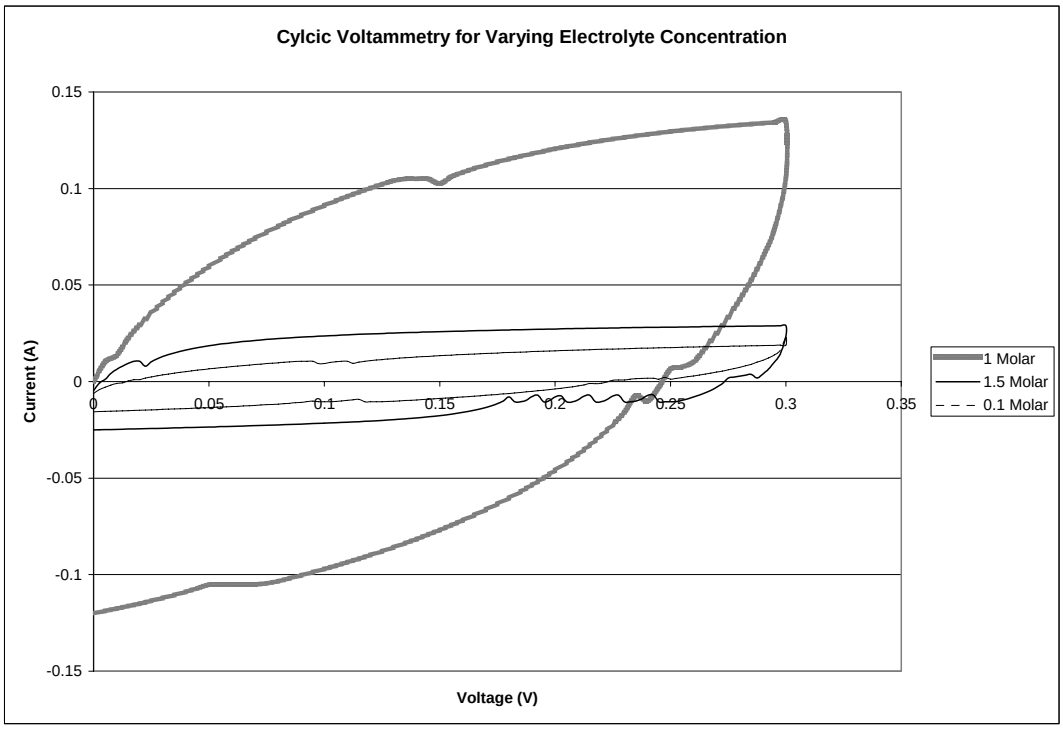

Figure 115: Current vs. Voltage Plot for Purified CNT Supercapacitors with Varying Molarity Electrolyte, 0.3V Max

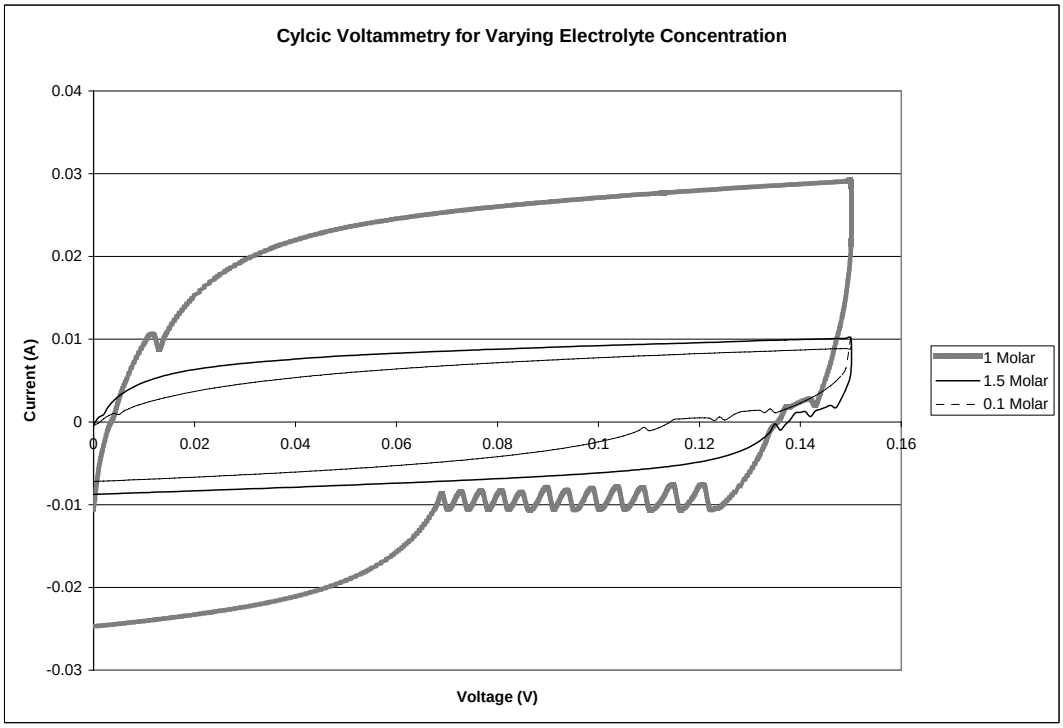

Figure 116: Current vs. Voltage Plot for Purified CNT Supercapacitors with Varying Molarity Electrolyte, 0.15V Max

CHAPTER 5

DISCUSSION OF RESULTS

The objectives of this work were (1) to analyze the effect of inherent necessary synthesis conditions on resulting carbon nanotubes, (2) to analyze the effect of external synthesis controls on resulting nanotubes and (3) create and test ECDL supercapacitors based on CNTs and suggest CNT synthesis pathways which may enhance ECDL properties. Several necessary synthesis conditions were analyzed, including synthesis temperature, synthesis time, and various catalytic systems. Furthermore, an external electric field was applied during synthesis to examine its effects as an external variable. Finally, ECDL supercapacitors were made using CNTs and tested against commercially available ECDL supercapacitors.

When considering the results, it is important to note that the CNTs produced are likely a mixture of SWNT, bundled SWNT and MWNT. This helps to explain the wide range of nanotube diameters present in many samples. Future TEM analysis will provide further insight into this matter.

5.1 Effect of Nickel Catalyst Film Thickness

As film thickness decreased, so did average CNT diameter (Figure 41). However, the standard deviation in tube diameter is still rather large. Nanotube nucleation occurs due to the decomposition of hydrocarbon precursor gasses on the nickel particles. When the soak temperature is reached in the CVD tube, the patterned nickel film has formed small nanoclusters of varying size. Due to Ostwald ripening, larger clusters form at the expense of small clusters.

As precursor gasses begin to decompose, a wide variety of nickel particles are available for CNT nucleation. Growth of CNTs continues until the nickel catalyst particle is enclosed in the tip of the tube. Throughout the period of the soak, nickel particles continue to shrink and grow simultaneously. This process is largely based on the surface energy of the catalyst layer. As described in § 4.7 (pg. 121), nanotubes grow initially in the bulk regions of the pattern, where there are few features. Higher surface energy regions show less dense CNT growth. This suggests that the higher surface areas such as edges are slower to form catalyst particles suitable for CNT nucleation.

Additionally, it can be inferred that synthesis time on nickel catalyst films can be increased in order to nucleate and grow more CNTs. As catalyst film thickness decreases, the resultant nickel particles which form are smaller, resulting in the decrease in average nanotube diameter.

5.2 Effect of Five Minute Hydrogen Gas Pretreatment Prior to Soak Stage

The effect that the pretreatment has on the catalyst layer and resulting CNTs is remarkable. The volume of tubes that were synthesized reduced drastically, and the diameters of the CNTs are far more uniform in size. The average diameter remains consistent with the results in § 4.1. The hydrogen gas (1) effectively inhibit nickel catalyst particle growth or shrinkage beyond a certain size and/or (2) severely slows the rate of decomposition and diffusion of precursor gasses on the catalyst particle surface.

It is also important to note the length and morphology of the CNTs. In the case of tubes without the pretreatment, a significant degree of twisting and disorder is observed,

and tubes have a wide range of lengths. The tubes resulting from the pretreatment show generally straight morphology and uniform length.

Analysis of SEM images reveal that option (1) is most likely not responsible for the increased diameter control, as large nickel particles are observed in several cases. Assuming that the decomposition rate has slowed due to the presence of hydrogen, the volume of nanotubes which were produced would be smaller. This agrees with results. The shortness of the CNTs produced also support this concept. The slower the hydrocarbons decompose and diffuse on a catalyst particle, the more likely that the tube is to be capped and growth terminated.

5.3 Effect of Soak Time

Altering the soak time showed no trend in CNT diameter statistics. This supports the idea that nanotube nucleation is dependant on the decomposition and diffusion of carbonaceous gasses on catalyst particles. The rate of decomposition is high enough that synthesis of CNTs occurs very rapidly. The quantity of tubes produced in three minutes is visible to the naked eye, but certainly not large enough to be collected. The quantity of tubes generally increased as growth time increased. This result suggests that soak time can be lengthened until complete consumption of catalyst material has occurred.

CNTs produced on the alumina supported iron catalyst system show a trend for a significant increase in overall tube diameter. The increase in tube diameter and the wide distribution rage of diameters is a result of the catalyst itself. The alumina supported iron catalyst system offers no control on the catalyst particle size or position on the substrate.

Additionally, the size of iron particles in the catalyst solution ranges greatly due to aggregation and clustering. Iron particles and particle aggregates were observed to be between 3nm and 500nm in size. The iron particles may behave in a similar manner as the nickel particles at the soak temperature, but the iron particles may already be in large agglomerates, resulting in the large diameter nanotube bundles. Nanotubes produced on the iron catalyst did not exhibit tip growth as the CNTs produced on nickel catalyst did.

Root growth was evident for nanotubes produced on the iron catalyst on silicon substrates. This is most likely due to the interaction between the catalyst material and the substrate. When the catalyst is well anchored to the substrate, CNTs are more likely to exhibit root growth. Conversely, when the catalyst and substrate exhibit a weak connection, CNTs will detach the particle from the substrate and grow with the catalyst at the tube tip.

5.4 Effect of Applied Voltage During CNT Synthesis

The application of a voltage had a very small effect on the CNTs. Local regions of several samples showed some slight alignment, whereas other samples showed an increase in CNT coiling. Analysis of Figure 68A and B shows that even in highly aligned regions, CNT morphology is not ideal. CNTs show a preference towards alignment when the cathode wire is placed above the sample.

Although CNTs grown on nickel catalyst under an applied voltage do not exhibit alignment, they still exhibit traces of interaction with the field. Coiled CNTs were rarely observed on nickel catalyst particle without the presence of an applied voltage. In fact,

coiled CNTs observed on nickel catalyst only occurred under the influence of an applied voltage or with the use of acetylene gas. The lack of CNT alignment in nickel catalyst systems may be due in part to the growth mechanism. CNTs on nickel catalyst exhibit tip growth, which implies that in order for tube growth to continue, carbon atoms must diffuse through the exposed Ni particle. For the case of the iron catalyst, the catalyst particle remains anchored to the substrate and after nucleation of the tube begins. Carbon atoms have no interaction with the iron particle after completing the nucleation process, and only interact with other carbon atoms on the body of the tube.

CNTs grown with acetylene gas rather than ethylene showed a much higher tendency to coil under the influence of an applied field. Acetylene gas decomposes at a significantly higher rate than ether methane or ethylene because it is much lass stable at high temperatures. CNT coils most likely occur because of a rapid diffusion of carbon atoms on catalyst particle, resulting in an increased CNT growth rate. The applied voltage may assist in increasing CNT growth rate, which thus in turn leads to coiling. The regularity of the coiled CNTs is due to the catalyst used, as iron particles show regular coil morphologies compared to coiled CNTs on Nickel particles. While coiled CNTs were produced on both catalysts, the rate of acetylene decomposition on iron may still be higher than on nickel, resulting in a more uniform, regular coil.

This argument may also be applied to the aligned tubes as well. If the rate of decomposition of ethylene and methane is increased, tubes may have a tendency to exhibit alignment. The applied voltage may increase the rate of precursor gas decomposition in both catalyst systems, but only achieve a fast enough rate on the iron catalyst to demonstrate aligned growth.

5.5 Self Aligned Carbon Nanotubes

Using a temperature in between 700°C and 780° in combination with acetylene gas resulted in self aligned CNTs. Only the iron catalyst system yielded CNTs which aligned perpendicular to the substrate. The reason for this may lie in the Iron/Carbon phase diagram (Figure 117). Nanotube alignment occurs near the eutectoid point for this system. This suggests that the solution of iron and carbon that forms preceding CNT growth is close to a eutectoid solution. The key to forming self aligned nanotubes may be linked to the percent of carbon dissolved in the catalyst layer at a specific temperature.

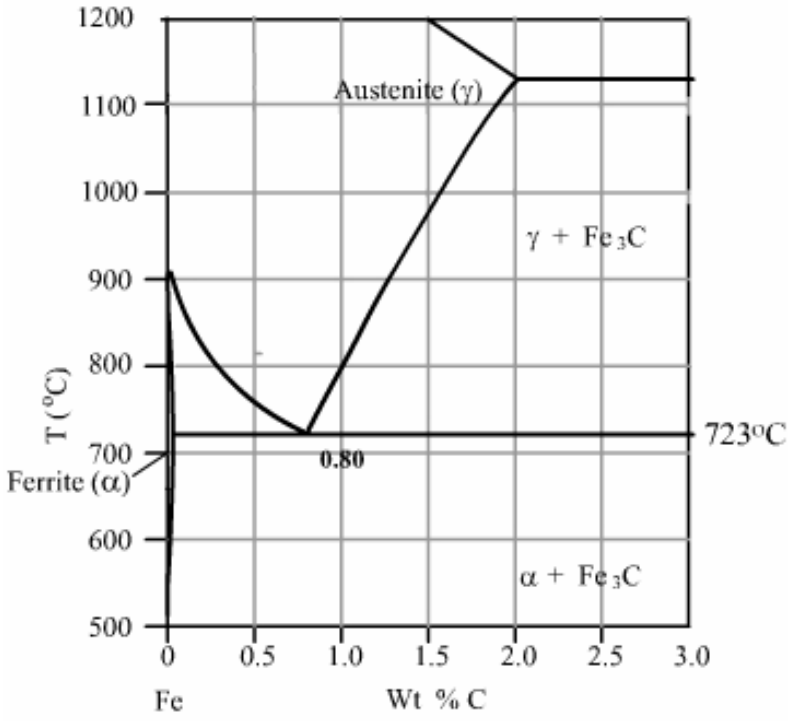

Figure 117: Iron/Carbon Phase Diagram

The unusual shapes which were seen form as a result of catalyst application. Drying the liquid alumina supported iron catalyst solution with an inert gas spray results in a non-uniform film. Essentially, some of the catalyst dries in a peculiar pattern, and

CNTs nucleate and grow in structures which follow the shape of the pattern. The wave like morphology of the aligned CNTs seems to be unaffected by an applied DC voltage. The distance between the wave peaks is smaller when under an applied field of any strength. It is a possibility that the CNT waves are affected by an alternating current voltage which may be remnant from the sourcemeter converting of the incoming voltage from the wall receptacle. If this is true, it suggests that CNT morphology may be controlled by an alternating current voltage.

5.6 Effect of Precursor Gasses and Flow Rates

Using only methane gas (HPCNT recipe) drastically reduced the volume of nanotubes produced, as well as the length of tubes produced. The absence of ethylene most likely contributes to the low volume of tubes, as ethylene gas has a higher decomposition rate than methane. Since methane is slower to decompose on the nickel catalyst particles, the amount of tubes which nucleate in the soak period is small. Additionally, since carbon atoms must continue to decompose and diffuse on the nickel particle at the tube tip, the CNT growth rate is slow as well, resulting in short tubes. Impurity carbon materials were not found as a result of this recipe. This indicates that methane gas alone does not contribute to the formation of amorphous or graphitic carbon under these synthesis conditions.

Increasing the volume of ethylene gas used in synthesis (UHYCNT recipe) has a few effects on the CNTs produced. While the volume of CNTs increased, the quality of the tubes decreased, and the diameter distribution widened. All these are a direct result of the fast decomposition rate of ethylene gas. CNT nucleation and growth have

increased radically, and a downside of this is a buildup of impurity carbon materials. Replacing the ethylene gas with acetylene increases the volume of nanotubes even more, and results in some of the largest diameter bundled CNTs. The amount of amorphous materials present when using acetylene gas was much lower than with ethylene.

5.7 Effect of Synthesis Temperature

As mentioned in section 4.7, CNTs produced from the Ni/IPA catalyst system result is an extraordinarily large volume compared to other catalyst systems/recipe combinations. As the soak temperature increased, the diameter distribution become narrow and shifted significantly towards smaller values. At low temperatures, individual catalyst particles remain isolated from one another, and tube nucleation and growth occur on a wide range of catalyst sizes.

As temperature is increased to 700°C, the nickel particles begin to form larger agglomerates at the expense of smaller particles (Figure 92). However, nucleation manages to occur only on some small particles before they are consumed into a larger cluster. This results in a much lower average diameter and a significantly low volume of CNTs. At 800°C, large nickel agglomerates form before precursor gasses can initiate nucleation of tubes, explaining both the large nickel particles observed in Figure 93, as well as the lack of CNTs for the entire sample.

When the synthesis temperature reaches 900°C, agglomerates have formed a bulk nickel solid, which behaves with bulk properties similar to the patterned nickel film. Here, the bulk nickel forms a wide range of catalyst particles, which in turn nucleate a wide diameter range of CNTs.

5.8 Effect of Synthesis Temperature Using Acetylene Gas

The quantity of CNTs produced with the acetylene gas at low synthesis temperatures is remarkably higher than before. Again, as the soak temperature increased, the diameter distribution become narrow and shifted significantly towards smaller values. However, the amount of impurity carbon material increased significantly, while the quantity of CNTs dropped.

At 800°C, CNTs were present, unlike when using ethylene gas. However, raising the temperature to 900°C resulted in no CNTs but nearly 100% impurity carbon material. This suggests that each gas interacts with the catalyst differently. The formation of a solid solution on the nickel catalyst particles which is necessary for CNT nucleation has a dependence on the hydrocarbon gas.

When a voltage was applied to the CVD furnace during synthesis there was a notable increase the in amount of coiled CNTs at 500°C. This is most likely due to an increased growth rate of the CNTs. Again, it may be that the applied voltage is increasing the rate of acetylene decomposition, which in turn increases the rate at which carbon atoms saturate the catalyst. This results in a faster CNT growth rate which in turn leads to coiling.

5.9 Macro Scale Results

Clearly the exclusive use of ethylene gas at 700°C results in a larger amount of CNTs on the bulk nickel film patterns. This again is due to the rate of decomposition of the gas. Since ethylene rapidly decomposes on nickel particles at this temperature, the

amount of tubes which nucleate increases significantly. This suggests that increasing the deposition time will result in production of CNTs until all of the available catalyst material is consumed and encapsulated within the CNTs.

For CNTs produced on the nickel patterns, the fact that nanotube growth is more dense in some regions is curious. However, the regions where growth is dense are usually in 'open areas' on each pattern. That is, the CNT rich regions occur where no features exist on the pattern. These areas are free surfaces which are likely to have a lower surface energy than features such as corners or edges. These regions of the catalyst film pattern will be the first to experience particle formation. Therefore, CNTs are more likely to nucleate and grow in areas where the nickel is available as particles rather than bulk solids.

5.10 ECDL Supercapacitor Results

Clearly the use of purified CNTs has a profound effect on the performance of the supercapacitors. Purifying the CNTs removes amorphous carbon and other materials which are detrimental to the electrochemical storage of the CNTs. Removing these impurities opens the pore network with bulk CNT films used in the electrodes. Therefore, more ions can be stored by the tubes. It is important to note that the shapes of the CV plots for both the supercapacitors fabricated in this work and the commercially available supercapacitor are similar. The asymmetrical nature of the plots is a result of the pseudocapacitive nature of the supercapacitors. The more rectangular the CV curves become, the more reversible the ion storage is.

Additionally, the molarity of the TEATFB/ACN electrolyte affects the performance of the CNT supercapacitors. When the amount of ions in the electrolyte solution is too low (0.1M), there are simply not enough ions to store as charge. Furthermore, when the molarity of the electrolyte solution is too high (1.5M), there are too many ions overcrowding the CNT pore network, resulting in low ion storage. When the concentration of ions in the electrolyte is 1M, an acceptable number of ions are available to travel freely throughout the pore network, and be stored without interference.

The effect of the sweep rate on the resulting CV plot is drastic. At the faster sweep rate of 0.030V/s, the CV curve is slow to reach its maximum value. The ions cannot easily move throughout the CNT network with a rapidly changing voltage. When the sweep rate is slower (0.015V/s), the ions respond quickly, and are able to penetrate the CNT network rapidly. This results in a more rectangular CV shape, indicating high reversibility.

CHAPTER 6

CONCLUSIONS

The equipment and testing methods used in the present work are well established research methods which have the potential to be implemented in an industrial scale manufacturing process. CNTs represent an interesting class of nanomaterials which have uses in application on the bulk scale, as well as in the nano regime. However, the control over the synthesis of CNTs is currently minimal. The multiplicity of catalyst systems and synthesis methods for CNTs makes it difficult to decide the best route for CNT synthesis.

The goals of the research were (1) to analyze the effect of inherent synthesis conditions on resulting carbon nanotubes, (2) to analyze the effect of external synthesis controls on resulting nanotubes and (3) create and test ECDL supercapacitors based on CNTs and suggest CNT synthesis pathways which may enhance ECDL properties.

The effects of the inherent synthesis conditions such as catalyst, precursor gas, and temperature on CNTs were analyzed. The state of the catalyst material plays an important role in CNT manufacturing. It was observed that by decreasing the thickness of a patterned bulk nickel film, average CNT diameter decreases, but with some degree of variance. Applying other controls, such as a gaseous hydrogen pretreatment of the catalyst before synthesis occurs reduces this variance significantly. Both the nickel and the iron catalyst systems produce a negligible quantity of CNTs for use in bulk applications.

The length of synthesis was evaluated as well. The quantity of CNTs appeared to have increased as time increased, but the diameter and length of CNTs showed no

recognizable pattern. These results show that nucleation and growth of CNTs is a dynamic process occurring through the entirety of the synthesis process, and that CNT diameter is dependant only on the state of the catalyst particles.

Furthermore, synthesis precursor gasses influence CNT physical properties radically. The decomposition rate of various carbonaceous gasses affects the nucleation and growth rate of CNTs, which subsequently effect tube diameter and length. A small number of short, small diameter CNTs can be produced using only the slowly decomposing methane gas. Conversely, a large number of long, variable diameter CNTs can be synthesized with a combination of acetylene, methane and ethylene.

The decomposition rate of the gasses and the nucleation and growth rates of CNTs seem to be slightly effected by an applied DC voltage. This effect is similar to the effects produced by more complex CVD systems, such as PECVD or Microwave CVD. A better relationship between catalyst, applied voltage, synthesis gas and subsequent CNT nucleation and growth rate needs to be established.

The Ni/IPA catalyst system represents a novel way to produce of large quantity of CNTs inexpensively and at low temperature. This makes possible a way to synthesize CNTs on novel substrates, such as aluminum, which cannot withstand typical CVD CNT synthesis temperatures. Additionally, the catalyst system shows promising results for strict diameter control at specific temperatures. Using acetylene gas with CNT synthesis on the Ni/IPA catalyst was able to produce a measurable quantity of CNTs at relatively low temperatures. This is an exciting new catalyst system which needs to be comprehensively studied.

Finally, bulk quantities of CNTs were used as active material in ECDL supercapacitors. The results show that CNT based devices are inevitable as long as processing technology continues to advance. The Ni/IPA catalyst system demonstrates the ability to produce bulk quantities of CNTs at low temperatures. This is especially promising for the possible synthesis of bulk quantities of CNTs directly onto aluminum electrodes for ECDL supercapacitors.

CHAPTER 7

FUTURE WORK

The ability to use CNTs, and other nanomaterials, in nanoscale devices and applications is one of the pressing issues of materials science. Additionally, CNTs are sought after for bulk applications. For nanoscale applications, the combination of top down technologies and bottom up synthesis is necessary for success. For bulk applications, novel, inexpensive manufacturing processes need to be developed such that thousands of kilograms can be economically produced in a week or faster.

New tools such as electron beam lithography are surpassing state of the art substrate design. E-beam lithography has the possibility to pattern specifically shaped and sized catalyst particles. The effect of the surface energy on CNT nucleation, growth, chirality and physical properties should be studied. Figure 118 shows a CNT synthesized between 32nm Nickel dots which were patterned by E-beam lithography.

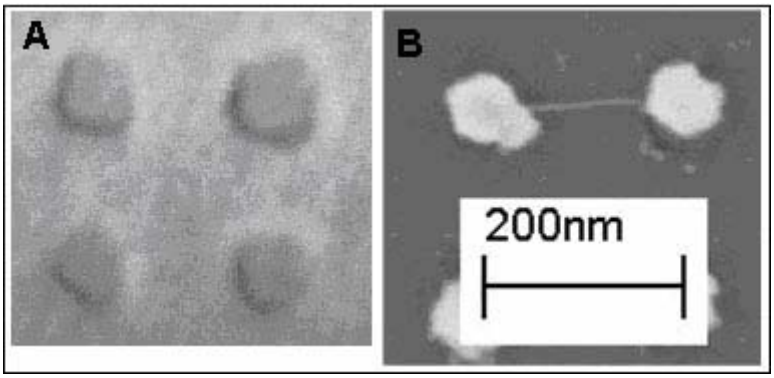

Figure 118: (A) 32 nm Nickel Dots Patterned with E-beam Lithography (B) Single CNT Grown Between 32 nm Nickel Dots

Additionally, the decomposition and diffusion rates of precursor gasses on specific catalyst need to be analyzed in depth in order to exhibit CNT length, diameter, nucleation and growth rate, and alignment control. Factors which enhance decomposition

and diffusion rates of synthesis gasses, such as the effect of an applied electric field need to be further studied. Alternating Current fields should be studied in depth to analyze the effect of frequency, waveform and magnitude on CNT nucleation and growth rates.

The Ni/IPA catalyst system produced the largest quantity of CNTs in this research, and has not been previously investigated. A major drawback of CVD synthesis is the inability to continually introduce new catalyst material to the chamber in a dynamic synthesis process. A new processing technique similar to the HiPCO process should be developed for this catalyst system. The equipment could utilize a spray injection of the liquid catalyst solution into a CVD chamber while simultaneously flowing carbon precursor gasses. A process like this could operate at relatively low temperatures and produced gram or kilogram quantities of CNTs in a short period of time. This low operating temperature CVD, coupled with the inexpensive catalyst provide a reasonable pathway for economical bulk CNT production.

Finally, bulk CNT processing for ECDL supercapacitors electrodes needs to be investigated further. A systematic study of additional binder materials and compatible electrolytes for CNT electrodes needs to be established.

APPENDIX A: COMPREHENSIVE SEM IMAGES FOR DATA ANALYSIS

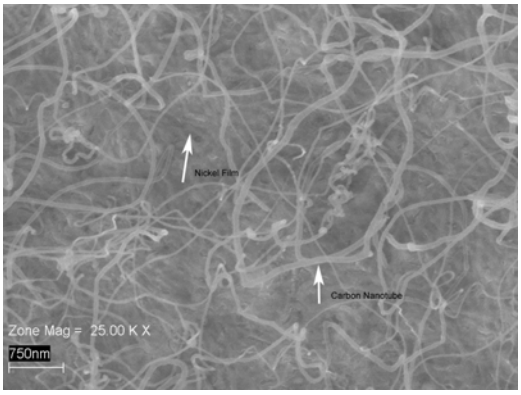

Figure A1: BCNT 100Ni 1

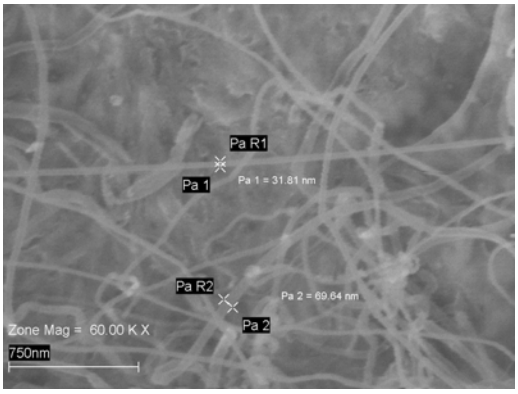

Figure A2: BCNT 100Ni 2

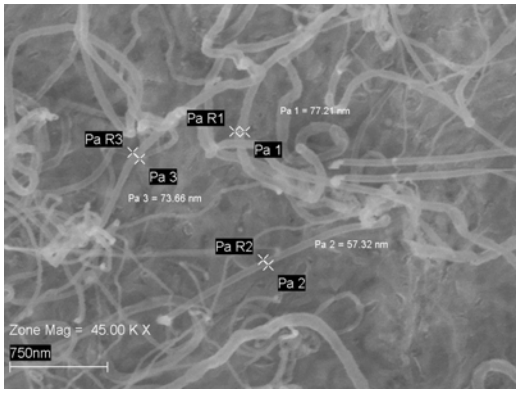

Figure A3: BCNT 100Ni 3

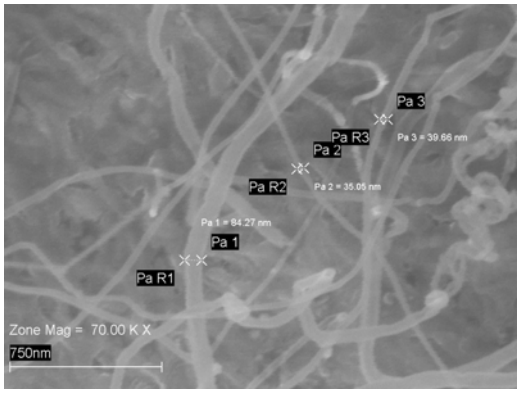

Figure A4: BCNT 100Ni 4

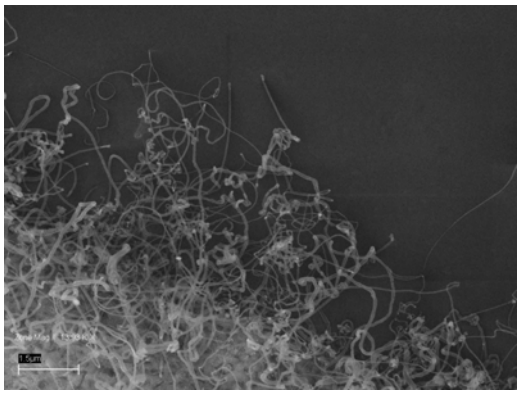

Figure A5: BCNT 100Ni 5

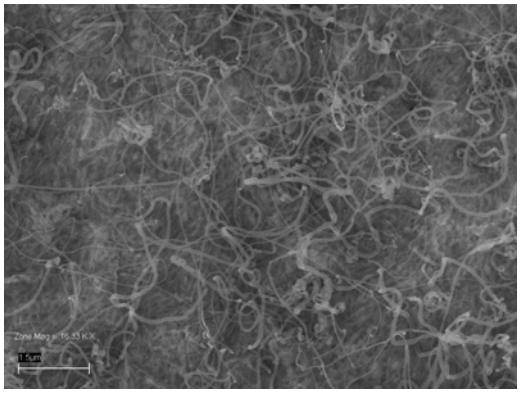

Figure A6: BCNT 100Ni 6

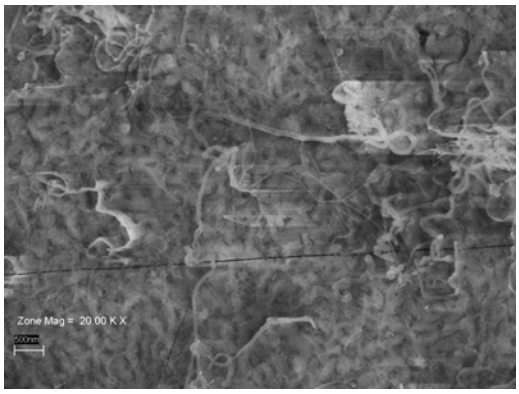

Figure A7: BCNT 100Ni 7

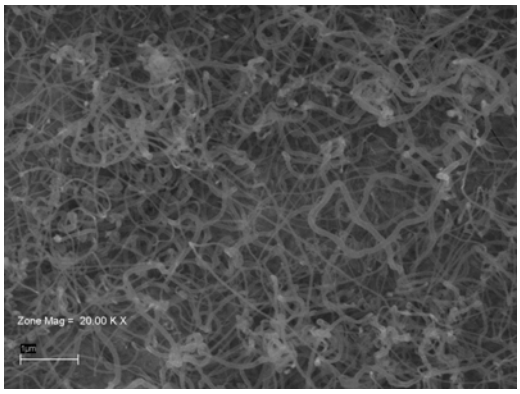

Figure A10: BCNT 100Ni 10

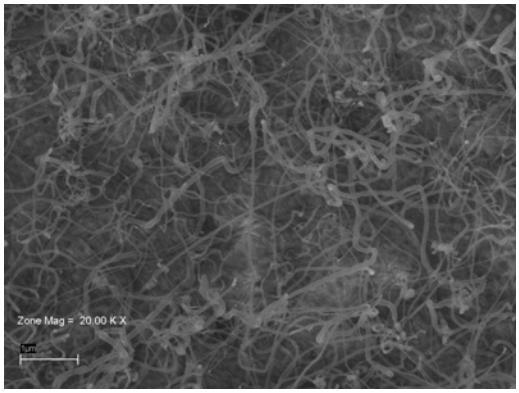

Figure A8: BCNT 100Ni 8

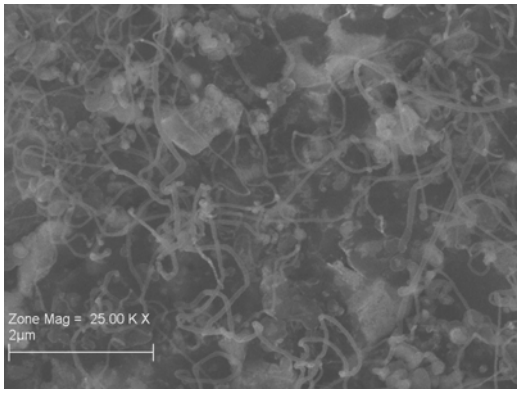

Figure A11: BCNT 80Ni 1

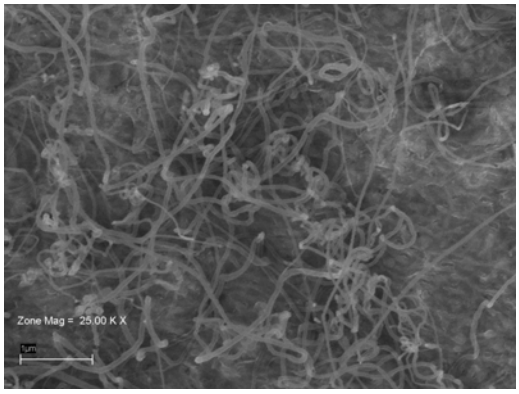

Figure A9: BCNT 100Ni 9

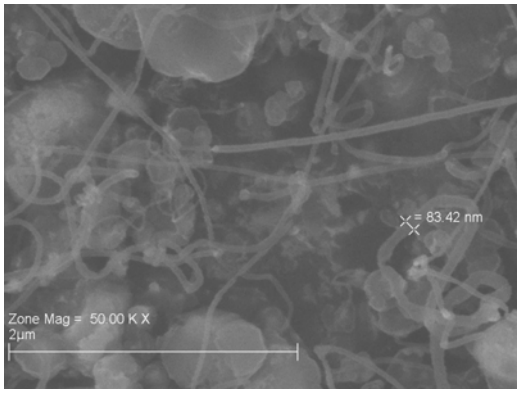

Figure A12: BCNT 80Ni 2

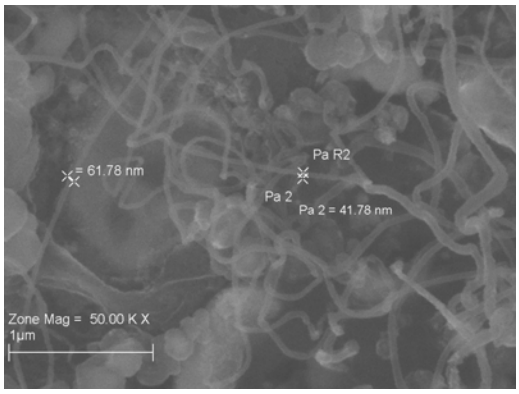

Figure A13: BCNT 80Ni 3

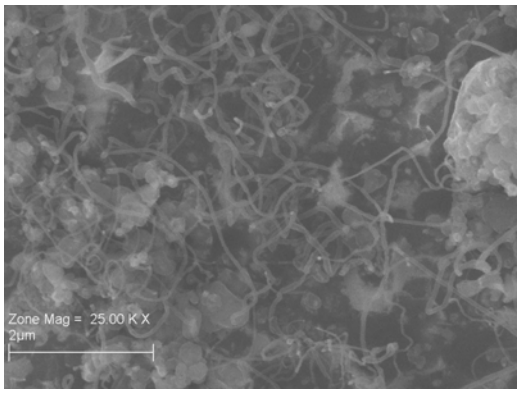

Figure A16: BCNT 80Ni 6

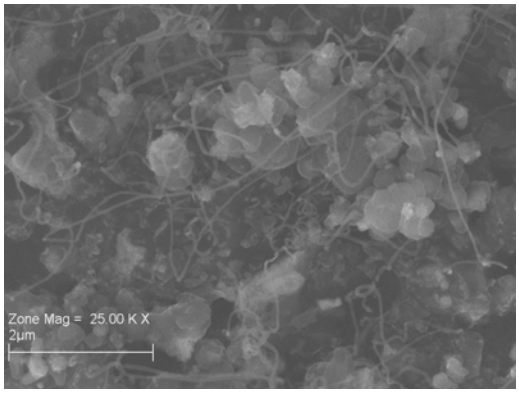

Figure A14: BCNT 80Ni 4

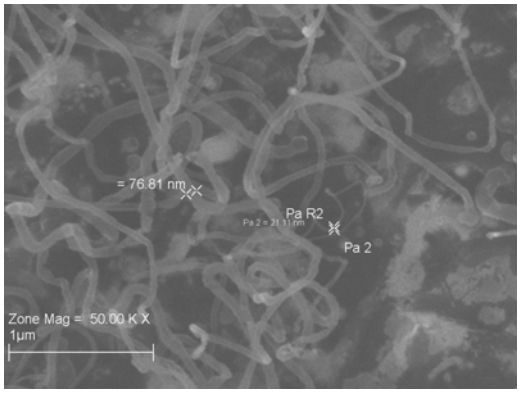

Figure A17: BCNT 80Ni 7

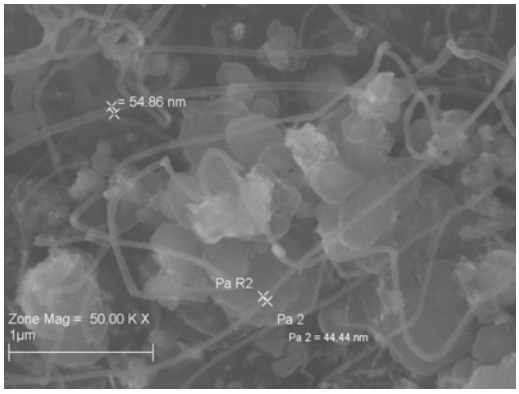

Figure A15: BCNT 80Ni 5

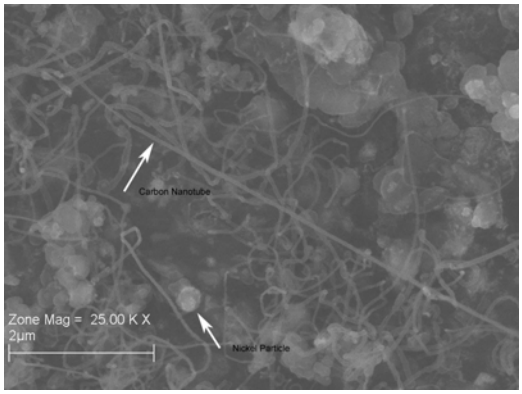

Figure A18: BCNT 80Ni 8

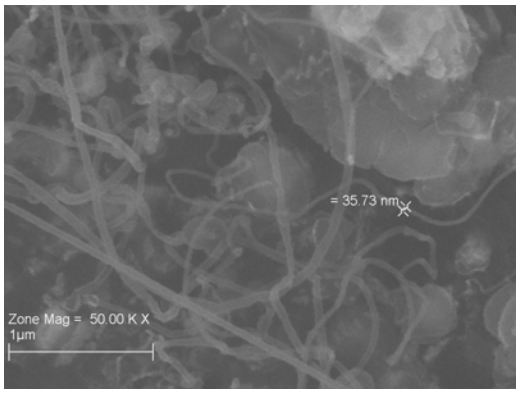

Figure A19: BCNT 80Ni 9

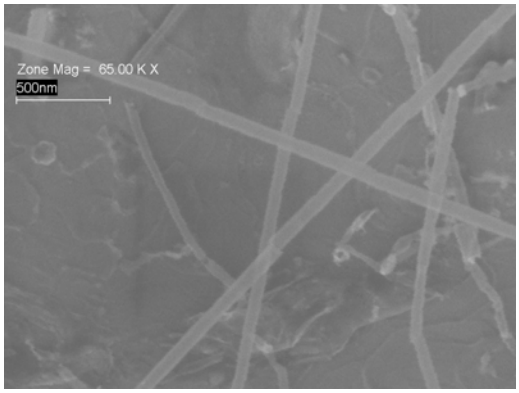

Figure A20: BCNT 80Ni 10

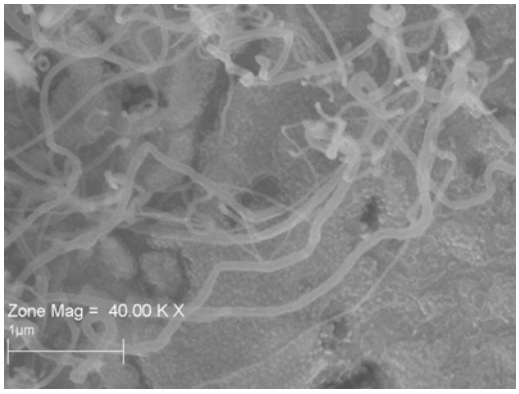

Figure A21: BCNT 60Ni 1

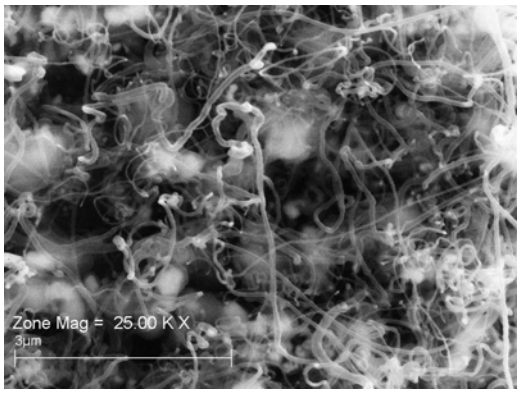

Figure A22: BCNT 60Ni 2

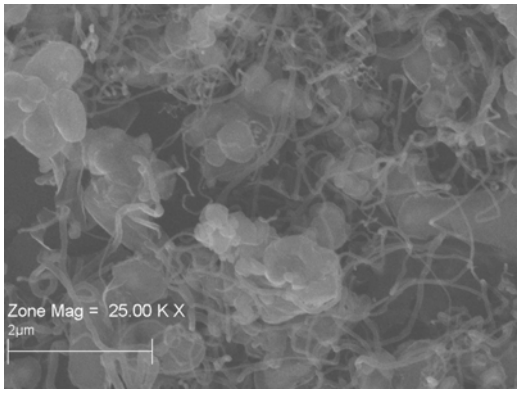

Figure A23: BCNT 60Ni 3

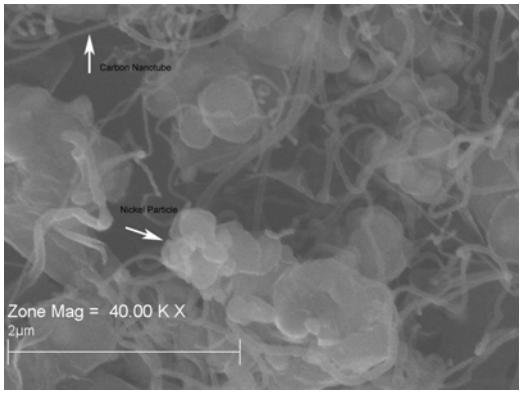

Figure A24: BCNT 60Ni 4

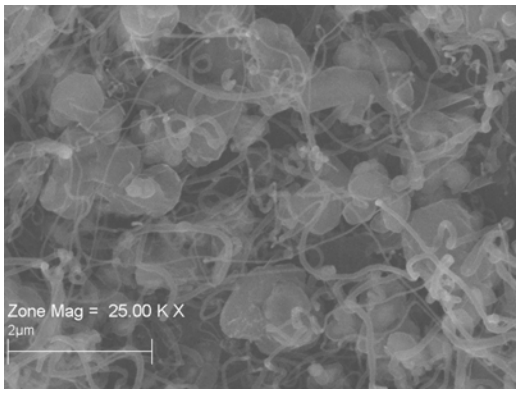

Figure A25: BCNT 60Ni 5

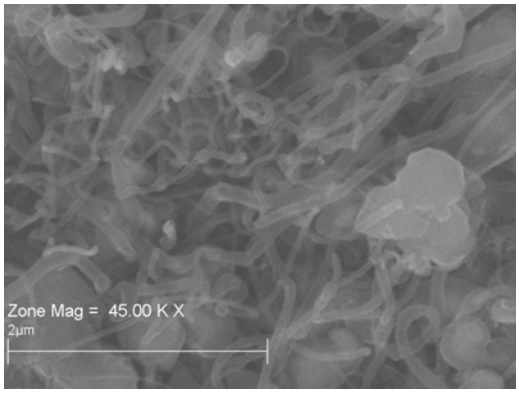

Figure A26: BCNT 60Ni 6

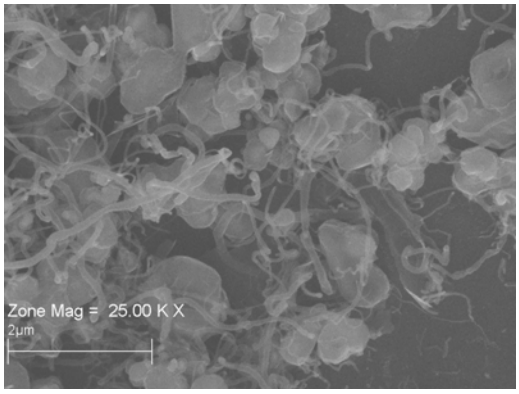

Figure A27: BCNT 60Ni 7

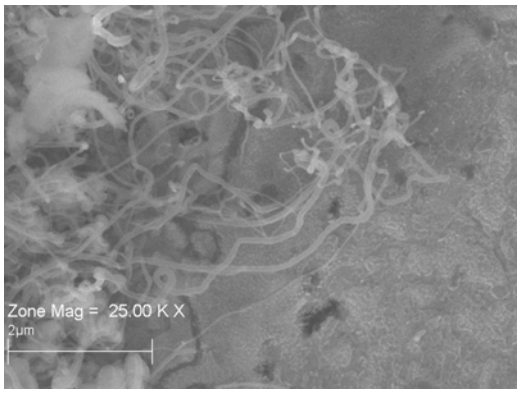

Figure A28: BCNT 60Ni 8

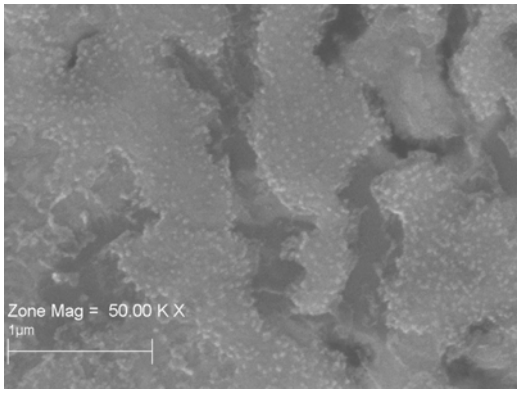

Figure A29: BCNT 60Ni 9

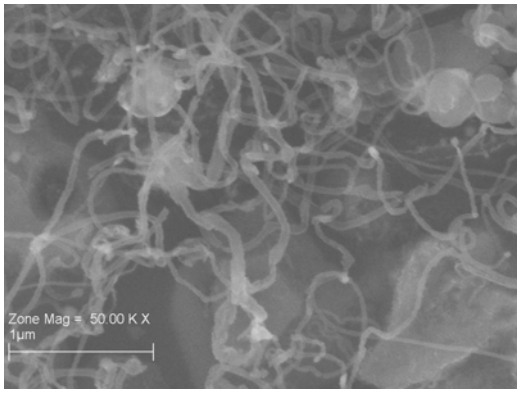

Figure A30: BCNT 60Ni 10

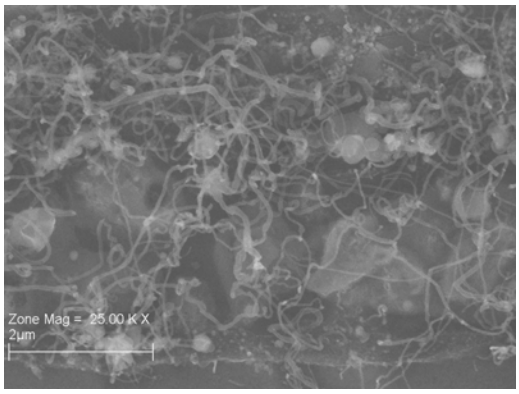

Figure A31: BCNT 60Ni 11

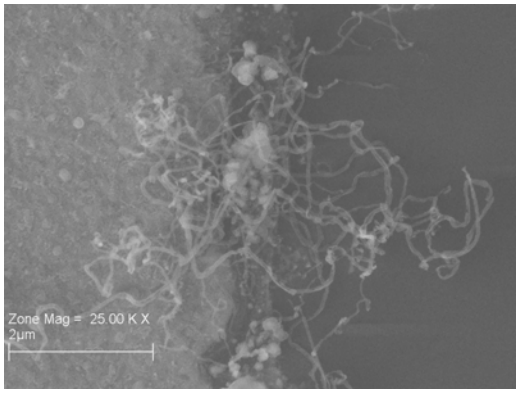

Figure A32: BCNT 60Ni 12

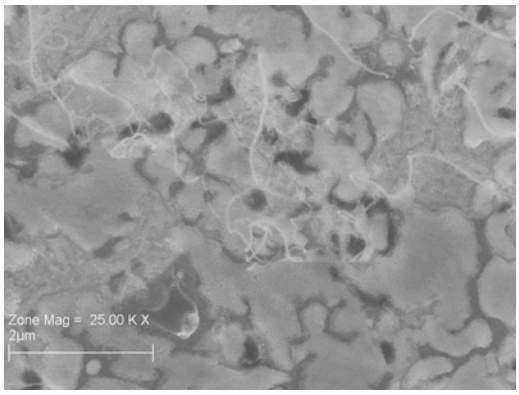

Figure A33: BCNT 60Ni 13

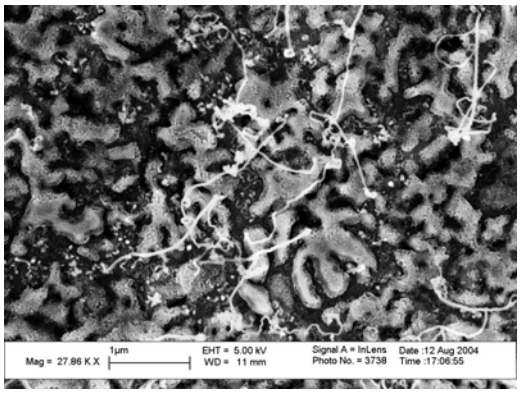

Figure A34: BCNT 40Ni 1

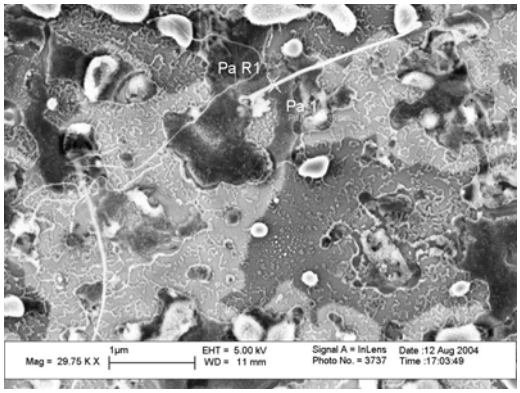

Figure A35: BCNT 40Ni 2

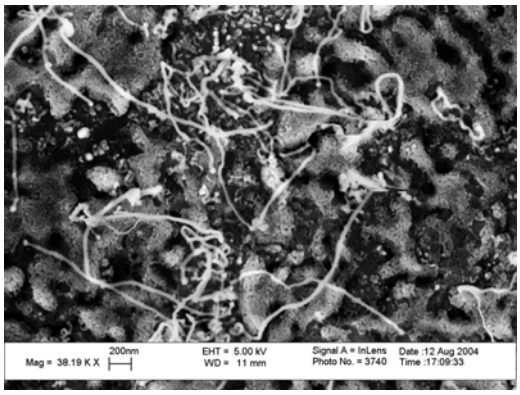

Figure A36: BCNT 40Ni 3

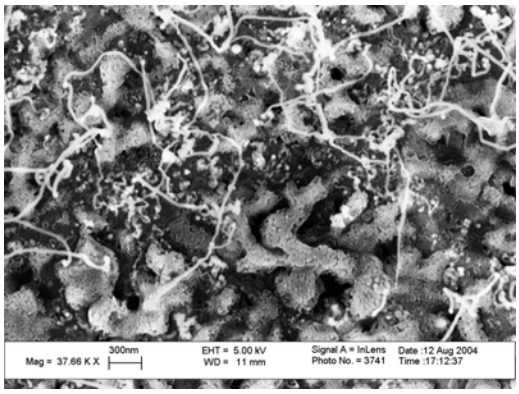

Figure A37: BCNT 40Ni 4

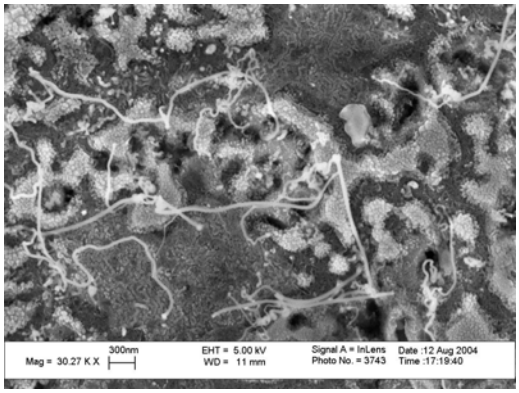

Figure A38: BCNT 40Ni 5

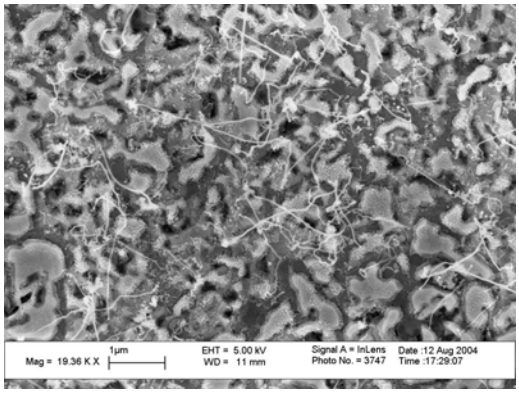

Figure A39: BCNT 40Ni 6

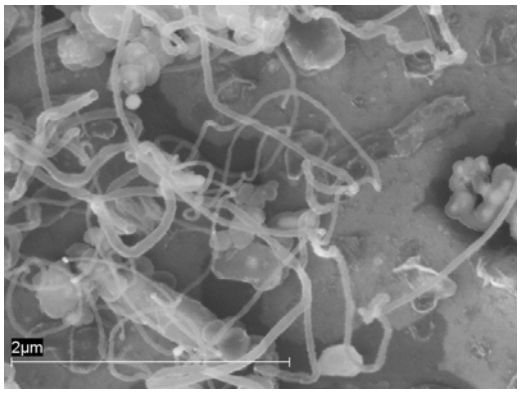

Figure A40: BCNT 40Ni 7

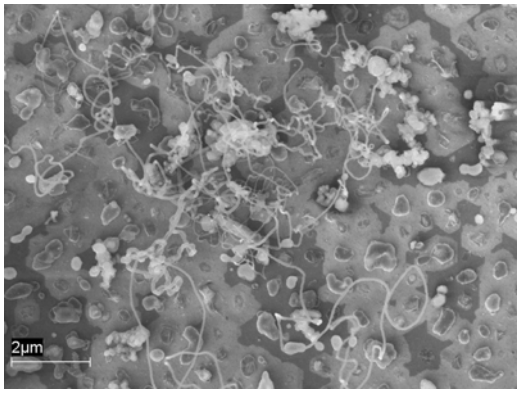

Figure A41: BCNT 40Ni 8

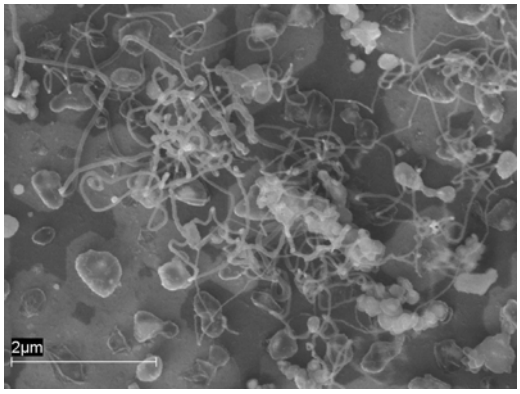

Figure A42: BCNT 40Ni 9

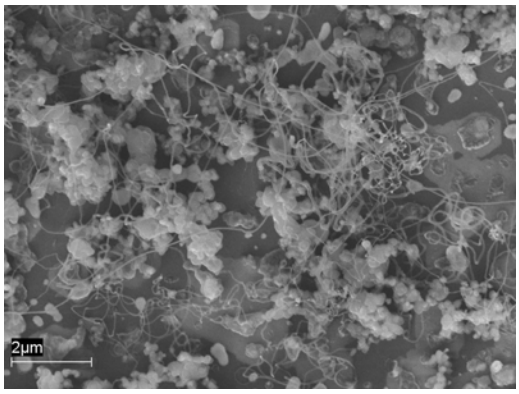

Figure A43: BCNT 40Ni 10

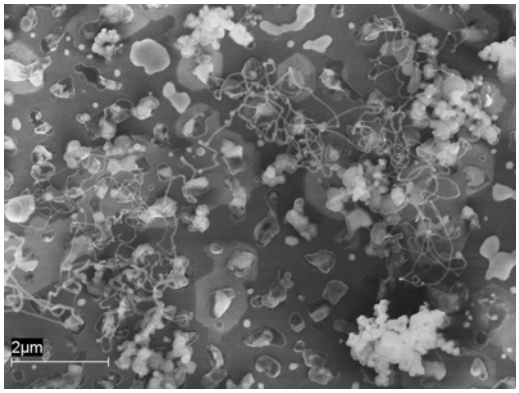

Figure A44: BCNT 40Ni 11

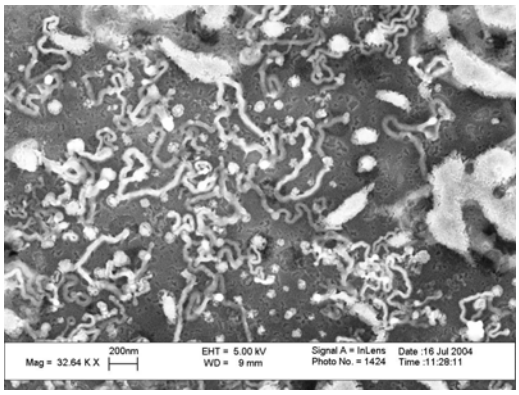

Figure A45: BCNT 20Ni 1

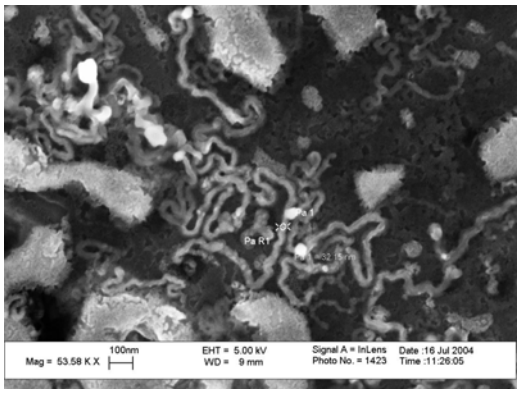

Figure A46: BCNT 20Ni 2

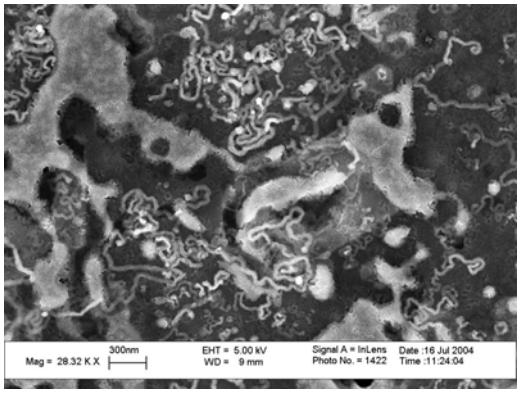

Figure A47: BCNT 20Ni 3

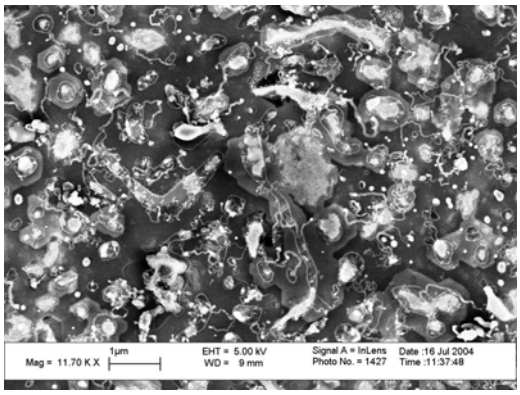

Figure A48: BCNT 20Ni 4

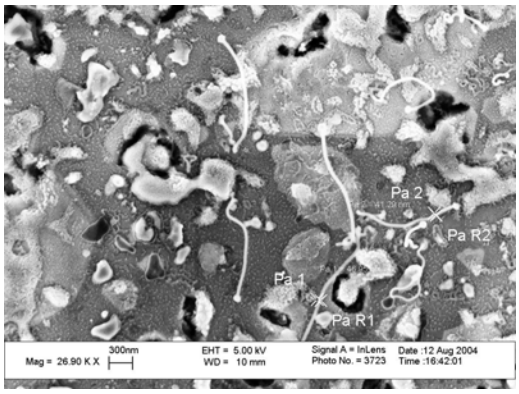

Figure A49: BCNT 20Ni 5

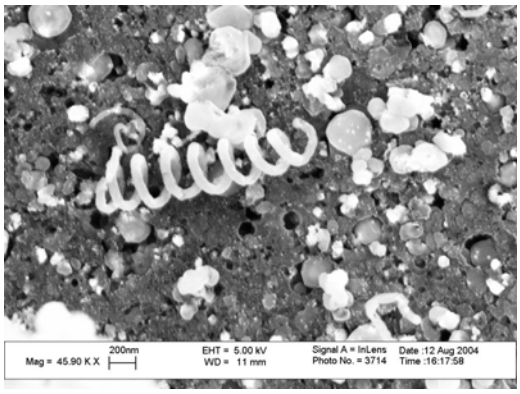

Figure A52: BCNT 20Ni 7

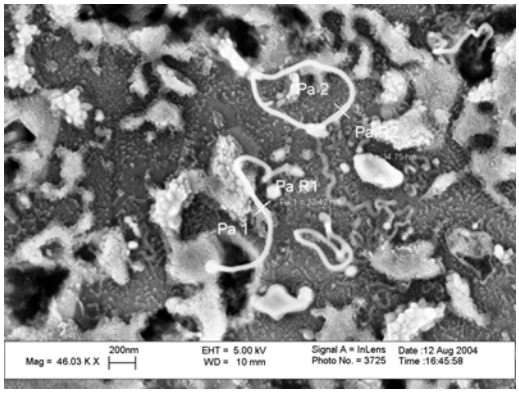

Figure A50: BCNT 20Ni 6

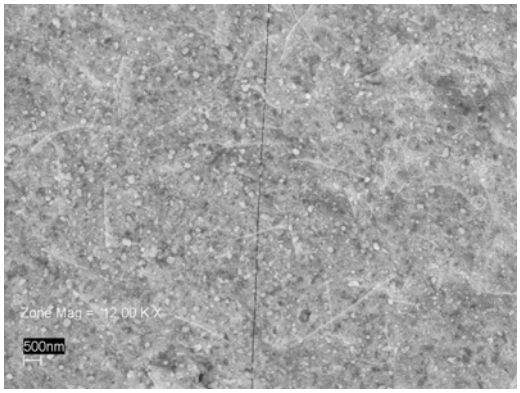

Figure A53: BCNT 5mH 100Ni 1

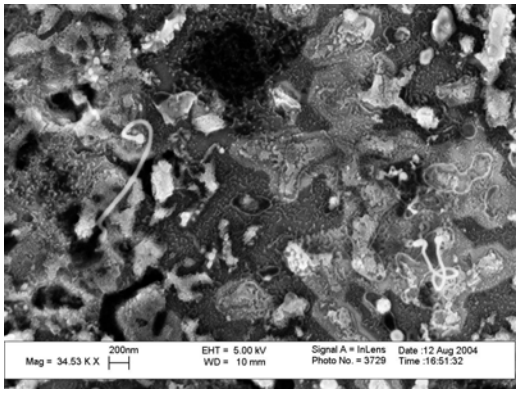

Figure A51: BCNT 20Ni 6

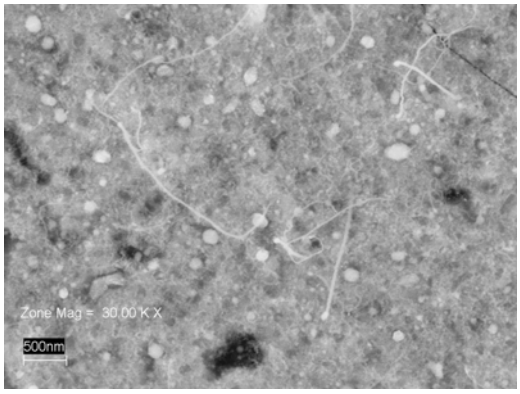

Figure A54: BCNT 5mH 100Ni 2

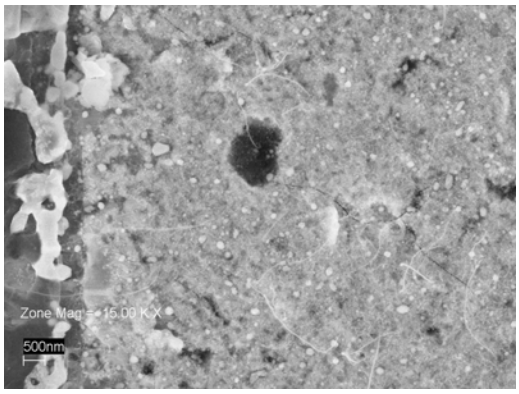

Figure A55: BCNT 5mH 100Ni 3

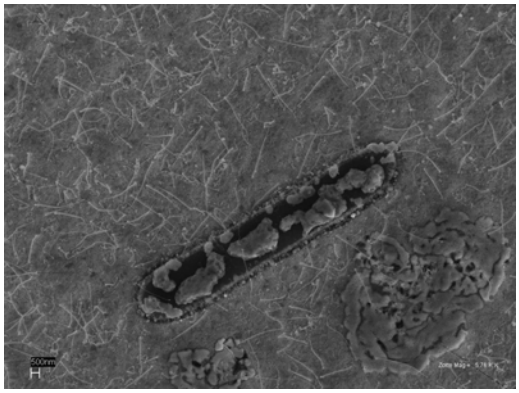

Figure A56: BCNT 5mH 100Ni 4

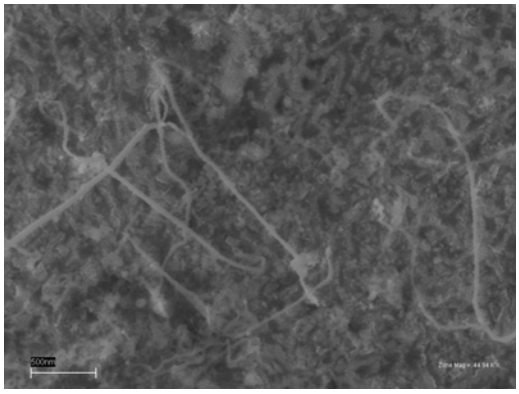

Figure A57: BCNT 5mH 100Ni 5

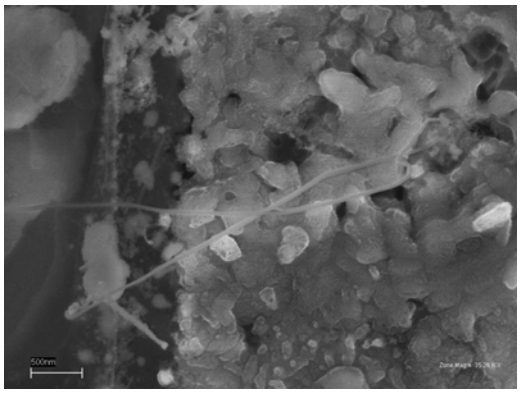

Figure A58: BCNT 5mH 100Ni 6

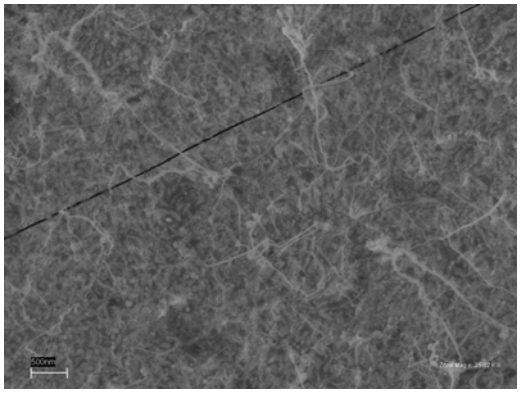

Figure A59: BCNT 5mH 100Ni 7

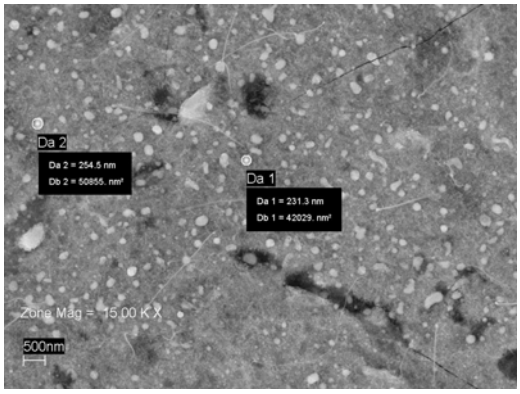

Figure A60: BCNT 5mH 100Ni 8

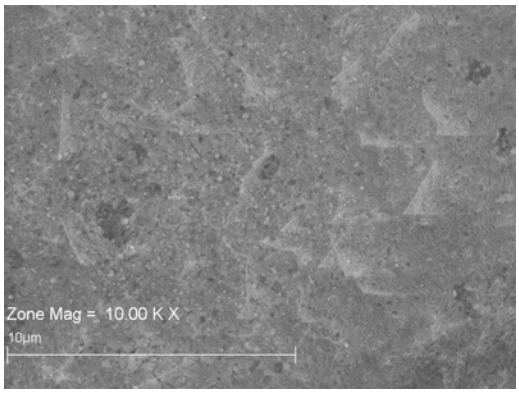

Figure A61: BCNT 5mH 100Ni 9

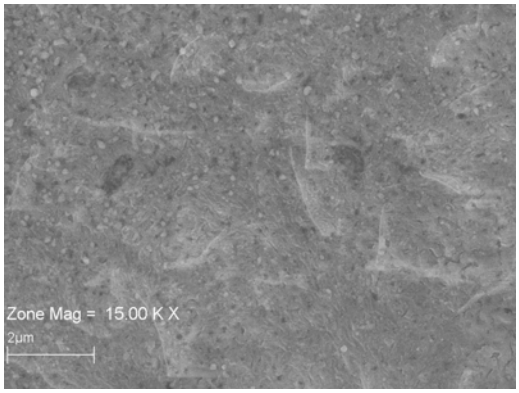

Figure A62: BCNT 5mH 100Ni 10

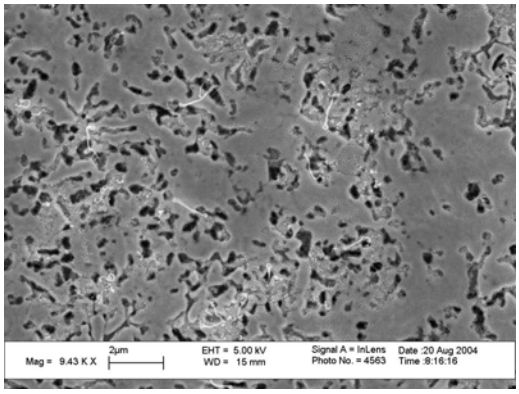

Figure A63: BCNT 5mH 80Ni 1

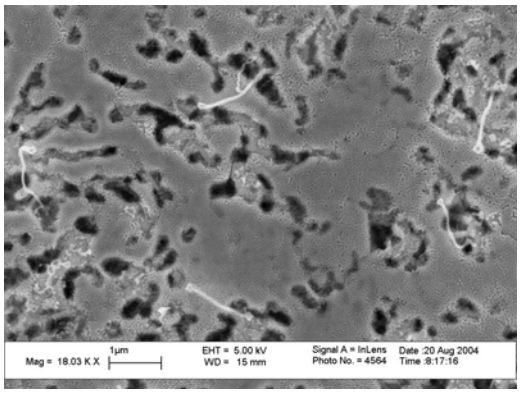

Figure A64: BCNT 5mH 80Ni 2

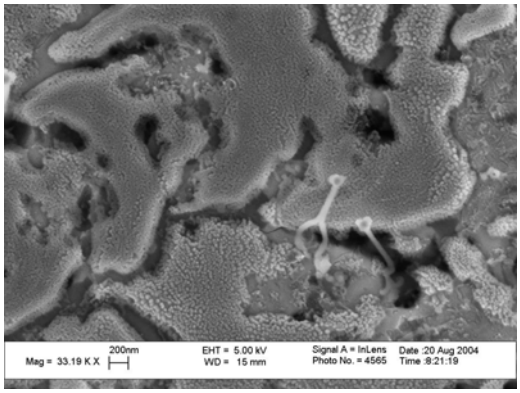

Figure A65: BCNT 5mH 80Ni 3

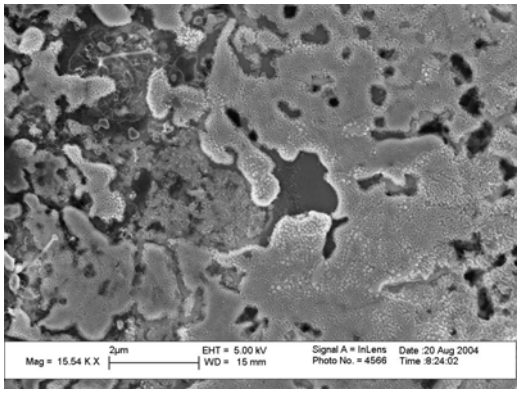

Figure A66: BCNT 5mH 80Ni 4

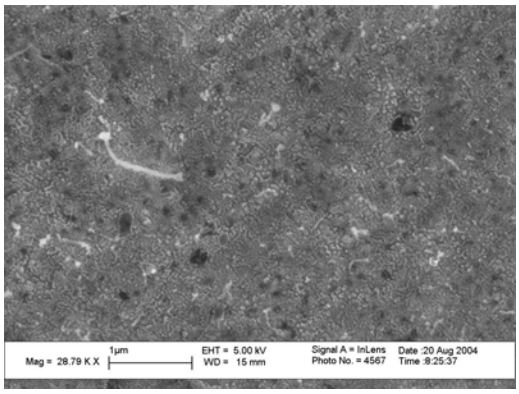

Figure A67: BCNT 5mH 80Ni 5

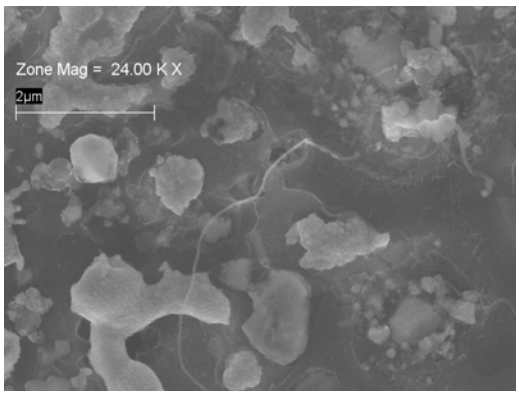

Figure A68: BCNT 5mH 80Ni 6

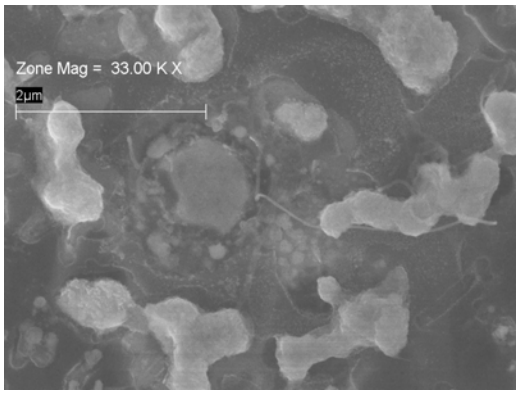

Figure A69: BCNT 5mH 80Ni 7

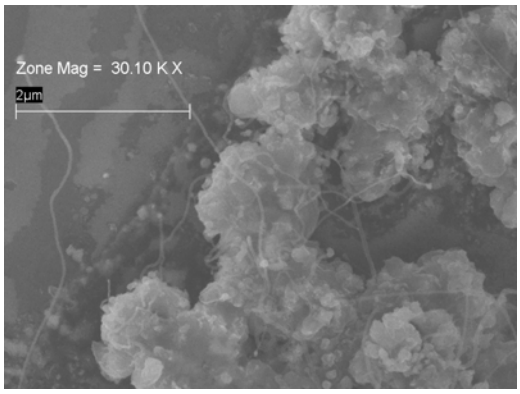

Figure A70: BCNT 5mH 80Ni 8

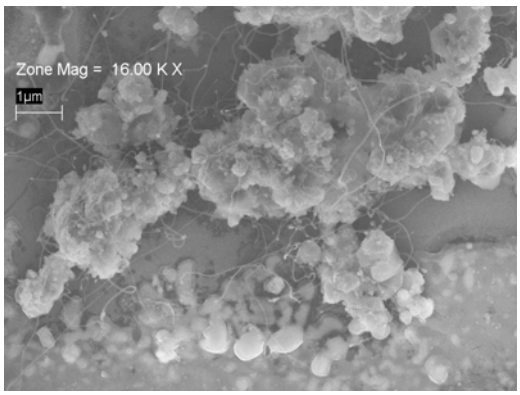

Figure A71: BCNT 5mH 80Ni 9

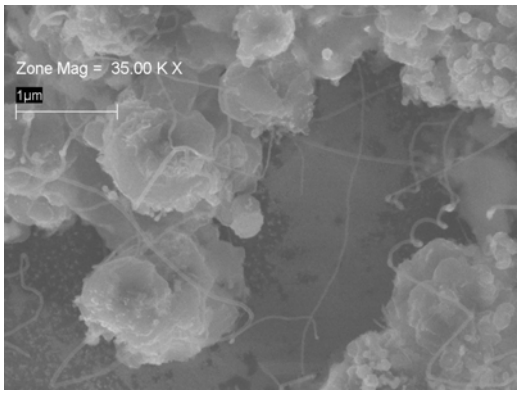

Figure A72: BCNT 5mH 80Ni 10

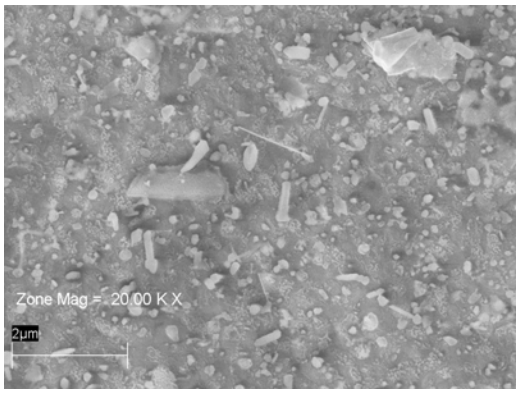

Figure A73: BCNT 5mH 80Ni 11

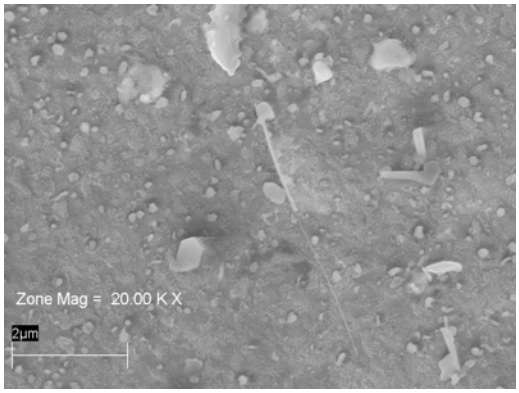

Figure A74: BCNT 5mH 80Ni 12

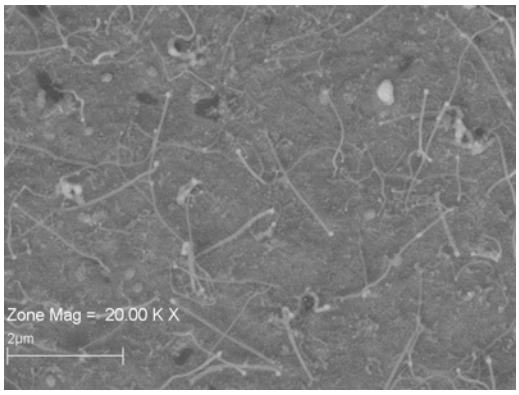

Figure A75: BCNT 5mH 60Ni 1

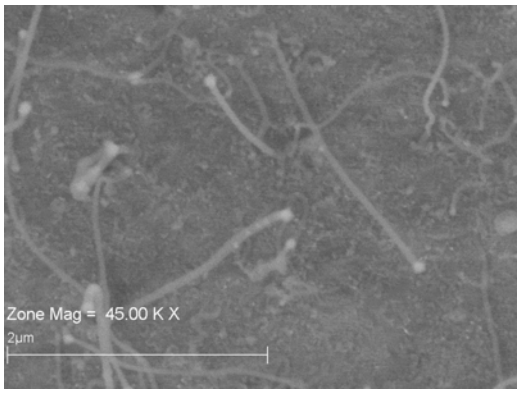

Figure A76: BCNT 5mH 60Ni 2

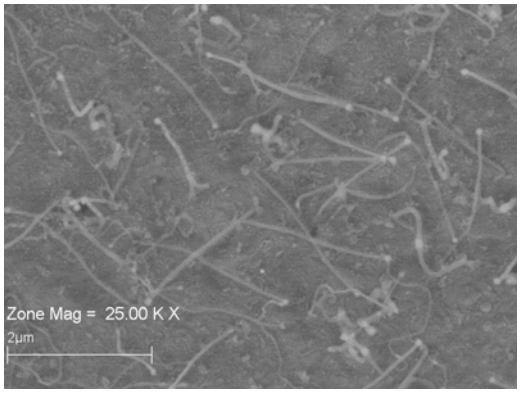

Figure A77: BCNT 5mH 60Ni 3

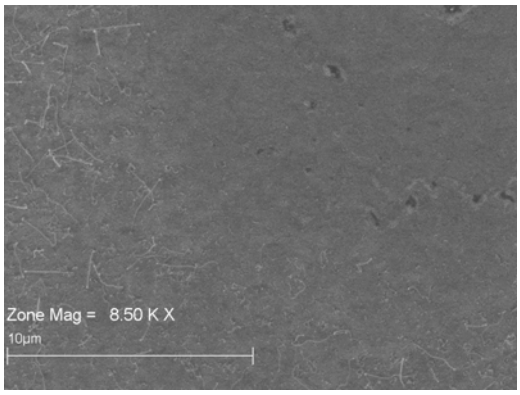

Figure A78: BCNT 5mH 60Ni 4

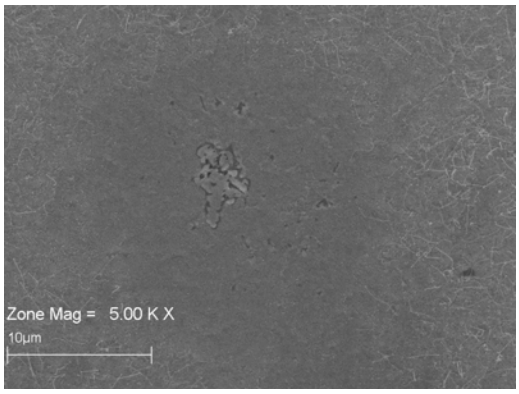

Figure A79: BCNT 5mH 60Ni 5

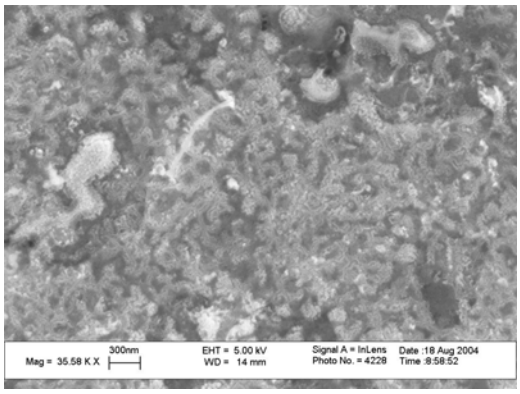

Figure A82: BCNT 5mH 40Ni 1

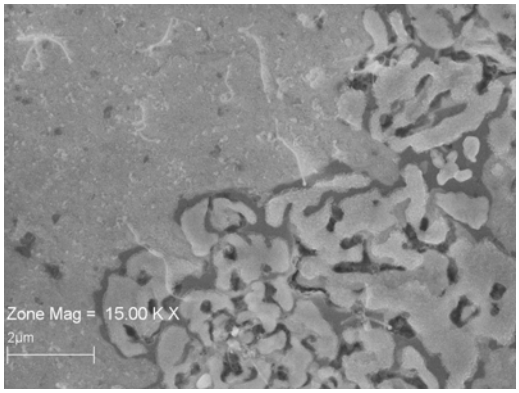

Figure A80: BCNT 5mH 60Ni 6

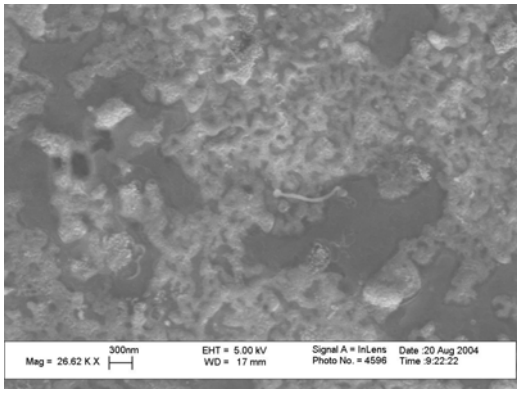

Figure A83: BCNT 5mH 40Ni 2

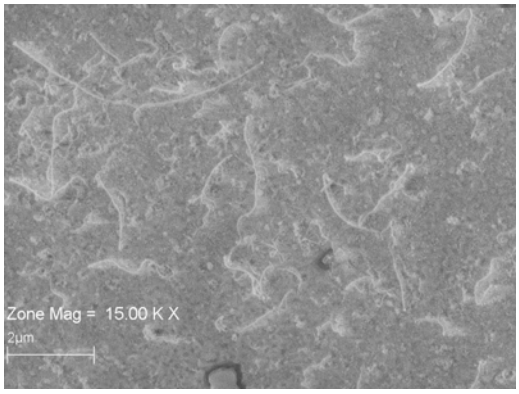

Figure A81: BCNT 5mH 60Ni 7

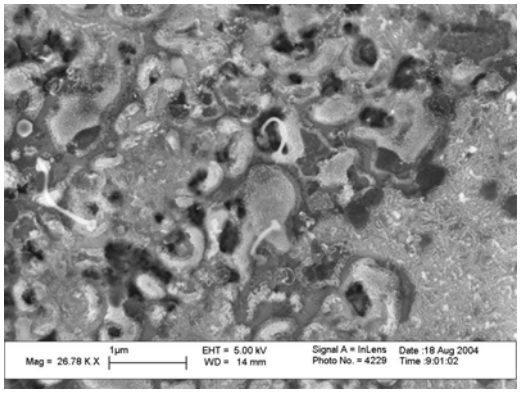

Figure A84: BCNT 5mH 40Ni 3

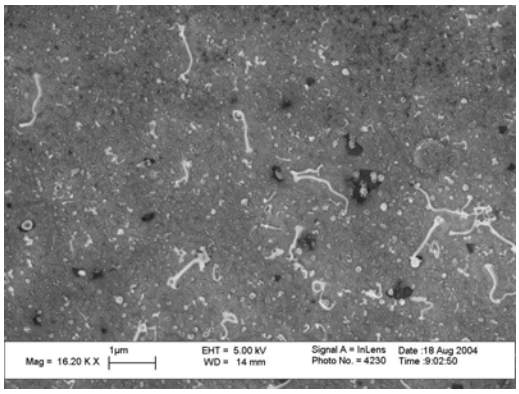

Figure A85: BCNT 5mH 40Ni 4

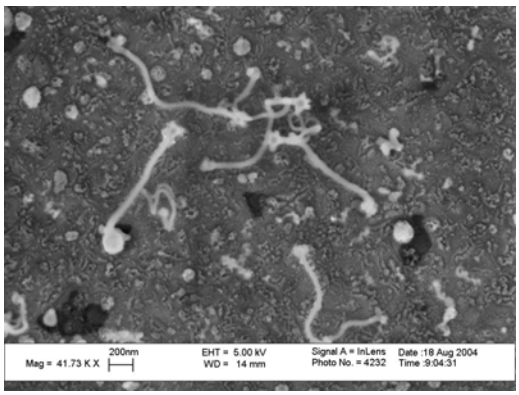

Figure A86: BCNT 5mH 40Ni 5

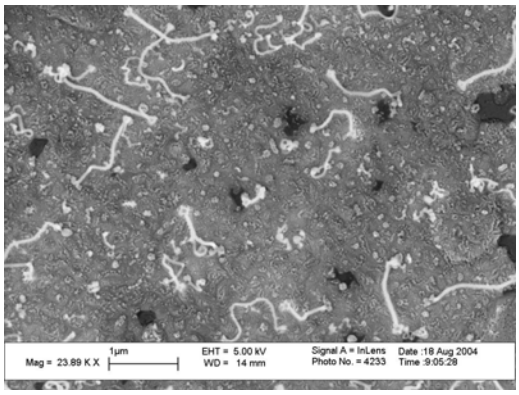

Figure A87: BCNT 5mH 40Ni 6

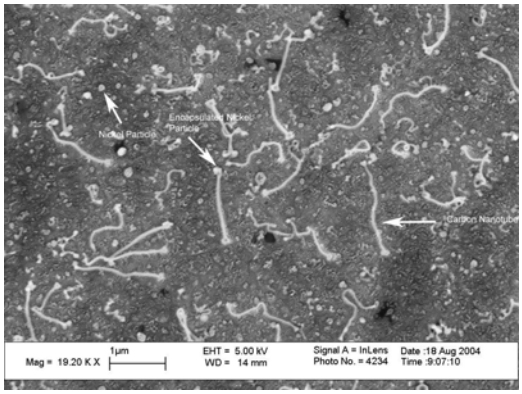

Figure A88: BCNT 5mH 40Ni 7

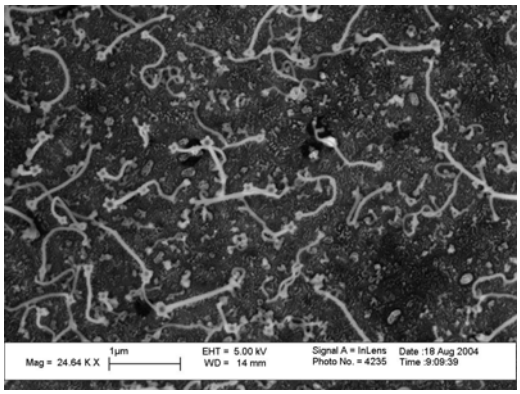

Figure A89: BCNT 5mH 40Ni 8

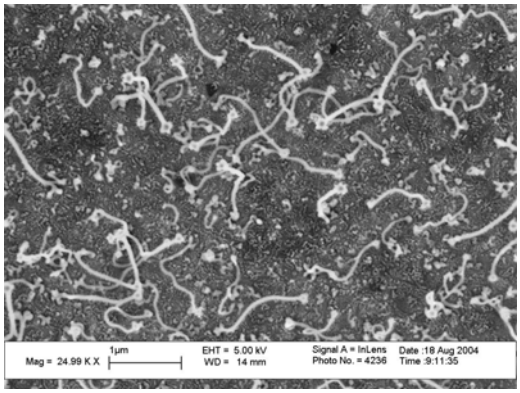

Figure A90: BCNT 5mH 40Ni 9

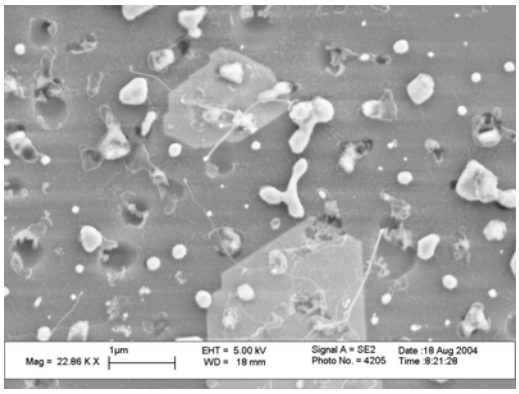

Figure A91: BCNT 5mH 20Ni 1

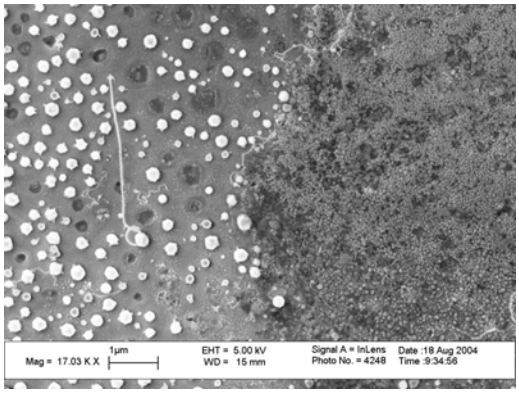

Figure A92: BCNT 5mH 20Ni 2

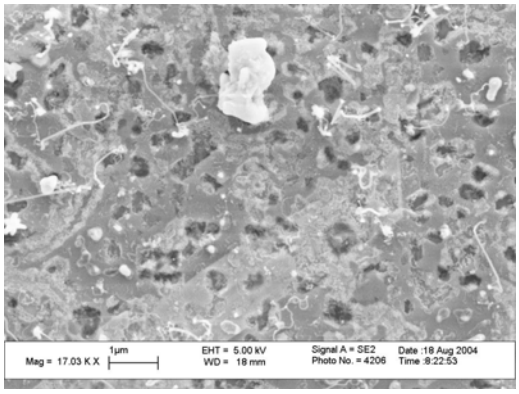

Figure A93: BCNT 5mH 20Ni 3

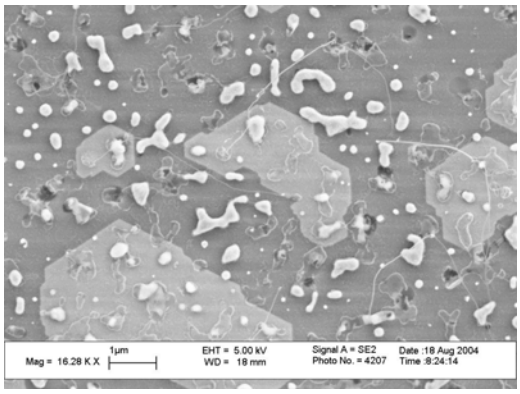

Figure A94: BCNT 5mH 20Ni 4

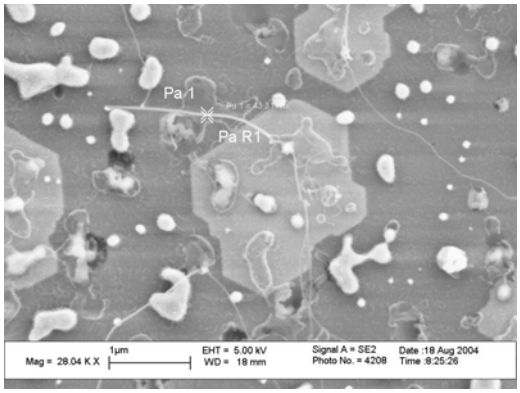

Figure A95: BCNT 5mH 20Ni 5

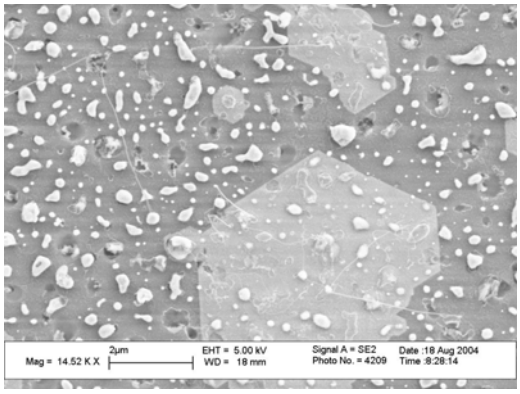

Figure A96: BCNT 5mH 20Ni 6

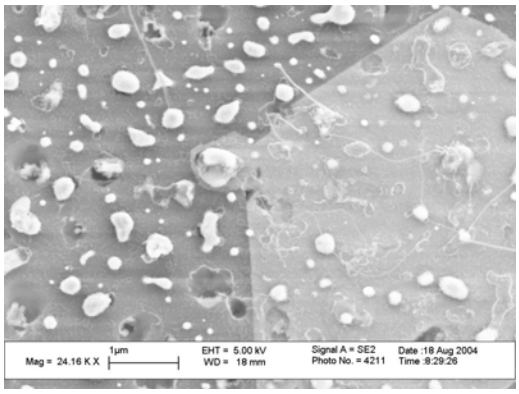

Figure A97: BCNT 5mH 20Ni 7

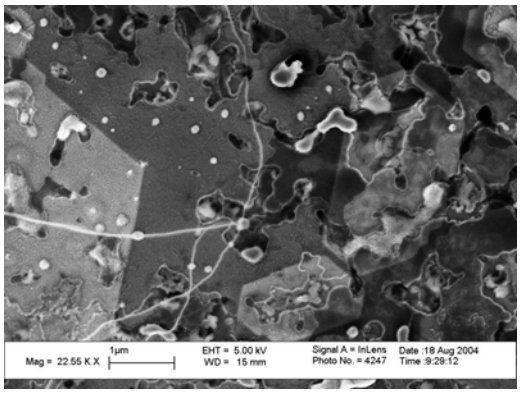

Figure A100: BCNT 5mH 20Ni 10

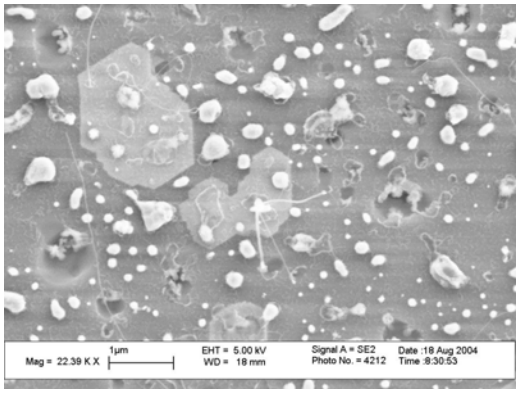

Figure A98: BCNT 5mH 20Ni 8

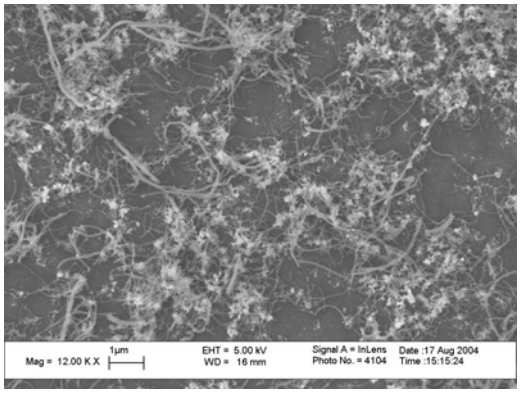

Figure A101: HYCNT ASFe 3m 1

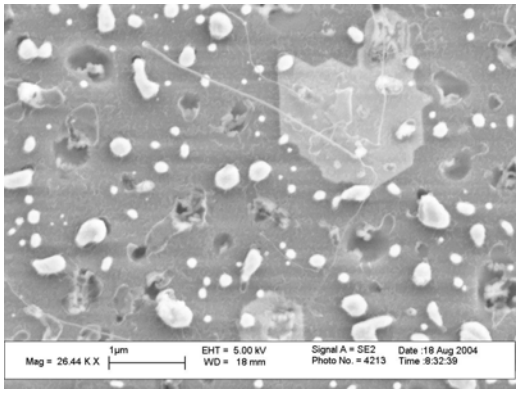

Figure A99: BCNT 5mH 20Ni 9

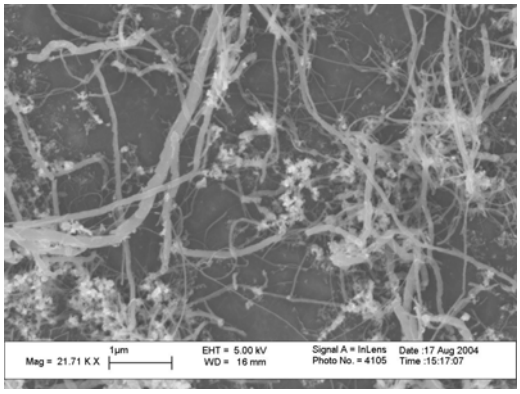

Figure A102: HYCNT ASFe 3m 2

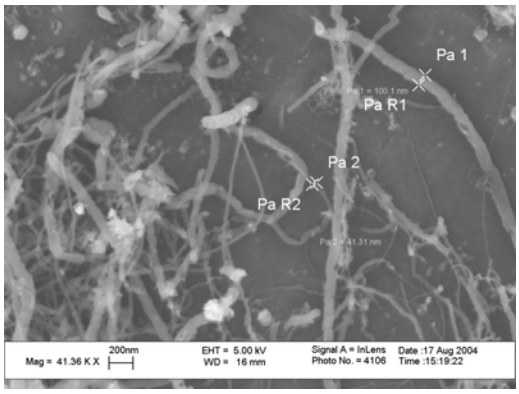

Figure A103: HYCNT ASFe 3m 3

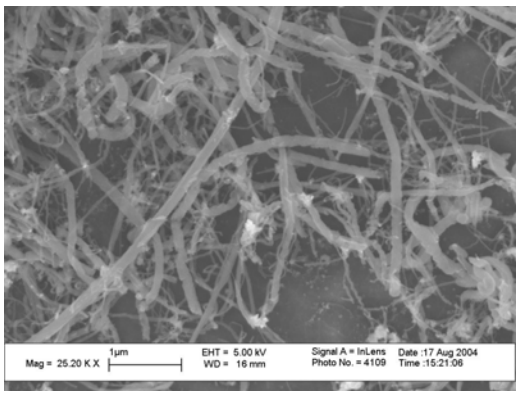

Figure A104: HYCNT ASFe 3m 4

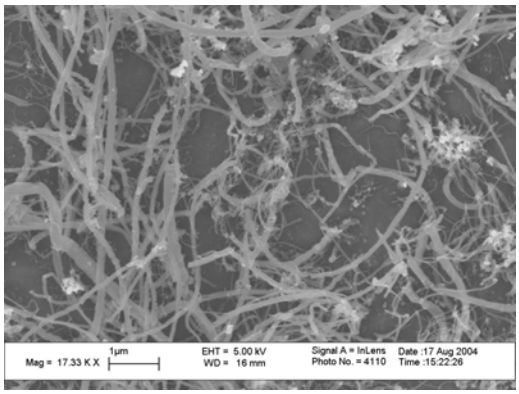

Figure A105: HYCNT ASFe 3m 5

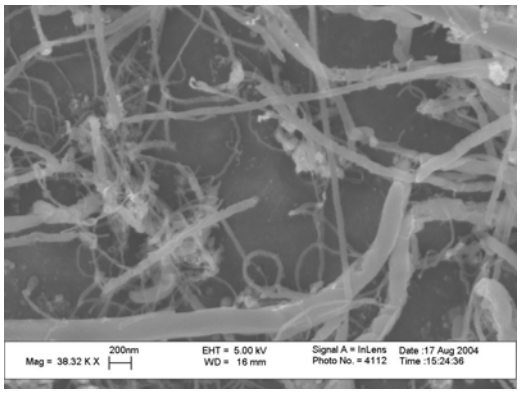

Figure A106: HYCNT ASFe 3m 6

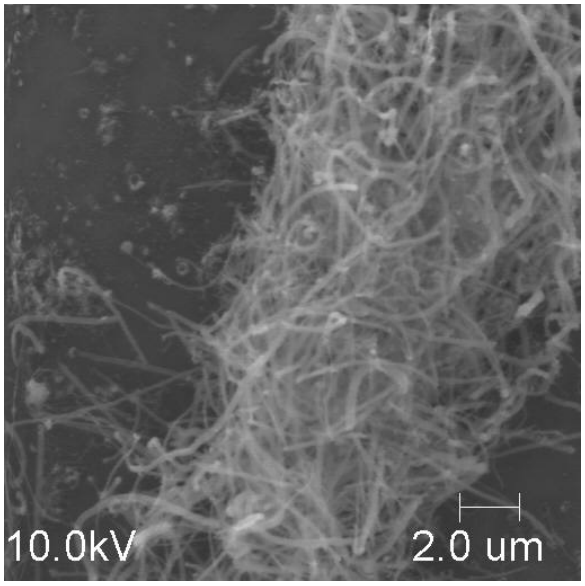

Figure A107: HYCNT ASFe 3m 7

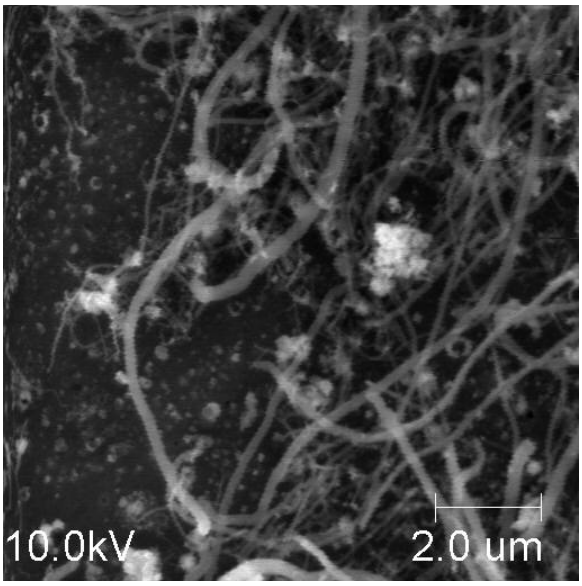

Figure A108: HYCNT ASFe 3m 8

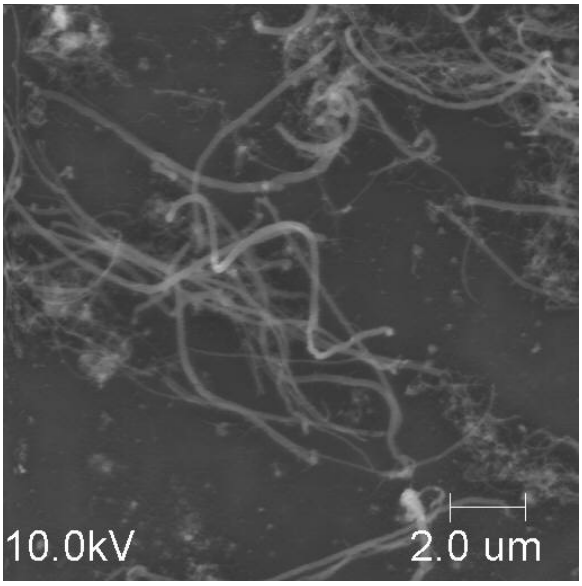

Figure A109: HYCNT ASFe 3m 9

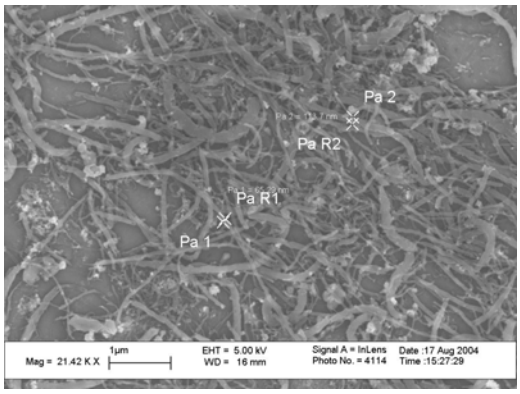

Figure A110: HYCNT ASFe 6m 1

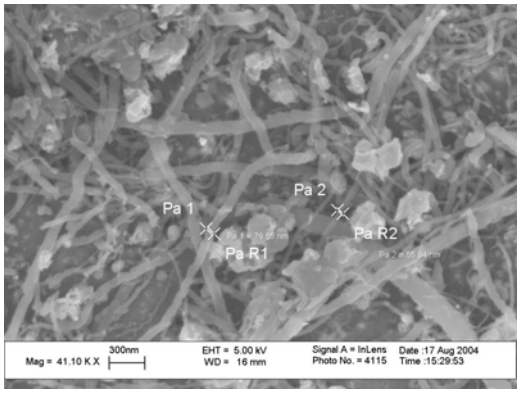

Figure A111: HYCNT ASFe 6m 2

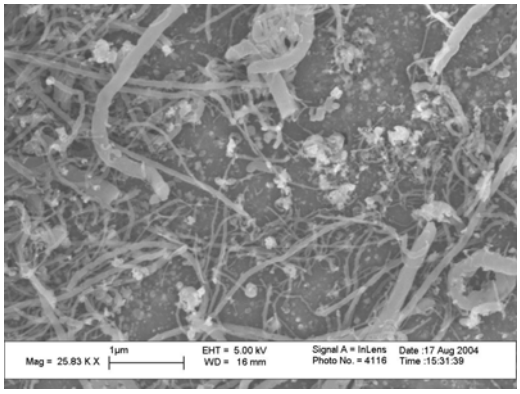

Figure A112: HYCNT ASFe 6m 3

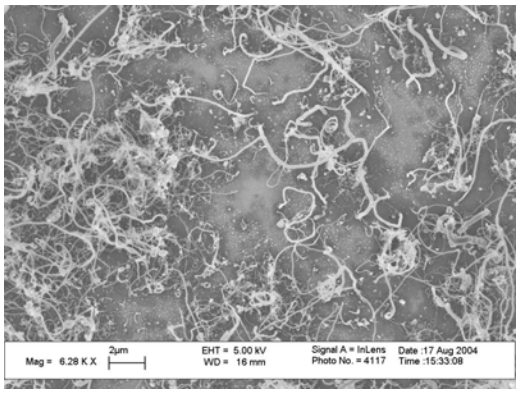

Figure A113: HYCNT ASFe 6m 4

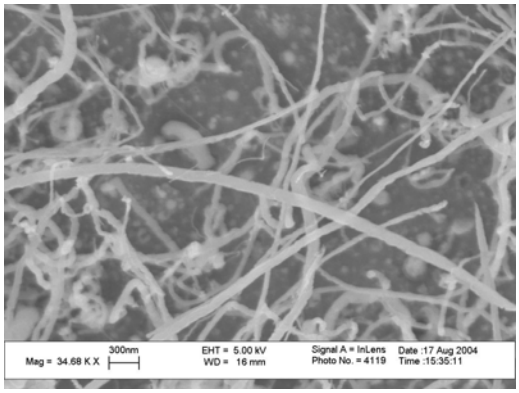

Figure A114: HYCNT ASFe 6m 5

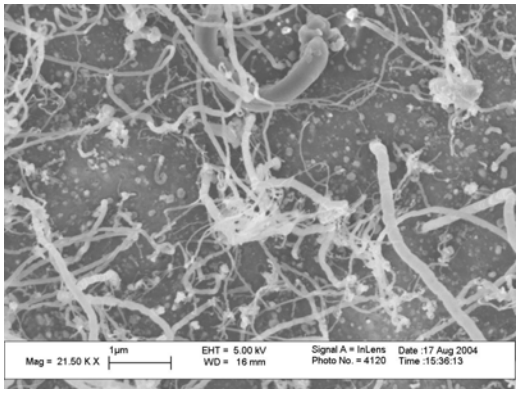

Figure A115: HYCNT ASFe 6m 6

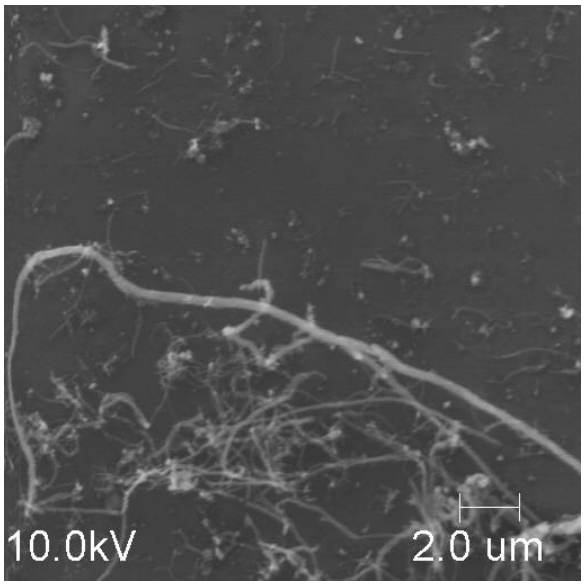

Figure A116: HYCNT ASFe 6m 7

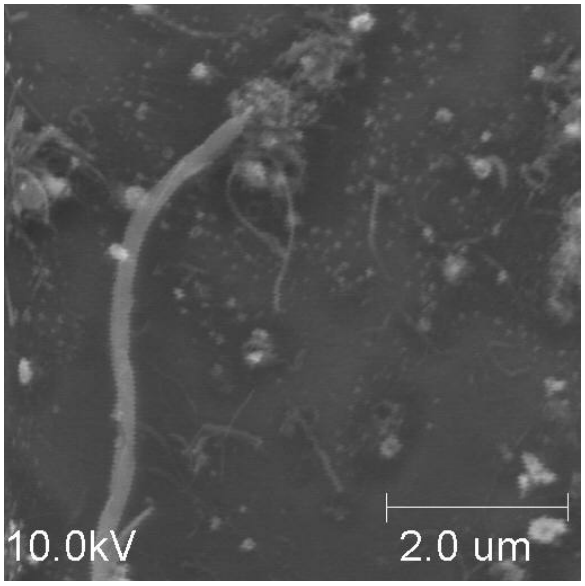

Figure A117: HYCNT ASFe 6m 8

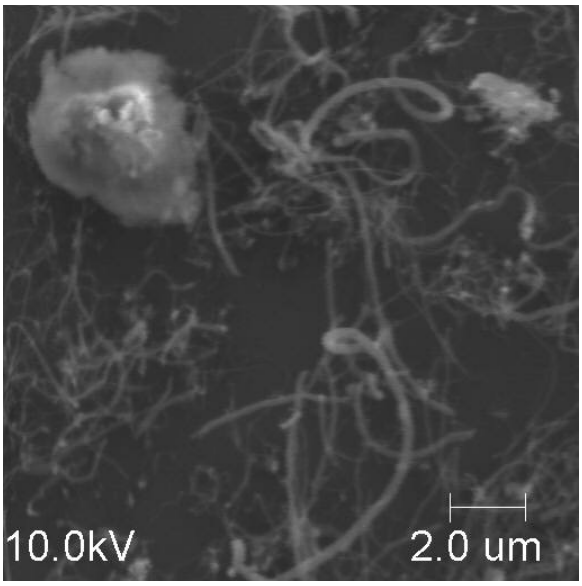

Figure A118: HYCNT ASFe 6m 9

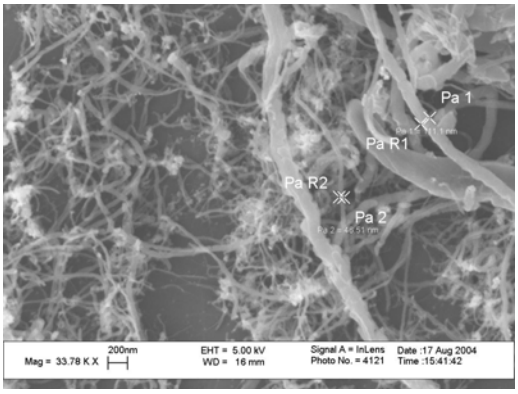

Figure A119: HYCNT ASFe 9m 1

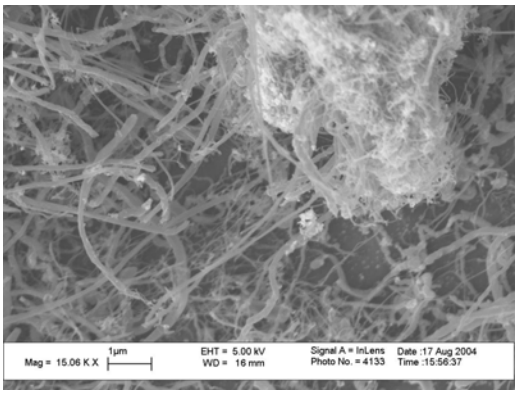

Figure A120: HYCNT ASFe 9m 2

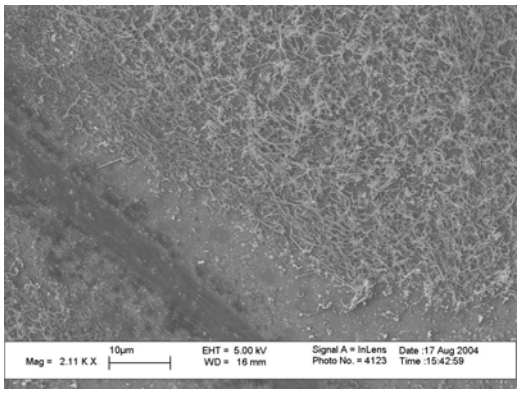

Figure A121: HYCNT ASFe 9m 3

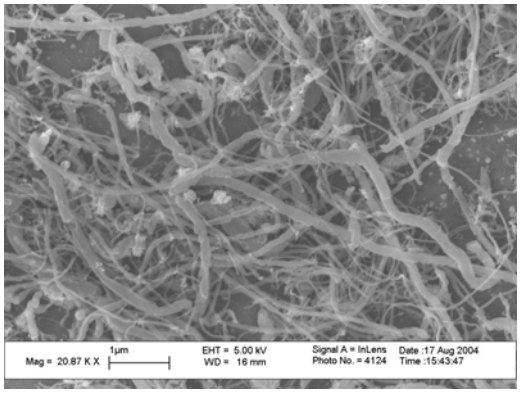

Figure A122: HYCNT ASFe 9m 4

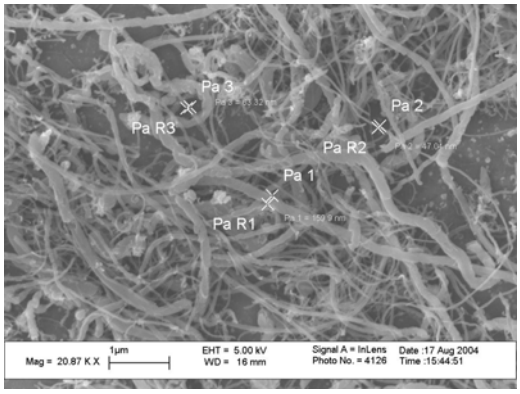

Figure A123: HYCNT ASFe 9m 5

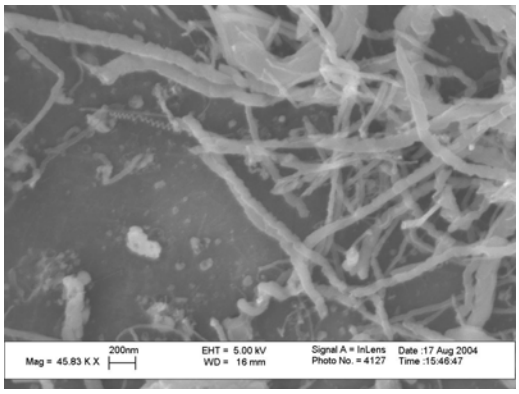

Figure A124: HYCNT ASFe 9m 6

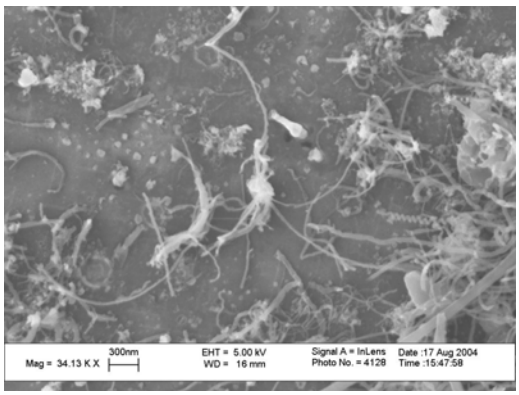

Figure A125: HYCNT ASFe 9m 7

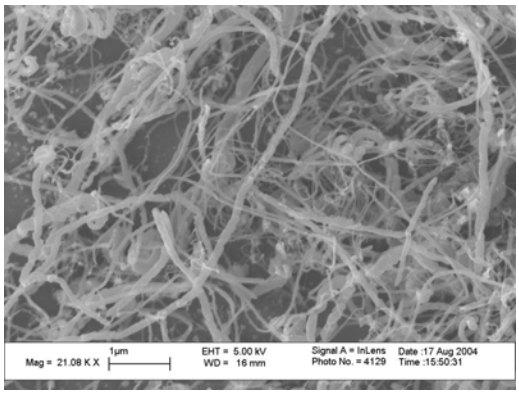

Figure A126: HYCNT ASFe 9m 8

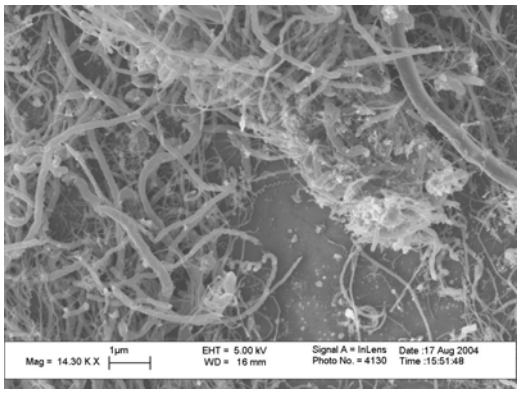

Figure A127: HYCNT ASFe 9m 9

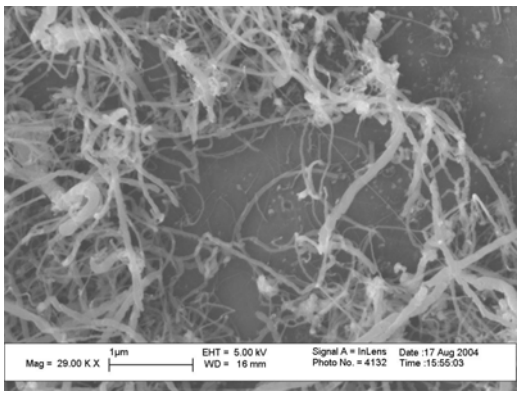

Figure A128: HYCNT ASFe 9m 10

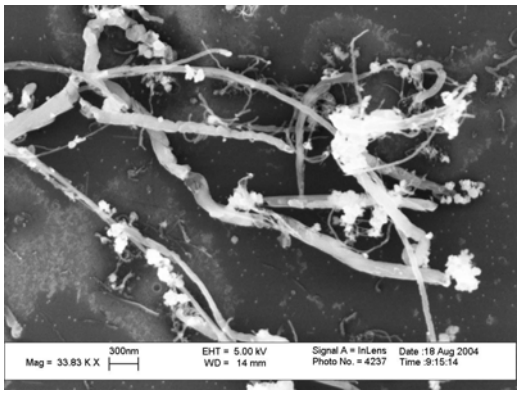

Figure A129: HYCNT ASFe 12m 1

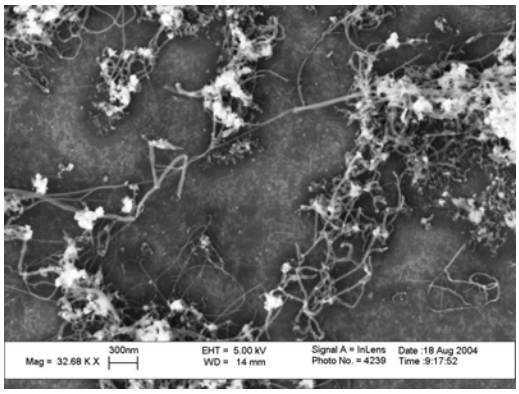

Figure A130: HYCNT ASFe 12m 2

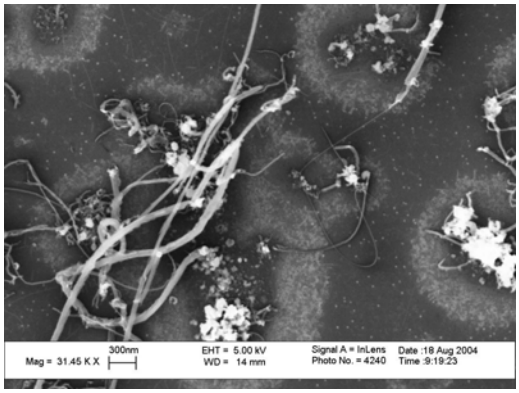

Figure A131: HYCNT ASFe 12m 3

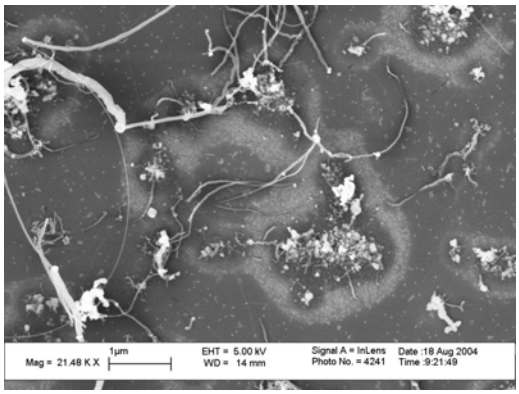

Figure A132: HYCNT ASFe 12m 4

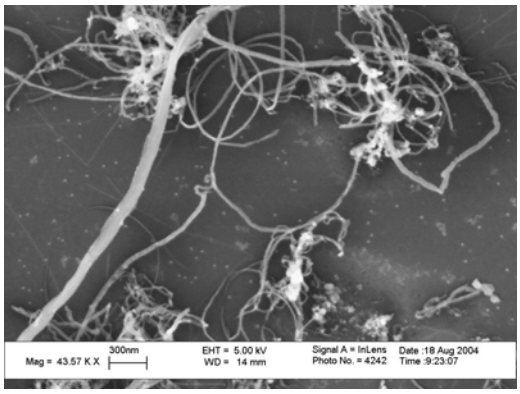

Figure A133: HYCNT ASFe 12m 5

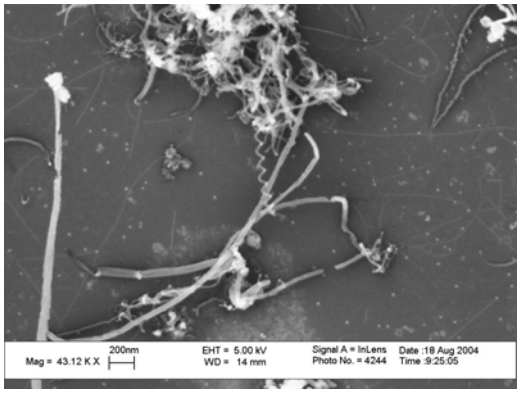

Figure A134: HYCNT ASFe 12m 6

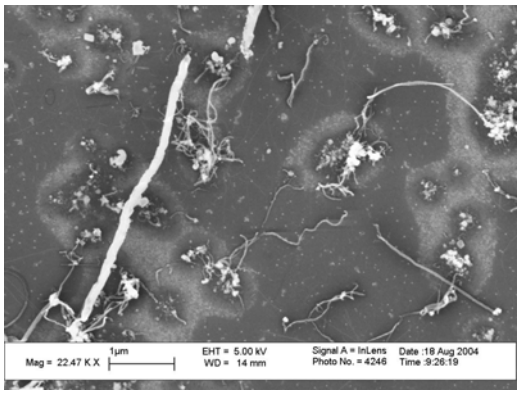

Figure A135: HYCNT ASFe 12m 7

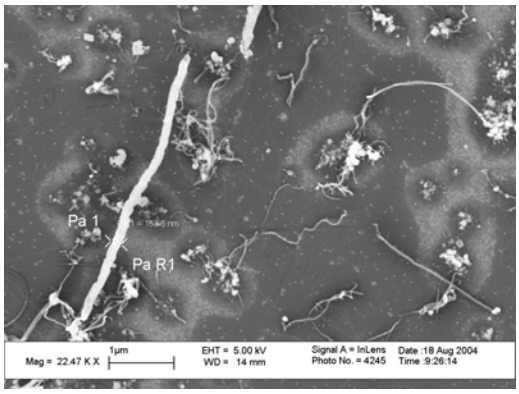

Figure A136: HYCNT ASFe 12m 8

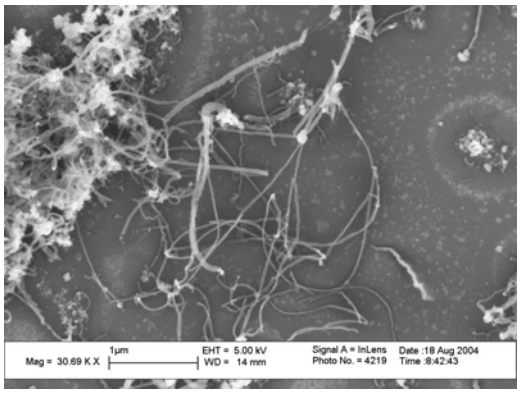

Figure A139: HYCNT ASFe 15m 3

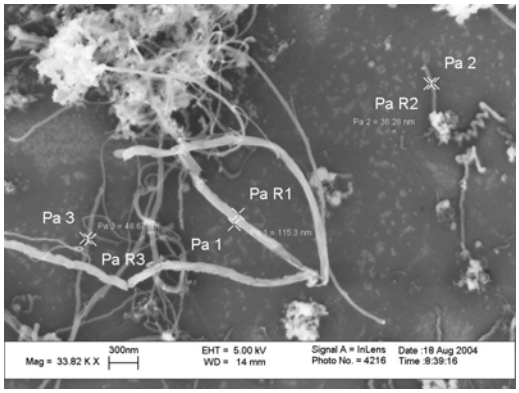

Figure A137: HYCNT ASFe 15m 1

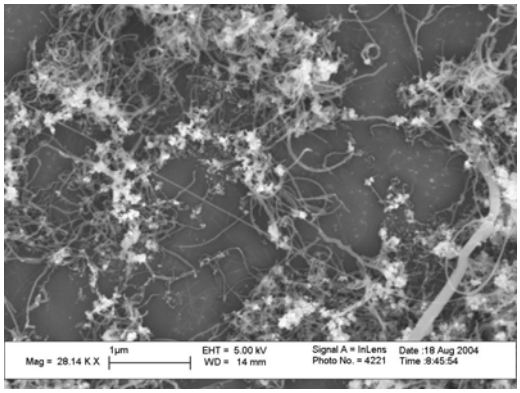

Figure A140: HYCNT ASFe 15m 4

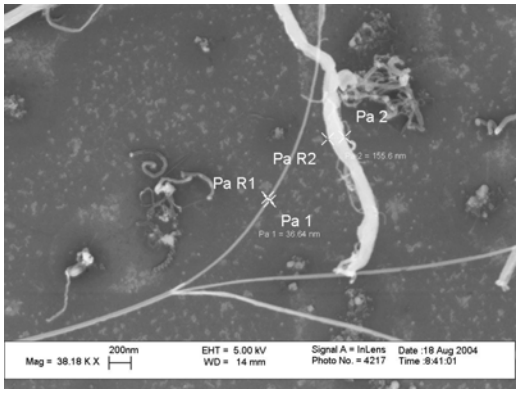

Figure A138: HYCNT ASFe 15m 2

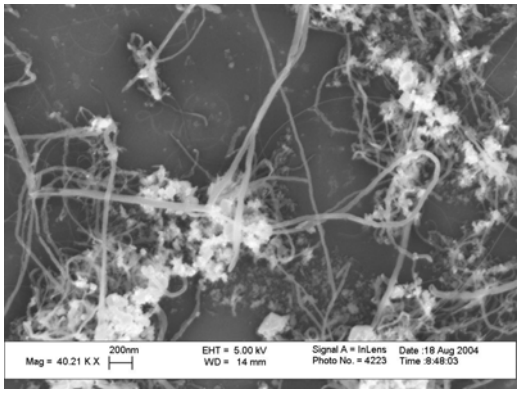

Figure A141: HYCNT ASFe 15m 5

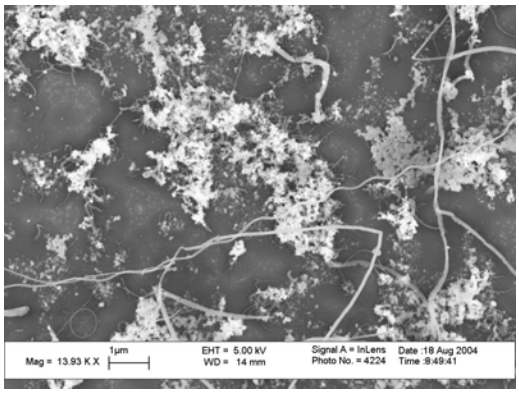

Figure A142: HYCNT ASFe 15m 6

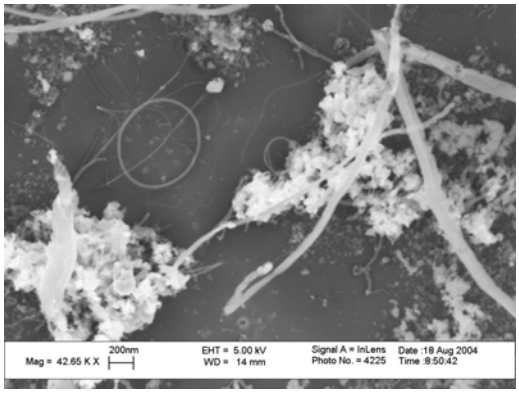

Figure A143: HYCNT ASFe 15m 7

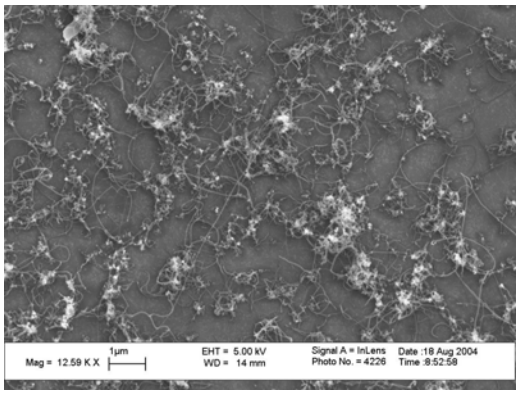

Figure A144: HYCNT ASFe 15m 8

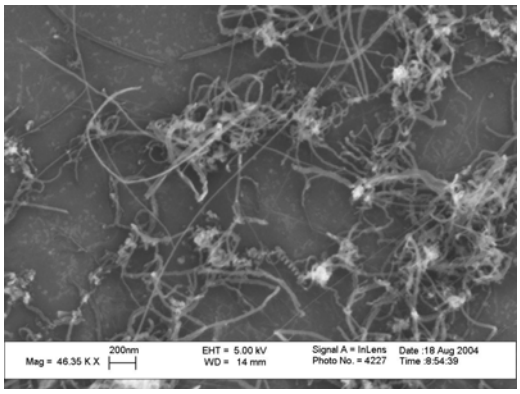

Figure A145: HYCNT ASFe 15m 9

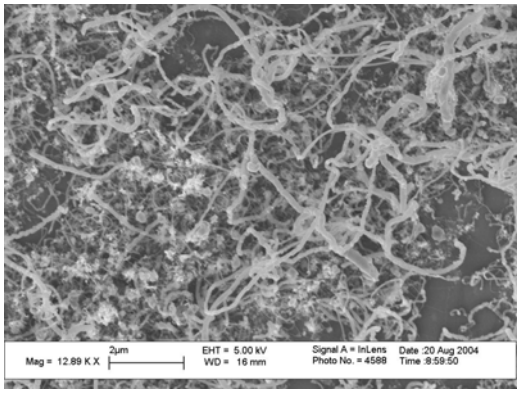

Figure A146: UHYCNT ASFe 10V 1

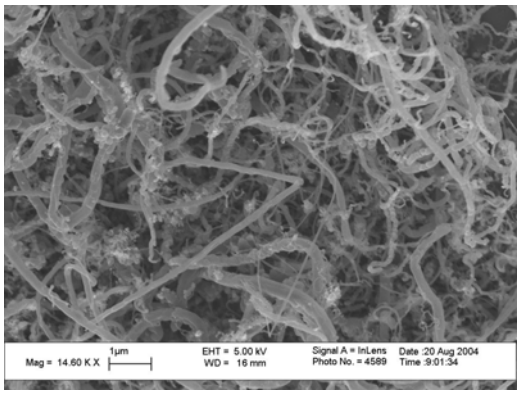

Figure A147: UHYCNT ASFe 10V 2

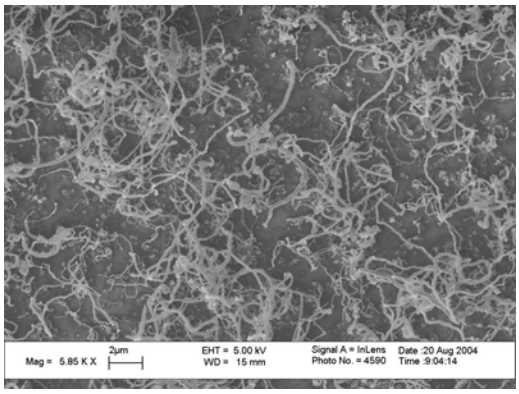

Figure A148: UHYCNT ASFe 10V 3

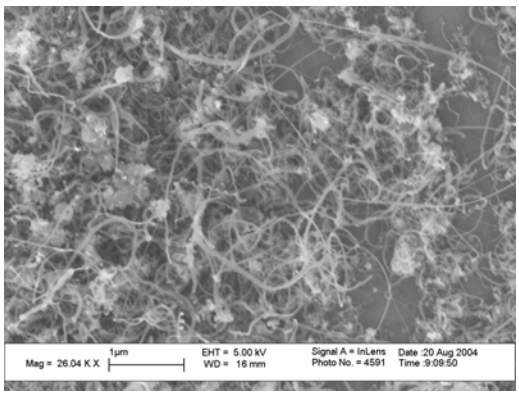

Figure A149: UHYCNT ASFe 10V 4

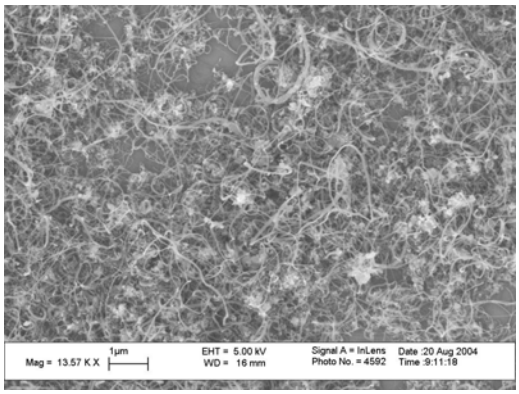

Figure A150: UHYCNT ASFe 10V 5

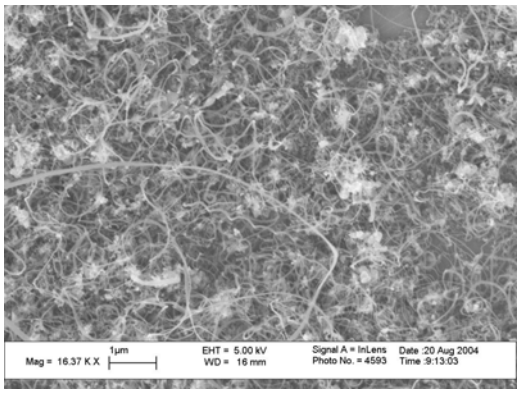

Figure A151: UHYCNT ASFe 10V 6

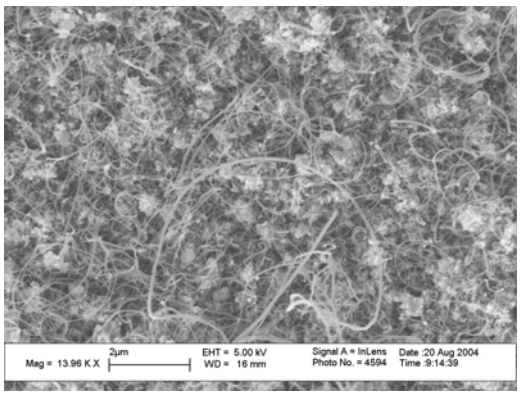

Figure A152: UHYCNT ASFe 10V 7

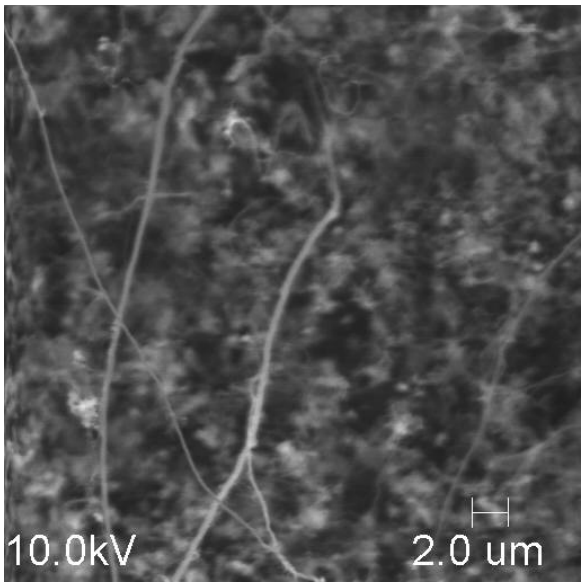

Figure A153: UHYCNT ASFe 20V 1

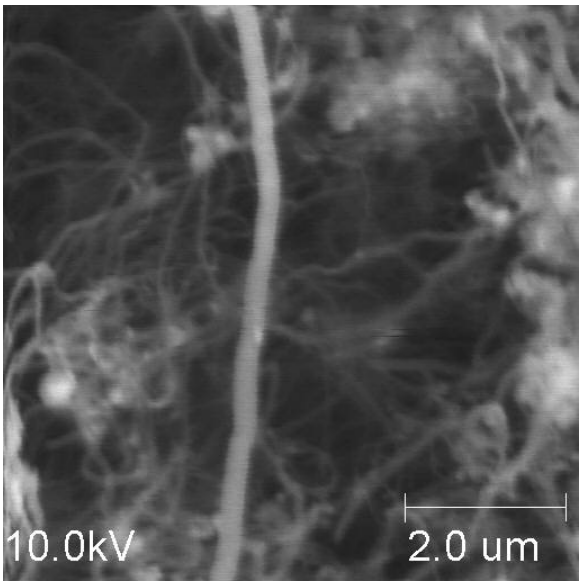

Figure A154: UHYCNT ASFe 20V 2

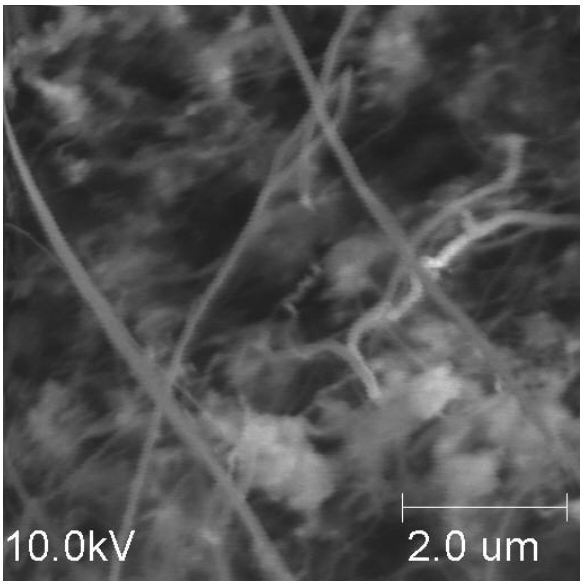

Figure A156: UHYCNT ASFe 20V 4

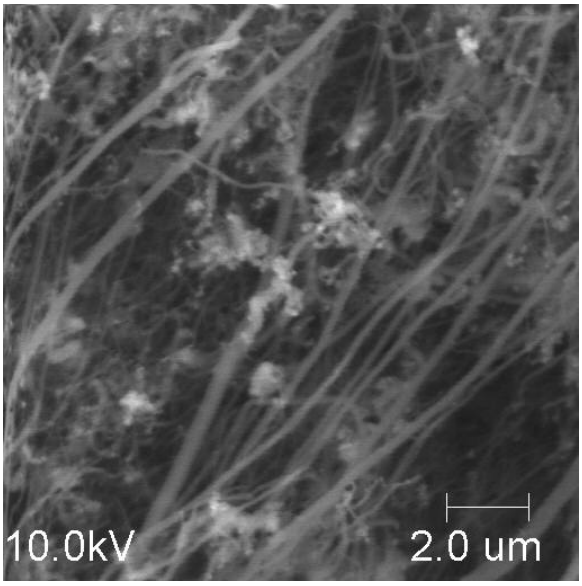

Figure A155: UHYCNT ASFe 20V 3

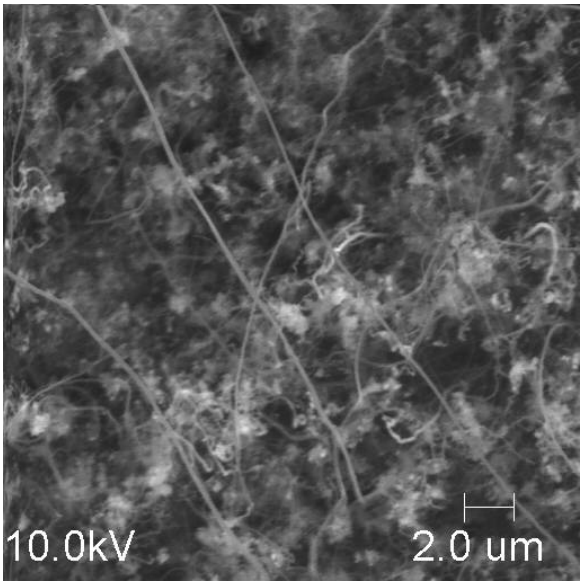

Figure A157: UHYCNT ASFe 20V 5

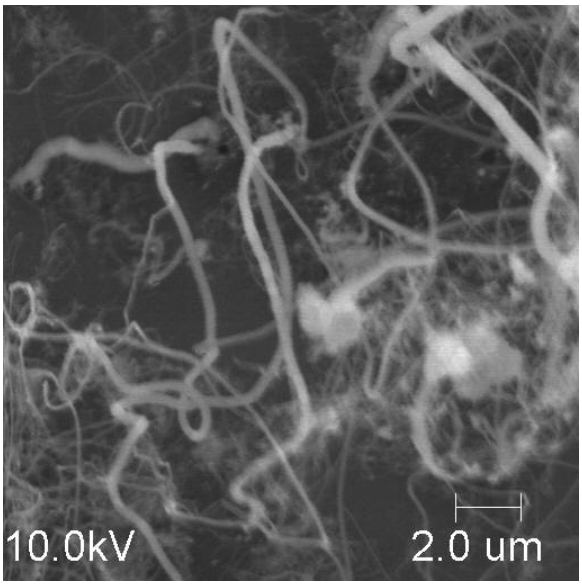

Figure A158: UHYCNT ASFe 20V 6

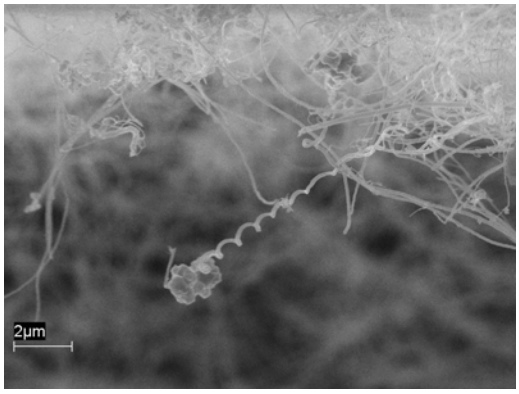

Figure A159: UHYCNT ASFe 30V 1

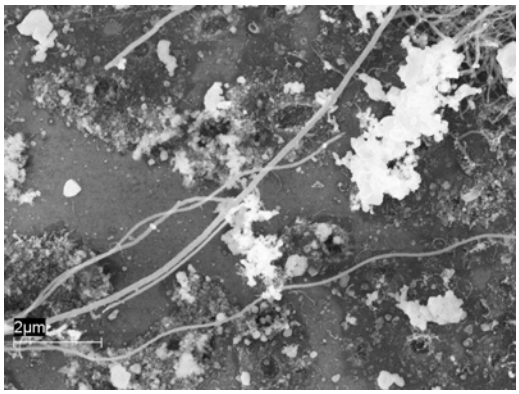

Figure A160: UHYCNT ASFe 30V 2

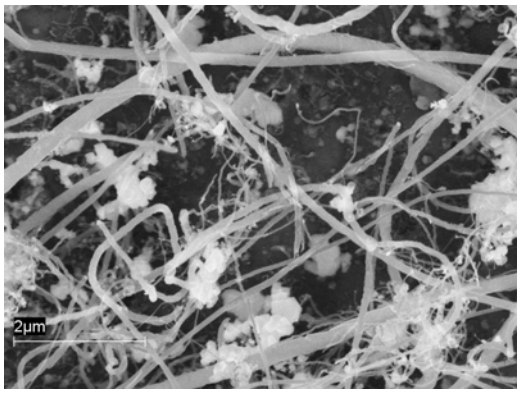

Figure A161: UHYCNT ASFe 30V 3

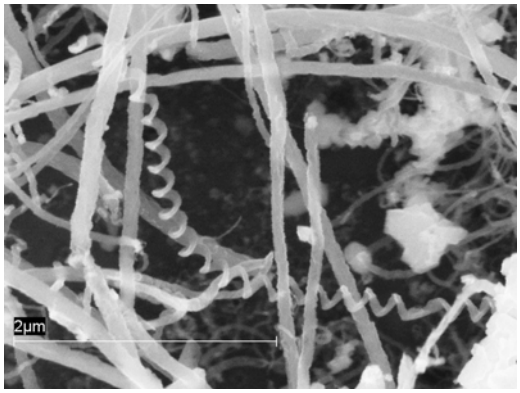

Figure A162: UHYCNT ASFe 30V 4

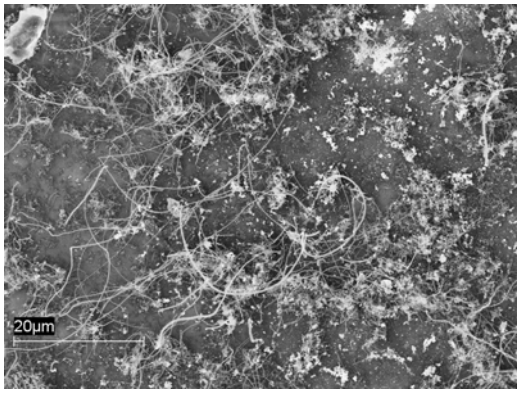

Figure A163: UHYCNT ASFe 30V 5

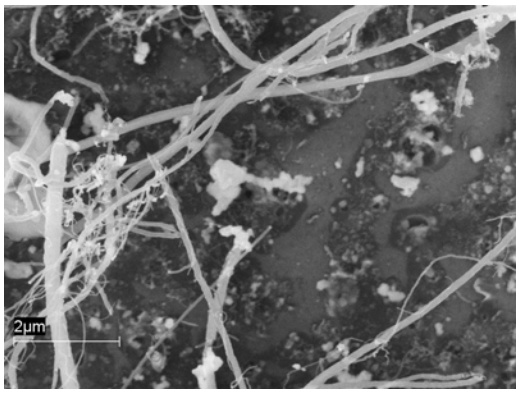

Figure A164: UHYCNT ASFe 30V 6

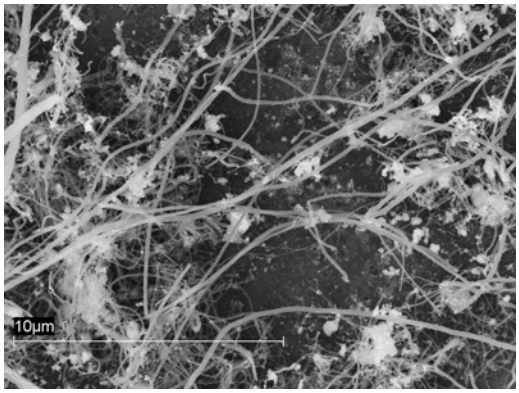

Figure A165: UHYCNT ASFe 30V 7

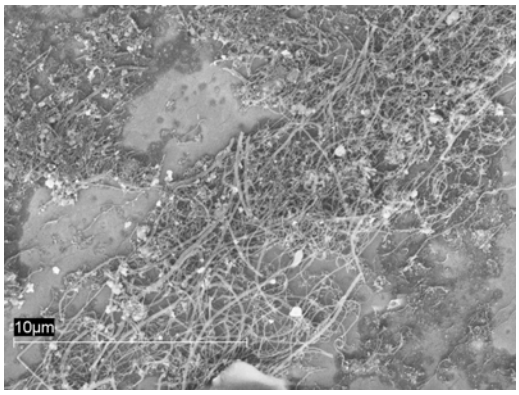

Figure A166: UHYCNT ASFe 30V 8

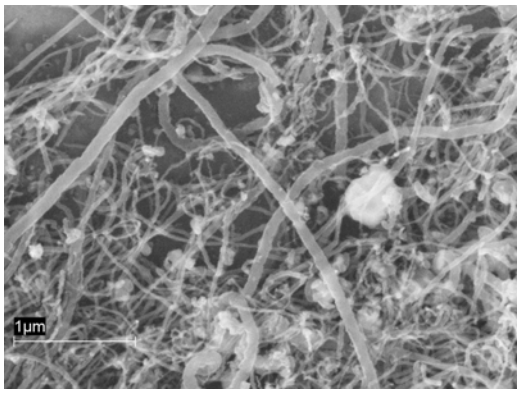

Figure A167: UHYCNT ASFe 30V 9

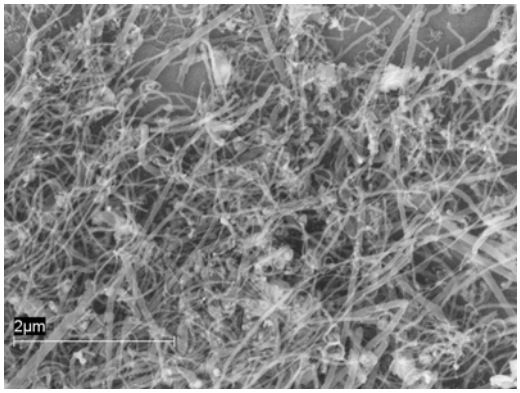

Figure A168: UHYCNT ASFe 30V 10

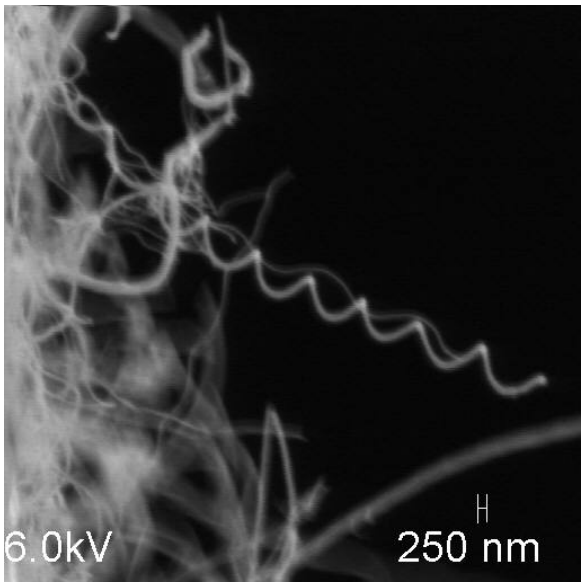

Figure A169: UHYCNT ASFe 30V 11

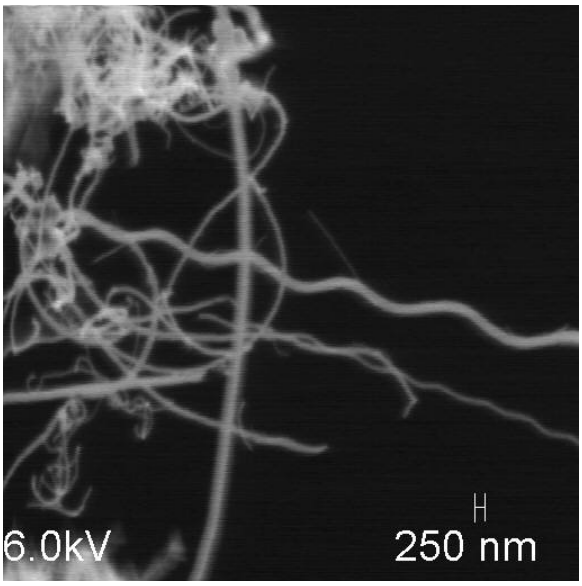

Figure A170: UHYCNT ASFe 30V 12

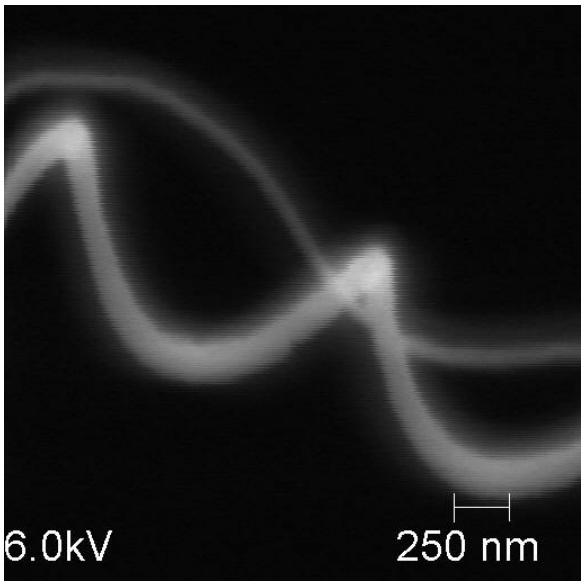

Figure A172: UHYCNT ASFe 30V 14

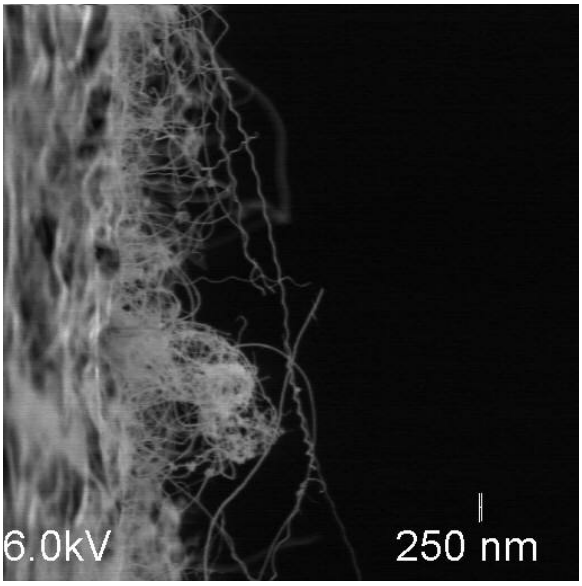

Figure A171: UHYCNT ASFe 30V 13

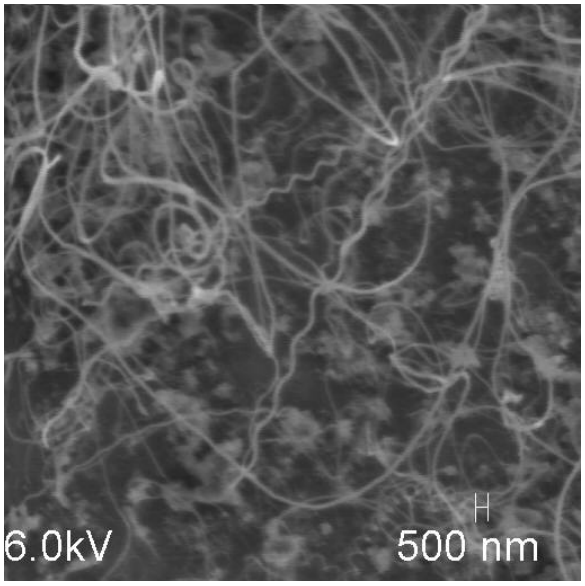

Figure A173: UHYCNT ASFe 40V 1

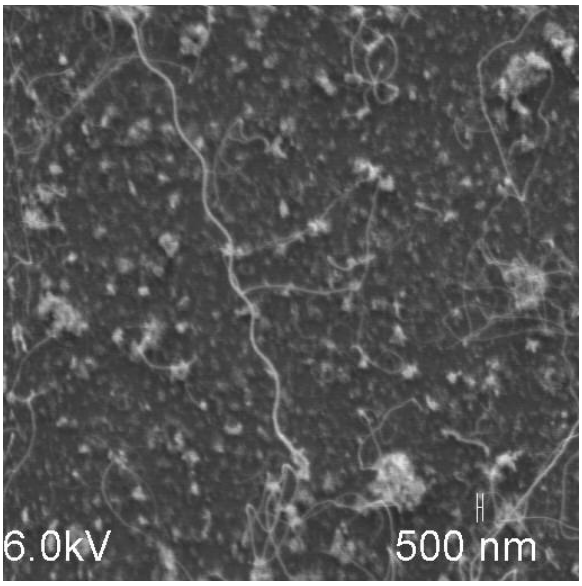

Figure A174: UHYCNT ASFe 40V 2

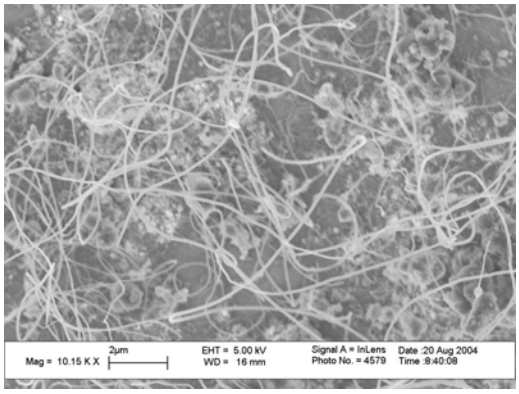

Figure A175: UHYCNT ASFe 40V 3

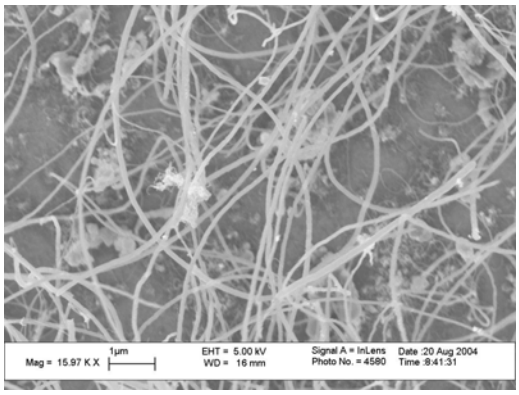

Figure A176: UHYCNT ASFe 40V 4

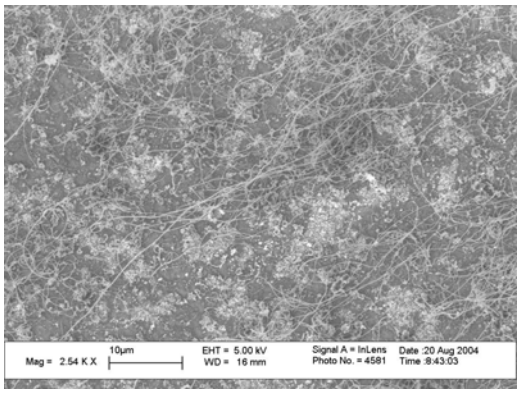

Figure A177: UHYCNT ASFe 40V 5

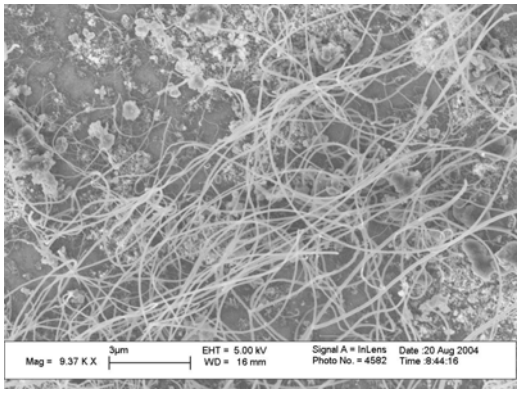

Figure A178: UHYCNT ASFe 40V 6

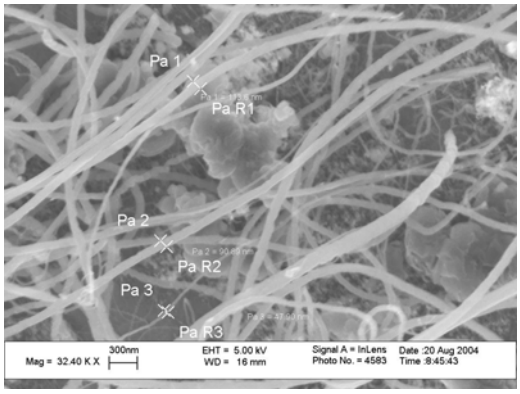

Figure A179: UHYCNT ASFe 40V 7

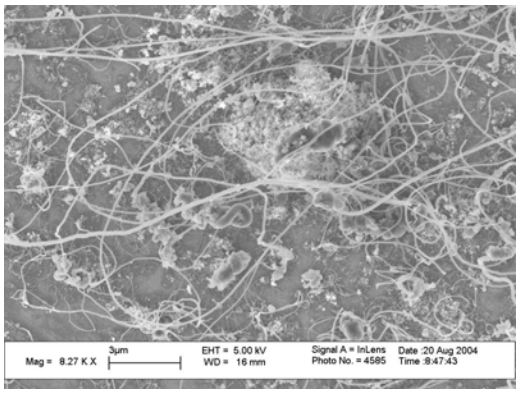

Figure A180: UHYCNT ASFe 40V 8

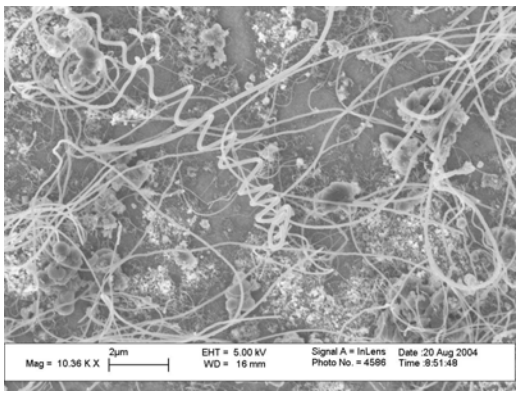

Figure A181: UHYCNT ASFe 40V 9

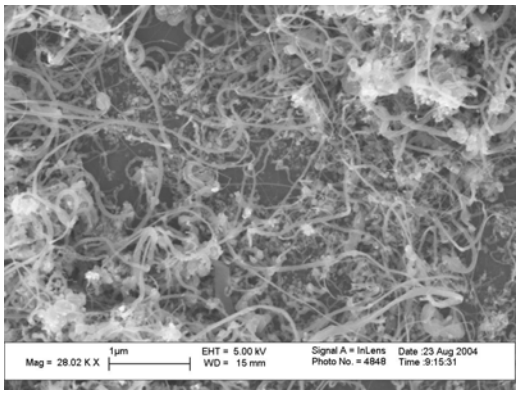

Figure A182: UHYCNT ASFe 50V 1

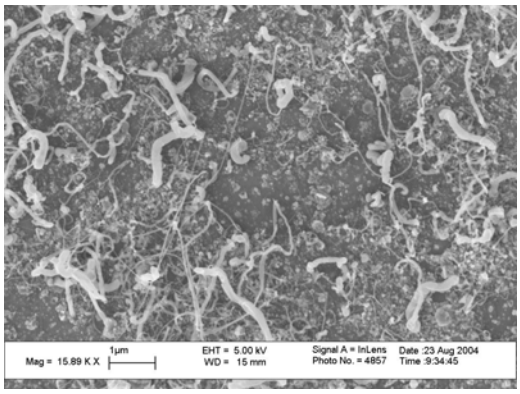

Figure A183: UHYCNT ASFe 50V 2

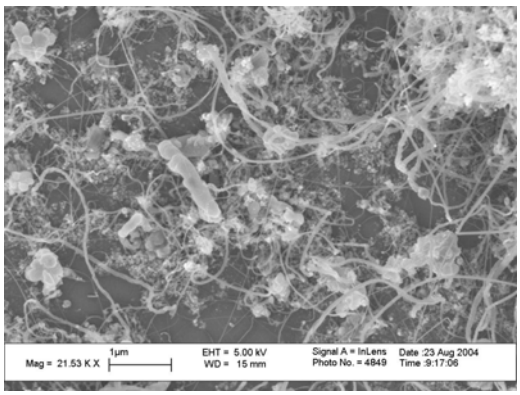

Figure A184: UHYCNT ASFe 50V 3

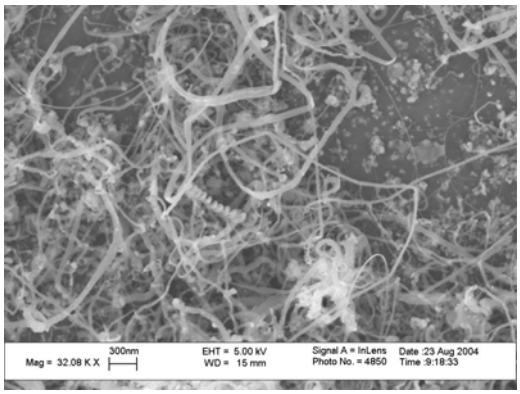

Figure A185: UHYCNT ASFe 50V 4

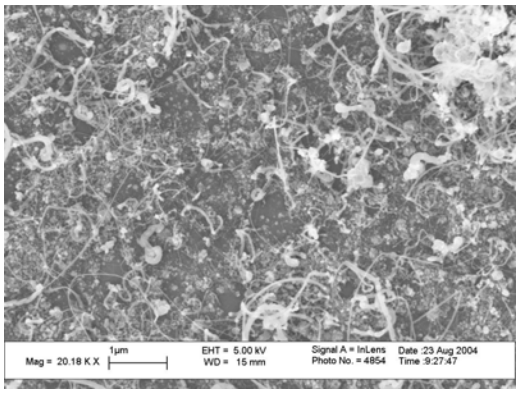

Figure A186: UHYCNT ASFe 50V 5

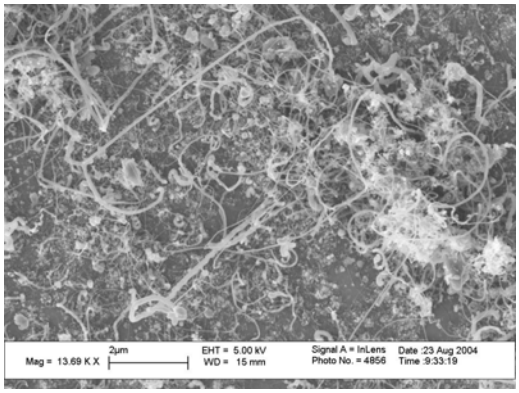

Figure A187: UHYCNT ASFe 50V 6

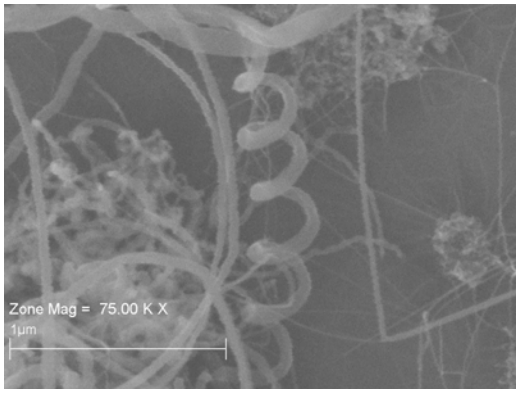

Figure 188: UHYCNT ASFe 50V 7

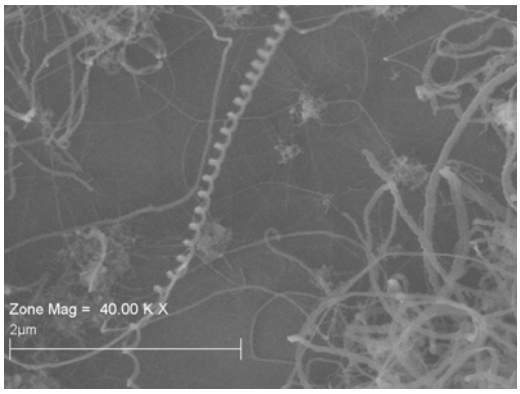

Figure A189: UHYCNT ASFe 50V 8

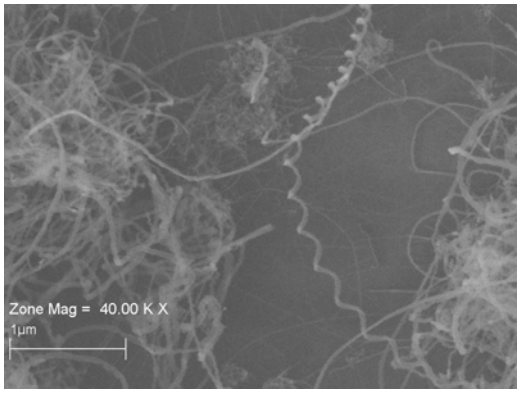

Figure A190: UHYCNT ASFe 50V 9

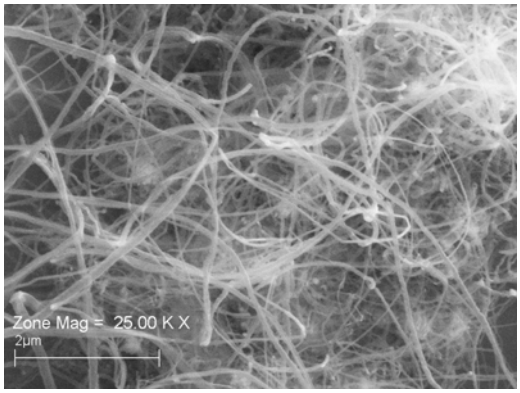

Figure A191: UHYCNT ASFe 50V 10

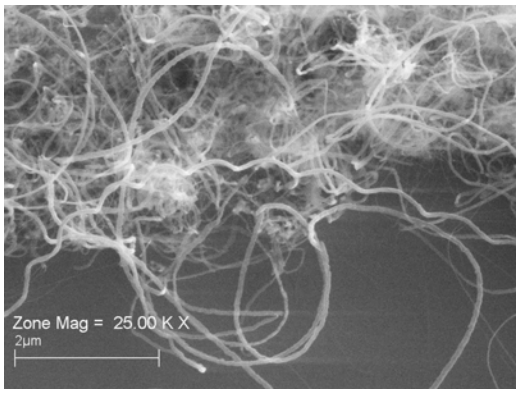

Figure A192: UHYCNT ASFe 50V 11

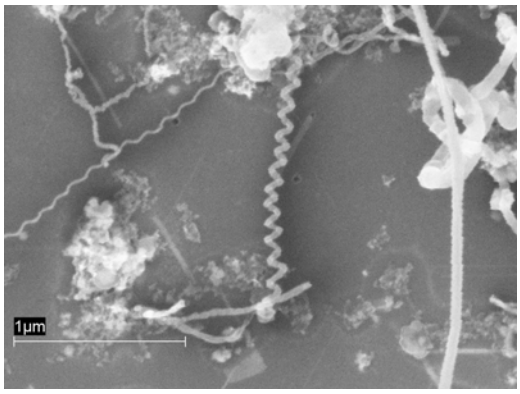

Figure A195: AcUHYCNT ASFe 50V 3

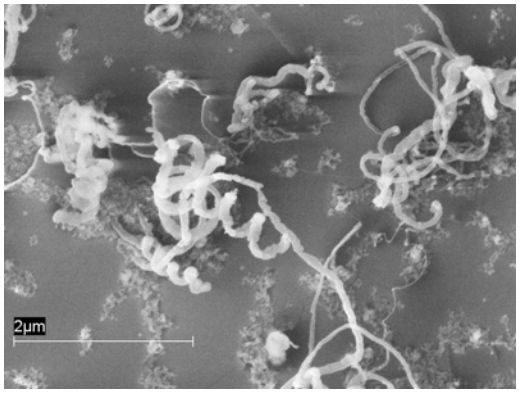

Figure A193: AcUHYCNT ASFe 50V 1

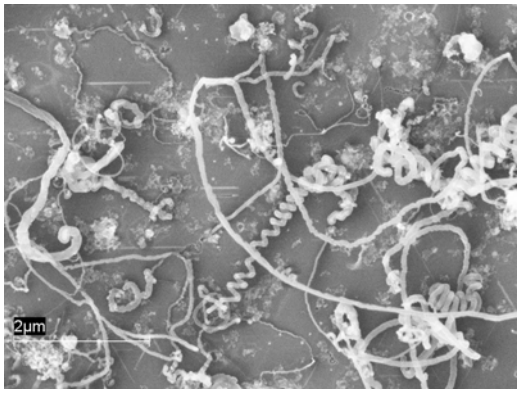

Figure A196: AcUHYCNT ASFe 50V 4

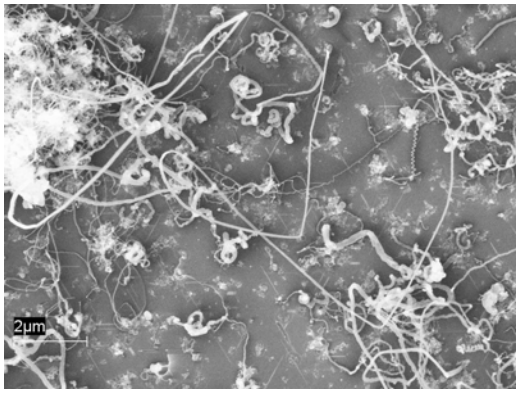

Figure A194: AcUHYCNT ASFe 50V 2

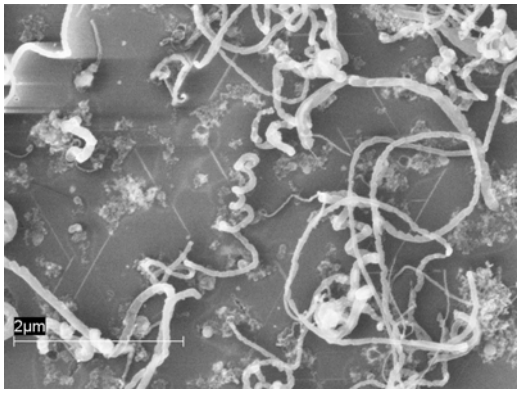

Figure A197: AcUHYCNT ASFe 50V 5

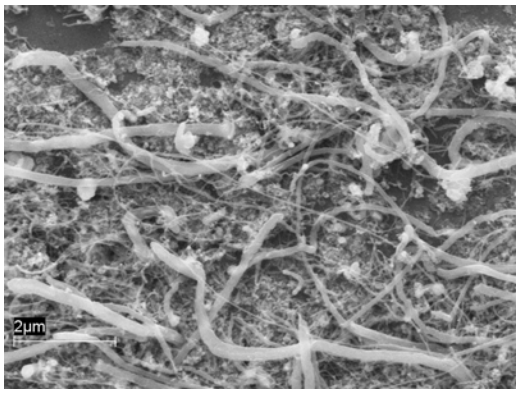

Figure A198: AcUHYCNT ASFe 50V 6

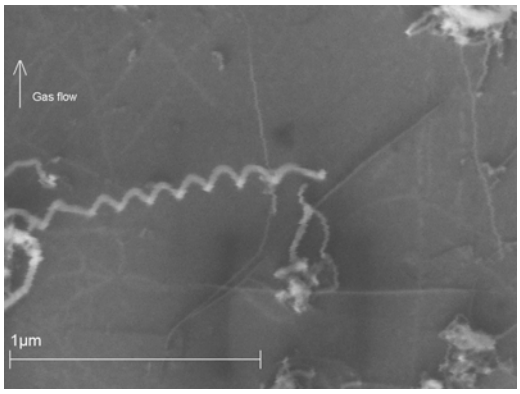

Figure A201: AcUHYCNT ASFe 50V 19

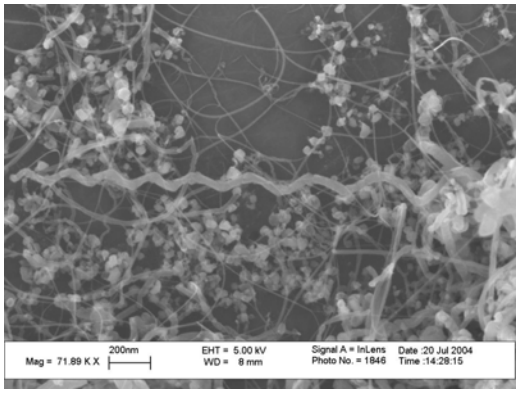

Figure A199: AcUHYCNT ASFe 50V 7

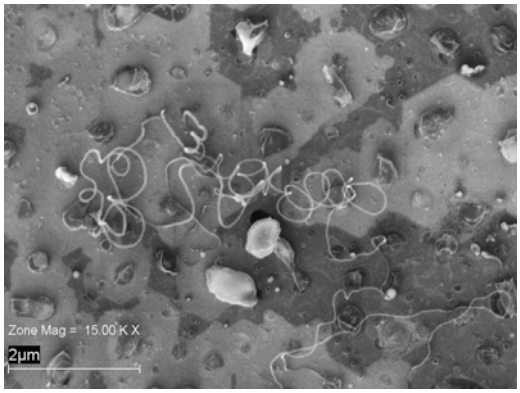

Figure A202: UHYCNT 40Ni 50V 1

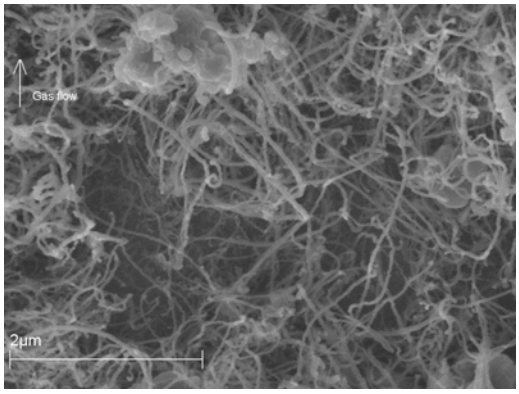

Figure A200: AcUHYCNT ASFe 50V 8

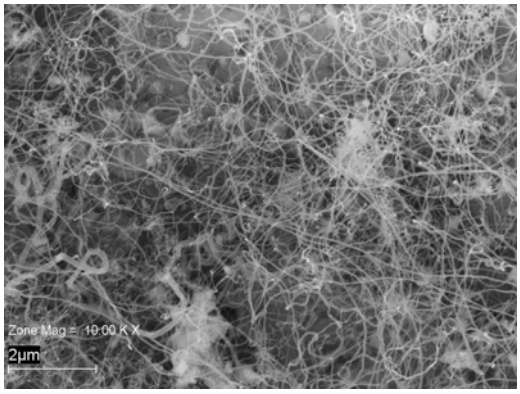

Figure A203: UHYCNT 40Ni 50V 2

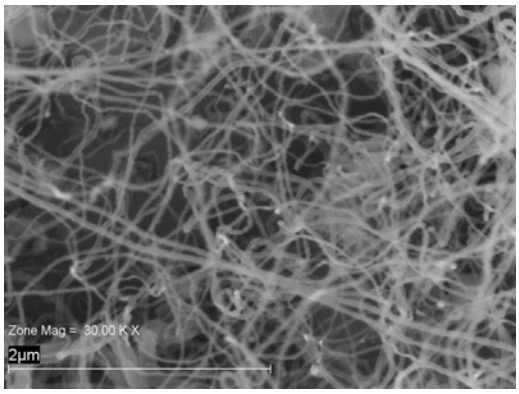

Figure A204: UHYCNT 40Ni 50V 3

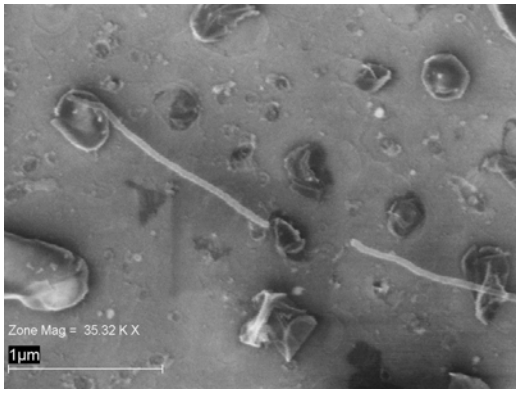

Figure A205: UHYCNT 40Ni 50V 4

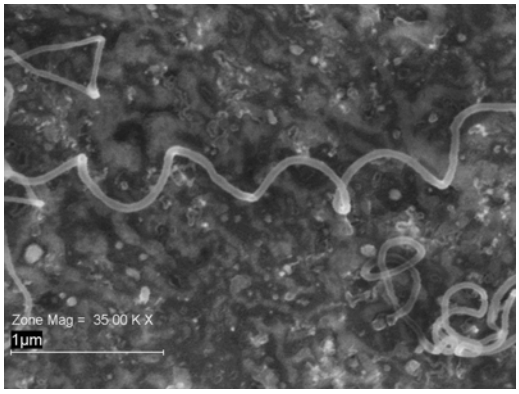

Figure A206: UHYCNT 80Ni 50V 1

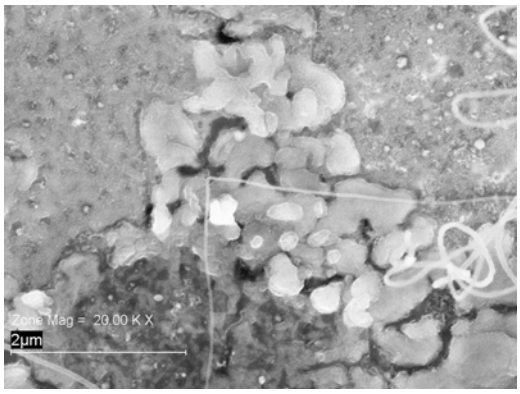

Figure A207: UHYCNT 80Ni 50V 2

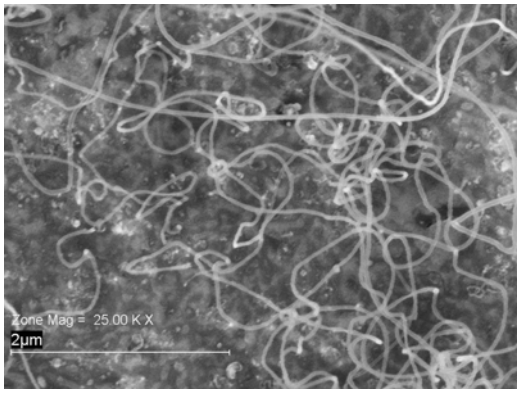

Figure A208: UHYCNT 80Ni 50V 3

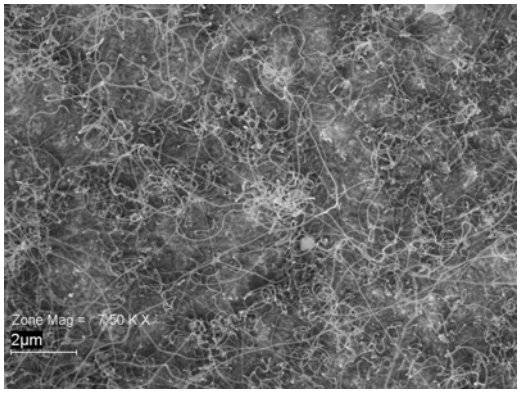

Figure A209: UHYCNT 80Ni 50V 4

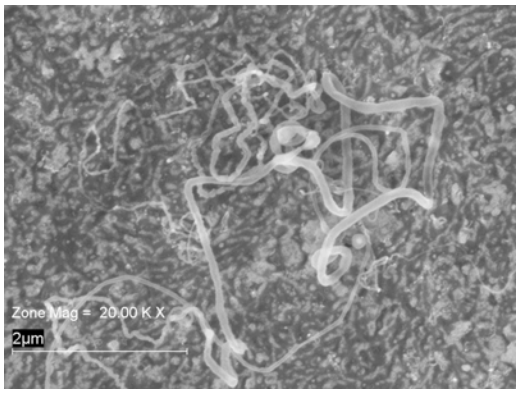

Figure A210: UHYCNT 80Ni 50V 5

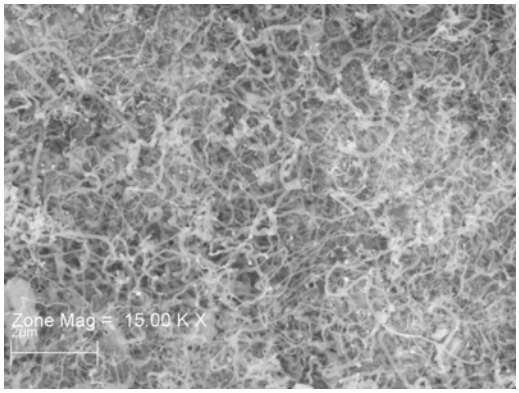

Figure A211: UHYCNT 80Ni 50V 6

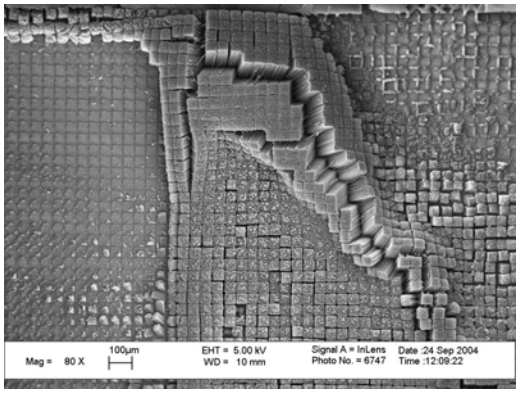

Figure A212: SA AcUHCNT ASFe 740P1

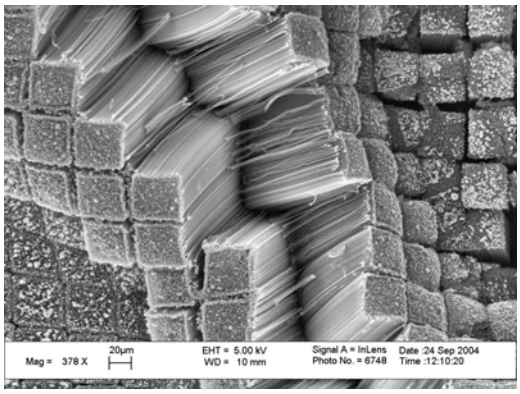

Figure A213: SA AcUHCNT ASFe 740P2

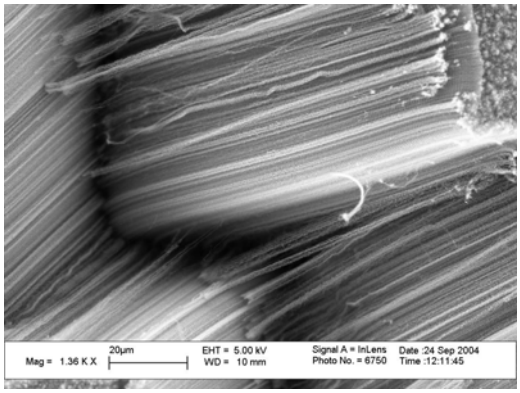

Figure A214: SA AcUHCNT ASFe 740P3

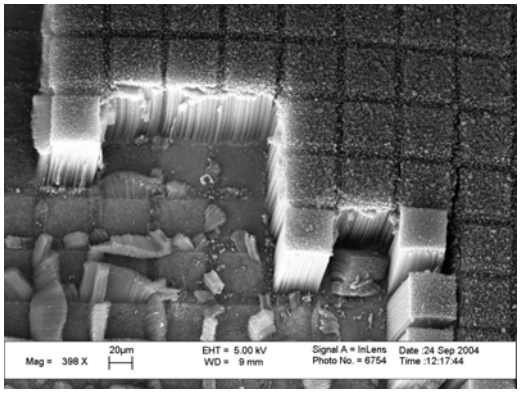

Figure A215: SA AcUHCNT ASFe 740P4

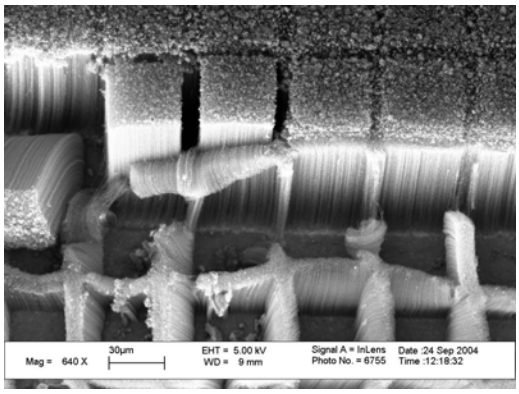

Figure A216: SA AcUHCNT ASFe 740P5

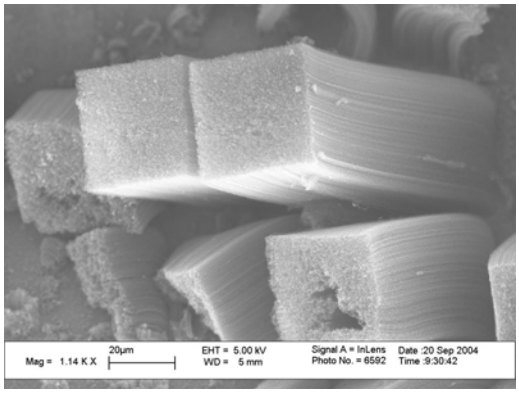

Figure A217: SA AcUHCNT ASFe 740P6

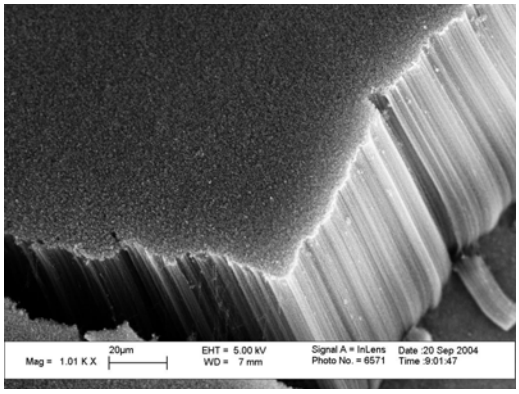

Figure A218: SA AcUHCNT ASFe 740P7

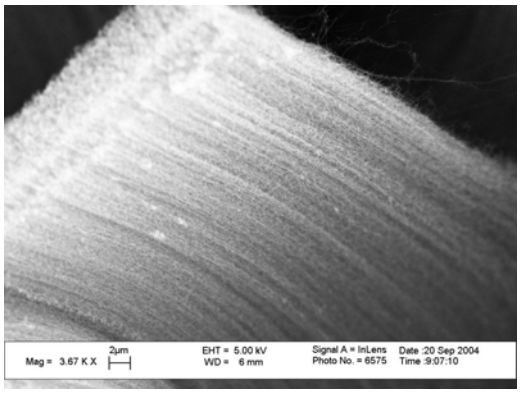

Figure A219: SA AcUHCNT ASFe 740P8

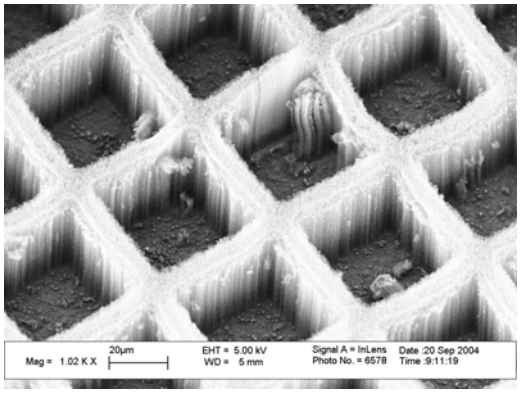

Figure A220: SA AcUHCNT ASFe 740P9

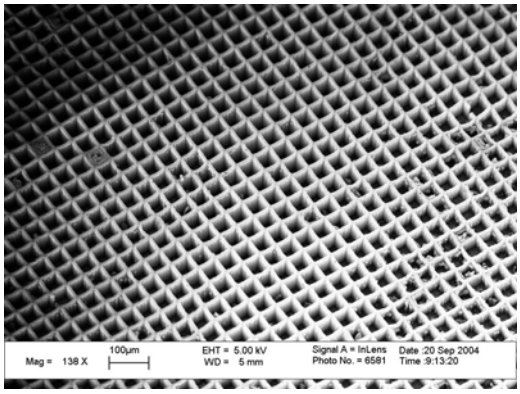

Figure A221: SA AcUHCNT ASFe 740P10

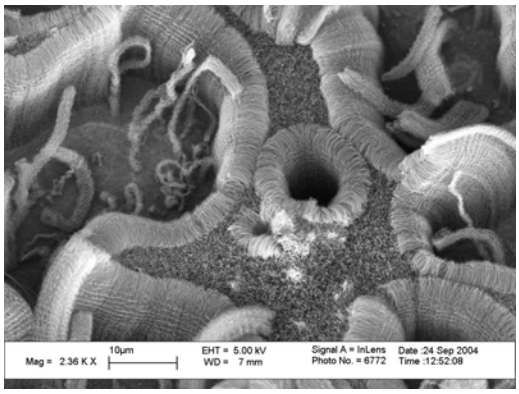

Figure A222: SA AcUHCNT ASFe 740 1

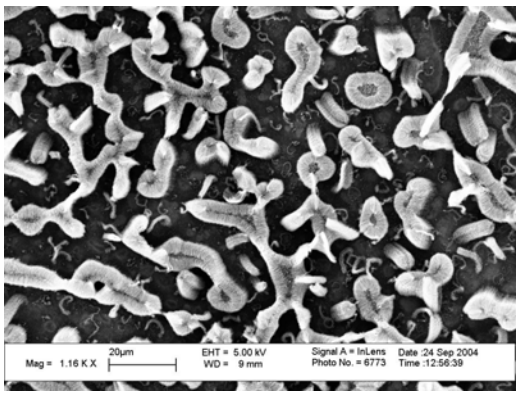

Figure A223: SA AcUHCNT ASFe 740 2

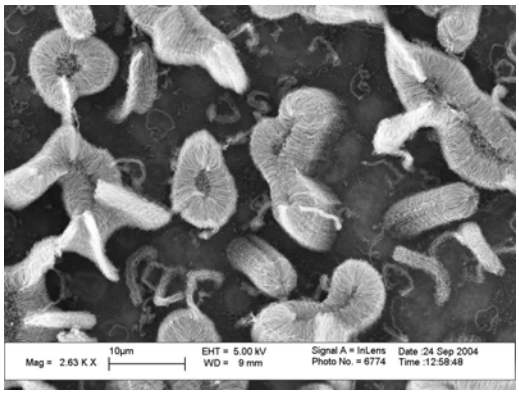

Figure A224: SA AcUHCNT ASFe 740 3

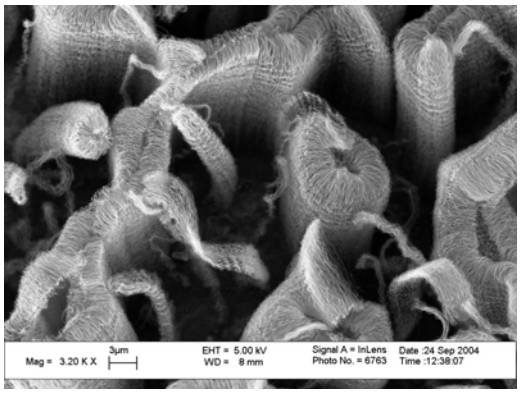

Figure A225: SA AcUHCNT ASFe 740 4

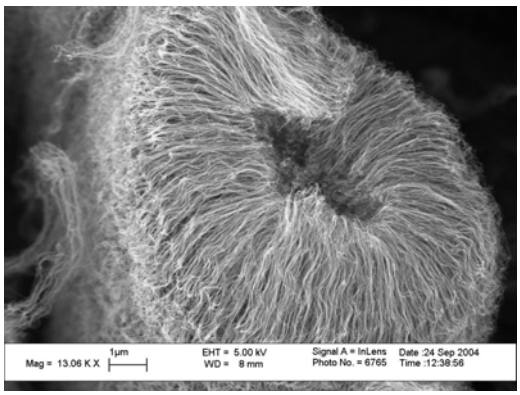

Figure A226: SA AcUHCNT ASFe 740 5

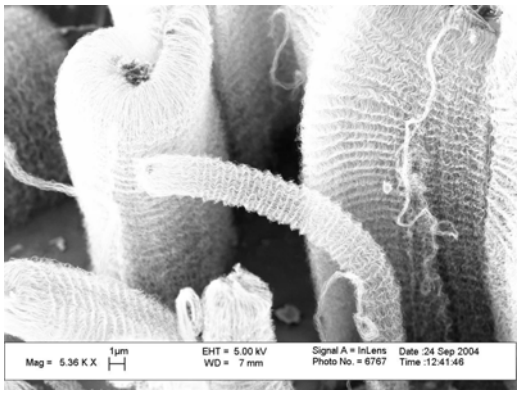

Figure A227: SA AcUHCNT ASFe 740 6

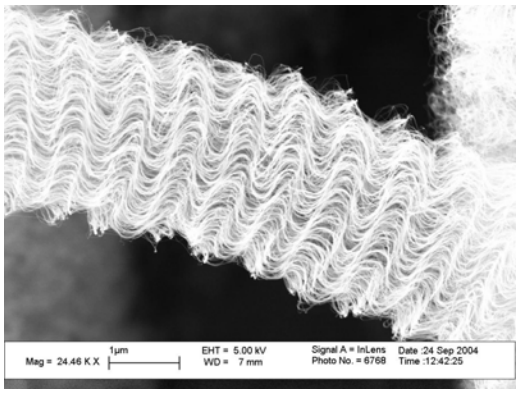

Figure A228: SA AcUHCNT ASFe 740 7

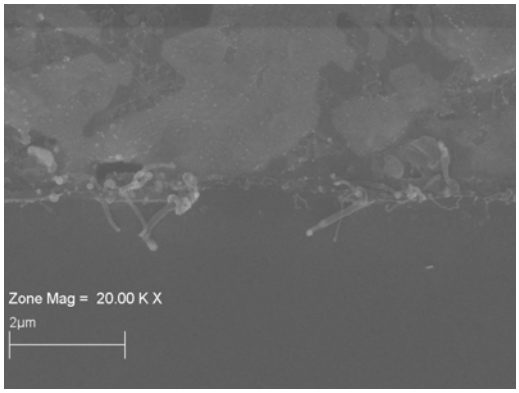

Figure A229: HPCNT 60Ni 1

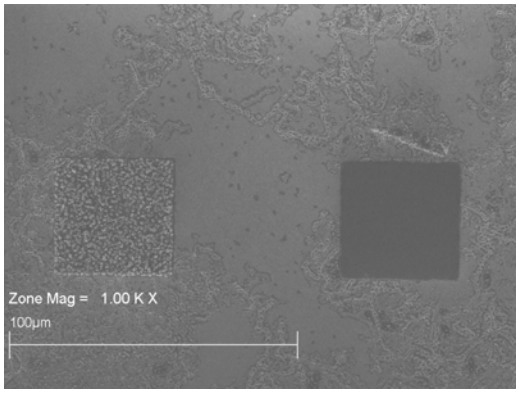

Figure A230: HPCNT 60Ni 2

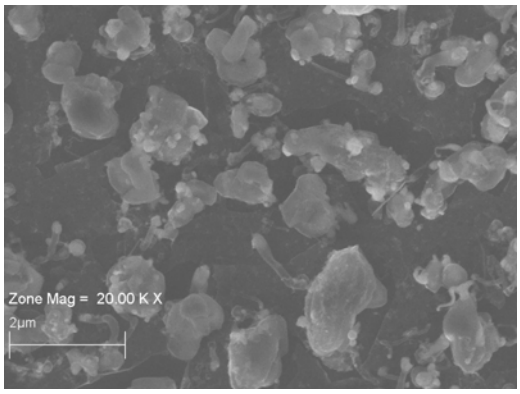

Figure A231: HPCNT 60Ni 3

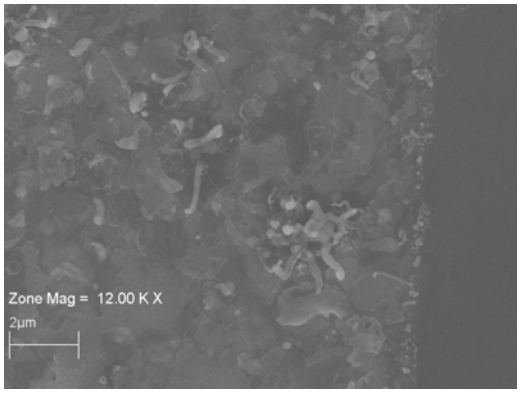

Figure A232: HPCNT 60Ni 4

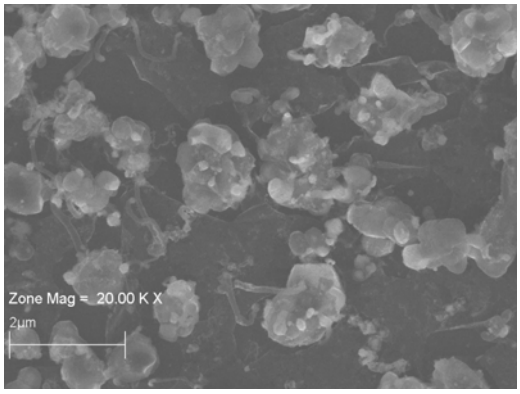

Figure A233: HPCNT 60Ni 5

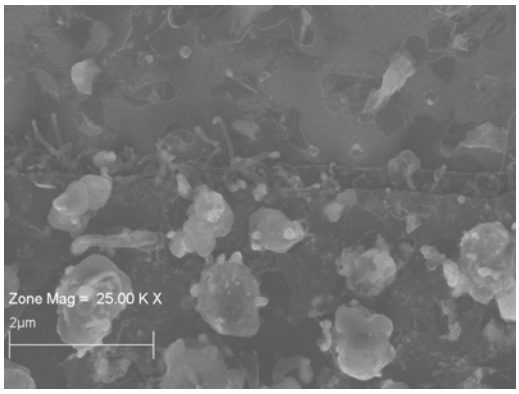

Figure A234: HPCNT 60Ni 6

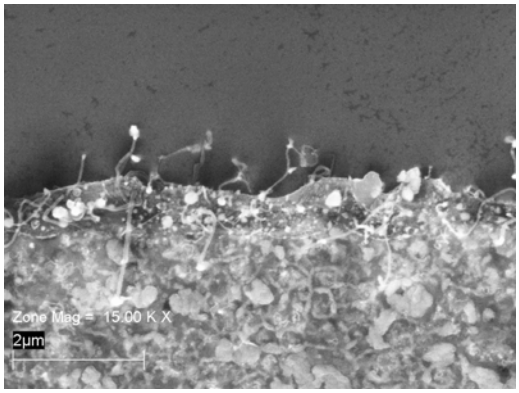

Figure A235: HPCNT 60Ni 7

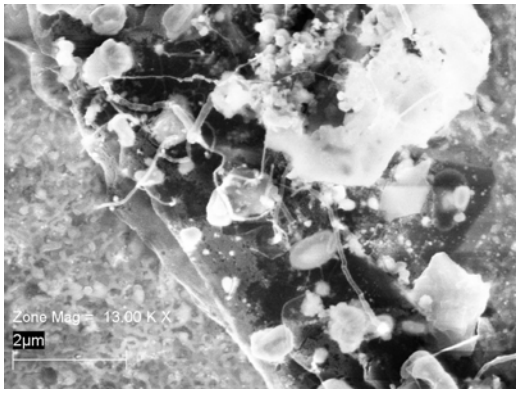

Figure A236: HPCNT 60Ni 8

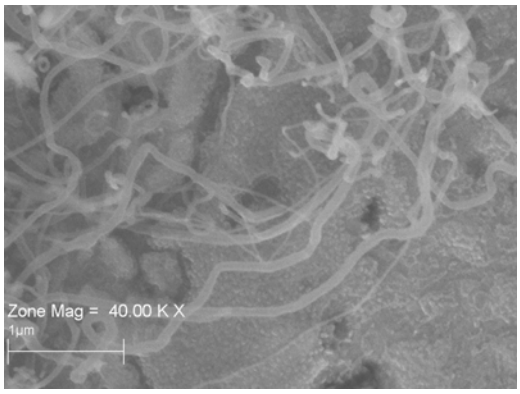

Figure A237: BULK CNT 60Ni 1

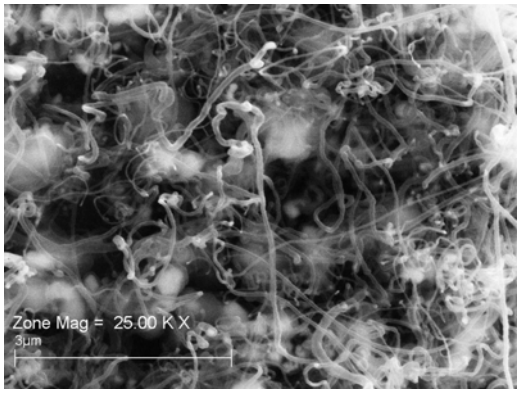

Figure A238: BULK CNT 60Ni 2

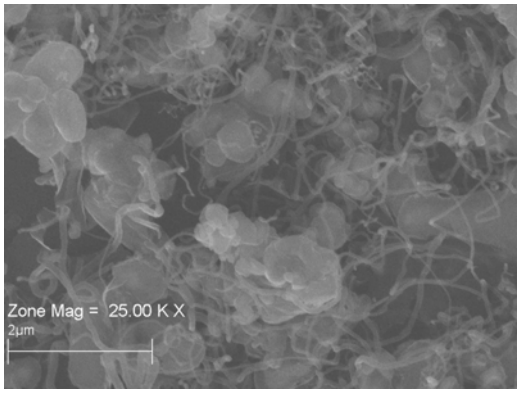

Figure A239: BULK CNT 60Ni 3

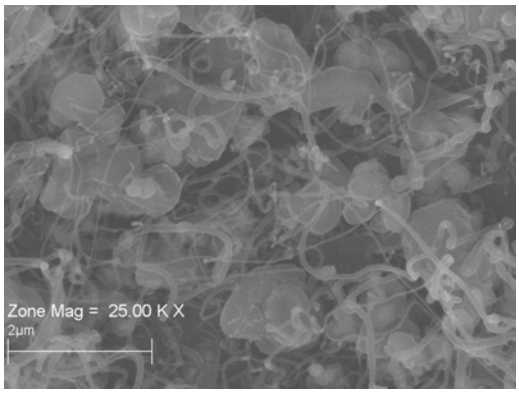

Figure A240: BULK CNT 60Ni 4

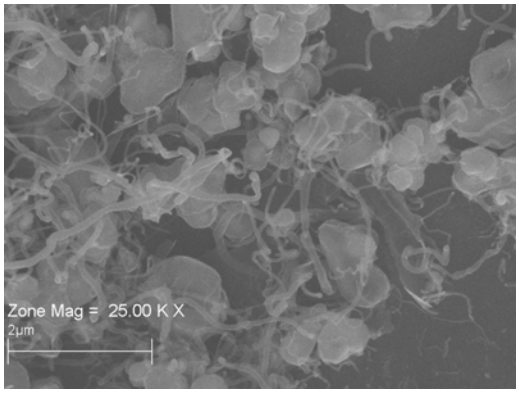

Figure A241: BULK CNT 60Ni 5

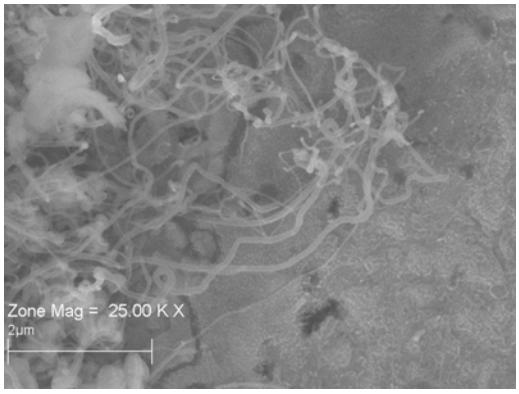

Figure A242: BULK CNT 60Ni 6

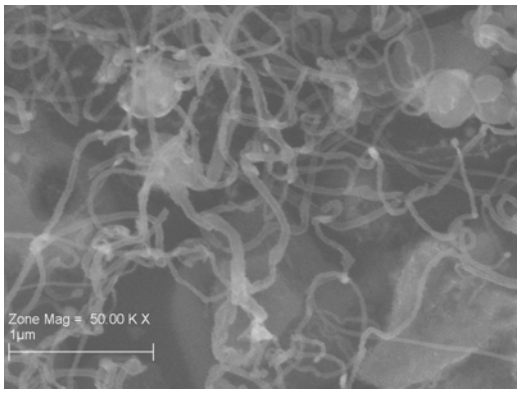

Figure A243: BULK CNT 60Ni 7

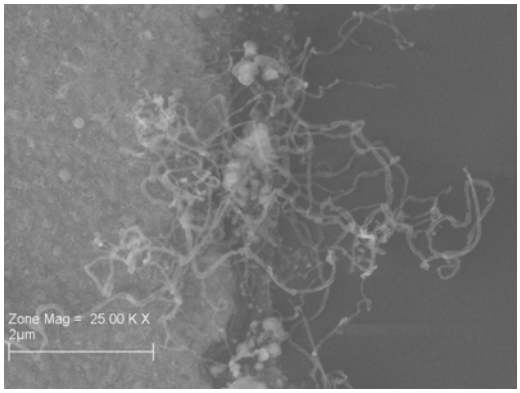

Figure A244: BULK CNT 60Ni 8

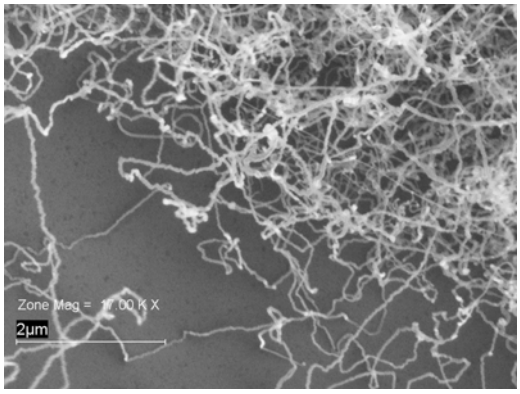

Figure A245: UHYCNT 60Ni 1

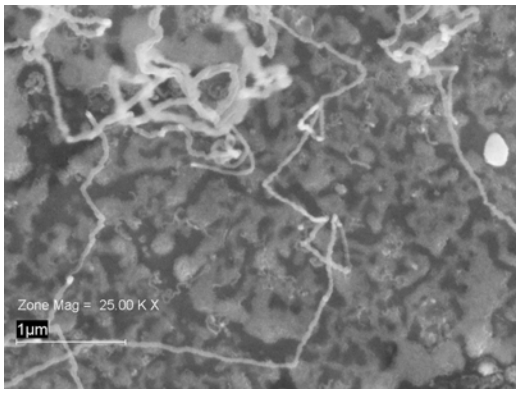

Figure A246: UHYCNT 60Ni 2

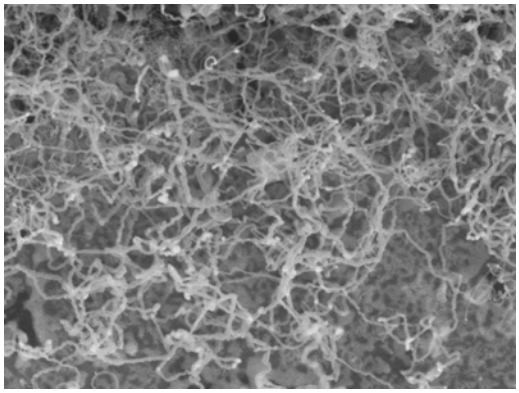

Figure A247: UHYCNT 60Ni 3

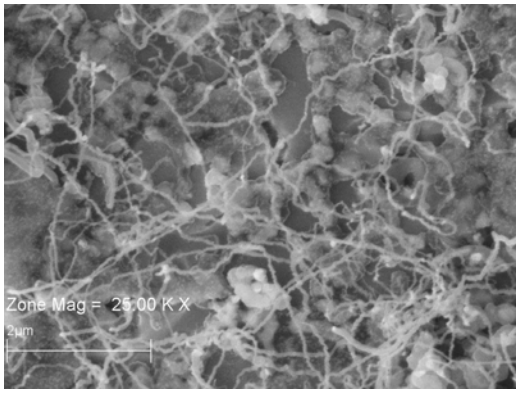

Figure A248: UHYCNT 60Ni 4

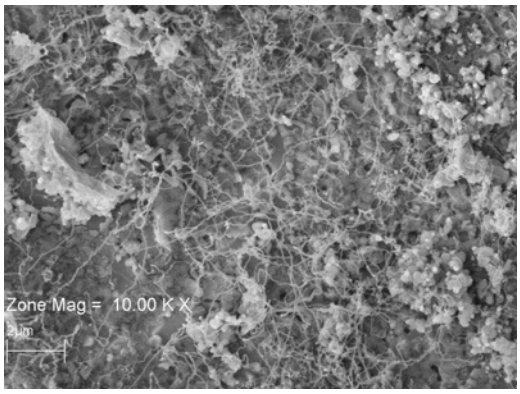

Figure A249: UHYCNT 60Ni 5

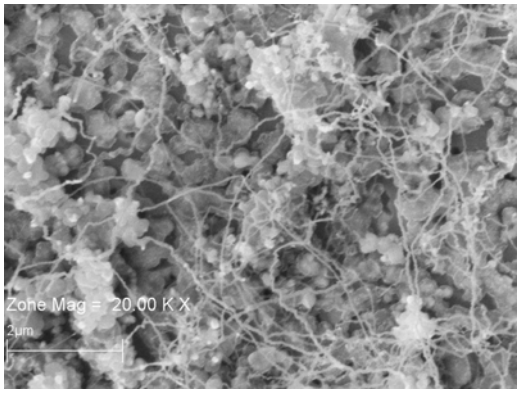

Figure A250: UHYCNT 60Ni 6

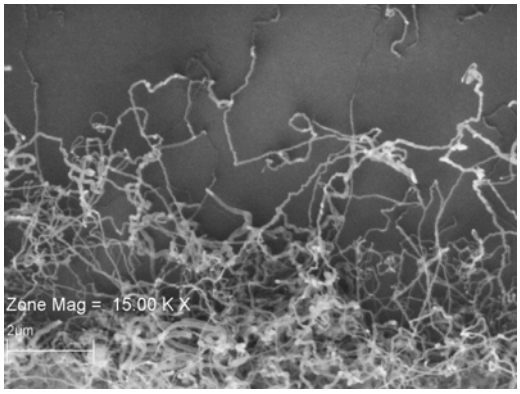

Figure A251: UHYCNT 60Ni 7

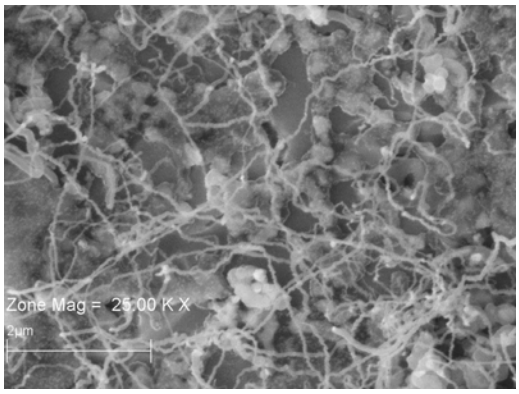

Figure A252: UHYCNT 60Ni 8

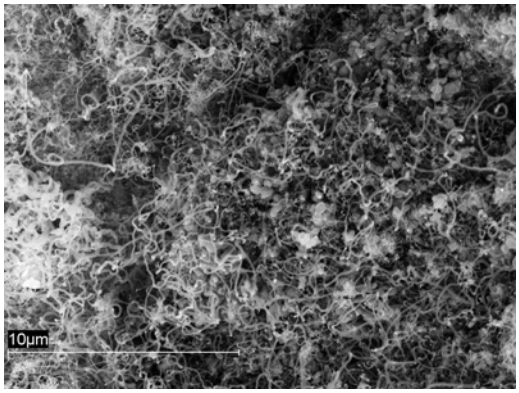

Figure A253: AcUHYCNT 60Ni 1

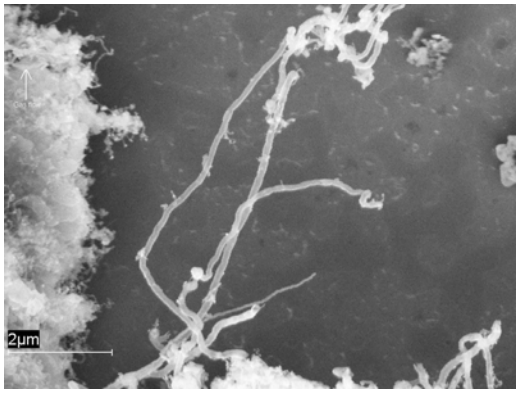

Figure A254: AcUHYCNT 60Ni 2

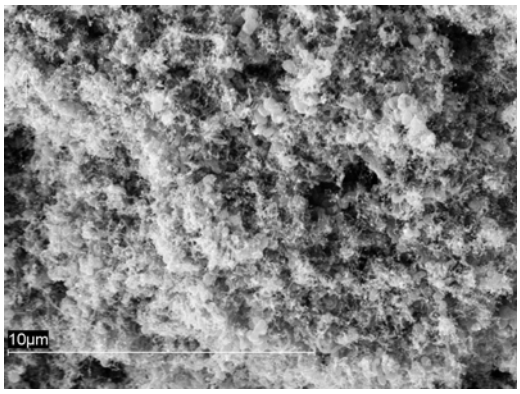

Figure A255: AcUHYCNT 60Ni 3

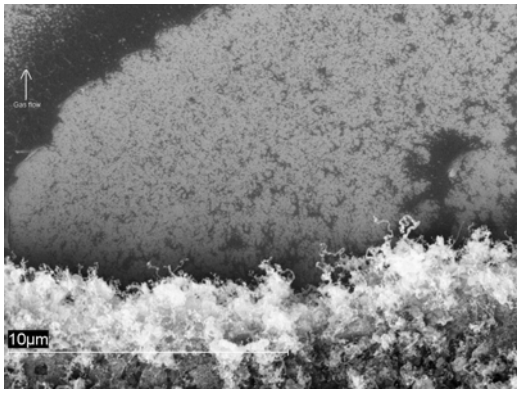

Figure A256: AcUHYCNT 60Ni 4

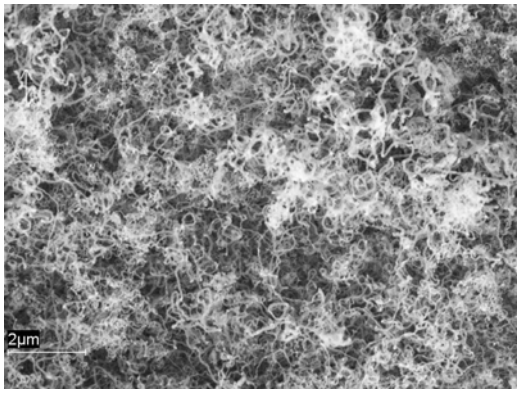

Figure A257: AcUHYCNT 60Ni 5

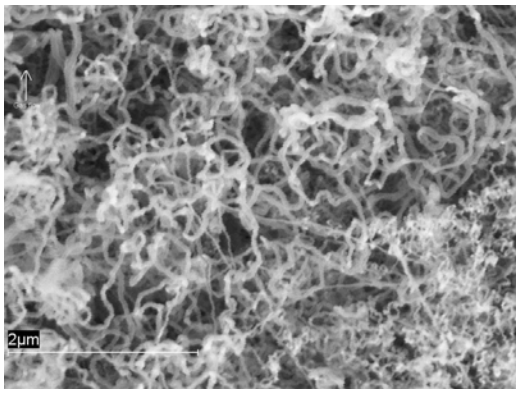

Figure A258: AcUHYCNT 60Ni 6

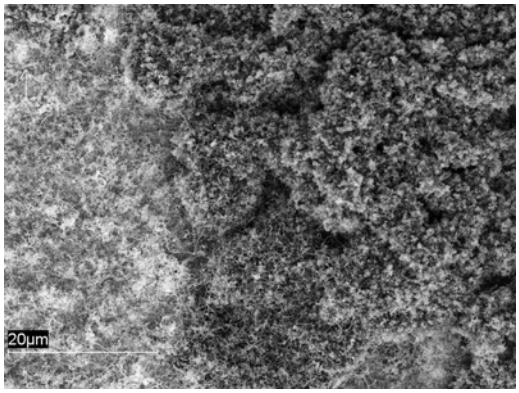

Figure A259: AcUHYCNT 60Ni 7

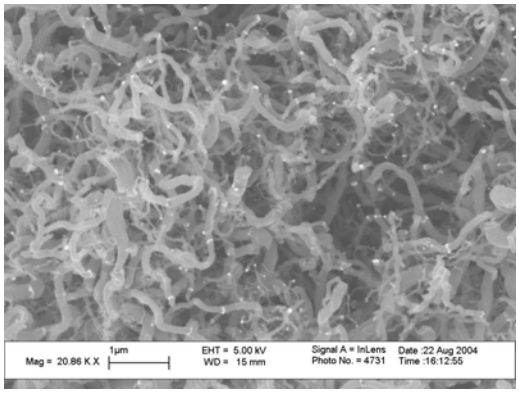

Figure A260: BULK CNT Ni IPA 500 1

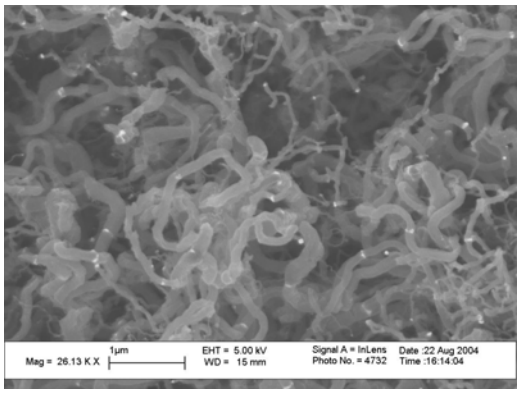

Figure A261: BULK CNT Ni IPA 500 2

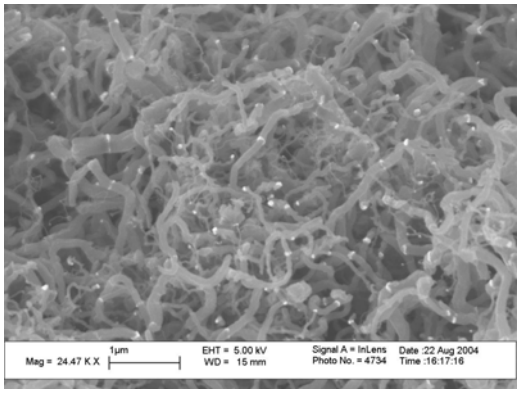

Figure A262: BULK CNT Ni IPA 500 3

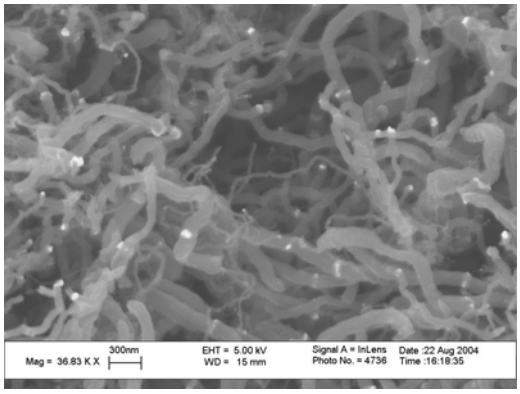

Figure A263: BULK CNT Ni IPA 500 4

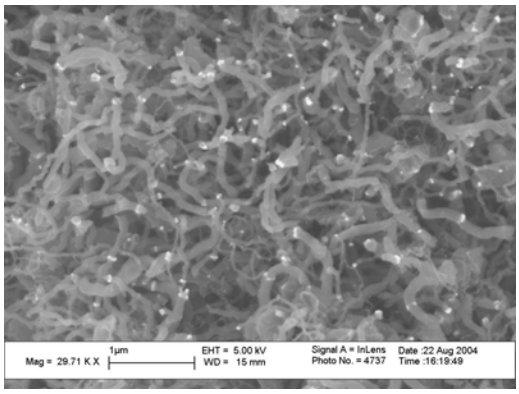

Figure A264: BULK CNT Ni IPA 500 5

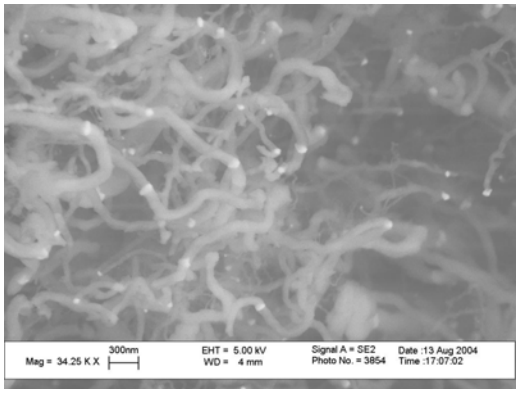

Figure A265: BULK CNT Ni IPA 500 6

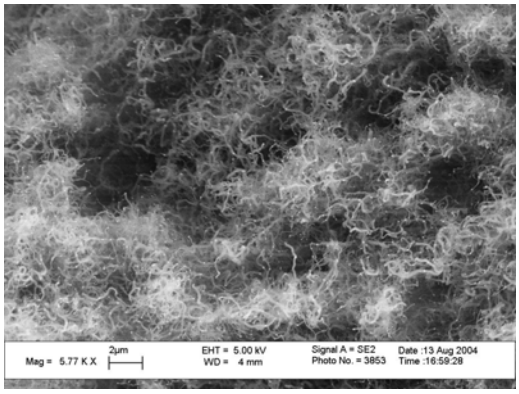

Figure A266: BULK CNT Ni IPA 500 7

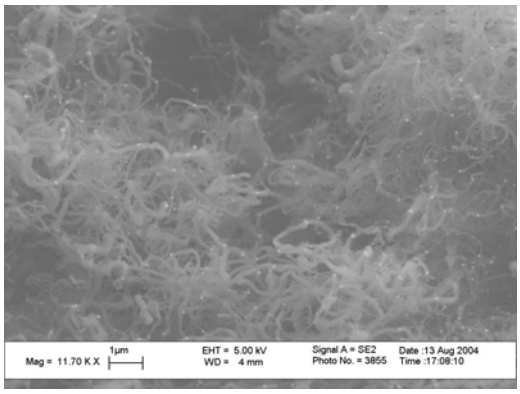

Figure A267: BULK CNT Ni IPA 500 8

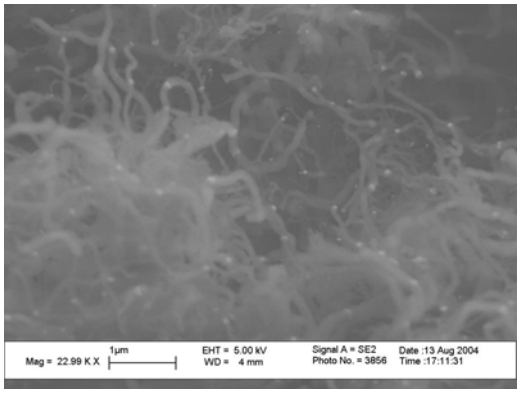

Figure A268: BULK CNT Ni IPA 500 9

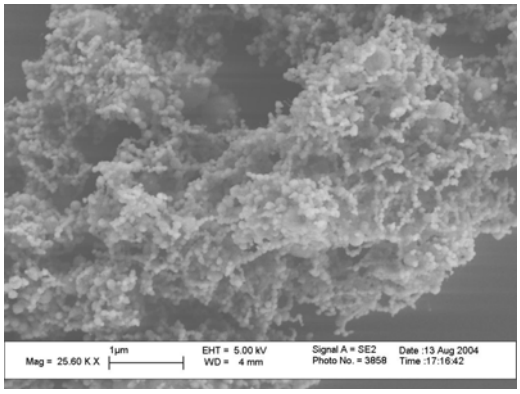

Figure A269: BULK CNT Ni IPA 500 10

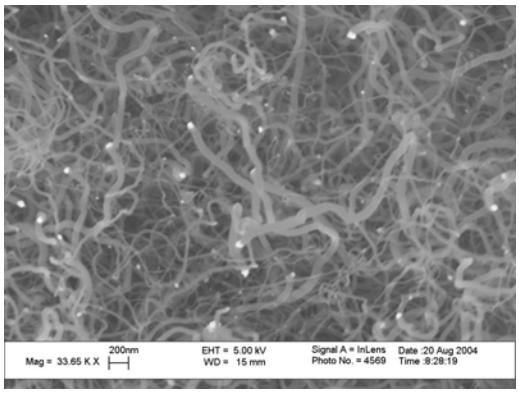

Figure A270: BULK CNT Ni IPA 600 1

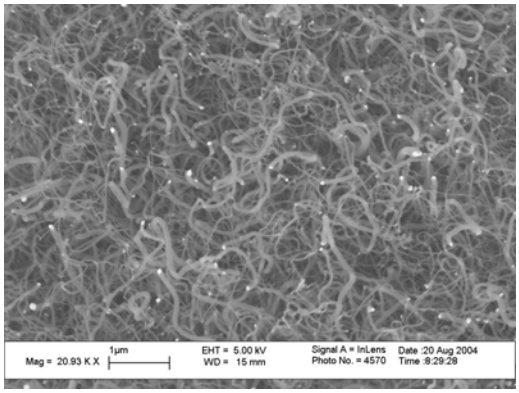

Figure A271: BULK CNT Ni IPA 600 2

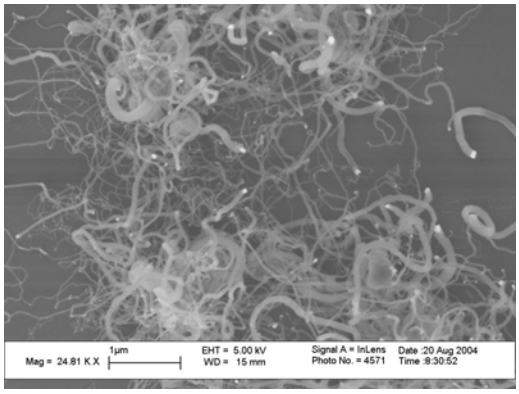

Figure A272: BULK CNT Ni IPA 600 3

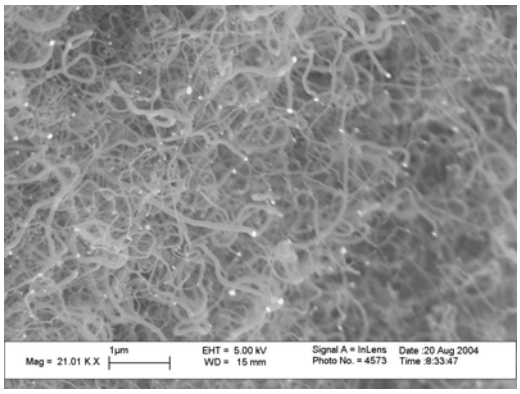

Figure A273: BULK CNT Ni IPA 600 4

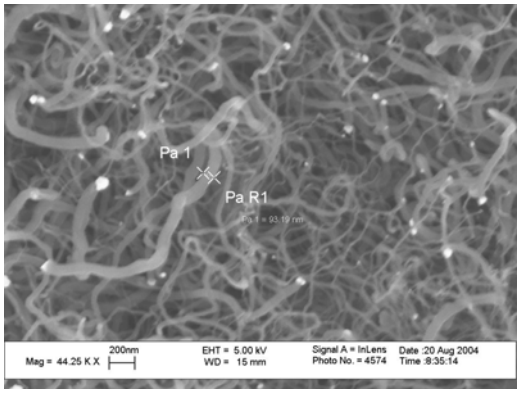

Figure A274: BULK CNT Ni IPA 600 5

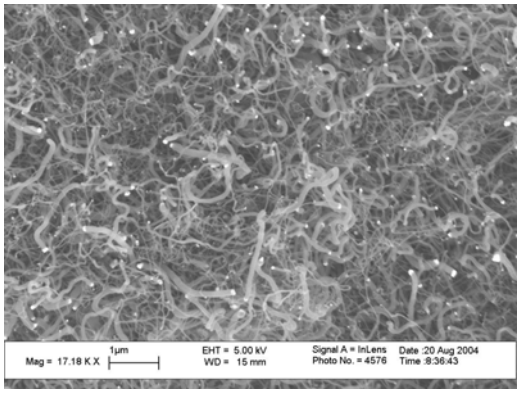

Figure A275: BULK CNT Ni IPA 600 6

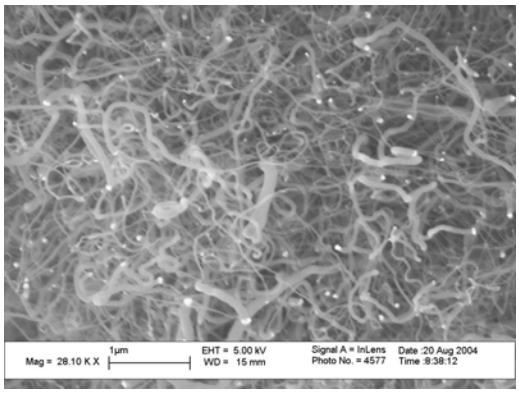

Figure A276: BULK CNT Ni IPA 600 7

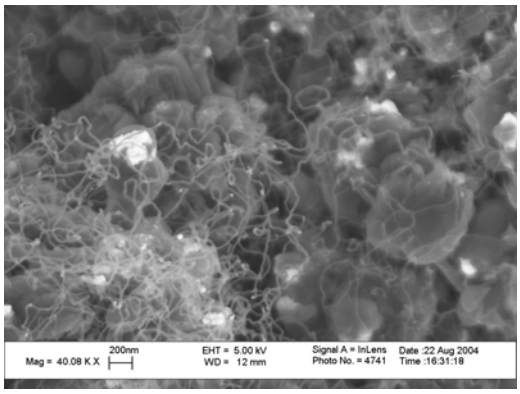

Figure A279: BULK CNT Ni IPA 700 3

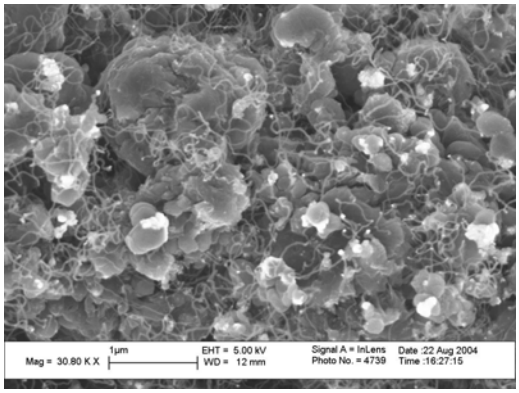

Figure A277: BULK CNT Ni IPA 700 1

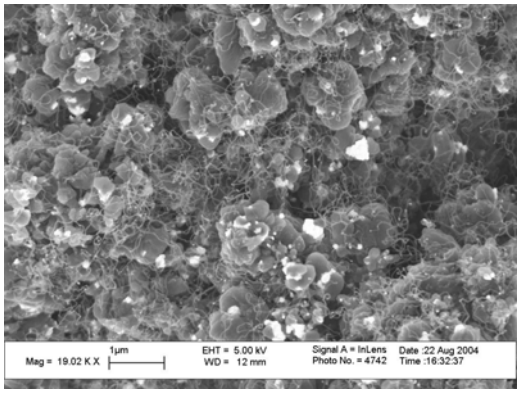

Figure A280: BULK CNT Ni IPA 700 4

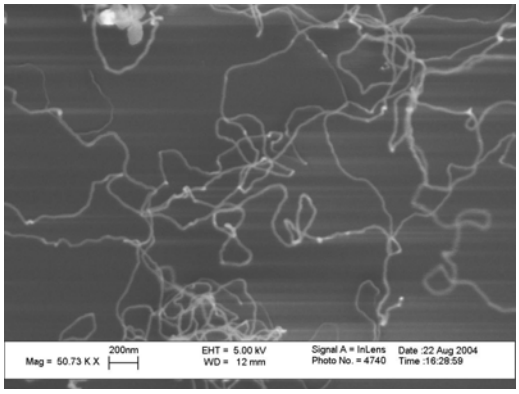

Figure A278: BULK CNT Ni IPA 700 2

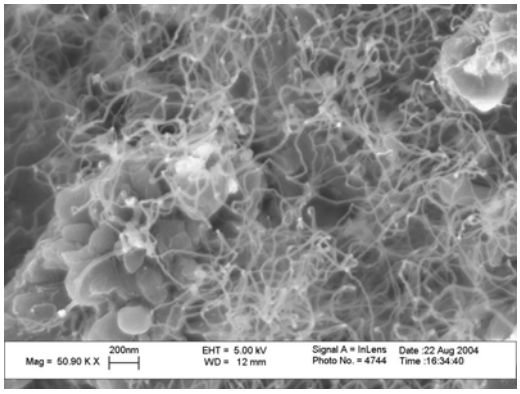

Figure A281: BULK CNT Ni IPA 700 5

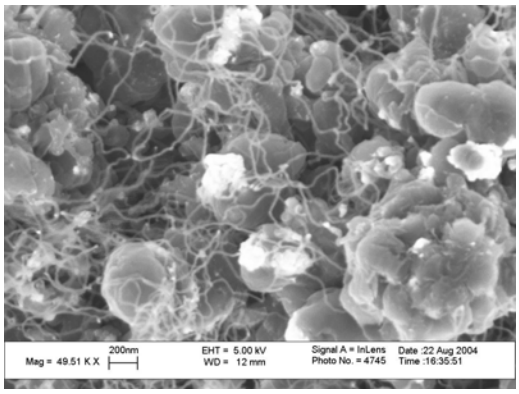

Figure A282: BULK CNT Ni IPA 700 6

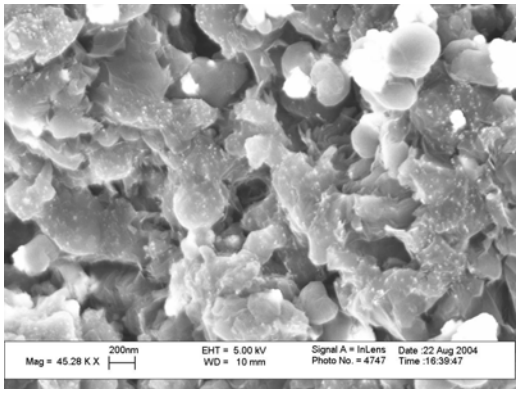

Figure A283: BULK CNT Ni IPA 800 1

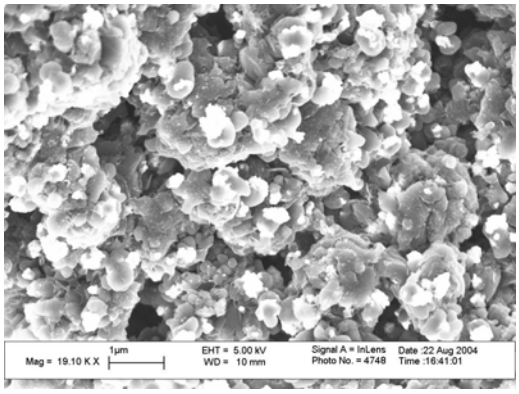

Figure A284: BULK CNT Ni IPA 800 2

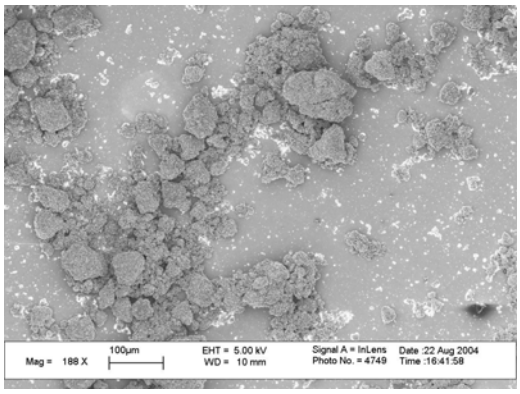

Figure A285: BULK CNT Ni IPA 800 3

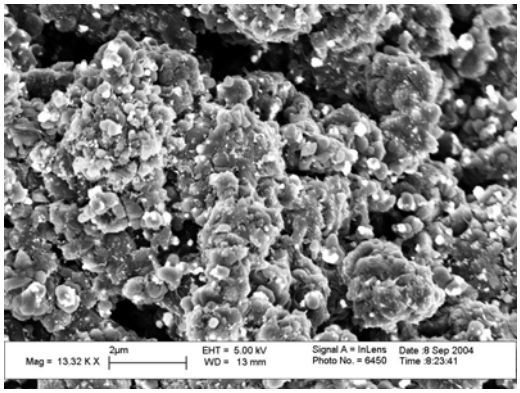

Figure A286: BULK CNT Ni IPA 800 4

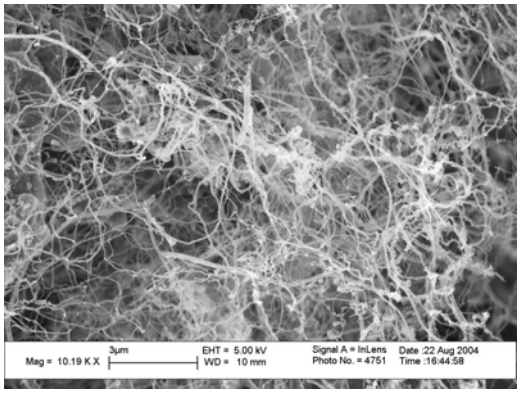

Figure A287: BULK CNT Ni IPA 900 1

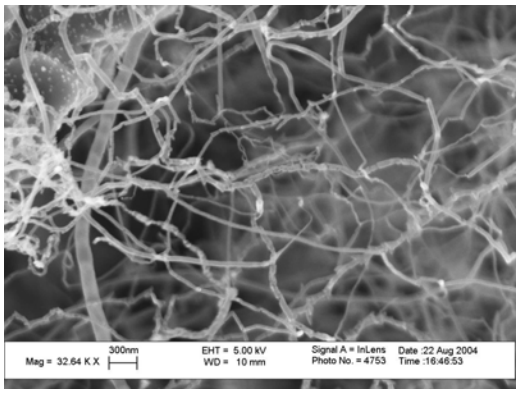

Figure A288: BULK CNT Ni IPA 900 2

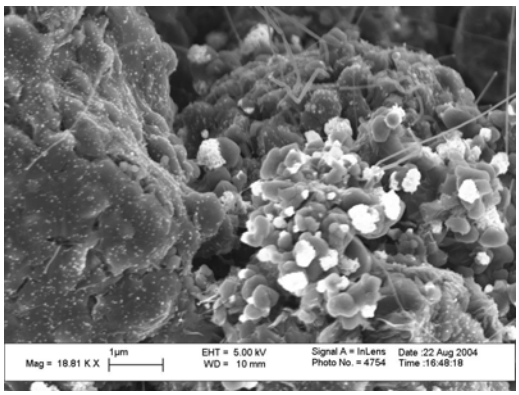

Figure A289: BULK CNT Ni IPA 900 3

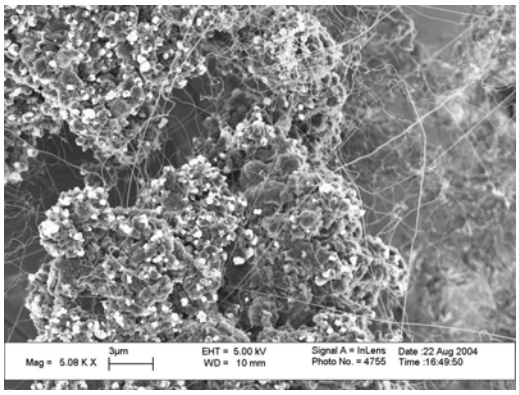

Figure A290: BULK CNT Ni IPA 900 4

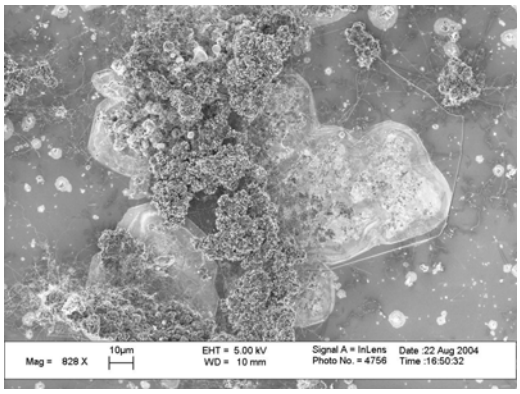

Figure A291: BULK CNT Ni IPA 900 5

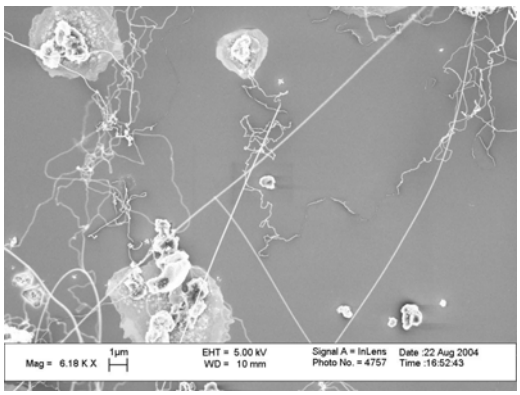

Figure A292: BULK CNT Ni IPA 900 6

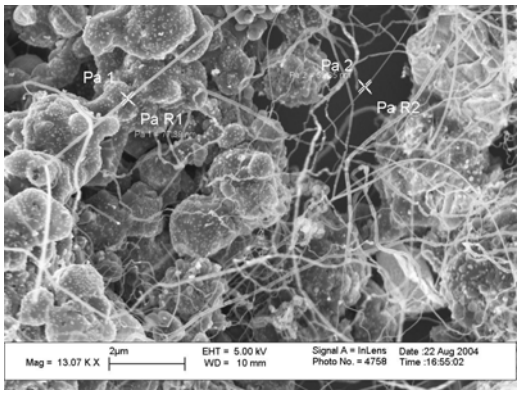

Figure A293: BULK CNT Ni IPA 900 7

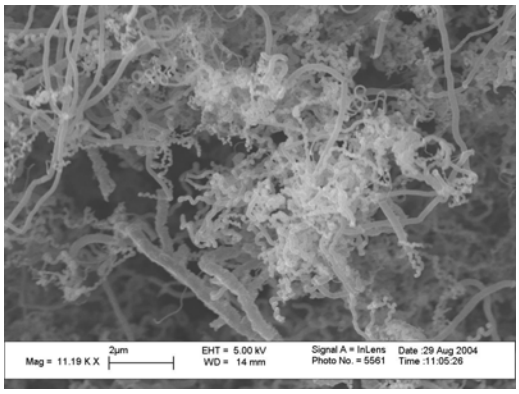

Figure A294: AcUHYCNT Ni IPA 500 1

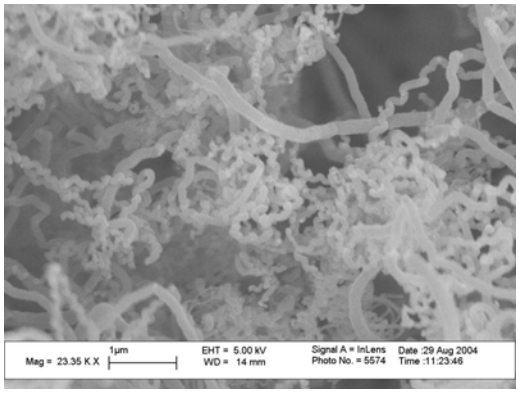

Figure A295: AcUHYCNT Ni IPA 500 2

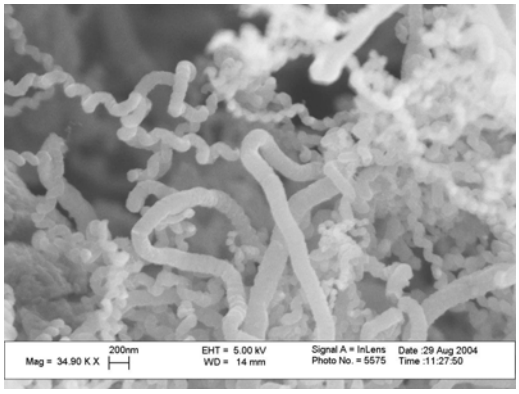

Figure A296: AcUHYCNT Ni IPA 500 3

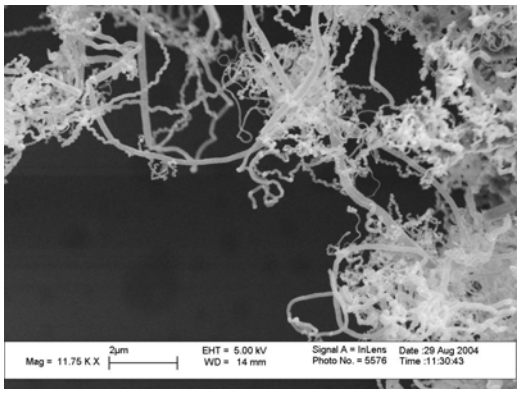

Figure A297: AcUHYCNT Ni IPA 500 4

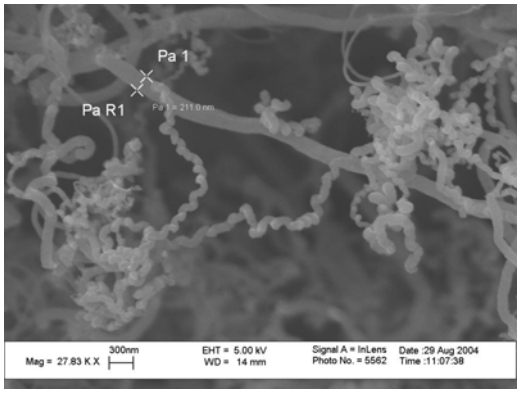

Figure A298: AcUHYCNT Ni IPA 500 5

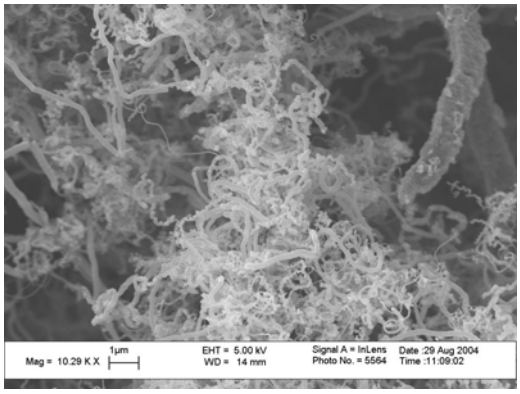

Figure A299: AcUHYCNT Ni IPA 500 6

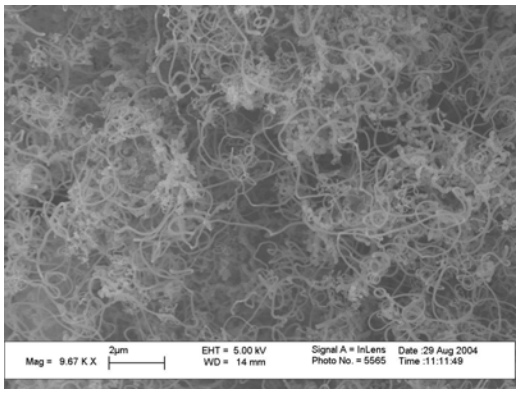

Figure A300: AcUHYCNT Ni IPA 500 7

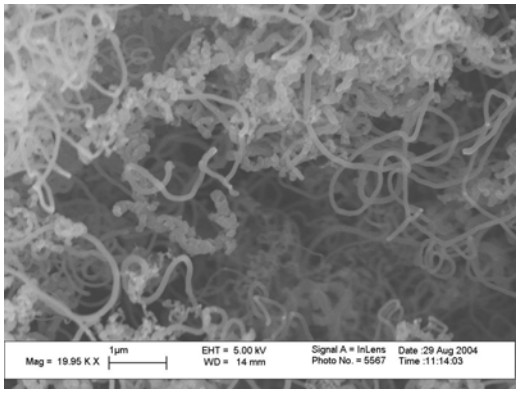

Figure A301: AcUHYCNT Ni IPA 500 8

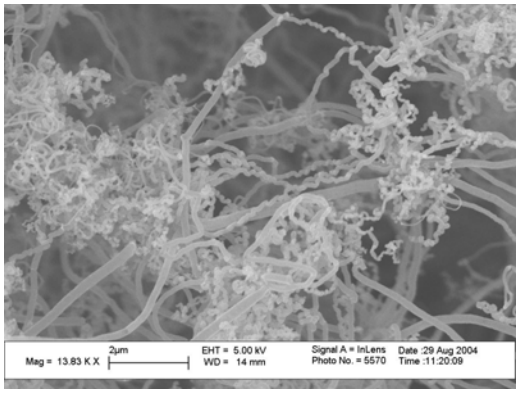

Figure A302: AcUHYCNT Ni IPA 500 9

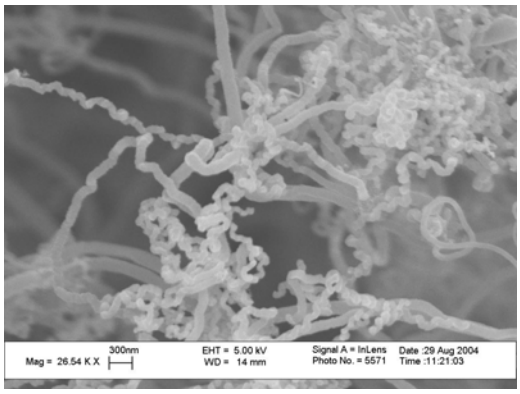

Figure A303: AcUHYCNT Ni IPA 500 10

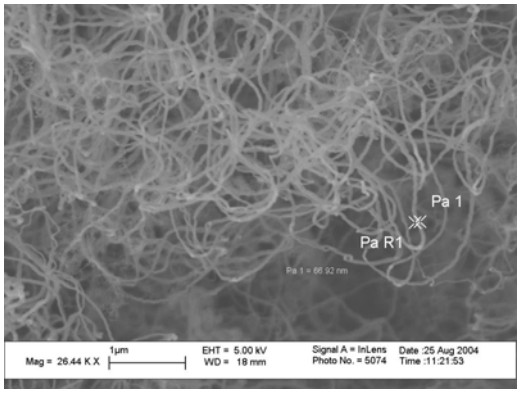

Figure A304: AcUHYCNT Ni IPA 600 1

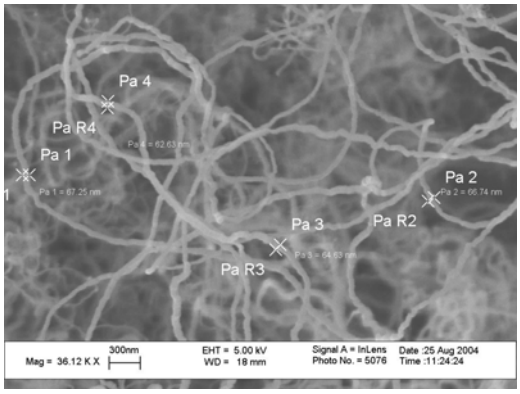

Figure A305: AcUHYCNT Ni IPA 600 2

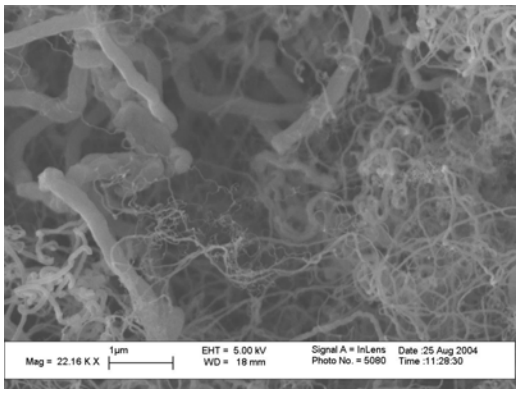

Figure A306: AcUHYCNT Ni IPA 600 3

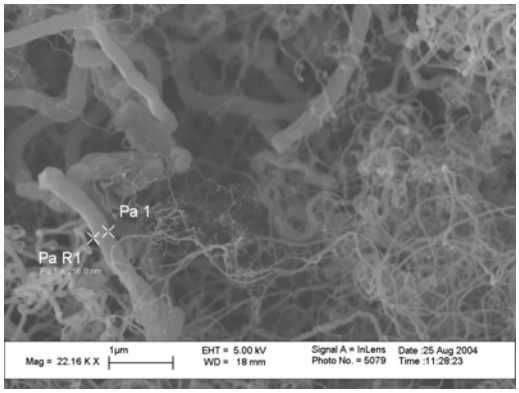

Figure A307: AcUHYCNT Ni IPA 600 4

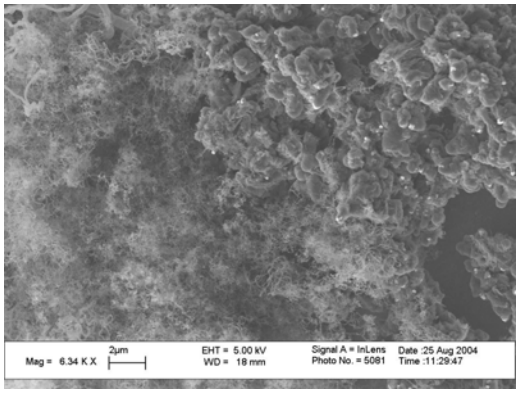

Figure A308: AcUHYCNT Ni IPA 600 5

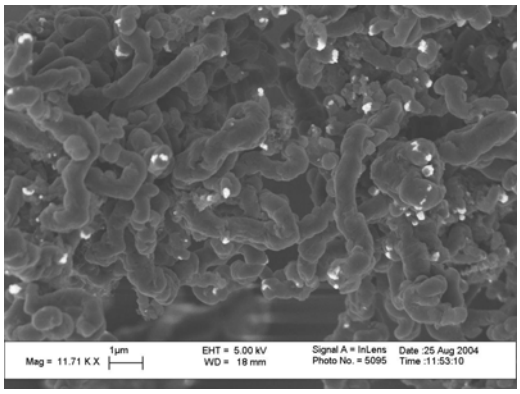

Figure A309: AcUHYCNT Ni IPA 700 1

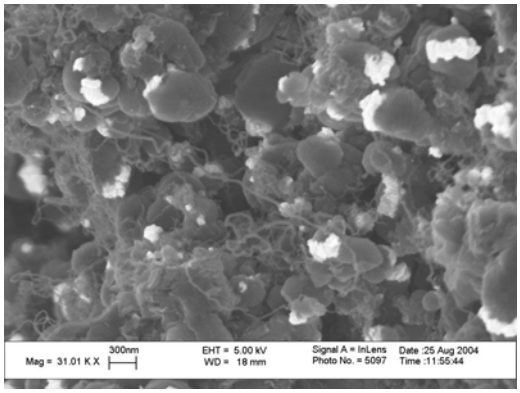

Figure A310: AcUHYCNT Ni IPA 700 2

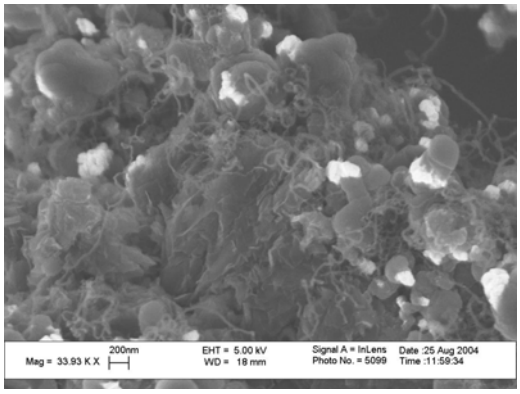

Figure A311: AcUHYCNT Ni IPA 700 3

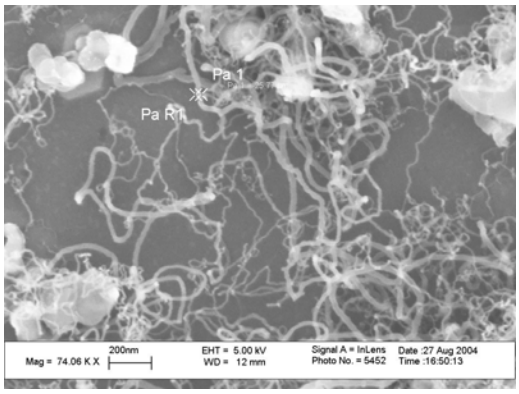

Figure A312: AcUHYCNT Ni IPA 700 4

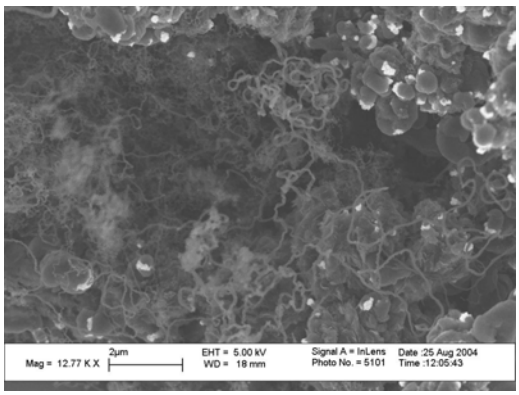

Figure A313: AcUHYCNT Ni IPA 700 5

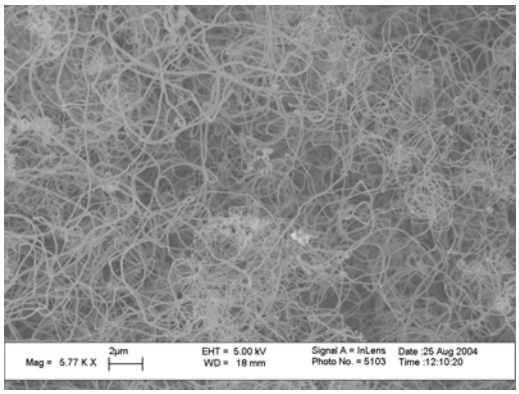

Figure A314: AcUHYCNT Ni IPA 800 1

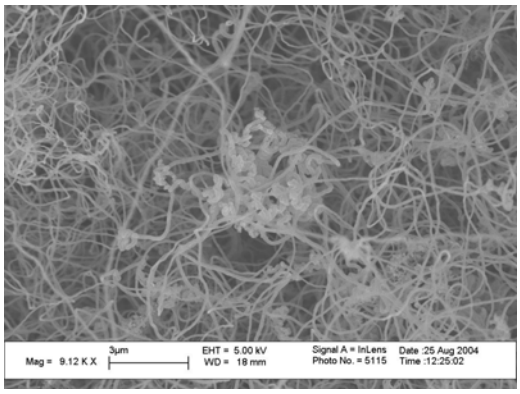

Figure A315: AcUHYCNT Ni IPA 800 2

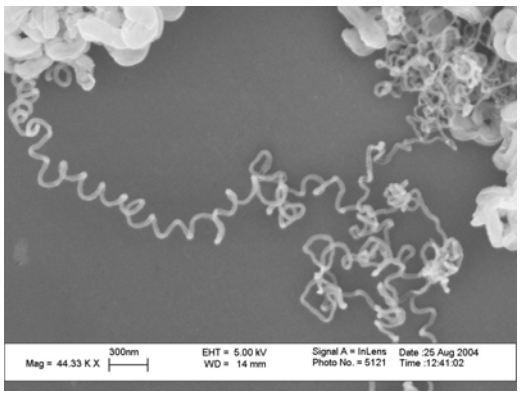

Figure A316: AcUHYCNT Ni IPA 800 3

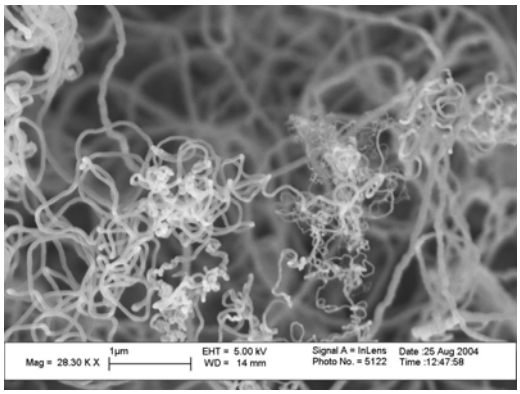

Figure A317: AcUHYCNT Ni IPA 800 4

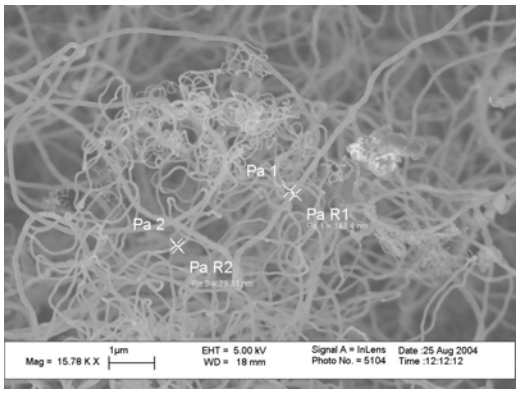

Figure A318: AcUHYCNT Ni IPA 800 5

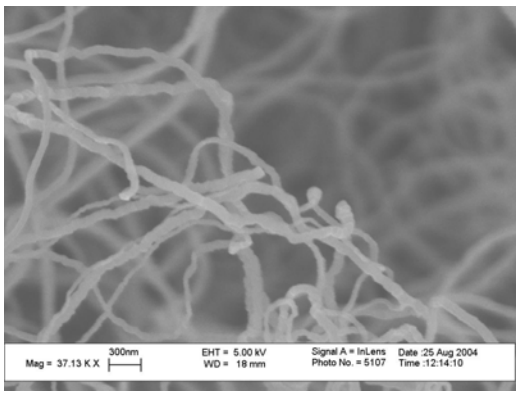

Figure A319: AcUHYCNT Ni IPA 800 6

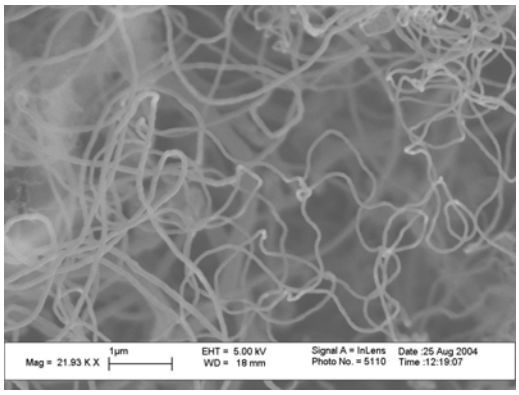

Figure A320: AcUHYCNT Ni IPA 800 7

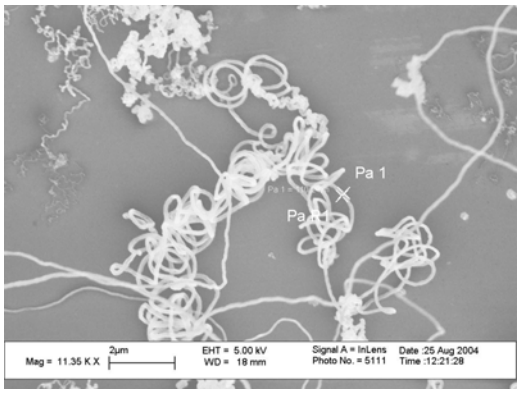

Figure A321: AcUHYCNT Ni IPA 800 8

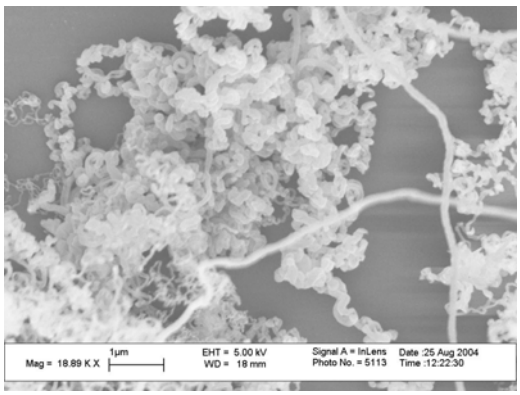

Figure A322: AcUHYCNT Ni IPA 800 9

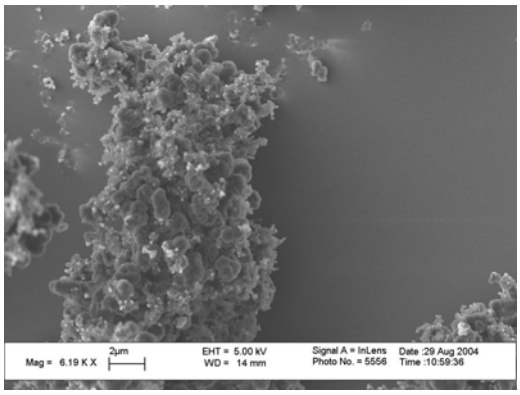

Figure A323: AcUHYCNT Ni IPA 900 1

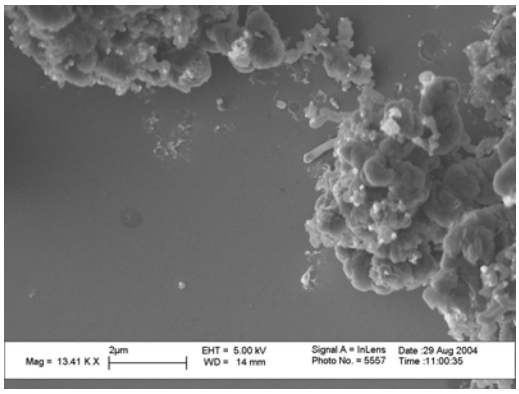

Figure A324: AcUHYCNT Ni IPA 900 2

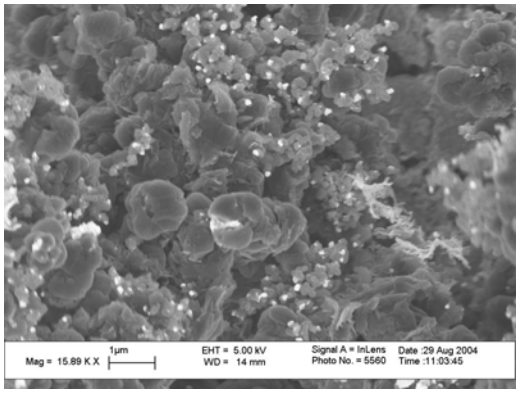

Figure A325: AcUHYCNT Ni IPA 900 3

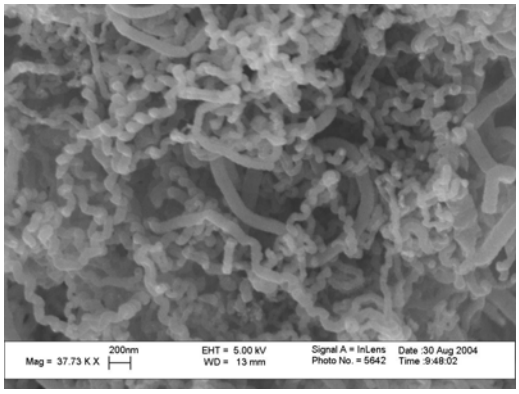

Figure A326: AcUHYCNT Ni IPA 500 50V 1

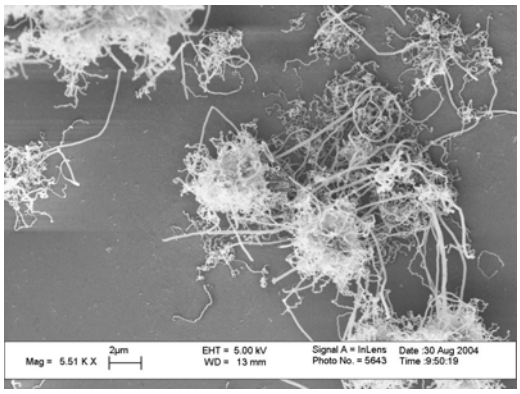

Figure A327: AcUHYCNT Ni IPA 500 50V 2

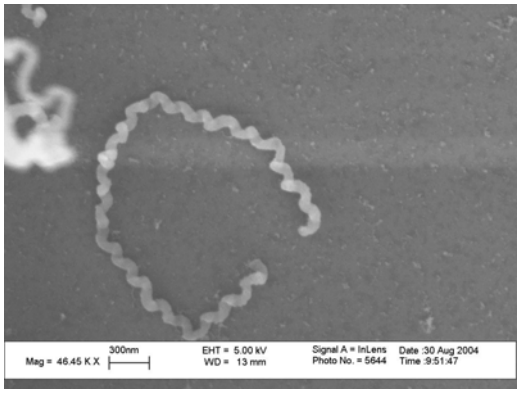

Figure A328: AcUHYCNT Ni IPA 500 50V 3

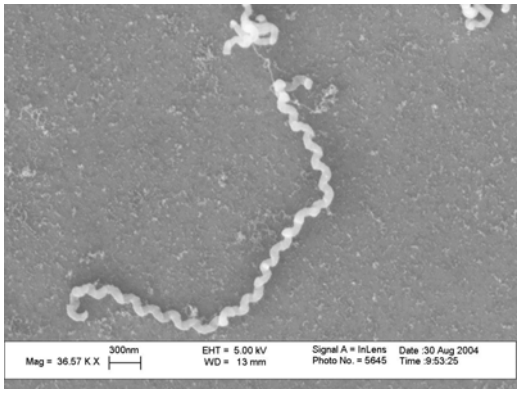

Figure A329: AcUHYCNT Ni IPA 500 50V 4

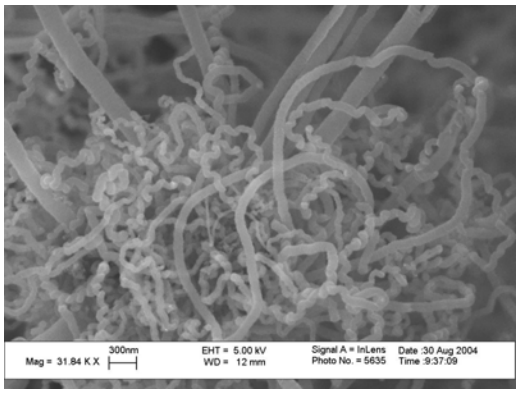

Figure A330: AcUHYCNT Ni IPA 500 50V 5

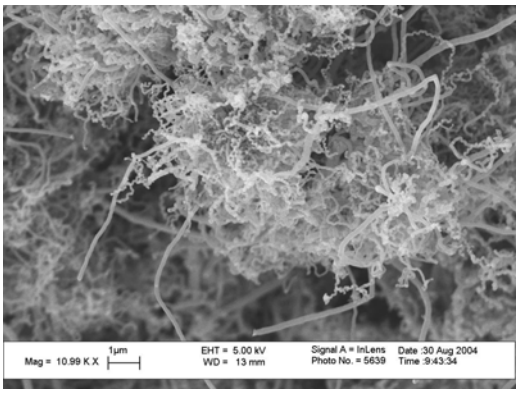

Figure A332: AcUHYCNT Ni IPA 500 50V 7

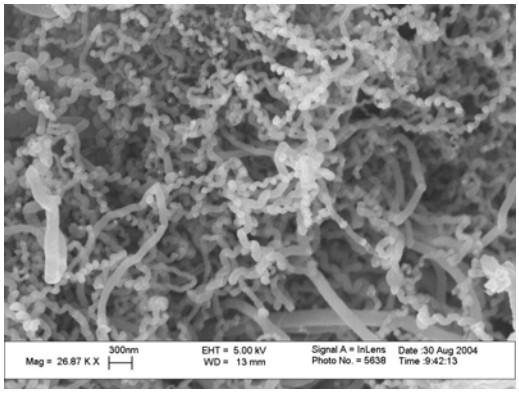

Figure A331: AcUHYCNT Ni IPA 500 50V 6

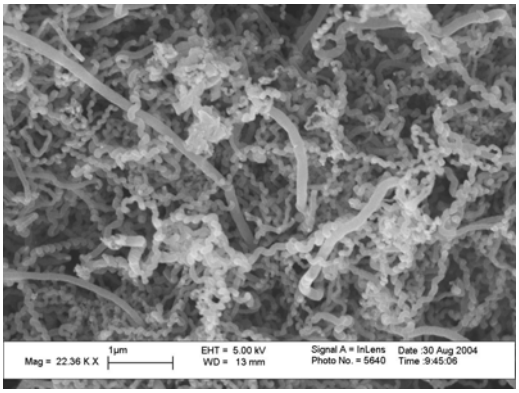

Figure A333: AcUHYCNT Ni IPA 500 50V 8

REFERENCES

[1] H.W. Kroto, J.R. Heath, S.C.O'Brien, R.F. Curl, R.E. Smalley; *C60 Buckminsterfullerene*, Nature **318** (1985) 162.

[2] A. Oberlin, M. Endo, T.Koyama; *Filamentous growth of carbon through benzene decomposition*, J. Cryst. Growth **32** (1976) 335.

[3] H.G. Tennent , "*Carbon fibrils, method for producing same and compositions containing same,*" U.S. Patent 4,663,230, May 5 1987.

[4] S. Iijima; *Helical Microtubules of Graphitic Carbon*, Nature **354** (1991) 56.

[5] M.S. Dresselhaus, G. Dresselhaus, P.C. Ecklund; *Physical Properties of Carbon Nanotubes*, Imperial College Press, London (1996).

[6] C. Li, T.-W. Chou; *Elastic Moduli of Multi-Walled Carbon Nanotubes and the Effect of van der Waals Forces*, Composite Science and Technology, **63** (2003) 1517.

[7] B.T. Kelly; *Physics of Graphite*, Applied Science Press, London (1981).

[8] S. Amelinckx, X.B. Zhang, D. Bernaerts, X.F. Zhang, V. Ivanov, J.B. Nagy, *A Formation Mechanism for Catalytically Grown Helix-Shaped Graphite Nanotubes*, Science **265** (1994) 635.

[9] M. Zhang, Y. Nakayama, L. Pan ; *Synthesis of Carbon Tubule Nanocoils in High Yield Using Iron-Coated Indium Tin Oxide as Catalyst* , Japan. J. Appl. Phys. **39** (2000) 1242.

[10]Y. Nakayama, *Proceedings from IS and T's NIP 18: International Conference on Digital Printing Technologies*, Society for Imaging Science and Technology, (2002) 458.

[11] R. Andrews, D. Jacques, D. Qian, T. Rantell; *Multiwall Carbon Nanotubes: Synthesis and Application*, Acc. Chem. Res **35** (2002) 1008.

[12] Park, *Chemical Vapor Deposition*, ASM International, Materials Park (2001).

[13] O. Zhou, H. Shimoda, B. Gao, S. Oh, L. Fleming, G.Yue; *Materials Science of Carbon Nanotubes: Fabrication, Integration, and Properties of Macroscopic Structures of Carbon Nanotubes*, Acc. Chem. Res **35** (2002) 1045.

[14] T. Ebbsen, Carbon Nanotubes: Preparation and Properties, CRC Press, Boca Raton, 1997.

[15] S. Huang, L. Dai, A. Mau; *Controlled Fabrication of Large-Scale Aligned Carbon Nanofiber/Nanotube Patterns by Photolithography*, Adv. Mater. **14** (2002) 1140.

[16] S. B. Sinnot, R. Andrews, D. Qian, A.M. Rao, Z. Mao, E.C. Dickey, F. Derbyshire; *Model of Carbon Nanotube Growth through Chemical Vapor Deposition*, Chem. Phys. Lett. **315** (1999) 25.

[17] R. T. K. Baker, P.S. Harris; *Formation of Filamentous Carbon in Chemistry and Physic of Carbon 14*, Marcel Dekker, New York (1978) 83.

[18] C. Ducati, I. Alexandrou, M. Chhowalla, G.A. J. Amaratunga, J. Robertson; *Temperature Selective Growth of Carbon Nanotubes by Chemical Vapor Deposition*, J. Appl. Phys **92** (2002) 3299.

[19] V. Vincguerra, F. Buonocore, G. Panzera, L. Occhipinti; *Growth Mechanisms in Chemical Vapor Deposited Carbon Nanotubes,* Nanotechnology **14** (2003) 655.

[20] J. Xie, C.L. Ong, V.K. Varadan, SPIE Int. Symp. On Smart Materials and Structures (San Diego).

[21] V.K. Varadan, J.Xie; *Synthesis of Carbon Nanocoils by Microwave CVD,* Smart Mater. Struct. **11** (2002) 728.

[22] Z.P Huang, D.Z Wang, J.G Wen, M. Sennet, H.Gibson, Z.F. Ren; *Effect of Nickel, Iron and Cobalt on Growth of Aligned Carbon Nanotubes*, Appl. Phys. A **74** (2002) 387.

[23] Y. Y. Wei, G. Eres, V.I. Merkulov, D.H. Lowndes; *Effect of Catalyst Film Thickness on Carbon Nanotube Growth by Selective Area Chemical Vapor Deposition,* Appl. Phys. Lett **78** (2001) 1394.

[24] H. Dai; *Carbon Nanotubes: Synthesis, Integration and Properties*, Acc. Chem. Res. **35** (2002) 1035.

[25] Y. Zhang, A. Chang, J. Cao, Q. Wang, W. Kim, Y. Li, N. Morris, E. Yenlimez, J. Kong, H. Dai; *Electric-Field Directed Growth of Aligned Single Walled Carbon Nanotubes*, Applied Physics Letters **79** (2001) 3155.

[26] J. Sohn, S. Lee; *Micropatterned Vertically Aligned Carbon-Nanotube Growth on a Si Surface or Inside Trenches,* Appl. Phys. A **74** (2002) 287.

[27] S. Niyogi, M,A. Hammon, H. Hu, B. Zhao, P. Bhowmik, R. Sen, M.E. Itkis, R.C. Haddon; *Chemistry of Single-Walled Carbon Nanotubes*, Accounts Chem. Res. **35** (2002) 1105.

[28] P. Poncharal, Z.L. Wang, D. Ugarte and W.A. De Heer, *Electrostatic Deflections and Electromechanical Resonances of Carbon Nanotubes*, Science, **283** (1999)1513.

[29] M. M. J. Treacy, T.W. Ebbesen, T.W. Gibson; *Exceptionally High Young's Modulus Observed for Individual Carbon Nanotubes,* Nature **381** (1996) 678.

[30] E. W. Wong, P. E. Sheehan, C. M. Lieber; *Nanobeam Mechanics: Elasticity, Strength, and Toughness of Nanorods and Nonotubes*, Science **277** (1997) 1971.

[31] J. P. Salvetat, J. M. Bonard, N. H. Thomson, A. J. Kulik, L. Farro, W. Bennit, L. Zuppiroli; *Mechanical Properties of Carbon Nanotubes*, J. Appl. Phys. A **69** (1999) 255.

[32] M.F. Yu, O. Lourie, M. Dyer, K. Moloni, T. Kelly; *Strength and Breaking Mechanism of Multiwalled Carbon Nanotubes under Tensile Load*, Science **287** (2000) 637.

[33] J.P. Lu; *Elastic Properties of Carbon Nanotubes and Nanoropes,* Phys. Rev. Lett. **79** (1997) 1297.

[34] S. Berber, Y.K. Kwon, D. Tomanek; *Unusually High Thermal Conductivity of Carbon Nanotubes,* Physical Review Letters **84** (2000) 4613.

[35] J. Hone, M. Whitney, A. Zettl, *Thermal Conductivity of Single Walled Carbon Nanotubes*, Synthetic Metals **103** (1999) 2498.

[36] J. Hone, M. C. Llaguno, M. J. Biercuk, A.T. Johnson, B. Batlogg, Z. Benes, J.E. Fisher; *Thermal Properties of Carbon Nanotubes and Nanotube Based Materials*, Appl. Phys. A **74** (2002) 339.

[37] A. Javey, M. Shim, H. Dai; *Electrical Properties and Devices of Large Diameter Single Walled Carbon Nanotubes*, Applied Physics Letters **80** (2002) 1064.

[38] M. Ouyang, J.L. Huang, C. Lieber; *Fundamental Electronic Properties and Applications of Single Walled Carbon Nanotubes*, Acc. Chem. Res. **35** (2002) 1018.

[39] A. Maiti, A. Svizhenko, M.P. Anantram; *Electronic Transport through Carbon Nanotubes: Effects of Structural Deformation and Tube Chirality*, Phys. Rev. Lett. **88** (2002) 126805.

[40] B.E.Conway; *Electrochemical Supercapacitors – Scientific Fundamentals and Technological Applications*, Kluwer Academic/Plenum, New York (1999).

[41] J. Bird; *Electrical and Electronic Principles and Technology*, Newnes, Oxford (2000), 54.

[42] S.O. Kasap; *Principles of Electrical Engineering Devices and Materials*, McGraw- Hill, New York (2000) 558.

[43] M. Brotherton, *Capacitors*, D. Van Nostrand Company, New York (1946) 59.

[44] A. Schneuwly, R. Gallay; *Properties and applications of supercapacitors from the state-of-the-art to future trends*, PCIM Proceedings Europe Official Proceedings of the Forty-First International Power Conversion Conference (2000) 115.

[45] M.Endo, T. Takeda, Y.J Kim, K. Kobisha, K. Ishii; *Structural Characterization of Carbon Nanofibers Obtained by Hydrocarbon Pyrolysis*, Carbon Sci. **1** (2001) 117.

[46] C. Emmenegger, Ph. Mauron, P. Sudan, P. Wenger, V. Herman, R. Gallay, A. Zuttel; *Investigation of Electrochemical Double Layer (ECDL) Capacitors Electrodes Based on Carbon Nanotubes and Activated Carbon Materials*, J. Power Sources (2003).

[47] Online: http://pl.legoff.free.fr/us/usscap.htm.

[48] Y. Kim, Online: http://www.reed-electronics.com/ecnmag/index.asp?layout=article&articleid=CA202159 &text= double+layer+capacitor.

[49] D. Qu; *Studies of the Activated Carbon used in Double Layer Supercapacitors*, J. Power Sources **109** (2002) 403.

[50] E. Frackowiak, F. Beguin; *Carbon Materials for the Electrochemical Storage of Engery in Capacitors*, Carbon **39** (2001) 937.

[51] R. Kötz, M. Carlen; *Principles and Applications of Electrochemical Capacitors*, Electrochim. Acta **45** (2000) 2483.

[52] J.H. Jang, S. Han, T. Hyeon, S.M. Oh; *Electrochemical Capacitor Performance of Hydrous Ruthenium Oxide/Mesoporous Carbon Composite Electrodes*, J. Power Sources **123** (2003) 79.

[53] R.J. Cava; *Future Directions in Solid State Chemistry: Report of the NSF-Sponsored Workshop*, Progress in Solid State Chemistry **30** (2002) 1.

[54] C. Niu, E.K. Sichel, R. Hoch, D. Moy, H. Tennent; *High Power Electrochemical Capacitors Based on Carbon Nanotube Electrodes*, Appl. Phys. Lett. **70** (1997) 11.

[55] R.Z. Ma, J. Liang, B.Q. Wei, B. Zhang, C.L. Xu, D.H. Wu; *Study of Electrochemical Capacitors Utilizing Carbon Electrodes*, J. Power Sources **84** (1999) 126.

[56] E. Frackowiak, S. Delpeux, K. Jurewicz, K. Szostak, D. Cazorla-Amoros, F. Beguin; *Enhanced Capacitance of Carbon Nanotubes through Chemical Activation*, Chem. Physics Lett. **361** (2002) 35.

[57] G. Arabale, D. Wagh, M. Kulkarni, I.S. Mulla, S.P. Vernekar, K. Vijayamohanan, A.M Rao; *Enhanced Supercapacitance of Multiwalled Carbon Nanotubes Functionalized with Ruthenium Oxide*, Chem. Physics Lett. **376** (2003) 207.

[58] Q. Xiao, X. Zhou; *The Study of Multiwalled Carbon Nanotube Deposited with Conducting Polymer for Supercapacitor*, Electrochim. Acta **48** (2003) 575.

[59] K.H. An, W.S. Kim, Y.S. Park, J.M. Moon, D.J. Bae, S.C. Lim, Y.S. Lee, Y.H. Lee; *Electrochemical Properties of High-Power Supercapacitors Using Single-Walled Carbon Nanotube Electrodes***,** Adv. Funct. Mater. **11** (2001) 387.